



University of Hamburg
Faculty of Mathematics,
Informatics and Natural Sciences
Department of Physics

Nuclear Resonance Scattering Study of Iridates, Iridium and Antimony Based Pyrochlores

Dissertation

zur Erlangung des Doktorgrades
des Fachbereichs Physik
der Universität Hamburg

vorgelegt von

Pavel Alexeev
aus Chekhov

Hamburg
2017

Whatever you are, be better
– *Lera Simacheva*

Gutachter der Dissertation:

Prof. Dr. Ralf Röhlsberger
Prof. Dr. Kornelius Nielsch

Mitglieder der Prüfungskommission:

Prof. Dr. Daniela Pfannkuche
Prof. Dr. Kornelius Nielsch
Prof. Dr. Ralf Röhlsberger
Prof. Dr. Raphaël P. Hermann
Dr. Hans-Christian Wille

Datum der Disputation:

7. April 2017

Vorsitzender des Prüfungsausschusses:

Prof. Dr. Daniela Pfannkuche

Vorsitzender des Fach-Promotionsausschusses:

Prof. Dr. Wolfgang Hansen

Dekan der MIN-Fakultät:

Prof. Dr. Heinrich Graener

Eidesstattliche Versicherung

Hiermit versichere ich an Eides statt, dass ich die vorliegende Arbeit selbstständig und ohne fremde Hilfe angefertigt und mich anderer als der im beigefügten Verzeichnis angegebenen Hilfsmittel nicht bedient habe. Alle Stellen, die wörtlich oder sinngemäß aus Veröffentlichungen entnommen wurden, sind als solche kenntlich gemacht. Ich versichere weiterhin, dass ich die Arbeit vorher nicht in einem anderen Prüfungsverfahren eingereicht habe und die eingereichte schriftliche Fassung der auf dem elektronischen Speichermedium entspricht. Ich bin mit einer Einstellung in den Bestand der Bibliothek des Fachbereiches einverstanden.

I, Pavel Alexeev confirm that the work presented in this thesis is my own. Where information has been derived from the other sources, I confirm that this has been indicated in the text. I confirm also that the thesis was not submitted to any other doctorate school and the submitted manuscript corresponds to the copy on the attached electronic memory device. I agree with the appearance of this work in the department library collection.

Hamburg, den

Unterschrift:

Abstract

This thesis shows the first synchrotron-based Mössbauer spectroscopy studies on iridium containing compounds and first vibrational spectroscopy on Sb containing compounds carried out at the P01 beamline of PETRA III. In this context, two types of x-ray monochromators have been developed: a monochromator for 73 keV photons with medium energy resolution, and a high-resolution backscattering monochromator based on a sapphire crystal. The monochromator for 73 keV x-rays is the key instrument for hyperfine spectroscopy on Iridium compounds, while the sapphire backscattering monochromator is purposed to vibrational spectroscopy on any Mössbauer resonances with the transition energies in the 20-50 keV range. Additionally, the signal detection for nuclear resonance scattering experiments at the beamline was significantly improved during this work, inspired by the high energies and low lifetimes of the employed resonances.

The first synchrotron-based hyperfine spectroscopy on Iridium-containing compounds was demonstrated by NRS on 73 keV resonance in ^{193}Ir . The results can be interpreted by dynamical theory of nuclear resonance scattering. In this work, special emphasis is set onto the electronic and magnetic properties of Ir nuclei in IrO_2 and in Ruddlesden-Popper (RP) phases of strontium iridates $\text{Sr}_{n+1}\text{Ir}_n\text{O}_{3n+1}$ ($n = 0, 1$). These systems are well-suited for studies with x-ray scattering techniques, since the scattered signal contains vast information about the widely tunable crystallographic and electronic structure of these systems; furthermore, studies with x-rays are less limited by absorption from iridium as it is the case for neutron scattering experiments. The hyperfine parameters in IrO_2 , SrIrO_3 and Sr_2IrO_4 have been measured via Nuclear Forward Scattering for the first time. Using the dynamical theory of NRS, the temperature and magnetic field dependence of the electric field gradient and magnetic hyperfine field on Ir nucleus have been determined for these compounds. In order to broaden the perspectives of NRS with the 73 keV resonance the first room temperature NRS on iridium metal is carried out. The results demonstrate NRS as a powerful research tool for the studies of iridium physics due to the high energy of the resonant photons and the high natural abundance of the ^{193}Ir isotope under study, paving the way for studies of magnetism and electronic properties under extreme conditions.

The second part of this work is dedicated to vibrational spectroscopy with Nuclear Inelastic Scattering (NIS). A sapphire backscattering monochromator was designed, installed and tested at the beamline. It provides high energy resolution due to the sub-mK tem-

perature control, though the resolution is limited from theoretically proposed sub-meV to meV by the quality of currently available sapphire crystals. With this device the energy resolution of 1.3(1) meV at 23.88 keV and of 3.2(4) meV at 37.13 keV was achieved. Following this development, the vibrational spectra of antimony in defect pyrochlore Ag-Sb-O compounds have been measured by means of NIS at 37.13 keV. Density of phonon states for the Sb(III) and for the Sb(V) site has been unambiguously revealed. The difference in site-specific antimony modes illustrates the importance of lattice dynamics for the engineering of these compounds.

Kurzfassung

In dieser Arbeit werden die ersten mit Synchrotronstrahlung durchgeführten Mössbauer-spektroskopischen Studien an iridiumhaltigen Verbindungen vorgestellt. Darüber hinaus wird die erste Röntgen-Analyse von Schwingungsmoden in antimonhaltigen, festen Lösungen an der Strahlführung P01 von PETRA III präsentiert. In diesem Zusammenhang wurden zwei Röntgenmonochromatoren entwickelt: ein Monochromator mit moderater Energieauflösung für 73 keV Photonen, sowie ein hochauflösender, saphir-basierter Rückstreumonochromator. Der Monochromator für 73 keV Strahlung ist für Hyperfeinspektroskopie an Iridium-haltigen Verbindungen gedacht. Der Rückstreumonochromator wurde für Schwingungsspektroskopie an allen Mössbauer-Resonanzen mit Übergangsenergien im Bereich von 20 bis 50 keV konzipiert. Inspiriert durch die Arbeit mit den hochenergetischen und kurzlebigen Mössbauer-Resonanzen wurde zusätzlich die Signalerfassungsmethode für die Kernresonanzstreuung an der Strahlführung P01 von PETRA III optimiert.

Die erste synchrotron-basierte Hyperfeinspektroskopie an Ir-haltigen Verbindungen wurde mittels Kernresonanzstreuung (NRS) am 73 keV Kernniveau des ^{193}Ir Isotops durchgeführt. Die Ergebnisse können durch die dynamische Theorie der Kernresonanzstreuung interpretiert werden. In dieser Arbeit werden die Studien der elektrischen und magnetischen hyperfeinen Wechselwirkungen an Ir in IrO_2 und in Ruddlesden-Popper (RP) Phasen von Strontium-Iridaten $\text{Sr}_{n+1}\text{Ir}_n\text{O}_{3n+1}$ ($n = 0, 1$) besonderes hervorgehoben. Innerhalb dieser Probensysteme gibt es eine große Variation der kristallographischen und elektronischen Struktur, wodurch sie für die Untersuchung mit den Methoden der Röntgenstreuung besonders interessant sind. Außerdem werden die Röntgenmethoden weniger als Neutronenexperimente durch die Absorption von Ir beeinflusst. Die Parameter von hyperfeinen Feldern in IrO_2 , in SrIrO_3 und in Sr_2IrO_4 wurden zum ersten Mal durch Nukleare Vorwärtsstreuung (NFS) bestimmt. Dank der experimentellen Ergebnisse und mit Hilfe der dynamischen Theorie der NRS, wurde die Temperaturabhängigkeit des elektrischen Feldgradienten am Ir-Kern und sowie des magnetischen Hyperfeinfeldes z.T. in Abhängigkeit vom äußeren Magnetfeld in diesen Verbindungen ermittelt. Dank der hohen Brillianz der Strahlungsquelle, konnten die ersten Raumtemperaturmessungen von Kernresonanzstreuung an Ir durchgeführt werden. Die Kombination aus hoher Brillianz, hoher Energie der Resonanz sowie der hohen natürlichen Isotopenhäufigkeit des ^{193}Ir ermöglichte es, die Kernresonanzstreuung als einzigartige Forschungsmethode für Ir-Verbindungen zu etablieren. Damit wurden die Voraussetzungen für künftige Studien von magnetischen und elektronischen Eigen-

schaften von Ir-Verbindungen unter Extremenbedingungen geschaffen.

Der zweite Teil dieser Arbeit ist der Phononenspektroskopie mittels Nuklear Inelastischer Streuung (NIS) gewidmet. Der Saphir-basierte Rückstreumonochromator wurde an der Strahlführung P01 von PETRA III konzipiert, aufgebaut und in Betrieb genommen. Die sub-mK präzise Temperaturregelung ermöglicht hohe sub-meV Energieauflösung, allerdings ist diese durch die Qualität des Saphirs auf wenige meV beschränkt. Es wurde eine Energieauflösung von 1.3(1) meV bei 23.88 keV und von 3.2(4) meV bei 37.13 keV mit diesem Monochromator erreicht. Durch diese Entwicklung konnten Phononenspektren von Sb in defekten Pyrochlor-Ag-Sb-O-Verbindungen durch NIS bei 37.13 keV gemessen werden. Phononenzustandsdichte für den Sb(III)- und für den Sb(V)-Platz wurden eindeutig ausgewiesen. Die Resultate über die gitterspezifische Schwingungsmoden veranschaulichen den Einfluss der Gitterdynamik auf die Eigenschaften dieser Verbindungen.

Contents

List of Figures	III
List of Tables	VII
Introduction	1
1 System under study: transition metal oxide iridates	5
2 System under study: binary oxides Ag-Sb-O	13
3 Theory	17
3.1 Hyperfine Interactions	17
3.1.1 Ferromagnetism	25
3.1.2 Antiferromagnetism	25
3.2 Mössbauer Effect	27
3.3 Lamb-Mössbauer factor	29
3.4 Nuclear Resonant Scattering	34
3.4.1 Nuclear Forward Scattering	34
3.4.2 Nuclear Inelastic spectroscopy: lattice vibrations	48
4 Experimental Techniques	55
4.1 Set-up for Nuclear Resonance Scattering	55
4.2 High-Resolution Monochromators	56
4.3 Detection of NRS signal	67
4.3.1 Avalanche photodiode detector	67
4.3.2 Detector electronics	70
4.4 Beam purity	71
4.5 Monochromator for NFS on Ir compounds	73
4.5.1 Design	73
4.5.2 Performance of the monochromator	78
4.6 Al ₂ O ₃ backscattering monochromator	84
4.6.1 Design	84
4.6.2 Performance at 23.88 keV at the ¹¹⁹ Sn nuclear resonance	90
4.6.3 Performance at 37.13 keV at the ¹²¹ Sb nuclear resonance	94
5 Nuclear Forward Scattering at the ¹⁹³Ir resonance	97
5.1 Iridium and the 73 keV Mössbauer resonance in ¹⁹³ Ir	97
5.2 Lattice dynamics in Ir studied with NFS	101

6	Hyperfine interactions in iridium compounds	113
6.1	Electric hyperfine interactions in IrO_2 and in SrIrO_3	113
6.2	Combined hyperfine interactions in Sr_2IrO_4	118
7	Density of phonon states in Ag-Sb-O compounds	125
8	Conclusions and Outlook	133
A	Appendix	137
A.1	Modern x-ray sources: parameters and operation modes	137
A.2	Operation code for MCA device at P01 beamline	142
A.3	Script for a grid simulation in CONUSS	144
A.4	Some properties of the 73 keV photon beam at the P01 beamline	146
	Bibliography	149

List of Figures

1.1	Splitting of $5d$ orbitals in the presence of the crystal electric field and the spin-orbit coupling	7
1.2	Effect of SOC and Coulomb repulsion in iridates	9
1.3	Crystal structure and magnetic order in Sr_2IrO_4	11
2.1	Crystal structure of AgSbO_3 compound	14
2.2	Mössbauer spectra from Ag-Sb-O compounds	16
3.1	Dependence of the isomer shift on the oxidation state	18
3.2	Perturbation of nuclear levels under the influence of the hyperfine interactions	20
3.3	Effective magnetic field on nucleus in case of canted antiferromagnet . . .	26
3.4	Lattice vibrational states and corresponding transitions	28
3.5	Temperature dependence of the Lamb-Mössbauer factor	32
3.6	Mössbauer and NRS spectra: effect of the sample thickness	38
3.7	Integrated signal for dynamical beating	40
3.8	Effect of hyperfine splitting on MS and NFS spectra	43
3.9	Electric Field Gradient imaged by MS and NRS spectra and time-spectra .	46
3.10	Magnetic hyperfine interactions imaged by MS and NRS spectra and time-spectra	47
3.11	Procedure of treatment of NIS spectrum	50
4.1	A layout of a beamline	57

4.2	The most frequently used constructions of multiple-crystal monochromators	61
4.3	DuMond diagrams for two crystals	62
4.4	DuMond diagram for a wide Bragg angle range	63
4.5	Peak reflectivity of all Bragg reflections in Si and Al ₂ O ₃ at 295 K and 4 K .	65
4.6	Layouts of the backscattering experiments at P01 beamline of PETRA III and ID18 beamline of ESRF	66
4.7	Properties and setup of silicon APD detectors	69
4.8	Layout of electronics for measuring NRS	70
4.9	Beam time structure in the PETRA ring	72
4.10	DuMond diagram for the setup of MRM	75
4.11	CAD-model of the MRM	77
4.12	Sketch of the experimental setup for nuclear fluorescence measurements .	78
4.13	Temperature stability in the experimental hutch at the P01 beamline	78
4.14	Time-spectrum of x-rays scattered in the inelastic channel	81
4.15	Sketch of the experimental setup for NFS measurements on the 73 keV resonance of ¹⁹³ Ir	82
4.16	Instrumental function of the MRM	83
4.17	Setup and cross-section of the backscattering monochromator	87
4.18	Sensitivity of temperature measurements	88
4.19	Temperature stability during temperature control	88
4.20	Temperature control with a fast temperature change	89
4.21	Spectral reflectivities of 1 mm thick and 5 mm thick sapphire crystals mea- sured around ¹¹⁹ Sn resonance energy of 23.88 keV	91

4.22	Measured temperature stability during temperature control with heat load by the 23.88 keV x-ray beam	92
4.23	Temperature map for thick sapphire crystal	93
4.24	Instrumental function of sapphire crystal measured around the ^{121}Sb resonance energy	95
4.25	NFS spectrum measured on Sb_2O_3 powder with ^{121}Sb resonance	96
5.1	NFS spectra from Ir	103
5.2	Temperature dependence of the Lamb-Mössbauer factor in Ir	104
5.3	DPS in Ir: measured and calculated	106
5.4	Comparison of DPS in two fcc metals: Ir and $\gamma\text{-Fe}$	109
6.1	NFS time spectra for IrO_2	115
6.2	NFS time spectra for SrIrO_3	117
6.3	NFS time spectra of Sr_2IrO_4 by XRS magnetic moments model	120
6.4	NFS time spectra of Sr_2IrO_4	120
6.5	XANES spectra of Sr_2IrO_4 and IrO_2	122
7.1	Temperature dependence of Lamb-Mössbauer factors in AgSbO_3 and in AgSb_3O_7 measured with Mössbauer spectroscopy	126
7.2	NIS spectra for AgSbO_3 and in AgSb_3O_7	127
7.3	Phonon density of states for Sb ions in AgSbO_3 and in AgSb_3O_7	128
7.4	Local environment of Sb in AgSbO_3 and in AgSb_3O_7	131
A.1	A layout of accelerator chain	139
A.2	Undulator	139
A.3	Rocking curve of P01 beamline DCM at 73 keV	146

A.4	Divergence of the beam reflected by DCM and energy bandpass	147
A.5	Divergence of the beam incident of MRM	147
A.6	Beam size before and after MRM	148

List of Tables

3.1	Optimal thickness and expected NFS count-rate for Ir metal	41
4.1	Energy and lifetimes of several excited states studied by NRS	72
4.2	Main design parameters of the MRM for 73 keV x-rays.	74
4.3	Summary of the measured properties of the MRM.	83
5.1	Properties of the Mössbauer transitions in Iridium	99
5.2	Lattice dynamics properties of Ir studied by INS.	107
5.3	Lattice dynamics properties of Ir	111
7.1	Lattice dynamics in AgSbO_3 and AgSb_3O_7	129
7.2	Lattice dynamics of Sb(III) and Sb(V)	131
A.1	Properties of PETRA III and ESRF photon sources	140
A.2	Parameters of filling patterns for the PETRA ring	141

List of Abbreviations

APD	Avalanche Photo-Diode
BS HRM	Backscattering High Resolution Monochromator
CEF	Crystal Effective Field
DAC	Diamond Anvil Cell
DCM	Double Crystal Monochromator (= High Heat Load Monochromator)
DPS	Density of Phonon States
EFG	Electric Field Gradient
ESRF	European Synchrotron Radiation Facility
FWHM	Full Width at Half Maximum
HRM	High-Resolution Monochromator
INS	Inelastic Neutron Scattering
I-N₂	Liquid Nitrogen
MRM	Medium Resolution Monochromator
MS	Mössbauer Spectroscopy
NFS	Nuclear Forward Scattering
NIS	Nuclear Inelastic Scattering

NIST National Institute of Standards and Technology

NRS Nuclear Resonance Scattering

PETRA Positron-Electron Tandem Ring Accelerator

PIN p-i-n diode detector

RF Radio Frequency

RIXS Resonant Inelastic X-ray Scattering

RMS Root Mean Square

RT Room Temperature

SOC Spin-Orbit Coupling

SR Synchrotron Radiation

TMO Transition Metal Oxide

XRD X-Ray Diffraction

Introduction

The recent development of high-brilliant x-ray sources significantly broadened the field of condensed matter research, establishing most sensitive tools for understanding the fundamental correlations between macroscopic and microscopic material properties [1, 2]. A vast amount of theoretical hypotheses proposed in the early years of the 20th century became accessible for experimental proof with the modern light sources only in the late 1980s - 2000s, with the evolution of the instruments for x-ray and neutron scattering experiments [1, 2, 3]. Several interesting techniques, like coherent and inelastic x-ray scattering were newly developed and elaborated for general users of large scale facilities in the last 30 years. Particularly, coherent elastic and incoherent inelastic scattering techniques like x-ray magnetic scattering and inelastic x-ray scattering made possible the direct measurement and correlation of microscopic magnetism [2], lattice vibrations and electronic transport in one of the most interesting puzzle, the origin of high-temperature superconductivity in 3d transition metal oxides (TMO) like cuprates [4]. 3d TMOs demonstrate vast solid state physics phenomena including superconductivity, giant magnetoresistance, multiferroicity. These effects have been clearly explained by strong correlations between electrons [5, 6].

The most recent studies propose heavy-element (high- Z) compounds to be the more attractive subject of studies in the field of electron correlations [7]. Although these compounds should show weak electronic correlation, strong coupling between spin and orbital electronic momenta modifies the ground state, and strong correlation between the electrons in the ground state emerges. This phenomenon gives rise to a plethora of exotic electron-confined structures like Weyl correlation, spin waves, topological states [7]. Notably, several of these states remain stable even at normal pressure and temperatures slightly lower than room temperature [8, 9]. These recently observed correlations are very intriguing since they involve both spin and orbital momenta, and reliable access to experimental studies of this kind of interaction was elaborated only recently by x-ray and neutron scattering techniques [10, 11, 12]. Particularly, the novel model of a spin-orbit induced electronic $j_{eff} = 1/2$ state was established in iridates [13, 14] and the significant impact of electronic spin and orbital moments and crystal field on the novel state was shown by x-ray magnetic and inelastic scattering and by x-ray absorption spectroscopy (see for instance Ref. [11, 12]). Most x-ray scattering and absorption techniques used for studies of iridates utilize L-edge electronic transitions mostly sensitive to the electrons on the outer shells whose correlations are not robust against high-temperatures and pressures [15]. The macroscopic probes show that magnetic order in iridates is pre-

served at temperatures as high as 200-300 K [10, 16]. Neutron scattering experiments on iridate compounds are generally very challenging due to the high absorption by Ir, the lack of large single crystals and the challenging interpretation of the results measured on powdered samples. Magnetic structures modeled from the measurements have been however reported in the recent literature [17, 18, 19], proposing several interesting effects like twinning in Sr_2IrO_4 [17] and spin reorientation with the moments pointing along c-axis when Sr_2IrO_4 is doped by Mn [19]. These effects were not observed by x-ray scattering techniques so far. The search for a technique which probes magnetism and charge distribution in the intermediate scale, between nuclear spin magnetism probed by neutrons and spin and orbit magnetism of the outer electrons probed by conventional x-ray techniques is, therefore, quite natural.

The purpose of a part of this thesis is to establish a new research tool for studies of magnetism and electronic properties in correlated systems by means of nuclear resonance scattering (NRS), a powerful technique relying on the bulk sensitivity of high-energy Mössbauer radiation and on the polarization of synchrotron radiation [2, 20]. This work establishes NRS techniques for studies of magnetic and electronic properties at Ir nuclei with photon energies of 73 keV. The results were achieved due to the significant development of the beamline instrumentation. Particularly, a special monochromator was installed and elaborated for the beamline; during this work the fast detectors and beam cleaning procedure have been established at PETRA III storage ring inspired by the work with the high energy and low lifetimes of non-iron Mössbauer isotopes. In order to broaden the applications of NRS, lattice vibrational spectroscopy was demonstrated for the first time on Ag-Sb-O compounds with pyrochlore structure similar to that of iridates. This became possible by nuclear resonant inelastic scattering of highly monochromatic 37 keV photons, an option which became accessible at the beamline with a high-resolution sapphire backscattering monochromator built, installed and tested in the framework of this thesis. Analysing the results of NIS on Ag-Sb-O, it is shown that the DPS of the Sb(III) and of the Sb(V) in AgSb_3O_7 can be obtained from the total DPS of Sb.

In the Chapters 1 and 2 I provide an overview on the geometry and physical properties of the systems studied in this work. I present the physical models that characterize 5d TMO referring to the recent theoretical and experimental studies on iridate compounds in Chapter 1. Correlation effects and magnetism are briefly discussed in that chapter. In the following Chapter 2 transport properties of Ag-Sb-O compounds are discussed addressing the crystal structure which is similar to iridate compounds.

An overview on general formalism of hyperfine interactions and the probability of the Mössbauer effect is given in the first part of the Chapter 3. Based on that treatment, I give an overview of the main results of the dynamical theory of nuclear resonance scat-

tering in the Chapter 3. Particularly, I discuss the impact of multiple scattering and hyperfine interactions on the nuclear resonance scattering function in frequency and time domains. Special accent is set onto the nuclear resonant scattering on ^{193}Ir isotope: the level schemes and radiation characteristics are discussed in detail for different hyperfine interactions and polarization directions. I show that nuclear forward scattering is a very sensitive technique for probing hyperfine interactions in iridates. The second part of the Chapter 3 is dedicated to the treatment of nuclear inelastic scattering, a method used for measurement of lattice vibrations. The formalism is described in steps for a model spectrum. As shown in the chapter 3, nuclear inelastic scattering is a valuable probe of site- and element-specific lattice vibrations.

A discussion of experimental aspects is given in Chapter 4. Particularly, I give an introduction to the dynamical theory of x-ray scattering with the focus on the design and operation of high-resolution monochromators, arguing the vital role of monochromatization in the suppression of non-resonant radiation in NRS experiments. I describe two monochromator devices designed, installed and tested at the P01 beamline of PETRA III: a monochromator for 73 keV photons with intermediate energy resolution used for the hyperfine spectroscopy on Ir compounds, and a high-resolution sapphire-based backscattering monochromator used for vibrational spectroscopy on any Mössbauer isotope with transition energy in the 20-50 keV range. The detection of the NRS signal and the purity of the electron beam in the PETRA storage ring are discussed in Chapter 4 and several developments in this area are described in detail.

The following Chapters 5-7 are dedicated to the results obtained on particular materials studied in this work. In Chapter 5 I show the results of the first Nuclear Forward Scattering (NFS) studies on Ir metal. The experimental data obtained for the 15-300 K temperature range are interpreted by dynamical scattering theory, and the temperature dependence of the Lamb-Mössbauer factor is extracted. Using complementary techniques of inelastic neutron scattering and of x-ray diffraction I derive thermodynamic parameters like the Debye temperature, mean atomic displacement parameter and force constant in Ir metal, making a comparison with *ab initio* studies on Ir given in the literature. Finally, I discuss the speed of sound in Ir derived from the present and previous studies. I show the first NRS studies of hyperfine interactions in iridate compounds in Chapter 6. Here, I unravel the electric field gradient in iridates with metallic ground states, IrO_2 and SrIrO_3 . I show that no magnetic hyperfine interactions are present in these compounds at the temperatures above 15 K. I present first measurements of the magnetic hyperfine fields at Ir in the antiferromagnetic insulator Sr_2IrO_4 , showing a change in the beating pattern of NRS time-spectrum upon application of external magnetic field of 0.53(5) T. All experimental data are interpreted by means of the dynamical theory of NRS.

Chapter 7 demonstrates first vibrational spectroscopy on silver antimonides, Ag-Sb-O , carried out at the P01 Dynamics Beamline of PETRA III. Using conventional formalism of nuclear inelastic scattering, I show the possibility to separate the contributions of Sb(III)

and Sb(V) vibrational modes to the total spectrum of Sb vibrations.

Chapter 8 concludes the results and provides a brief outlook on future developments linked to the current work.

1 System under study: transition metal oxide iridates

Complex oxides of $5d$ transition metals (TMO) attract large attention in recent years due to many elusive properties. Among others, the interesting phenomena of extended $5d$ orbitals and strong coupling between angular momentum and spin of electrons in these compounds give rise to exotic physical models of topological insulators [7], systems which should have metallic conductivity according to the conventional band theory but show insulating behavior [21]. The observation of unconventional superconductivity in the $4d$ oxide Sr_2RuO_4 [22] triggered the search of this effect in the isostructural $5d$ iridate perovskite Sr_2IrO_4 . Detailed theoretical studies proposed charge and magnetic interactions in iridate compounds to be in strong contrast to those observed in $4d$ and $3d$ oxides due to the strong mixing of orbital and spin momentum of the electrons in iridates [7].

Iridium is a $5d$ transition metal which has $[\text{Xe}] 4f^{14}6s^25d^7$ electron configuration. The $2s - 7d$ -electrons can be considered as valence electrons which participate in the bonding of Ir in a solid. When iridium is placed in oxygen surrounding, which is the case for the rutile structure of IrO_2 , two electrons from the $6s$ shell and two electrons from the $5d$ shell participate in the bonding and will be transferred to the $2p$ orbital of oxygen; the residual 5 electrons will occupy the $5d$ orbitals of Ir(IV) [10]. The transport properties are determined by the distribution of the electrons in the orbitals; the distribution is determined by the energy spectrum of the orbitals which is in turn determined by their configuration [21].

At this point the configuration of the $5d$ orbitals should be discussed. Crystal field theory allows to simplify the treatment of atomic orbitals by considering the symmetry of the ionic coordination. The orbitals are treated by their projections on manifolds defined by symmetry [23]. For the case of octahedral coordination of the iridium ion, two manifolds are possible: a doubly degenerated e_g manifold which is the basis for d -orbital projections d_{z^2} and $d_{x^2-y^2}$, and a triply degenerated t_{2g} manifold which includes d_{xy} , d_{xz} and d_{yz} projections [23]. The effect of this splitting is known as crystal electric field (CEF); it is shown in Fig. 1.1.

The 2 orbitals of the e_g manifold point towards the oxygen ions and, due to the electrostatic repulsion between iridium and oxygen electrons, have higher energies than the orbitals projected on the t_{2g} manifold [23]. Thus, electrons tend to fill first the t_{2g} orbitals. Hund's rule proposes that energy of the half-filled shell is the lowest when the spin is maximized, thus, giving a proposition that electrons can occupy the higher e_g state. In

iridium oxides and iridates discussed later this is not the case: the separation between e_g and t_{2g} orbitals is much larger than the Hund's coupling constant, and therefore the 5 electrons will occupy the lower t_{2g} orbitals forming a low, spin-1/2 state (Fig. 1.1).

Another contribution to the electronic state in iridium compounds is the strong coupling between spin and angular momentum, so called spin-orbit coupling (SOC), of electrons in $5d$ orbitals. This is a very interesting phenomenon which stimulates a large part of research nowadays. The reason is that the SOC scales with the fourth power of the atomic number and for $5d$ elements it is an order of magnitude larger than in $3d$ elements [24, 25]. Therefore, SOC cannot be treated as a small perturbation to the CEF in iridium compounds. The Hamiltonian for the spin-orbit coupling can be written by:

$$\hat{H}_{SO} = \lambda \cdot \hat{S} \cdot \hat{L} \quad (1.1)$$

with \hat{S} and \hat{L} the operators for spin and orbital angular momentum and λ the constant of spin-orbit coupling.

In the case of a large SOC the Hamilton operator of the system does not commute with \hat{S} and \hat{L} separately, thus, spin and orbital momentum cannot be observed independently. However, the Hamiltonian commutes with the total angular momentum \hat{J}^2 operator and thus J^2 is a good quantum number which can be observed experimentally [26].

In order to understand the meaning of \hat{J} in iridium compounds the angular momentum operator \hat{L} should be examined. It can be shown that for the $5d$ -states the matrix elements of \hat{L} are zero for the e_g manifold [27, 11]. 5 valence electrons of iridium occupy triply-degenerated t_{2g} manifold. Therefore, there is one hole in the ground state and the spin-orbit coupling problem is simplified: instead of coupling orbit and spin for each of many electrons, so-called j-j coupling [26], one can couple spin and orbital moments for one hole [13, 14] which is easier. By doing this the matrix elements of \hat{J} are equivalent to the matrix elements of the $-\hat{L}$ operator for p-states in the t_{2g} manifold [11]. Thus, the projection of its eigenvalue l onto the t_{2g} manifold can be given by the effective angular momentum $l_{eff} = -1$ [23]. The addition of SOC removes the 3-fold degeneracy of the t_{2g} manifold. For IrO_2 , as discussed before, only one unpaired electron can be found in t_{2g} . The t_{2g} state can be described by the total angular momentum $j_{eff} = l_{eff} \pm s$ and therefore two states are possible: $j_{eff} = 1/2$ doubly degenerated by magnetic quantum number $m = \pm 1/2$, and $j_{eff} = 3/2$ quadruply degenerated by $m = \pm 1/2$ and $\pm 3/2$ [11]. Inspecting energy eigenvalues of these two states one can notice that $j_{eff} = 1/2$ has higher energy due to the minus sign in \hat{L} , and that the energy gap between $j_{eff} = 1/2$ and $j_{eff} = 3/2$ is $3\lambda/2$ (Fig. 1.1). Recent experimental studies of resonant elastic x-ray scattering and x-ray

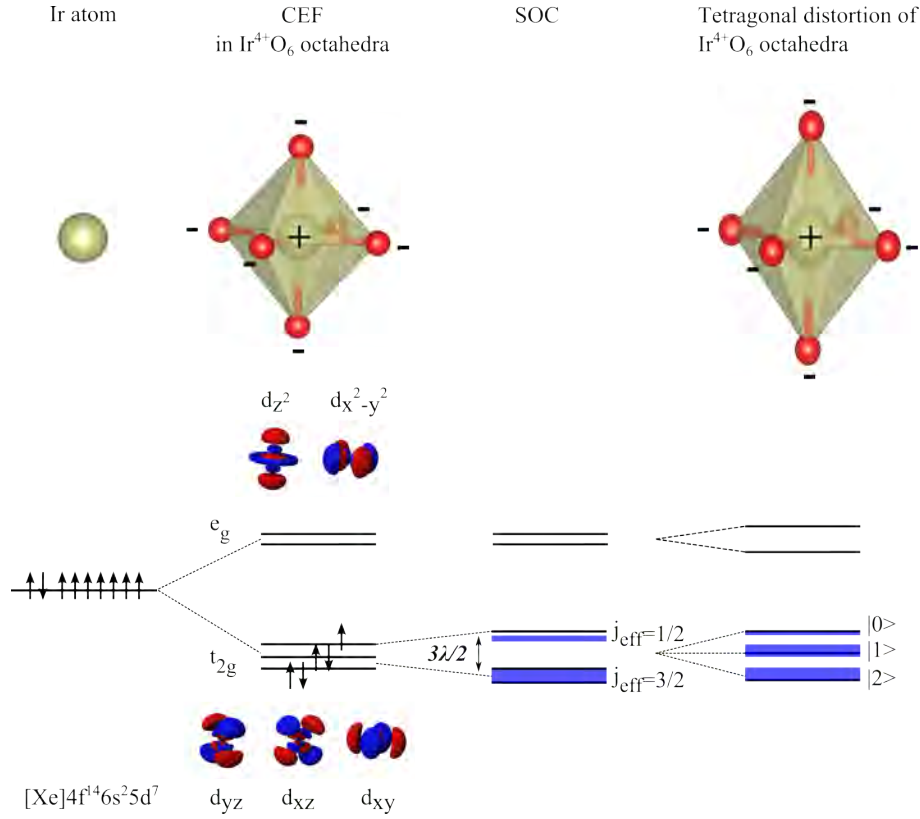


Figure 1.1: *Splitting of 5d orbitals and electronic states in the presence of the crystal electric field (CEF) and the spin-orbit coupling (SOC). The configuration of 5d orbitals is shown for the case of CEF. Black arrows show electronic spin and blue rectangles depict the state occupancy [12, 29]*

absorption spectroscopy at the near edge confirmed the presence of the $|j_{eff}, m_j\rangle$ states in IrO₂ [28]. Therefore, the magnetic moment in this compound exhibits both orbital and spin components. It is worth to remark that the spin-orbit interaction constant λ in iridates is typically about 0.4-0.5 eV which is an order of magnitude larger than in 3d compounds [7].

The 5 valence electrons present in the t_{2g} manifold will occupy $|j_{eff}, m_j\rangle$ states according to the Pauli exclusion principle: 4 electrons on the lower $j_{eff} = 3/2$ state and 1 electron on the upper $j_{eff} = 1/2$ level. This occurs without violating Hund's rules because the Hund's coupling constant is much lower than the energy gap between $j_{eff} = 3/2$ and $j_{eff} = 1/2$ [12].

The electronic structure of IrO₂ described above shows a hole in the upper energy level and thus IrO₂ should be metallic. Experimental work on IrO₂ confirms this statement [28].

The situation becomes more difficult when IrO₆ octahedra are placed in a layered structure like that of the perovskite iridate Sr₂IrO₄. The unit cell of Sr₂IrO₄ has a tetragonal

symmetry with the space group $I4_1/acd$ (Fig. 1.3) [16] and the $\bar{1}$ symmetry of the Ir site. IrO_6 octahedra form a squared lattice in the a - b plane in this compound (Fig. 1.3). It was observed experimentally that at ambient conditions Sr_2IrO_4 is an insulator, with a narrow band gap of about 0.4 eV, and shows an antiferromagnetic transition at 240 K [16]. This observation is surprising because *ab initio* calculations and conventional band theory predict metallic behavior for this compound [16]. Several theoretical models, involving Coulomb interactions and coupled Coulomb and magnetic interactions, have been developed in order to explain the unconventional behavior [7]. Fig. 1.2 shows the change in the band structure when the Coulomb repulsion between electrons in corner-sharing IrO_6 octahedra occurs. The system can be described by the Hubbard model which assumes an interplay of two Hamiltonians, a kinetic one describing tunneling of electrons ('hopping') between the site of the lattice \hat{H}_H , and the interaction term \hat{H}_I which forces electrons to localize at one site of the lattice [26]:

$$\hat{H} = \hat{H}_H + \hat{H}_I \sim a \cdot W + b \cdot U \quad (1.2)$$

with W the bandwidth of the non-interacting valence electrons.

The relation between the energy of the Coulomb repulsion U and W should be considered at this point (Fig. 1.2). In the absence of Coulomb repulsion ($U = 0$), a single electron band is formed and the Fermi level is located in the middle of the band: this is the case of a classical metal [21]. For the case of weak correlation when $0.5 < U/W < 1$ the electrons can be described as quasi-particles whose behavior can be approximated by a free electron model [5]. In the regime of strong correlation between electrons, $U/W \gg 1$, the electrons are localized in two bands, which are called lower and upper Hubbard bands [5]. The electronic structure for this case is the result of an interplay of Coulomb repulsion and SOC [5]. For 4d TMO it was shown that U is relatively small due to the strongly delocalized 4d states, and with the relatively low SOC, the ground state is metallic [30, 31]. In 5d TMO the SOC splits the ground state into $j_{eff} = 3/2$ and $j_{eff} = 1/2$ states, as mentioned before, and the bandwidth of the $j_{eff} = 1/2$ state is narrow, comparable in width to U . This leads to a splitting of the $j_{eff} = 1/2$ state into lower and upper Hubbard bands, separated by U , and the material becomes an insulator. Probing $j_{eff} = 1/2$ with angular resolved photoemission spectroscopy and x-ray resonant magnetic scattering validated this concept for Sr_2IrO_4 and Ba_2IrO_4 compounds [32, 33].

An interesting consequence of the strong coupling of electrons (the case of $U/W \gg 1$) is that the electrons are mainly localized and antiferromagnetic order between nearest neighbors occurs. In this case the magnetism can be treated by Heisenberg model with the Hamiltonian given by [12]:

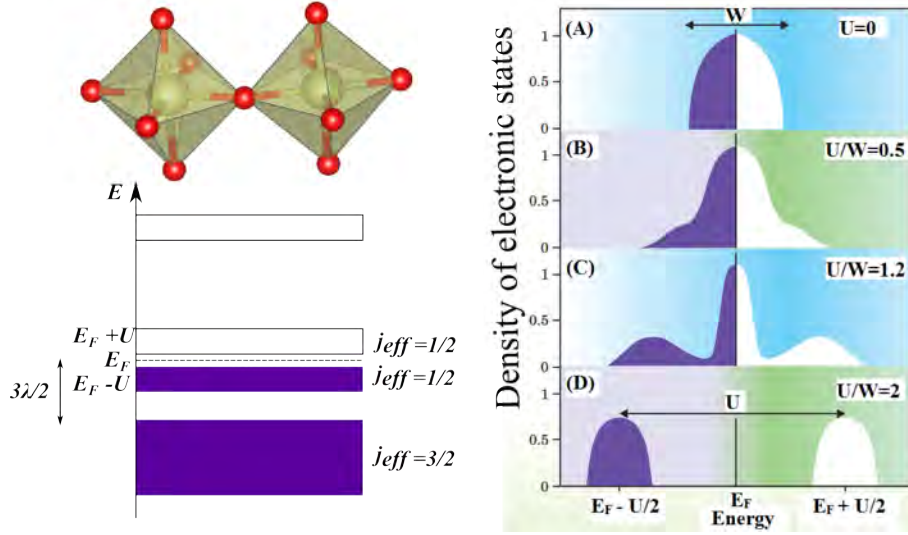


Figure 1.2: *Effect of SOC and Coulomb repulsion in iridates. Left panel displays band structure of corner-sharing octahedra. Right panel shows electron band structure for different ratios of electron interaction energy U and bandwidth of noninteracting electrons W . (A) is the case of free electrons (classical metal), (B) shows the case of a weak correlation (small U , Fermi liquid metal) and (C) is the case of strong correlation between electrons (moderate U , Hubbard model); the case of localized electrons (Mott insulator) is shown in panel(D). Adapted from [12, 5]*

$$\hat{H} = J \cdot \hat{S}_i \cdot \hat{S}_j \quad (1.3)$$

With J the Heisenberg constant for the exchange between the angular moments of two nearest neighbors, \hat{S}_i and \hat{S}_j . Note that $\hat{S}_i \cdot \hat{S}_j$ is the scalar product. This model is successfully used to describe low energy excitations in the layered perovskite iridates [11]. Hard X-ray RIXS can be used to obtain the complete magnon dispersion curves across the entire Brillouin zone [11]. The dispersion of magnetic excitations in Sr_2IrO_4 does resemble that in the high-temperature superconductor La_2CuO_4 [34], giving a perspective for realizing of superconductivity in iridates. A very interesting result reported in the Ref. [11, 10] is that the energy of magnetic excitations is of the same order of magnitude as the Coulomb interaction U , thus suggesting the same origin of electronic and magnetic properties.

Note that for the magnetic properties of layered iridates the magnetic moments in the model $j_{eff} = 1/2$ state are determined by magnetic quantum numbers given by the scheme of electronic levels. The scheme of electronic levels is in turn strongly dependent on the interaction between electrons of neighboring IrO_6 octahedra. Therefore, magnetic properties of iridates, in contrast to the pure spin magnetism, do depend on the configuration of d -orbitals given by the lattice geometry and bonding [26].

The total magnetic interaction is described by two contributions: the first one is an

isotropic term describing antiferromagnetic order by equation 1.3 and the second is an anisotropic term, usually called Dzyaloshinskii-Moriya interaction [14]:

$$\hat{H} = J_1 \cdot \hat{S}_i \cdot \hat{S}_j + J_2 \cdot [\hat{S}_i \times \hat{S}_j] \quad (1.4)$$

with J_1 and J_2 the coupling constants for isotropic and anisotropic interaction, respectively, and $[\hat{S}_i \times \hat{S}_j]$ the vector product of \hat{S}_i and \hat{S}_j .

The magnitudes of the isotropic and anisotropic interactions depend on the geometry of the lattice [26]. In iridates, there are two boundary conditions for the orientation of the IrO_6 octahedra that must be considered [14]:

- (a) Corner-sharing geometry with an angle of 180° between the Ir-O and O-Ir bonds. For this case only the first term in equation 1.4 is considered and the anisotropic interaction is zero due to parallel orientation of S_i and S_j .
- (b) Edge-sharing geometry with an angle of 90° between the bonds, also called "honeycomb lattice". For this case the interaction is given solely by the anisotropic part, as the scalar product $\hat{S}_i \cdot \hat{S}_j$ in eq. (1.4) is zero for perpendicular S_i and S_j .

The structure of the layered perovskite iridate Sr_2IrO_4 with corner-sharing geometry and slight ($\sim 12^\circ$) rotation of IrO_6 octahedra around the c-axis (Fig. 1.3) does resemble the conditions for the case (a). It was recently shown that in strontium perovskite iridates the magnetic interactions measured by RIXS and the magnetic structure measured by x-ray magnetic scattering can be described by the isotropic Heisenberg interaction with a small admixture of an anisotropic term [11]. Particularly, the Heisenberg exchange interaction $J_1 = 60$ meV was derived [11] from the RIXS measurements [35] and the Dzyaloshinskii-Moriya interaction energy $J_2 \approx 27$ meV was estimated from the RIXS and XRMS measurements [36] on Sr_2IrO_4 single crystals.

For iridates $R_2\text{IrO}_4$ (R - rare earth ion) with pyrochlore structure the IrO_6 octahedra show edge-sharing geometry with a slight deviation of the Ir-O and O-Ir bonding angles from 90° . It was shown by RIXS that the magnetic excitations in $\text{Sm}_2\text{Ir}_2\text{O}_7$ pyrochlore iridate can be modeled by the Hamiltonian given by equation 1.4 with a significant anisotropic contribution [38]. The anisotropic contribution is believed to be due to magnetic excitations with energies of several dozens of meV.

The resolution of currently used RIXS spectrometers is in the order of 20 meV which is higher than the energies of the magnetic excitations and splitting by crystal field proposed by experimental [11] and theoretical [14] studies. Inelastic neutron scattering ex-

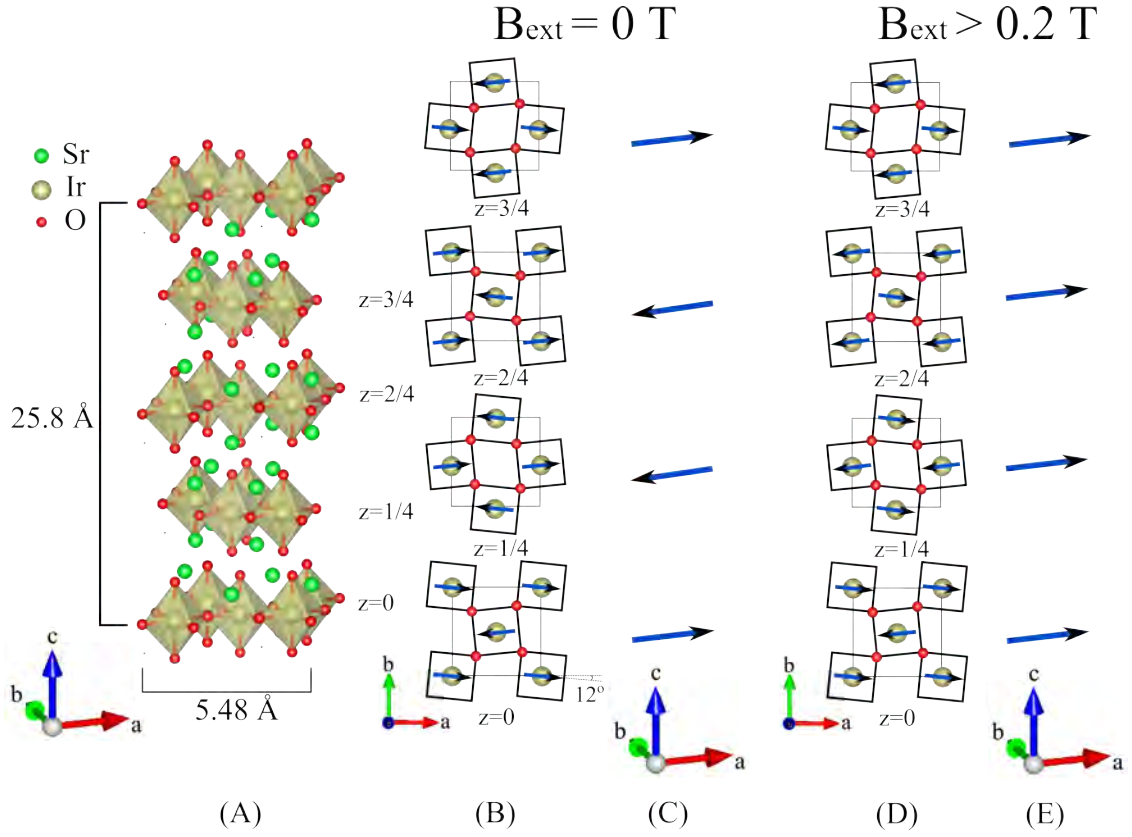


Figure 1.3: (A): crystal structure of Sr_2IrO_4 according to Ref. [16]. (B, D): Magnetic stacking patterns along the c-axis according to Refs. [37, 36]. Blue arrows show $j_{\text{eff}} = 1/2$ moments. The external magnetic field is zero in the (B) case, and larger than 0.2 T in the case (D). Panels (C) and (E) show the net magnetic moments within the IrO_6 layers and their stacking pattern along the c-axis in zero field (panel C) and in the fields larger than 0.2 T (panel E).

periments on iridium compounds are extremely difficult due to: (i) very high neutron absorption cross-section of iridium [39], and (ii) the small size of iridate single crystals. At this point NRS can be a suitable local, isotope-specific probe of electronic and magnetic properties [40]. The first realization of NRS experiments on Ir compounds is shown in this work.

2 System under study: binary oxides

Ag-Sb-O

Chemical methods for H_2 and O_2 production from water pave a way for a search of new, versatile catalytic materials. A so-called water splitting reaction, might be the most interesting and technically feasible method [41, 42]. In this method electrons and holes generated in a semiconductor by the photo-effect reduce $2H^+$ to H_2 and oxidize $2O^{2-}$ to O_2 [43]. The most intriguing possibility is the use of solar light for the generation of the charge carriers. Therefore, a relevant material for water splitting should effectively harvest the visible light with photon energies in the 1.6-3.3 eV range [41, 43, 44].

Binary oxides attract much attention due to the high catalytic activity in water oxidation processes. It was realized that the band gap in many of these compounds is close to the energies of visible light photons, and, - which is more important - the gap can be tuned in a wide range introducing defects or substituting the metal ions in the structure [43, 44]. Particularly, solid solutions with general formula $Ag_{2-x}Sb_{2+x}O_{6+y}$ ($0 \leq x \leq 1$) studied in this work are transparent semiconductor oxides with band gaps in the 2.23-2.72 eV range showing very low absorption of visible light [44, 45]. Especially interesting is the compound with $x = 0$, $y = 0$ which is more efficient in the production of O_2 , whereas Sb-rich compounds with $x \approx 1$ are more active in the reduction of H^+ , triggering the search for a composite system [46, 44].

A deeper understanding of factors influencing the electronic structure of $Ag_{2-x}Sb_{2+x}O_{6+y}$ solutions became necessary. Based on optical and electrical measurements, calculations of electronic band structure show that the direct band gap in $AgSbO_3$, 0.1 eV, is the smallest among mostly studied pyrochlore catalysts [47, 48]. Notably, the direct band gap is perfectly tuned for transmission of middle infrared waves with a wavelength of 12-15 μm , exactly in the transmission window of the Earth's atmosphere [49]. Therefore, this material should be a high-efficient catalyst in photochemical reactions [42] which was shown in the Ref. [50]. The calculations in the Ref. [47] show that the conduction band exhibits a significant dispersion. The indirect band gap which determines electric conductivity at ambient temperatures, is about 3 eV in these materials, comparable with the band gaps of the semiconductors most frequently used in photovoltaic devices [51].

The Ag-Sb-O compounds exhibit pyrochlore structure which for an ideal case, formula $A_2B_2O_6O'$, built by framework of BO_6 octahedra with intercalating network of $O'A_4$ tetrahedra (fig. 2.1). The two limiting compounds of the $Ag_{2-x}Sb_{2+x}O_{6+y}$ solid solution

row, $\text{Ag}_2\text{Sb}_2\text{O}_6$ ($x = 0$) and AgSb_3O_7 ($x = 1$), have a defect pyrochlore structure and should be discussed in detail. $\text{Ag}_2\text{Sb}_2\text{O}_6$ exhibits Ag ions at the *A*-site and Sb ions at the *B*-site (fig. 2.1); O' sites can be fully vacant, and the formula $\text{Ag}_2\text{Sb}_2\text{O}_6$ is often shortened to AgSbO_3 in the literature [48]. About a half of Ag at the *A*-site in AgSbO_3 can be substituted by Sb resulting in a stoichiometric composition AgSb_3O_7 . It was shown in Ref. [45] that the electronic band gap and catalytic activity significantly change upon transition from AgSbO_3 to AgSb_3O_7 and therefore it is interesting to study bonding in these compounds. The geometry of the defect pyrochlore structure is intermediate between corner- and edge-sharing octahedra with known interactions, already discussed in the section 1. The Ag-Sb-O compounds are thus good model systems for studies of correlations between structure, electronic and lattice excitations at the transition from one geometry to another [47]. Indeed, the factors influencing positions and bonding in Ag-Sb-O systems are not well understood, though relations between site disorder, valence and vibrational spectrum do provide conclusions about the origin of high conductivity in these compounds and help to engineer more efficient materials [47, 48, 44]. For instance, studies by x-ray diffraction (XRD) show that, in contrast to the perovskite structure, the angles between Sb-O-Sb bonds in AgSbO_3 are significantly lower and the distance between Sb and O ions is not very sensitive to the size of the *A*-site cation [47]. This suggests that filling pyrochlores with high-valence ions on the *A*-site could raise their catalytic activity. Measurements of visible light absorption [47] suggest that the band gap is mainly determined by bonding in the SbO_6 octahedra and the size of the Ag cation which is in turn determined by its oxidation state [52].

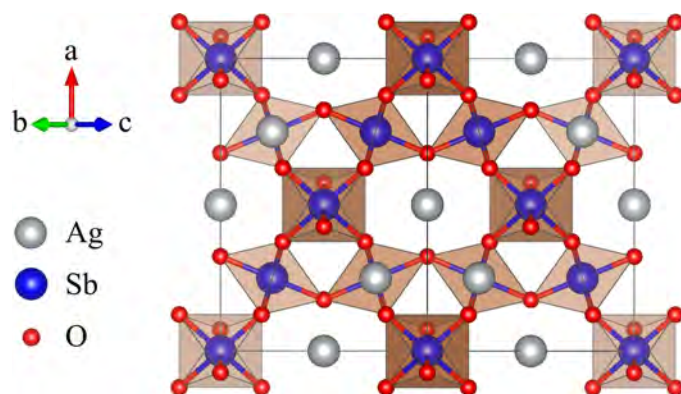


Figure 2.1: Crystal structure of anion-deficient pyrochlore $\text{Ag}_2\text{Sb}_2\text{O}_6$ (AgSbO_3) compound [47]. The Ag ion (grey) is in the *A*-site voids surrounded by SbO_6 octahedra. Figure is drawn according to the data from Ref. [53].

Because the Ag in Ag-Sb-O are electropositive ions, it might be naively assumed that these ions do not contribute to the electronic states near the Fermi level. However, *ab initio* studies suggest that the strong contrast between the size of the direct and indirect band gap is related to the strong mixing of $5s$ orbitals of Ag and Sb into the conduction band. A similar effect is observed in the stanate perovskite CdSnO_3 and explained by

interaction between Cd_2O and Sn_2O_6 sublattices [47]. X-ray photoemission spectroscopy and *ab initio* calculations show that a similar effect occurs at the top of the valence band of AgSbO_3 . Here, electronic states are formed by overlapping $2p$ - and $4d$ orbitals of O and Ag ions, respectively. Therefore, the position and bonding of Ag, Sb and O ions has significant impact on the electronic structure and should be studied in detail. Two good model systems for studying the interplay of bonding and electronic properties can be AgSbO_3 and AgSb_3O_7 , because the change in bonding in AgSb_3O_7 is only due to the presence of vacancies on the oxygen site: the case is analog to the substitution of Ag by the metals Na, K, and Tl as proposed before in the Ref. [48].

The analysis of XRD spectra is generally challenging for these compounds due to the high absorption and small difference in structure factors for Ag and Sb ions. Moreover, AgSbO_3 and AgSb_3O_7 are usually not stoichiometric, having structural disorder which makes the determination of the oxygen ion positions especially difficult. Although the positions of ions and electronic structure can be correlated by photoemission and absorption spectroscopy [50], the results are generally difficult to interpret for the bulk material [44, 45]. Neutron diffraction can be used as a probe for locating oxygen ions, despite of the high neutron absorption cross-section of Ag [48]. Indeed, very interesting information has been found by recent neutron scattering measurements on AgSbO_3 [48]: upon substitution of Ag by Na, K, and Tl the length of the Sb-O bond increases which promotes a decrease of the Ag-O bond length, and the same effect is expected from the increase of the oxygen content, as it is the case in AgSb_3O_7 . Because the maximum energy of the valence band is mainly determined by the overlap of Ag and O orbitals, the decrease of the Ag-O bond length and increasing overlap will significantly change the band gap.

A more closer look to the structure of the Ag-Sb-O compounds shows that Sb ions in AgSbO_3 are present in the oxidation state Sb(V), while AgSb_3O_7 contains Sb ions in both Sb(III) and Sb(V) states [45], which might be considered as sublattices with different oxygen coordination of Sb. The hypothesis of two sublattices is nicely proved by Mössbauer spectroscopy studies on AgSbO_3 [53] and on AgSb_3O_7 [45]. It is shown that AgSbO_3 (only Sb(V)) is solely characterized by a single line [45, 53], while AgSb_3O_7 exhibits an additional doublet due to the presence of Sb(III) (fig. 2.2) [45]. Considering line areas on the fig. 2.2, a Lamb-Mössbauer factor of 0.84(1) for the Sb(V) oxidation state can be found, which is larger than the Lamb-Mössbauer factor of 0.63(1) for Sb(III) [45]. This effect might be explained by smaller length of the Sb(V)-O bonds compared to that for the Sb(III)-O bonds. An analogous effect is observed in iron oxides with Fe(III) and Fe(II) oxidation states [54, 52]. A smaller bond length should also reflect in the higher force constants for Sb(V)-O bonds [52].

Nuclear Inelastic Scattering (NIS), explored in this work, is a well suitable technique for studies of bonding parameters and establishing correlations between oxygen deficiency

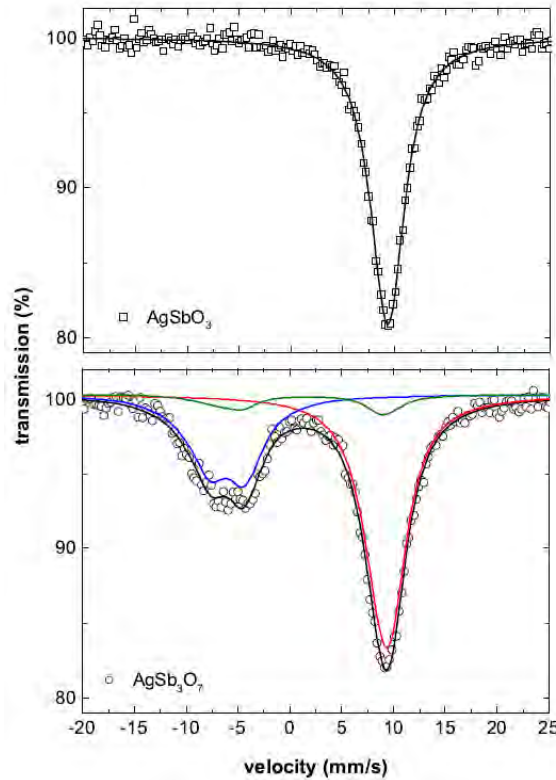


Figure 2.2: Mössbauer spectra from AgSbO_3 and AgSb_3O_7 obtained at 10 K and corresponding fits. AgSbO_3 contains only Sb(V) (red line), AgSb_3O_7 exhibits an additional doublet related to Sb(III) (blue line). Black lines show cumulative fit and the green line corresponds to the minor SbO_2 impurity in AgSb_3O_7 . Reproduced from Ref. [45].

and electronic properties. Several lattice dynamics parameters measured by NIS should be mentioned in detail, while a detailed treatment of the NIS technique is given in the chapter 3.4.2. First, NIS probes directly force constants of Sb-O bonds by measuring the density of phonon states of Sb ions only. Second, the speed of sound, measured by NIS, is a suitable probe of bond strength [55, 54]. High resolution of 3.2(4) meV (FWHM) obtained in the NIS experiment in this work does help to measure low-energy vibrations and therefore to determine elastic properties. It is worth to emphasize that the vibrations of Sb(V) ions should have higher energy than those of Sb(III) due to the smaller bond length since higher Lamb-Mössbauer factor for Sb(V) [45]. Thus, the contribution of vibrations of Sb(III) ions to the total vibration spectrum of AgSb_3O_7 is very low at elevated temperature and the total vibration spectrum is mainly determined by vibrations of Sb(V) ions. AgSb_3O_7 is therefore an interesting model system for the development of the NIS methodology: measuring the vibrations of Sb in AgSb_3O_7 at low and high temperatures allows one to differentiate experimentally between vibration spectra of ions with different oxidation states.

3 Theory

3.1 Hyperfine Interactions

The strong interaction between protons and neutrons in nuclei results in discrete nuclear states. Similarly to the electron shell model, these states can be described in terms of a nuclear shell model [56] with wave functions which determine important properties of the states, such as energy, parity and spin. Since the bonding inside the nucleus is very strong, energies of excited states are high and are typically in the range of several keV up to MeV. This work considers the 1st nuclear excited states with energies up to 100 keV.

Electric and magnetic fields created by electrons interacting with the nucleus lead to so-called hyperfine interactions. These interactions perturb the nuclear states, splitting and shifting them. The effect is described by a Hamiltonian given by a sum of electric and magnetic field contributions. Here, the most significant terms are the isomer shift \hat{H}_{is} , electric quadrupole \hat{H}_Q , and magnetic dipole term \hat{H}_M [56]:

$$\hat{H} = \hat{H}_0 + \hat{H}_{is} + \hat{H}_Q + \hat{H}_M + \dots \quad (3.1)$$

The \hat{H}_0 term describes the interaction inside the nucleus. It does not depend on the distribution of the electronic charge around the nucleus and therefore it is not discussed further.

The \hat{H}_{is} , the electric monopole interaction term, describes the Coulomb interaction between the charge in the nucleus and the shell electrons which penetrate the nucleus and result in a non-zero electronic charge density at the nucleus. This effect leads to an energy shift of the nuclear levels. The configuration of electron shells is different for different chemical environments. Thus chemical environments in different materials can be distinguished by probing the corresponding energy shifts of the nuclear levels. Since the interaction provides shift, the measurement of interaction strength is relative and requires a reference.

Assuming that the electronic charge density at the nucleus is constant, the energy of nuclear levels in sample under scope is shifted by:

$$\Delta E_{is} = \frac{2\pi}{3} Z e^2 \Delta \rho(0) (\langle R^2 \rangle_e - \langle R^2 \rangle_g) \quad (3.2)$$

relative to the energy of levels in the reference sample. In the eq. (3.2) $\Delta \rho(0)$ is the difference in electronic charge density at the nucleus in the sample and in the reference. This difference is determined by s -electrons. $\langle R^2 \rangle_e$ and $\langle R^2 \rangle_g$ are the mean square radii of the nucleus in excited and ground state, respectively. Z is the number of protons and e is the elementary charge.

The equation (3.2) gives the expression for the so-called isomer shift. It is found that any change in the valence shell of an atom, like a change in bonding, oxidation and spin state, affects the density of s -electrons in that atom. Therefore, the isomer shift can be used to characterize chemical and magnetic parameters of materials [54]. For instance, there is a correlation between the isomer shift and the valence state of an ion, as shown in the Fig. 3.1 for the case of ^{193}Ir nuclei¹.

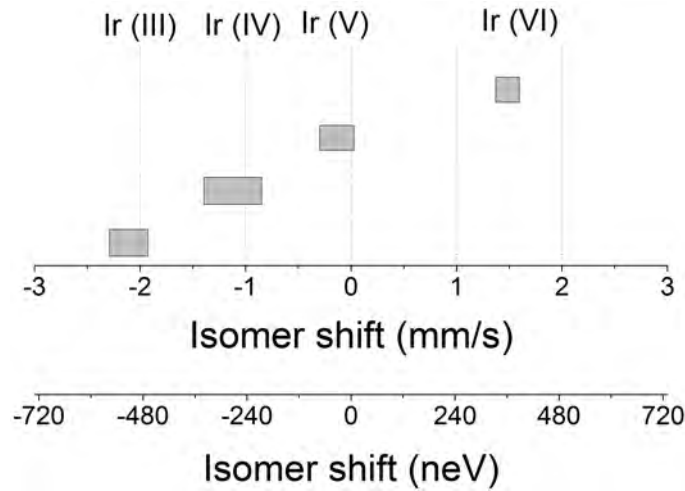


Figure 3.1: Dependence of the isomer shift on the Ir oxidation state (given by number in brackets) in Ir compounds [57, 58]. The shift is given relative to iridium metal reference.

¹the mm/s energy units are commonly used in nuclear spectroscopy. It can be converted to conventional energy units by the following equation: $\Delta E_{is} [\text{eV}] = E_\gamma [\text{eV}] \cdot \frac{\Delta E_{is} [\text{mm/s}]}{c}$, with E_γ the resonance energy, c the speed of light in vacuum. For the case of 73 keV resonance in ^{193}Ir the conversion is:
 $\Delta E_{is} [\text{neV}] \approx 243.33 \cdot \Delta E_{is} [\text{mm/s}]$

There is significant thermal motion of the nuclei at elevated temperatures. This effect changes the measured isomer shift by the so-called second-order Doppler shift δ_{SOD} :

$$\delta E = \delta E_0 + \delta_{SOD} \quad (3.3)$$

Probing the temperature dependence of δ_{SOD} gives information about the Debye temperature, which is an indicator for the rigidity of the lattice and is additionally sensitive to the environment of the nucleus. A detailed discussion of the importance of the Debye temperature is given in the section [3.3](#)

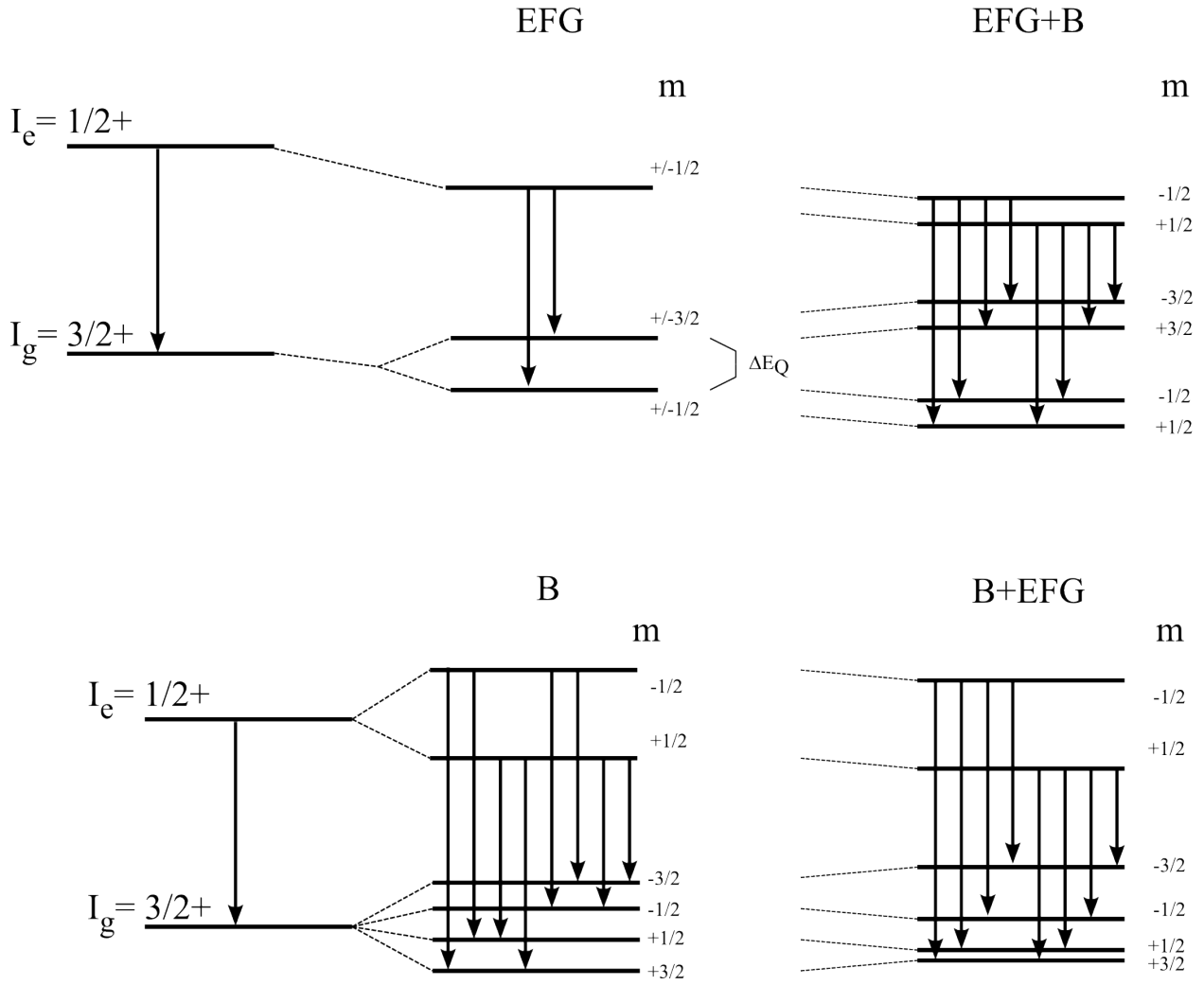


Figure 3.2: Perturbation of nuclear levels under the influence of electric field gradient (EFG) and magnetic interaction (**B**). The case of axially symmetric EFG ($\eta = 0$) and EFG principal axis pointing in the direction of **B**. m : magnetic quantum number. Example of the 73 keV Mössbauer transition in ^{193}Ir nucleus. Upper panel illustrates EFG interaction with perturbation by a small magnetic interaction, while lower panel shows magnetic interaction case perturbed by a small EFG. Note that the radiation has M1+E2 character, thus transitions with $\Delta m = 0, \pm 1, \pm 2$ and $\Delta I = 1, 2$ (8 lines) are allowed.

The next term in the expansion (3.1) is the electric quadrupole interaction \hat{H}_Q . It is given by the interaction between the charge distribution inside the nucleus and the nonsymmetric electric field around the nucleus created by the spatial distribution of electrons surrounding the nucleus and neighboring atoms of ions. If the electric field potential around the nucleus is not isotropic, the deviation from spherical symmetry is given by the electric field gradient (EFG) which is a 3x3 second rank tensor of second derivatives of the electric potential:

$$V_{ij} = \frac{\partial^2 V}{\partial x_i \partial x_j} \quad (3.4)$$

It is possible to find a coordinate system where $V_{ij} = 0$ for $i \neq j$ and $V_{xx} + V_{yy} + V_{zz} = 0$. Thus, the EFG is fully determined by two parameters: its projection on the quantization axis, V_{zz} , and asymmetry parameter given by:

$$\eta = \left| \frac{V_{xx} - V_{yy}}{V_{zz}} \right|. \quad (3.5)$$

The asymmetry parameter η becomes zero when the nucleus site has a threefold or higher symmetry.

The electric field gradient V_{zz} has two contributions. One is the lattice contribution V_{zzlat} which is present when the Mössbauer atom resides in a lattice with non-cubic symmetry or any impurities or lattice distortions are located close to the atom. This contribution is not directly transferred to the nucleus, but via polarization of the electronic shell, which enhances the impact of lattice contributions to the EFG. The second contribution to the EFG is an anisotropic distribution of electrons in the valence shell V_{zzval} . The general expression for the EFG is given by:

$$V_{zz} = V_{zzlat}(1 - \gamma_\infty) + V_{zzval}(1 - R) \quad (3.6)$$

where γ_∞ the Sternheimer anti-shielding factor determines impact of polarization of electronic shell on V_{zzlat} , and R shows the attenuation of V_{zzval} by core electrons.

The electric quadrupole interaction splits nuclear levels into $\lfloor (2I + 1)/2 \rfloor$ sub-levels. The energies of sub-levels are given by:

$$E_Q = \frac{eQV_{zz}}{4I(2I-1)} (3m_I^2 - I(I+1)) \sqrt{1 + \frac{\eta^2}{3}} \quad (3.7)$$

where m_I the magnetic quantum number of sub-level, Q is the electric quadrupole moment of the nucleus, and e is the elementary charge. Only nuclear states with a spin $I > 1/2$ show non-zero quadrupole moment and exhibit quadrupole interaction. If for instance the nuclear state has a spin $I = 3/2$ it is split into two sub-levels while the state with spin $I = 1/2$ is un-split; this is for instance the case for the nuclear levels of ^{193}Ir and ^{57}Fe . The quadrupole moment Q of the nucleus is positive for nuclei which have prolate shape and negative for oblate shape. It is evident from eq.(3.7) that a change in the quadrupole interaction can only occur if the EFG is changed (change in V_{zz} or in η). For the case of axially symmetric EFG ($\eta = 0$) sub-levels in the ground state with a spin $I = 3/2$ have eigenvalues $E_Q(\pm \frac{3}{2}) = \frac{eQV_{zz}}{2}$. The energy gap between split sub-levels, the so-called quadrupole splitting, is given by the difference of two transition energies, from the excited $m_e = |\pm \frac{1}{2}\rangle$ to the ground $m_g = |\pm \frac{1}{2}\rangle$ and from the excited $m_e = |\pm \frac{3}{2}\rangle$ to the ground $m_g = |\pm \frac{3}{2}\rangle$ state:

$$\Delta E_Q = E_Q(\pm \frac{3}{2}) - E_Q(\pm \frac{1}{2}) = \frac{eQV_{zz}}{2} \quad (3.8)$$

The situation becomes more complicated if the EFG is not axially symmetric ($\eta \neq 0$). In this case the sub-levels are given generally by superposition of m_I -states and the intensity of the transition can vary according to η and the superposition law [56]. However, states with half-integer spin, which is the case for the ground and first excited states in ^{57}Fe and ^{193}Ir , respectively, remain doubly degenerate for any asymmetry parameter. This is the consequence of the Kramers theorem which states double degeneracy for systems with half-integer spin in electric field [56].

The next term in the Hamiltonian given in eq.(3.1) is the magnetic hyperfine interaction \hat{H}_M . This yields splitting of nuclear levels similar to the Zeeman effect usually observed in electronic systems by optical spectroscopy. The magnetic hyperfine interaction, or nuclear Zeeman effect, was not possible to measure for ground and excited state simultaneously until the discovery of the Mössbauer effect. Nuclear Magnetic Resonance (NMR) measures magnetic moment of ground state and perturbed angular correlation (PAC) technique probes moments of excited state only.

The magnetic hyperfine interaction is the interaction between the nuclear magnetic moment and the magnetic field at the nucleus. The eigenvalues of the Hamiltonian \hat{H}_M , the

energies of the sub-levels, are given by:

$$E_m = -g_N \mu_N m_I |\mathbf{B}_{eff}| \quad (3.9)$$

where g_N is the Landé factor, the g-factor for nuclear levels; $\mu_N = \frac{e\hbar}{2m_p c} \approx 5.051 \cdot 10^{-27} \text{ J/T}$ is the nuclear magneton, m_I is the magnetic quantum numbers of the level with the spin I , and $|\mathbf{B}_{eff}|$ is the effective magnetic field at the nucleus.

The magnetic hyperfine interaction splits nuclear levels with spin I into $(2I+1)$ sub-levels with magnetic quantum numbers m_I . Analyzing eq. (3.9) an interesting observation appears for the case of pure magnetic hyperfine interaction. In this case the excited and ground states split by $|E_m - E_{-m}| = 2g_N \mu_N I |\mathbf{B}_{eff}|$ (energy gap between $m = +3/2$ and $m = -3/2$ and between $m = +1/2$ and $m = -1/2$ in the Fig. 3.2: lower panel, in the center). Moreover, the distance between the sub-levels is equal to $|E_m - E_{m-1}| = g_N \mu_N |\mathbf{B}_{eff}|$.

The possible transitions are given by selection rules which determine the spatial distribution and polarization of emitted radiation. Therefore, it is worth to briefly review the quantum mechanical description of radiation emitted by de-excitation of discrete levels. Generally, a photon emitted in a transition from a state with spin I_e to the state with the spin I_g can carry angular momentum L in the range $|I_e - I_g| \leq L \leq I_e + I_g$. Particularly for the case of ^{193}Ir and ^{57}Fe , the angular momentum carried by the photon can be $L = 1$ and $L = 2$ since the transitions occur between the states with the spins $1/2$ and $3/2$. Moreover, the ground and excited state have the same parity (s. Fig. 3.2), and therefore the emitted radiation can be characterized by electric quadrupole (E2, where 2 denotes photon angular momentum $L = 2$) and magnetic dipole (M1, with 1 pointing to photon angular momentum $L = 1$) radiation [56]. The corresponding change in magnetic quantum number is $\Delta m = 0, \pm 1$ for M1 radiation and $\Delta m = 0, \pm 1, \pm 2$ for E2 radiation for the case of unpolarized radiation². Therefore, 8 lines can be observed in this case as shown in the Fig. 3.2 [56].

The magnetic field $|\mathbf{B}_{eff}|$ in (3.9) measured by Mössbauer or NRS technique is the sum of several contributions and usually called effective field. Generally, the \mathbf{B}_{eff} is a vector sum of two components, the field produced by the electronic configuration of the atom itself, called magnetic hyperfine field \mathbf{B}_{hf} and the field produced by macroscopic conditions for the sample \mathbf{B}_{surr} :

²Polarized radiation is sensitive to preferred orientation of magnetic moment. This case will be discussed in details in the NRS theory section 3.4

$$\mathbf{B}_{eff} = \mathbf{B}_{hf} + \mathbf{B}_{surr} \quad (3.10)$$

The \mathbf{B}_{hf} is a vector sum of magnetic fields produced by direct and indirect interactions of the electronic system with the nucleus.

\mathbf{B}_{hf} has four contributions:

$$\mathbf{B}_{hf} = \mathbf{B}_{core} + \mathbf{B}_{orb} + \mathbf{B}_{dip} + \mathbf{B}_{trhf} \quad (3.11)$$

\mathbf{B}_{core} is the core polarization term. It exists because core s -electrons can penetrate the nucleus. A non-zero probability of finding an electron in the nucleus leads to the interaction between the nuclear magnetic moment and the spin density of core electrons at the nucleus. \mathbf{B}_{core} is usually called Fermi contact interaction and it is the most significant contribution to \mathbf{B}_{hf} . The origin of the Fermi contact interaction is the spin polarization of core electrons. From quantum mechanics it is known that the energy of interaction between electrons is maximal for electrons with opposite spins. For the Ir^{4+} ion studied in this work, the electronic d shell is half-occupied by electrons and cumulative spin of d orbitals is non-zero. The non-zero cumulative spin of d electrons polarizes the spin of the system and core electrons with opposite spin are thus repelled into the direction of the nucleus, increasing the density of s -electrons (and electron spin) in the nucleus. The Fermi contact field has thus an opposite direction to the field generated by the spins of the d electrons. The same is correct for f -electrons, as shown for Eu [59].

The orbital angular momentum interaction term \mathbf{B}_{orb} exists due to the interaction of the magnetic moment of the nucleus with the total orbital angular momentum of electrons in the open shells. It cancels for angular momentum $L = 0$, for instance, for ions with fully-, half- and non-occupied outer shells. \mathbf{B}_{dip} is given by the direct interaction between the spin of the nucleus and the spin of the valence electrons. The dipolar term \mathbf{B}_{dip} is zero for fully-, half- and non-occupied shells and if the environment of the nucleus has cubic symmetry. It is worth to note that typically $\mathbf{B}_{dip} \propto \Delta E_Q$ [60].

\mathbf{B}_{trhf} is the transferred hyperfine field. It exists due to the interaction between the spin of the nucleus and the spin of magnetic ions surrounding the nucleus. An important contribution to the transferred hyperfine field is the polarization of core electrons of non-magnetic ions by magnetic ions, also called "super-exchange interaction". \mathbf{B}_{trhf} may also arise with metallic bonding, where conduction electrons penetrate the nucleus and polarize it. The effect which is called RKKY (Ruderman, Kittel, Kasuya, and Yosida) interaction [21]. A non-cubic environment of nucleus can also lead to a non-zero \mathbf{B}_{trhf} term.

The field \mathbf{B}_{surr} is determined by macroscopic conditions like externally applied magnetic

field \mathbf{B}_{ext} and a demagnetization field. \mathbf{B}_{surr} is given as the vector sum:

$$\mathbf{B}_{surr} = \mathbf{B}_{ext} + D\mathbf{M} \quad (3.12)$$

where D is the demagnetization factor which takes the shape of the sample into account, \mathbf{M} is the magnetization. For spherical particles $D = 0$, while for a foil $D = \frac{8\pi}{3}$ for magnetization normal to the surface and $D = 0$ for magnetization in the plane of the foil. $D\mathbf{M}$ is usually directed opposite to \mathbf{B}_{ext} .

Comparing the contributions to \mathbf{B}_{eff} , the Fermi contact term \mathbf{B}_{core} is usually larger than the orbital \mathbf{B}_{orb} and the dipolar term \mathbf{B}_{dip} . The Fermi contact term usually does not change even in high external fields and is always antiparallel to the spin of outer electronic shells ($d-$ or $f-$). Since \mathbf{B}_{eff} is a vector sum, it depends on the direction of contributing magnetic moments. In the following several cases of magnetic order are analyzed.

3.1.1 Ferromagnetism

In a ferromagnet the atomic magnetic moments are aligned in one direction within a domain in the absence of external fields. The magnetic moment of the domains can be fully aligned in these materials at moderate fields, typically less than 0.5 T. For these materials, $|\mathbf{B}_{eff}|$ is equal to $|\mathbf{B}_{hf}|$ in the absence of external fields. \mathbf{B}_{eff} measured in ferromagnetic materials with zero angular orbital momentum of outer shells (e.g. α -Fe) is equal in the magnitude to the Fermi contact field \mathbf{B}_{core} (33 T for α -Fe). Small external fields can align electronic spin but do not change the electronic configuration of the ions and thus $|\mathbf{B}_{eff}|$ is given by the Fermi contact field $|\mathbf{B}_{core}|$ minus the field $|\mathbf{B}_{surr}|$. For instance, $|\mathbf{B}_{eff}|$ in the α -Fe foil magnetized in the foil plane in the external field of 13 T will be equal to 20 T.

3.1.2 Antiferromagnetism

In an antiferromagnetic material half of the magnetic moments orient antiparallel with respect to the other half, and the macroscopic magnetization is aspiring to zero. The preferable orientation of moments can be described by the two magnetic sub-lattices, each having one orientation. In a perfect anti-ferromagnetic material two sub-lattices show exactly antiparallel magnetization. The total magnetic moment in this case is zero. In the presence of rather small external fields, e.g. up to 4 T for NiO, the magnetic moments are oriented perpendicular to the field [61]. The measured effective field for the

perfect anti-ferromagnetic material, being a vector sum of \mathbf{B}_{hf} and \mathbf{B}_{surr} , will be given by:

$$|\mathbf{B}_{eff}| = \sqrt{|\mathbf{B}_{hf}|^2 + |\mathbf{B}_{surr}|^2} \quad (3.13)$$

This relation was found to be valid for instance for NiO, which can be described by two sub-lattices with nearly antiparallel moments as shown in the Ref. [61]. Magnetic moments in an antiferromagnetic material can also slightly deviate from the exact antiparallel alignment by a small angle. In this case the material is called a canted antiferromagnet. Small fields usually do not align the canted moments inside the domain. In this case the measured $|\mathbf{B}_{eff}|$ will be determined by the canting angle ϕ_{cant} between magnetic sub-lattices and their orientation with respect to the field \mathbf{B}_{surr} . The derivation of $|\mathbf{B}_{eff}|$ is explained in the Fig. 3.3 for the case of two nuclear sites with non-equal magnetic hyperfine fields \mathbf{B}_{hf1} and \mathbf{B}_{hf2} , respectively.

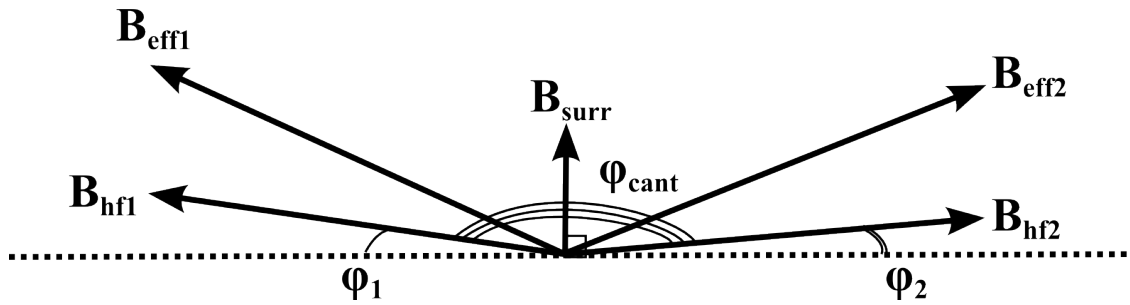


Figure 3.3: A sketch for the calculation of effective magnetic field on nucleus in case of canted antiferromagnet. \mathbf{B}_{hf1} and \mathbf{B}_{hf2} are the magnetic hyperfine fields at the 1st and 2nd site, respectively (s. text).

3.2 Mössbauer Effect

The Mössbauer effect is the recoilless emission or absorption of γ -quanta by nuclei. The effect was discovered by R.L. Mössbauer in 1958 [62, 63]. He demonstrated that the γ -quanta emitted by the decay of the excited state of ^{191}Ir can be resonantly absorbed by a sample containing ^{191}Ir nuclei.

In the process of emission of γ -quanta the momentum is conserved and transferred to the emitting nucleus, thus the energy of emitted quanta is smaller than the energy of the excited state E_0 due to the recoil of the nucleus: $E_\gamma = E_0 - E_R$ where E_γ energy of transition, E_R - recoil energy which for the unbound nucleus is:

$$E_R \cong \frac{E_\gamma^2}{2Mc^2} \quad (3.14)$$

with M the mass of the nucleus. For the same reason, the energy of the absorbed quanta must be higher than the energy of the transition: $E_\gamma = E_0 + E_R$. Therefore, in order to observe resonant absorption, the energy shift $2E_R$ should be less than the linewidth of the resonance Γ . The recoil energy is in the order of 10^{-3} to 10^{-2} eV for typical Mössbauer transitions with $E_0 < 100$ keV. The linewidth of the resonance Γ is related to the lifetime of the excited state τ_0 as: $\Gamma = \frac{\hbar}{\tau_0}$. Here, τ_0 is typically in the range 10^{-1} - 10^3 ns and Γ is thus in the 10^{-6} - 10^{-9} eV range. These values are much smaller than the energy shift $2E_R$. For an unbound nucleus the condition of resonant absorption is thus not fulfilled because the mass of the nucleus is small and the energy of the transition, E_γ , is high.

In a solid, the re-emission of resonantly absorbed photons might be described by de-excitation of states without change in the lattice state, $|e\rangle |n\rangle \rightarrow |g\rangle |n\rangle$ or with a change of the vibration states, $|e\rangle |n\rangle \rightarrow |g\rangle |m\rangle$ with $m \neq n$, as shown in the Fig. 3.4.

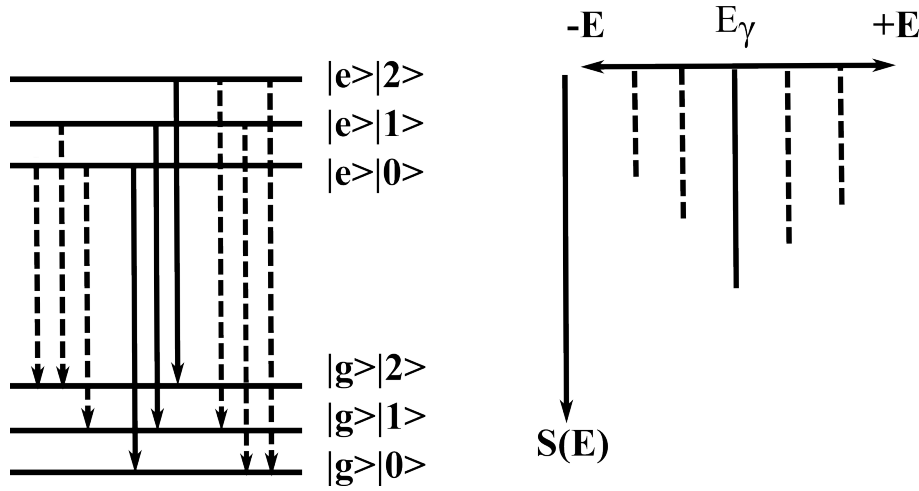


Figure 3.4: Lattice vibrational states and corresponding transitions: the solid lines show recoilless emission of x-rays, dashed lines present phonon-assisted transitions. Left panel: a sketch of level schema; right panel: a sketch of probability density of the corresponding transitions. Reproduced from Ref. [64].

The de-excitation of the states with change of the vibration states can occur with creation, $|e\rangle|n\rangle \rightarrow |g\rangle|n+m\rangle$, or annihilation, $|e\rangle|n\rangle \rightarrow |g\rangle|n-m\rangle$ of m number of phonons. The processes are shown in the fig 3.4 by dashed lines. These processes provide a direct probe of lattice vibrations and will be treated in the section 3.4.2.

There is a finite probability that a photon is emitted or absorbed by nucleus without creation or annihilation of phonons. The effect is called the Mössbauer effect or recoil-free resonant absorption and emission of photons. The effect is similar to the elastic (Bragg) scattering of x-rays from the lattice planes in a crystal. Here, the momentum transfer to the lattice planes occurs without change of energy. The effect increases with lowering the temperature and decreasing interatomic distances (e.g. using hydrostatic compression), with decreasing atomic displacement [54, 52]. A detailed description of the probability of the Mössbauer effect will be given in the next section 3.3.

One should note that the linewidth of the Mössbauer radiation is extremely small due to the absence of recoil. It is thus a very sensitive spectroscopic probe and its longitudinal coherence length is very high. Indeed, the longitudinal coherence length in vacuum is roughly equal to $\frac{\hbar c}{\Gamma}$ and thus for Mössbauer radiation is in the 0.1-1000 meter range.

3.3 Lamb-Mössbauer factor

The probability of the recoilless absorption or emission of γ -rays, the Mössbauer effect, is given by the Lamb-Mössbauer factor. It can be derived using the description of emission of γ -quanta by the nucleus in a crystal lattice.

The vector potential of an electromagnetic wave emitted by nuclei is given by:

$$\mathbf{A}(t) = \mathbf{A}_0 e^{i\omega_0 t} \quad (3.15)$$

with $\mathbf{A}_0(t)$ is the normal vector and ω_0 is the resonance frequency of the emitted wave.

At elevated temperatures lattice vibrations exist which can be treated as oscillators. Frequency of m th of oscillator $\Omega(t)_m$ is given by the Doppler shift:

$$\Omega(t)_m = \omega_0 \left[1 + \frac{v_m(t)}{c} \right] \quad (3.16)$$

With $v_m(t)$ being the displacement of oscillator divided by time (velocity of oscillator) and c is the speed of light.

In a first approximation the vibration spectrum can be described by a set of harmonic oscillations. For this case the time dependence of the displacement of the oscillators from their equilibrium position can be approximated by a Fourier series. Using this approximation, the vector potential of the emitted wave is given by:

$$\mathbf{A}(t) = \mathbf{A}_0 e^{i\omega_0 t} e^{ikx_0 \sin(\Omega_m t)} \quad (3.17)$$

with k is the wavevector of non-shifted radiation (corresponds to the E_γ , energy of nuclear transition), x_0 is the amplitude of oscillation. The exponential part can be rewritten as a series of products of Bessel functions J_n of the first kind and harmonic waves with the frequencies $\omega_0 + n\Omega_m$ which approximate the movement of m -th oscillator with the frequency Ω_m :

$$\mathbf{A}(t) = \mathbf{A}_0 \sum_{n=-\infty}^{+\infty} \prod_{m=1}^{3N} J_n(kx_m) e^{i(\omega_0 + n\Omega_m)t} \quad (3.18)$$

N is the number of oscillators.

The probability to observe a wave with $\mathbf{A}_0(t)$ is given by the squared module of its amplitude, $|\mathbf{A}_0(t)|^2$. Then, the probability of recoilless absorption, i.e. with zero-phonon transfer, is given by:

$$f_{LM} = \prod_{m=1}^{3N} J_0(kx_m)^2 \quad (3.19)$$

The definition of the mean squared displacement of an oscillator $\langle x^2 \rangle = \sum_m \frac{x_m^2}{2}$ can be used to re-write the formula to:

$$f_{LM}(T) \approx e^{-k^2 \langle x^2 \rangle} = e^{-\frac{E_\gamma^2 \cdot 4\pi^2}{\hbar^2 c^2} \langle x^2 \rangle (T)} \approx e^{-\langle x^2 \rangle (T) \left[\frac{\text{\AA}^2}{(E_\gamma [\text{keV}])^2 / 3.8938} \right]} \quad (3.20)$$

From this definition one can immediately see that f_{LM} decreases with increasing transition energy E_γ . While the mean squared displacement of the nucleus $\langle x^2 \rangle (T)$ is in the order of 10^{-4} nm^2 the upper limit of transition energies should be not higher than 100-150 keV in order to observe a significant effect of recoilless absorption. As shown in the eq. (3.20), $\langle x^2 \rangle$ and f_{LM} are functions of temperature: $\langle x^2 \rangle$ increases and f_{LM} decreases with increasing temperature.

Two approaches exist to describe the Lamb-Mössbauer factor: a classical and a quantum-mechanical. The classical approach assumes that the vibrational spectrum of a solid is continuous and the mean squared displacement is directly proportional to temperature. In the classical approximation f_{LM} can be calculated by the equation (3.20) given above.

In quantum mechanics the spectrum of lattice vibrations (phonons) is discrete. Quantum mechanics treats the phonon spectrum by the density of phonon states and the number of occupied states.

The Lamb-Mössbauer factor can be written as:

$$f_{LM} = \exp \left[-\frac{2E_R}{3N\hbar} \int_0^{\Omega_{max}} \frac{1}{e^{\hbar\Omega/k_B T} - 1} + 1/2 \cdot \frac{g(\Omega)}{\Omega} d\Omega \right] \quad (3.21)$$

with $g(\Omega)$ - density of phonon states and Ω_{max} - maximal frequency of the phonon spectrum. The integral is applied over all states with frequencies Ω [56]

One can see that the determination of density of phonon states $g(\Omega)$ and E_R provides the knowledge of f_{LM} .

It is usually difficult to measure the density of phonon states directly and therefore several approximations exist. First, the vibration spectrum can be approximated by the Einstein model. It states that only one frequency is present. In this case $\Omega = \Omega_{max} = \Omega_1$ and the equation (3.21) transforms to:

$$f_{LM} = \exp \left[-\frac{E_R}{\hbar\Omega_1} \right] \quad (3.22)$$

This simple model is very useful for the description of isotropic modes, e.g. the optical vibration modes and in some special cases where the measured $g(\Omega)$ can be described by a single vibration mode (e.g. modes of filler in skutterudites [65, 66]). In a real solid the bonding between atoms is very strong so that oscillations of an atom affects the oscillations of its neighbors and the Einstein model is not correct anymore. The Debye model can be used instead.

The Debye model assumes that $g(\Omega)$ is a quadratic, continuous function of Ω and defined up to maximum frequency Ω_{Deb} where it has a maximum:

$$g(\Omega) = \begin{cases} \frac{9N}{\Omega_{Deb}^3} \Omega^2 & \text{for } \Omega < \Omega_{Deb} \\ 0 & \text{for } \Omega > \Omega_{Deb} \end{cases} \quad (3.23)$$

From equation (3.23) and equation (3.21) f_{LM} is given by [54]:

$$f_{LM} = \exp \left[-\frac{6E_R}{k_B\Theta_{Deb}} \left[\frac{1}{4} + \left(\frac{T}{\Theta_{Deb}} \right)^2 \int_0^{T_D/T} \frac{x}{e^x - 1} dx \right] \right] \quad (3.24)$$

Here, Θ_{Deb} is the Debye temperature.

The exact solution of this equation can be obtained by numerical methods. However, for the two limiting cases, at high and at low temperature, the equation can be simplified. At low temperatures ($T \ll \Theta_{Deb}$) it transforms to:

$$f_{LM} = e^{-\frac{E_R}{k_B\Theta_{Deb}} \left(\frac{3}{2} + \frac{\pi^2 T^2}{\Theta_{Deb}^2} \right)} \quad (3.25)$$

While at high temperatures ($T > \Theta_{Deb}$) $\ln f_{LM}$ is a linear function of temperature:

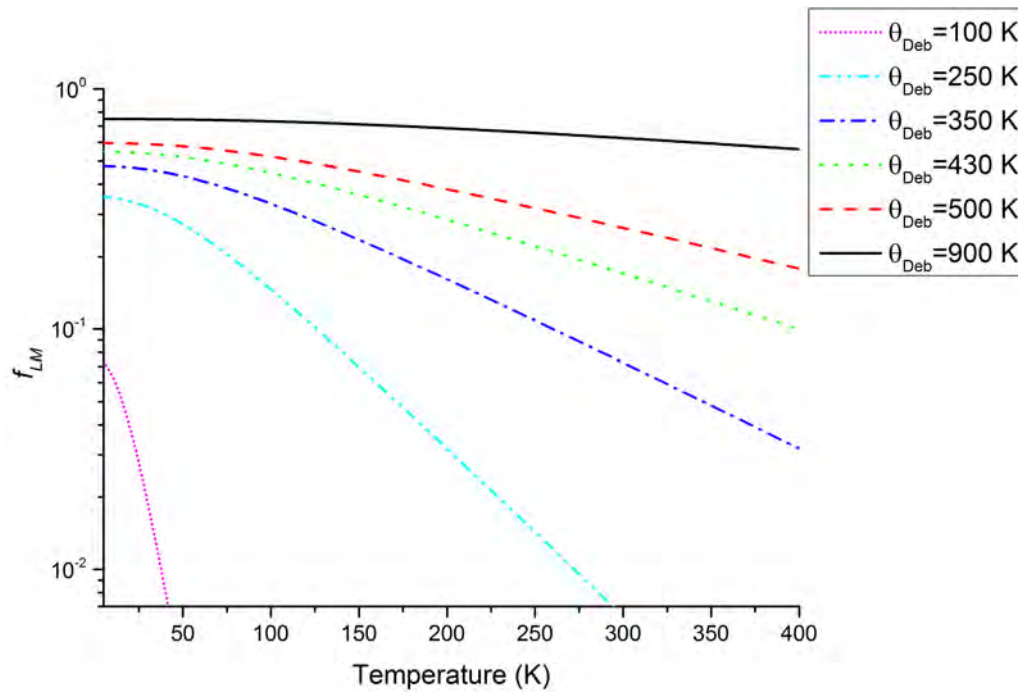


Figure 3.5: Temperature dependence of the Lamb-Mössbauer factor calculated after the Debye model for different Debye temperatures Θ_{Deb} in the case of 73 keV transition in ^{193}Ir nucleus.

$$f_{LM} = e^{-\frac{E_R}{k_B \Theta_{Deb}} T} \quad (3.26)$$

The Lamb-Mössbauer factor can also be calculated when the phonon density of states is known. In this case it is given by [67]:

$$f_{LM} = \exp \left[-E_R \int \frac{g(E)}{E} \frac{1 + e^{\frac{E}{k_B T}}}{1 - e^{\frac{E}{k_B T}}} dE \right] \quad (3.27)$$

Analyzing the equation (3.27) one can see that f_{LM} is weighted by $1/E^n$ with $1 < n < 2$. Thus, mainly low energy vibrations contribute to f_{LM} .

It is notable that f_{LM} increases with decreasing temperature and becomes significant at temperatures below Θ_{Deb} . This is the limitation of Mössbauer spectroscopy: the incident photon flux per linewidth of the resonance should be very high in order to be able to observe resonant absorption at elevated temperatures.

The temperature dependence of the Lamb-Mössbauer factor is shown in the Fig. 3.5 for the case of 73 keV transition in ^{193}Ir . The Debye temperatures are in the range of the values given in the literature for Ir compounds. For Ir metal studied in this work 430 K is the most frequently cited Debye temperature [21, 68].

Until this point the vibrations of the crystal lattice were considered as harmonic. However, the anharmonicities are always present and have an impact on f_{LM} . Among other effects, anharmonicity of lattice vibrations explains the non-zero thermal expansion of materials. Given the thermal expansion ϵ the Lamb-Mössbauer factor can be determined by [69]:

$$\ln f_{LM} = \frac{\ln f'_{LM}}{1 + 6\gamma_G \epsilon} \quad (3.28)$$

where f'_{LM} is the measured Lamb-Mössbauer factor, ϵ is the relative thermal expansion, $\gamma_G = -\frac{V}{E} \frac{dE}{dV}$ is the Grüneisen parameter with V is the volume of the unit cell, E is the energy of vibrational mode.

The effect of thermal expansion is significant for the correction of interference between electronic and nuclear absorption in MS with very intense sources, however, it is less important for the hyperfine spectroscopy on the systems studied in this work. For Ir metal, typical Grüneisen parameter values are in the 2.3-2.5 range and thermal expansion is about $6 \cdot 10^{-6}$. Thus, even at room temperature the contribution of thermal expansion to the value of f_{LM} is only 10^{-3} (one tenth of a percent).

3.4 Nuclear Resonant Scattering

3.4.1 Nuclear Forward Scattering

The natural linewidths of Mössbauer excited levels are in the order of $\text{feV-}\mu\text{eV}$ [2]. When the nucleus is surrounded by electrons, hyperfine interactions between the nucleus and the electronic system result in the splitting of the nuclear levels into sub-levels, as shown in the section 3.1 [2, 20, 54]. The magnitude of the splitting is in the order of $\text{neV-}\mu\text{eV}$ in solids. The extremely narrow nuclear resonance linewidth, in order of $\text{feV-}\mu\text{eV}$, makes spectroscopy by nuclei a very sensitive tool of research.

In conventional Mössbauer spectroscopy a source with almost single line emission spectrum is used to generate photons of the same energy as the Mössbauer transition in nuclei in the sample [54]. The obtained spectrum is a convolution of the emission spectrum of the source and the transmission spectrum of the sample over the energy region defined by the Doppler shift of the source or the sample [54]. In the case of Nuclear Forward Scattering (NFS) a synchrotron is used as photon source and the object of study is the time-dependence of the delayed radiation field which follows the excitation of nuclear levels by the synchrotron radiation (SR) pulse. In an NFS experiment it is assumed that all sub-levels are excited simultaneously; the photons produced during the decay interfere with each other in forward direction and produce a characteristic beating pattern in time [2, 20]. Therefore, the incident beam should have a bandwidth of some μeV at least to be able to cover the entire energy range of the hyperfine splitting and measure the hyperfine parameters. The undulator radiation has an energy bandwidth of the order of 50-150 eV. The radiation outside the region of nuclear resonance is not resonantly scattered by nuclei and contributes as a strong background signal at about 100 ps after excitation (so-called "prompt" signal due to the fast electronic scattering events). The latter results in an overload of detectors and acquisition electronics if no further reduction of photon flux is applied [2, 20]. Monochromators aim to reduce the energy bandwidth and thus lower the prompt signal from electronic scattering events. It is worth to mention that monochromators should also have high efficiency in order to maintain high count-rates in NFS experiment [2, 20]. A detailed overview of monochromators is given in chapter 4.2. Since the radiation scattered by the nuclei is delayed in time, only photons arriving between pulses of synchrotron radiation (SR) are counted; the prompt SR pulses aren't acquired by the detection electronics. For further increase of countrates APD detectors with high efficiency and detector electronics with high dynamical range are used. This assures earlier start counting times and high countrates. The chapter 4.3 provides an overview of detection techniques for NRS.

For the case of NFS the radiation scattered in forward direction is collected. Thus in NFS

experiments all optical elements, sample environment components, and detectors are placed in line with the beam path downstream to the source, except the case of backscattering geometry [2, 20]. The following chapters give a theoretical description of NFS inspired by References [2, 70, 64, 71, 72].

Scattering by bound nucleus

Absorption and re-emission of x-rays by nuclei can be described by scattering. The amplitude of the scattered wave E_S scales with the amplitude of the incident wave E_i as:

$$E_S(w) = f(w)E_i(w) \quad (3.29)$$

$f(w) = |f(w)| e^{i\varphi(w)}$ being the scattering function which has amplitude $|f(w)|$ and phase $\varphi(w)$. $f(w)$ gives a full description of the system interacting with the excitation pulse.

A SR excitation pulse is very short in the time domain. It can be described by a Dirac δ -function with a maximum at the resonance frequency w_0 :

$$\delta(t) = \frac{1}{2\pi} \int_{-\infty}^{+\infty} e^{iw_0 t} dt \quad (3.30)$$

The response of the system to the excitation pulse is a convolution of the scattering function and the Dirac δ -function.

For the case of a single bound nucleus without hyperfine interactions it is given by:

$$f(t) = -i \frac{1}{8\pi} \sigma_N f_{LM} \beta \frac{1}{\tau_0} e^{iw_0 t - \frac{t}{2\tau_0}} \quad (3.31)$$

Thus, scattering by a single nucleus is given by the nuclear resonant cross-section σ_N , Lamb-Mössbauer factor f_{LM} , abundance of nuclei β , lifetime τ_0 of excited state, and transition frequency w_0 . The nuclear resonant cross-section σ_N depends on the energy of incident x-rays E , the internal conversion coefficient α and the spin of the excited and ground states, I_e and I_g :

$$\sigma_N = \frac{2\pi\hbar^2 c^2}{E^2} \frac{1}{1 + \alpha} \frac{2I_e + 1}{2I_g + 1} \quad (3.32)$$

Multiple scattering by ensemble of nuclei: dynamical beats

In a solid state the wave scattered by a nucleus can be re-scattered by neighboring nuclei: the effect is called multiple scattering. The theoretical treatment of this case is similar to that given by the dynamical theory of diffraction of x-rays on electrons (see e.g. Ref. [70]). An ensemble of nuclei without hyperfine interactions should be considered at this point. Waves re-scattered by each nucleus will interfere. For disordered systems like non-crystalline or very fine powdered samples only the waves re-scattered in forward direction will interfere constructively. The transmitted field E_{tr} will be a sum of the incident E_i and forward scattered field E_{NFS} :

$$E_{tr} = E_i + E_{NFS} \quad (3.33)$$

Scattering from a set of thin targets having thickness dz along the direction z is considered in order to treat the effect of multiple nuclear scattering. Here, the fraction of wave transmitted by each target is given by:

$$dE_{tr} = -iE_{tr} \frac{2\pi}{k} f(w) N_R dz \quad (3.34)$$

where N_R is the number of resonant nuclei.

After integration over the length one obtains:

$$E_{tr} = E_i e^{-i \frac{2\pi}{k} f(w) N_R z} \quad (3.35)$$

The excitation field E_i cannot be approximated by a δ -function at this point since the SR source does emit a set of wavelengths. Instead, the incident wave is described by a set of harmonics:

$$E_i = E_{i0} e^{i\omega t} \quad (3.36)$$

Integrating the transmitted field over all harmonics and taking the Fourier-transformed scattering amplitude into account gives:

$$E_{tr} = E_{i0} \frac{\Gamma}{\hbar} e^{-\frac{att}{2}} \left[\delta(t) + e^{i\omega_0 t - \tau/2} \frac{T_{eff}}{2} \frac{J_1(\sqrt{T_{eff}\tau})}{\sqrt{T_{eff}\tau}} \right] \quad (3.37)$$

where E_{i0} is the amplitude of incident wave, $att = \sigma_{ph0} n_0 d$ electronic absorption term with σ_{ph0} is the photoelectric absorption cross-section, n_0 is the number of atoms per unit volume, d is the sample thickness $\tau = \frac{t}{\tau_0} T_{eff} = \sigma_N f_{LM} N_R d$ is the effective thickness, J_1 is the Bessel function of the first kind and first order.

The first term in brackets is the field generated by the incident wave promptly scattered by electrons. The second term describes the amplitude E_{NFS} of the delayed field generated by photons scattered by nuclei in forward direction.

For early times after excitation and small T_{eff} so that $\frac{T_{eff}}{\tau} < 3$, E_{NFS} can be written as:

$$E_{NFS} \cong e^{-\frac{att}{2}} \frac{T_{eff}}{2} e^{-\tau/2(1+\frac{T_{eff}}{4})} \quad (3.38)$$

One can see that with increase of the effective thickness T_{eff} the amplitude of the forward scattered field E_{NFS} tends to decay faster, the effect is called "speed-up".

In a NFS experiment the intensity of the forward scattered field is measured. It is the square of the amplitude E_{NFS} :

$$I_{NFS} = I_0 \frac{\Gamma}{\Delta E} \frac{1}{4\tau_0} e^{-\frac{t}{\tau_0}} \left(\frac{J_1(\sqrt{T_{eff}\tau})}{\sqrt{T_{eff}\tau}} \right)^2 \quad (3.39)$$

Due to the presence of the Bessel function the time dependence of I_{NFS} has a pronounced beating pattern strongly dependent on the effective thickness T_{eff} . In order to demonstrate the effect of sample thickness, a comparison of NFS time spectra and energy spectra of NFS and MS is depicted in the Fig.3.6 [70].

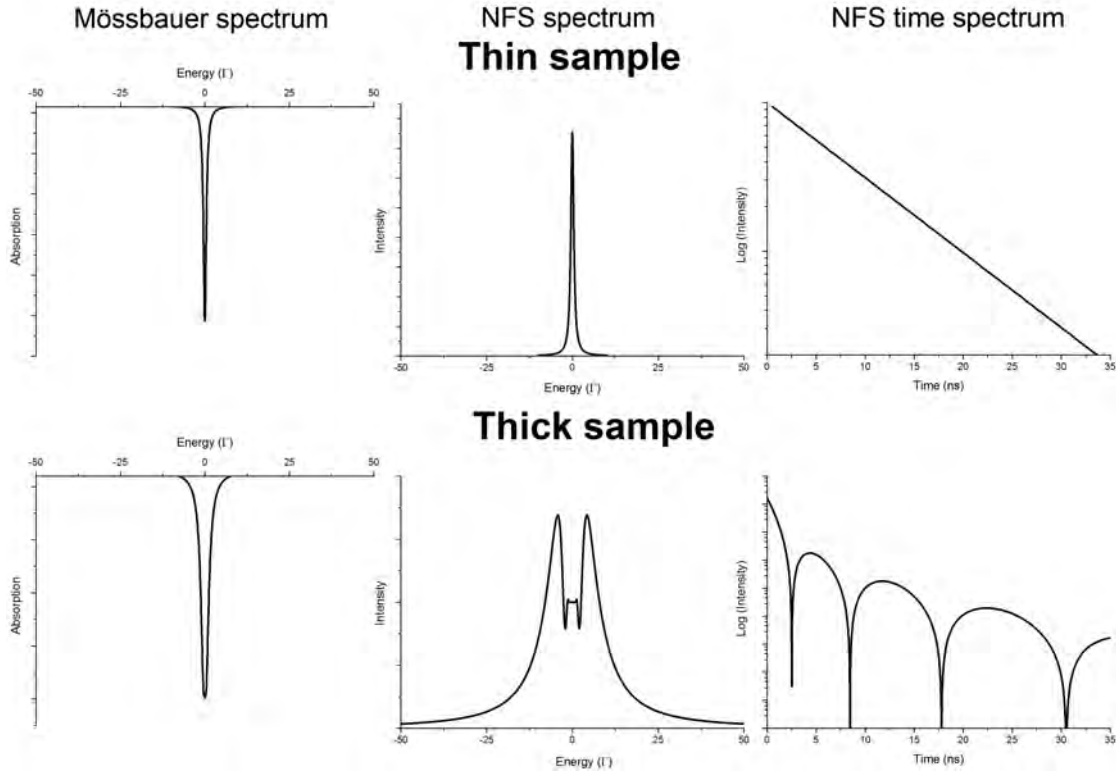


Figure 3.6: Mössbauer and NFS spectra: dynamical beating and speed up effects. Calculations are given for the case of 73 keV resonance in ^{193}Ir .

At small T_{eff} the response lines in energy domain are Lorentzian functions of energy, for MS as well as for NFS. In the time domain I_{NFS} is described by an exponential decay for small T_{eff} (fig 3.6, upper right panel). With an increase of the effective thickness the width and intensity of the response line in MS increase. A Fourier-transformed NFS spectrum shows behavior similar to that in MS until some critical value of the effective thickness is achieved. Above this critical value the intensity of the scattered wave cannot exceed the intensity of the incident wave. Instead, the intensity is re-distributed on the wings of the resonance line and a double hump pattern of the spectrum is formed (fig 3.6, lower center panel). Notably, the maxima are symmetric around the resonance and the separation between them does increase with further increase of the effective thickness. The intensity of NFS in time domain shows a pronounced beating pattern (fig 3.6, lower right panel) at large effective thicknesses which is called dynamical beating [2, 70]. The period of beats does increase with time and with decrease of effective thickness [2, 70].

The thickness of the sample has significant influence on count-rate of NFS. It is especially important to optimize sample thickness in NFS experiments with short-living excited states in order of 2-8 ns, because the speed-up effect deteriorates NFS countrates at times even earlier than lifetimes of the excited states. Moreover, with incorrectly determined sample thicknesses the beating pattern can show a minimum of I_{NFS} at early times which

leads to low NFS signal. Therefore, the thickness of samples should be optimized for each specific study.

The optimal sample thickness d_{opt} is defined as the thickness which gives a trade-off between electronic absorption and nuclear resonance scattering. In the following it is shown how sample thickness can be optimized for NFS and how countrates can be estimated in the absence of hyperfine interactions. This is the case of Ir metal studied in this work. The optimal sample thickness d_{opt} can be found calculating the maximum of intensity of the NFS signal integrated over the time window between start counting time t_1 and time of arrival of the next SR pulse t_2 . It is given by the time integral:

$$R(d) = \int_{t_1}^{t_2} S(d, \tau_0, l_e, l_n) dt \quad (3.40)$$

where:

$$S(d, \tau_0, l_e, l_n) = e^{-\frac{d}{l_e}} e^{-\frac{t}{\tau_0}} \left(\frac{d}{4\tau_0 l_n} \right)^2 \sigma^2 \left(\frac{d \cdot t}{4\tau_0 l_n} \right) \tau_0 \quad (3.41)$$

with $\sigma^2(\frac{d \cdot t}{16\tau_0 l_n})$ being a square of the function defined as $\sigma(x) = \frac{J_1(2\sqrt{x})}{\sqrt{x}}$; $J_1(x)$ is the Bessel function of the first order and first kind, τ_0 is the lifetime of the excited state, l_e is the electronic absorption length, $l_n = \frac{1}{\mu_n f_{LM}}$ is the nuclear absorption length, μ_n is the nuclear attenuation coefficient, and f_{LM} is the Lamb-Mössbauer factor.

Note that the start counting time t_1 significantly influences the maximum of the integrated intensity $R(d)$ ³. The dependence of $R(d)$ on d is shown in Figure 3.7 for different start counting times t_1 .

³It is worth to notice here that nuclear absorption length l_n in eq. (3.41) includes Lamb-Mössbauer factor which decreases with temperature. Analyzing eq. (3.41), one notes that the optimal thickness increases with temperature.

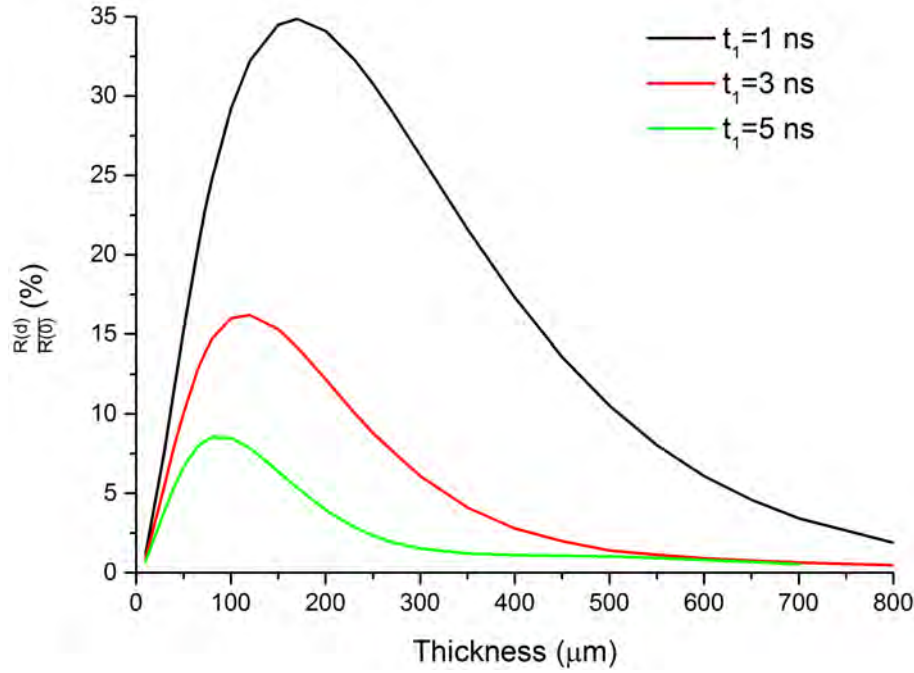


Figure 3.7: The dependence of $\frac{R(d)}{R(0)}$ on d for different start counting times t_1 for elemental Ir. The Lamb-Mössbauer factor is taken equal to 0.37 according to Ref. [57]. Electronic absorption length of $176\mu\text{m}$ was calculated from density of Ir using software ATHENA [73].

For the 73 keV transition in ^{193}Ir isotope and the Ir metal sample studied in this work the relevant parameters are $\tau_0 = 8.4\text{ ns}$ and $l_e = 174.9\mu\text{m}$. The values of the optimal thickness are calculated for different temperatures and different start counting times t_1 . The results of calculation are shown in the table 3.1: the optimal thicknesses are in the $46\text{-}200\mu\text{m}$ range for the case studied in this work.

Based on the efficiency of the monochromator and APD detectors, it is possible to estimate the flux of photons in an NFS experiment. It is given by:

$$I_{NFS} = I_0 \frac{\Gamma}{\Delta E} R(T_{eff}) \eta_{APD} \eta_{mono} + B \quad (3.42)$$

with I_0 being the flux of incident photon beam, ΔE is the energy bandpass of the monochromator, η_{APD} is the efficiency of the multielement APD detector, η_{mono} is the efficiency of the monochromator and B is the flux of background radiation.

Obviously, the two critical parameters for the countrate are the late start time for counting and the efficiency of the APD detector. The late start time for counting is related to the presence of spurious electron bunches in the synchrotron ring and due to overload of

detectors and/or electronics. The parasitic bunches can be removed by an efficient procedure of beam cleaning, as described later in the section 4.4. The count-rate values can be improved by the use of a stack of thin APD detectors with small capacitance [74]. The former assures that more resonant photons are acquired and the later makes accessible earlier starting times for counting which is described in details in the Chapter 4.3.

For the 73 keV resonance in ^{193}Ir the natural linewidth Γ is 75 neV. The flux of photons at 73 keV is measured to be $3.8 \cdot 10^6$ ph/(meV·s) at P01 beamline. The flux of photons in an NFS experiment on elemental Ir is calculated using eq. (3.42) for different sample temperatures and start times for counting. The energy bandpass was taken as $\Delta E = 112$ meV (theoretical value for energy bandpass of the monochromator, see Chapter 4.5) and the efficiencies of the monochromator and APD were assumed to be $\eta_{APD} = \eta_{mono} = 1$. The obtained values are shown in the table 3.1.

Temperature of Ir foil, [K]	Start time for counting, [ns]	Optimal thickness, [μm]	NFS count-rate, [Hz]	Time desired for collecting of a reasonable* number of counts, [min.]
50**	3	115	65	2.3
	5	85	34	4.4
	9	62	12	13
300#	3	265	6.2	24
	5	250	4.4	34
	9	225	2.2	70

Table 3.1: Optimal thickness and expected NFS count-rate for Ir metal as a function of different counting start time t_1 .

* Assuming 9000 counts; the number is based on experience with NFS experiments on Ir

** $f_{LM}=0.37$

$f_{LM}=0.044$

Magnetic and electric hyperfine interactions: quantum beats

In the presence of hyperfine interactions nuclear levels split into several sub-levels and several transitions are allowed, as mentioned in chapter 3.1.

The amplitude of NFS given by equation (3.29) above will be modified to include hyperfine interactions. For this case it is given by [70]:

$$f^{ss'}(\omega, \omega_0) = \text{const} \sum_{\Delta m} \frac{\frac{\Gamma_0}{2\hbar}}{\omega - \omega_0(\Delta m) - i\frac{\Gamma_0}{2\hbar}} \mathcal{C}^2(m_e, m_g, \Delta m) P^{ss'}(\Delta m) \quad (3.43)$$

with $\omega_0(\Delta m)$ - photon frequency of transition

\mathcal{C} - Clebsch-Gordan coefficients which describes the strength of the transition

s - polarization state of incident wave

s' - polarization state of scattered wave and

$P^{ss'}(\Delta m)$ - polarization factor

When the hyperfine splitting is much larger than the linewidth of the resonance, an analytical expression for the scattering function and intensity of NFS can be found [70].

The equation for the intensity of NFS is given by the square of the NFS amplitudes. For the simple case of 2 transitions due to electric quadrupole interaction with equal probability of transtions the intensity of NFS is given by [70]:

$$I_{NFS} = I_0 \frac{\Gamma}{\Delta E} e^{-T_{eff}} e^{-att} 2J_1^2 \left(\sqrt{\frac{T_{eff}\Gamma}{2}} \right) \cos^2 \left(\frac{\Delta\omega t}{2} + \frac{T_{eff}\Gamma}{8\hbar\Delta\omega} \right) \quad (3.44)$$

The comparison of the Mössbauer and NFS spectra in the presence of hyperfine interactions is shown in the Fig. 3.8. The Bessel function and the squared cosine function in (3.44) give rise to a beating pattern similar to the case of multiple scattering described above. In the presence of hyperfine interaction the beating pattern is called "quantum beating". Comparing the equation (3.44) with the equation (3.6) which describes multiple scattering, the frequency in this case is modulated by \cos^2 . The intensity at the minima of I_{NFS} are equal to zero for a perfectly homogeneous sample. However, in an experiment these minima are smeared out due to the finite time resolution of the detector and by distribution of sample thickness.

In the equation for I_{NFS} , the product of the hyperfine splitting and the period of oscillations in the time spectrum can be approximated by a constant for the case of negligible T_{eff} and low electronic absorption [71]. For quadrupole splitting in ^{193}Ir it can be shown that:

$$\Delta E_Q \left[\frac{mm}{s} \right] \cdot T [ns] \approx 17 \quad (3.45)$$

From this equation one can see that the larger the magnitude of splitting, the higher the frequency of the beating pattern which is shown in the Fig. 3.8.

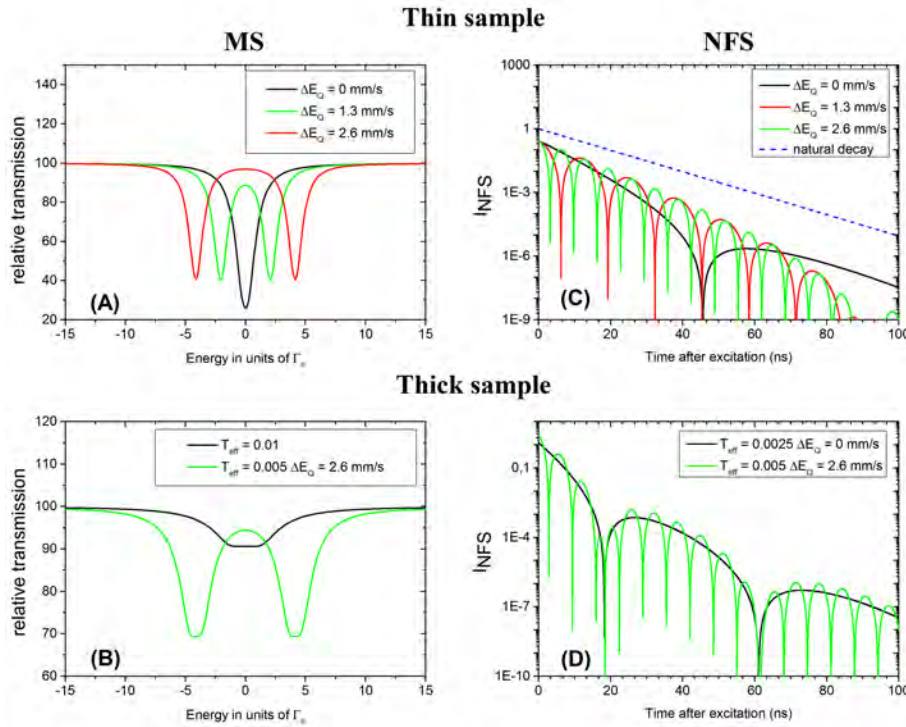


Figure 3.8: Effect of hyperfine splitting on MS and NFS spectra for the case of 73 keV transition in ^{193}Ir : (A) shows MS spectra for the case of single line and quadrupole splitting of $\Delta E_Q = 1.3$ and 2.6 mm/s and thin sample ($T_{eff} = 0.001$); (B) is for the same conditions as (A) but the multiple scattering effect is included with effective thickness $T_{eff} = 0.0025$ for the single line and $T_{eff} = 0.005$ for the splitting $\Delta E_Q = 2.6$ mm/s. Panels (C) and (D) show the corresponding NFS spectra for the cases (A) and (B). On the panel (C) note the speed-up of the decay compared to the natural decay (dashed line) even at small effective thicknesses. Inspired by Ref. [71].

In the general case of two transitions with non-equal probabilities the intensity of NFS is given by [70]:

$$\begin{aligned}
 I_{NFS} = I_0 \frac{\Gamma}{\Delta E} \frac{T_{eff}}{4t} e^{-T_{eff}} e^{-att \cdot \tau} \cdot \\
 \left[\exp \left\{ 2i \left(\omega_1 t + \frac{\alpha_2 \frac{T_{eff} \Gamma}{4\hbar}}{\omega_1 - \omega_2} \right) \right\} \alpha_1^2 \frac{J_1^2(\sqrt{\alpha_1 T_{eff} \tau})}{\alpha_1 T_{eff} \tau} + \right. \\
 + \exp \left\{ 2i \left(\omega_2 t + \frac{\alpha_1 \frac{T_{eff} \Gamma}{4\hbar}}{\omega_1 - \omega_2} \right) \right\} \alpha_2^2 \frac{J_1^2(\sqrt{\alpha_2 T_{eff} \tau})}{\alpha_2 T_{eff} \tau} + \\
 + 2 \cdot \exp \left\{ i \left(\omega_1 t + \frac{\alpha_2 \frac{T_{eff} \Gamma}{4\hbar}}{\omega_1 - \omega_2} \right) \right\} \alpha_1 \frac{J_1^2(\sqrt{\alpha_1 T_{eff} \tau})}{\sqrt{\alpha_1 T_{eff} \tau}} \cdot \\
 \left. \cdot \exp \left\{ i \left(\omega_2 t + \frac{\alpha_1 \frac{T_{eff} \Gamma}{4\hbar}}{\omega_1 - \omega_2} \right) \right\} \alpha_2 \frac{J_1^2(\sqrt{\alpha_2 T_{eff} \tau})}{\sqrt{\alpha_2 T_{eff} \tau}} \right] \quad (3.46)
 \end{aligned}$$

with ω_1 and ω_2 - frequencies of photons emitted in the transitions and α_1 and α_2 probability of the corresponding transitions.

The equation (3.46) includes multiple scattering effects. Notably, the minima of I_{NFS} are non-zero in contrast to the case of equal probabilities of transitions. This is due to the individual contributions to the sum in the square brackets. Including thickness effects, the contrast between maxima and minima of I_{NFS} becomes smaller compared to the case of resonances with the same probabilities.

Up to this point, no polarization effects have been considered. These can be included assuming that for resonance line with Δm and multipole transition Ql (Q is the radiation characteristics and l is the eigenvalue of radiation's angular momentum. $Q = M, L = 1$ for magnetic dipole and $Q = E, L = 2$ for electric quadrupole) the response to polarized radiation is the same as the response of a classical oscillator with $Ql, \Delta m$. In a collective excitation participate only those oscillators whose axis is parallel to the vector product of wave-vector and polarization vector. Particularly, the $\Delta m = 0$ oscillation is excited only when the quantization axis given by direction of EFG principal axis or magnetic moment \mathbf{m} is parallel, while $\Delta m = \pm 1$ oscillation is excited when quantization axis is perpendicular to the vector product of wave-vector and polarization vector (direction of pi -polarization in case of SR) [54]. The $\Delta m = \pm 2$ response (E2 radiation) does not have any component along π polarization direction of incident radiation. These facts are known from Mössbauer spectroscopy (MS) [54] but distinguishing direction of quantization axis is hindered for conventional Mössbauer spectroscopy with unpolarized photon source [71]. For NFS the determination of the quantization axis direction in the

polarization plane is accessible [2].

A more closer quantitative look on the polarization properties of coherent NRS is given by the matrix formalism in the Ref. [2, 75]. The scattering amplitude in eq. (3.29) can be written as:

$$\mathbf{f}(\omega) = \frac{2\pi}{k^2} \sum_j \rho_j (\mathbf{N}_j(\omega) + \mathbf{E}_j(\omega)) \quad (3.47)$$

The electronic scattering matrix $\mathbf{E}_j(\omega)$ scales with the atomic number Z and the total electronic absorption cross section depends on the strength of Compton scattering and photoelectric absorption. This term characterizes only promptly scattered radiation and therefore will not be discussed. The resonantly scattered radiation involved in the processes is, like resonant x-ray magnetic scattering and nuclear resonance scattering, fully described by the second matrix term $\mathbf{N}_j(\omega)$ in eq. (3.47). The general form for $\mathbf{N}_j(\omega)$ is given in the Ref. [76] by:

$$\mathbf{N}_j(\omega) = \frac{\pi(2I_n + 1)}{k} F_{ML} \delta(\omega' - \omega) e^{i(k' - k)R} \sum_{LL'\lambda\lambda'} \delta_{L\lambda} \delta_{L'\lambda'}^* \sum_n \frac{[\mathbf{T}_{Lni}^{(\lambda)}(\hat{k})]^* [\mathbf{T}_{L'ni}^{(\lambda)}(\hat{k}')] }{z_{ni}(\omega') - i} \quad (3.48)$$

where

$$\mathbf{T}_{Lni}^{(\lambda)}(\hat{k}) = \left[\frac{8\pi}{2I_n + 1} \right]^{1/2} \sum_{Mm} \mathbf{Y}_{LM}^{(\lambda)*}(\hat{k}) \mathcal{C}(I_i L I_n; m N) \langle I_i m | \phi_i \rangle \langle \phi_n | I_n m + M \rangle$$

and

$$z_{ni}(\omega') = \frac{2\hbar}{\Gamma} (\Omega_n - \Omega_i - \omega')$$

with $\mathbf{Y}_{LM}^{(\lambda)}$ being the vector spherical harmonics and $\delta_{L\lambda}$ multipole mixing coefficients.

Figure 3.9 shows simulated NFS energy and time-spectra for different orientations of the EFG's principal axis in the case of axially symmetric EFG ($\eta = 0$). An interesting observation emerges: the single line case occurs when V_{zz} directed parallel to the π -polarization direction of the incident beam. This is in contrast to NRS on ^{57}Fe where the single line case takes place when V_{zz} is parallel to the σ -polarization direction. In the figure 3.10 Mössbauer, NRS spectra and NFS time-spectra are shown for different orientations of the magnetic moment.

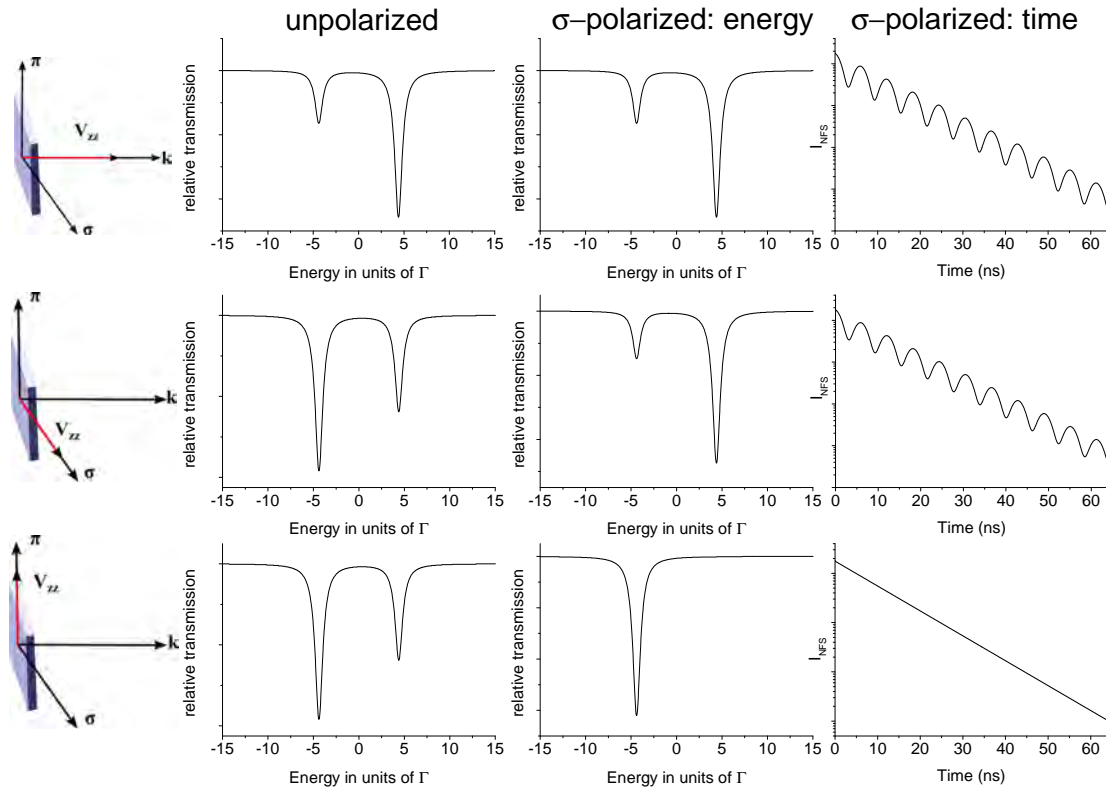


Figure 3.9: Comparison of absorption and time-spectra for different orientations of EFG principal axis and polarization of incident radiation. The example is given for hyperfine interactions in IrO_2 . Inspired by examples for ^{57}Fe [71, 2].

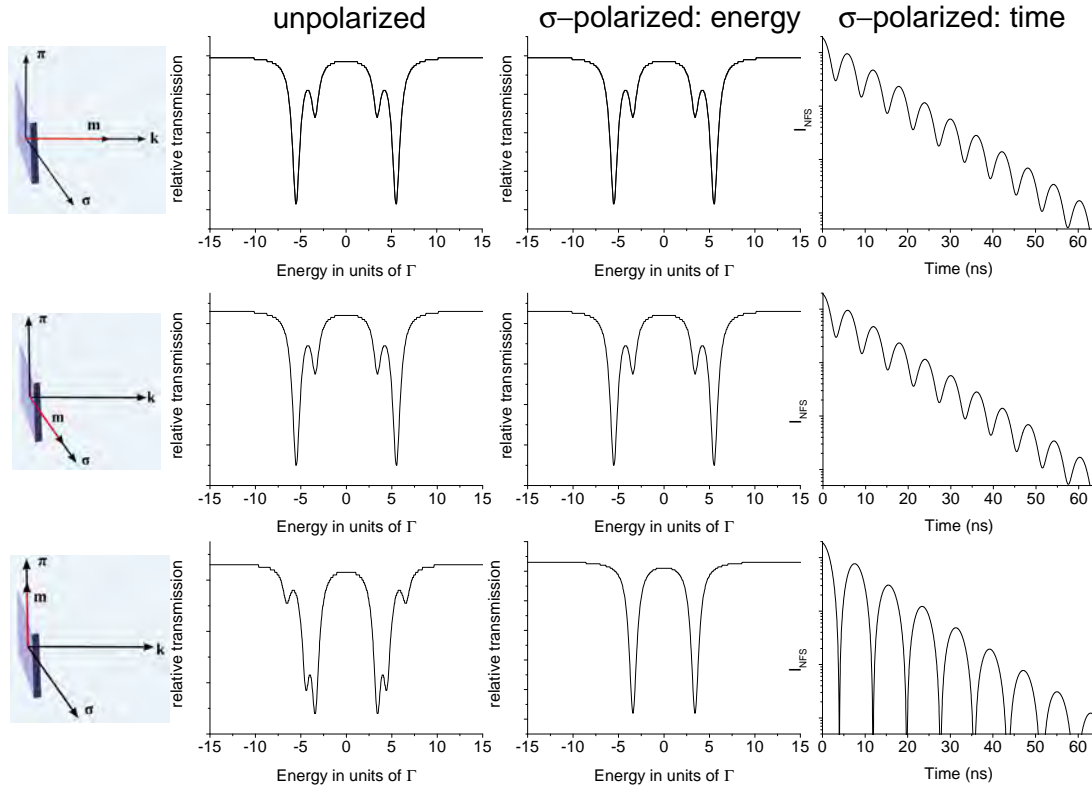


Figure 3.10: *Comparison of absorption and time-spectra for different orientations of magnetic field and polarization of incident radiation. The example is given for magnetic field on ^{193}Ir in Sr_2IrO_4 assuming $B_{\text{eff}} = 24\text{T}$. Inspired by examples for ^{57}Fe [71, 2].*

Another, more complex case for the calculation of I_{NFS} is when a distribution of the hyperfine field is present or a precession of the nuclear spin occurs in a time scale close to the time during that electron spins flip. These effects lead to a broadening of the resonance line and acceleration of resonance decay by $\frac{\Delta}{\Gamma}$ where Δ is the width of the experimental (broadened) resonance line and Γ is the natural linewidth of the resonance.

Concluding the NFS section, it is worth to remark that several software packages can be used for analyzing NFS spectra; the most frequently used ones are CONUSS [77] and MOTIF [78].

3.4.2 Nuclear Inelastic spectroscopy: lattice vibrations

Another branch of NRS is spectroscopy by nuclear inelastic scattering (NIS), a technique which probes lattice vibrations. The theoretical background of the technique was established soon after discovery of the Mössbauer effect [79, 80]. It was shown that Mössbauer effect provides an unique opportunity for studying lattice excitations (phonons) in the energy range of about hundred meV around the nuclear resonance energy [79]. However, the studies of phonons by conventional Mössbauer spectroscopy (MS) require Doppler shifts in the order of km/s and high photon flux from the source due to the low probability of phonon-assisted excitation and due to the very narrow linewidth [79]. Weiß and Langhoff reported [81, 82] on the measurements of phonon density of states (DPS) by MS. In their experiment an ultra centrifuge provided Doppler shifts in the order of 0.1 km/s, corresponding to the energy shift of 25 meV, and a strong, 370 MBq radioactive source was used. Such experiment is very challenging in realization. The appeared high-flux synchrotron sources with tunable photon energy provide access to the studies of lattice excitations by NIS. The first NIS experiments were carried out in 1990s and reported in Ref. [83, 84, 85].

A NIS spectrum is acquired by scanning the energy of incident x-rays and measuring the nuclear fluorescence signal integrated over the time window between synchrotron pulses. In this measurement, the nuclear resonance occurs at energies below and above the nuclear transition energy associated with annihilation and creation of phonons, respectively.

The technique is called Nuclear Inelastic Scattering and the name was chosen in order to preserve a comparison with the results obtained by inelastic neutron and x-ray scattering [86, 55]. There are two processes which are assisted by phonons: nuclear resonant inelastic coherent scattering (coherent inelastic) and nuclear resonant absorption (incoherent inelastic). The first process is given by resonant absorption and subsequent emission of γ -ray fluorescence radiation. [55]. The cross-section of this process depends on the momentum transfer and lifetime of phonons and thus allows studies of phonon dispersion relations. The experimental arrangement for observation of coherent inelastic scattering involves careful placement of detector at correct angle to the incident beam in order to select a segment of momentum space. Coherent inelastic scattering has not been observed so far.

The second process which is involved in NIS is nuclear resonant absorption. In this process the excited nuclear state decays either via γ -fluorescence or via internal conversion with a conversion electron leaving the atom. The resulting unoccupied electron level will be filled by outer electrons following by emission of characteristic x-rays or/and Auger electrons. The characteristic x-rays have energies lower than the resonance energy

and are emitted isotropically, thus, the detection probability for an absorption process is higher than that for scattering. The currently measured NIS spectra can be thus treated by the theory of nuclear resonant absorption [87].

An example of a NIS spectrum is given in Fig. 3.11. The central peak is due to elastic absorption. The energy axis is defined as the difference between the energy of the incident photons, E , and the energy of the nuclear transition, E_γ . Thus, phonon creation occurs at the positive part of the spectrum and phonon annihilation takes place at the negative energy part.

The cross section for NIS, $\sigma_{NIS}(E, k)$, is proportional to $S(E)$, the probability of nuclear transition with change of the lattice vibrational state. It is given by [87]:

$$\sigma_{NIS}(E, k) = \frac{\pi \sigma_N \Gamma}{2} S(E, k) \quad (3.49)$$

with σ_N - nuclear resonant cross-section and $S(E, k)$ is excitation probability density which depends on the wavevector k of the exciting photons.

The general form of the scattering function $S(E, k)$ is difficult to obtain. However, it was shown [87] that in the harmonic approximation $S(E)$ is given by:

$$S(E) = f_{LM} \left(\delta(E) + \sum_{n=1}^{\infty} S_n(E) \right) \quad (3.50)$$

with $\delta(E)$ - elastic (zero-phonon) contribution given by Dirac delta function. The single-phonon term $S_1(E)$ can be written as:

$$S_1(E) = E_R \frac{g(|E|)}{E} \frac{1}{1 - e^{-E/k_B T}} \quad (3.51)$$

Knowing the one-phonon term $S_1(E)$ allows obtaining the density of the phonon states (DPS). In order to find $S_1(E)$ three preliminary steps should be done.

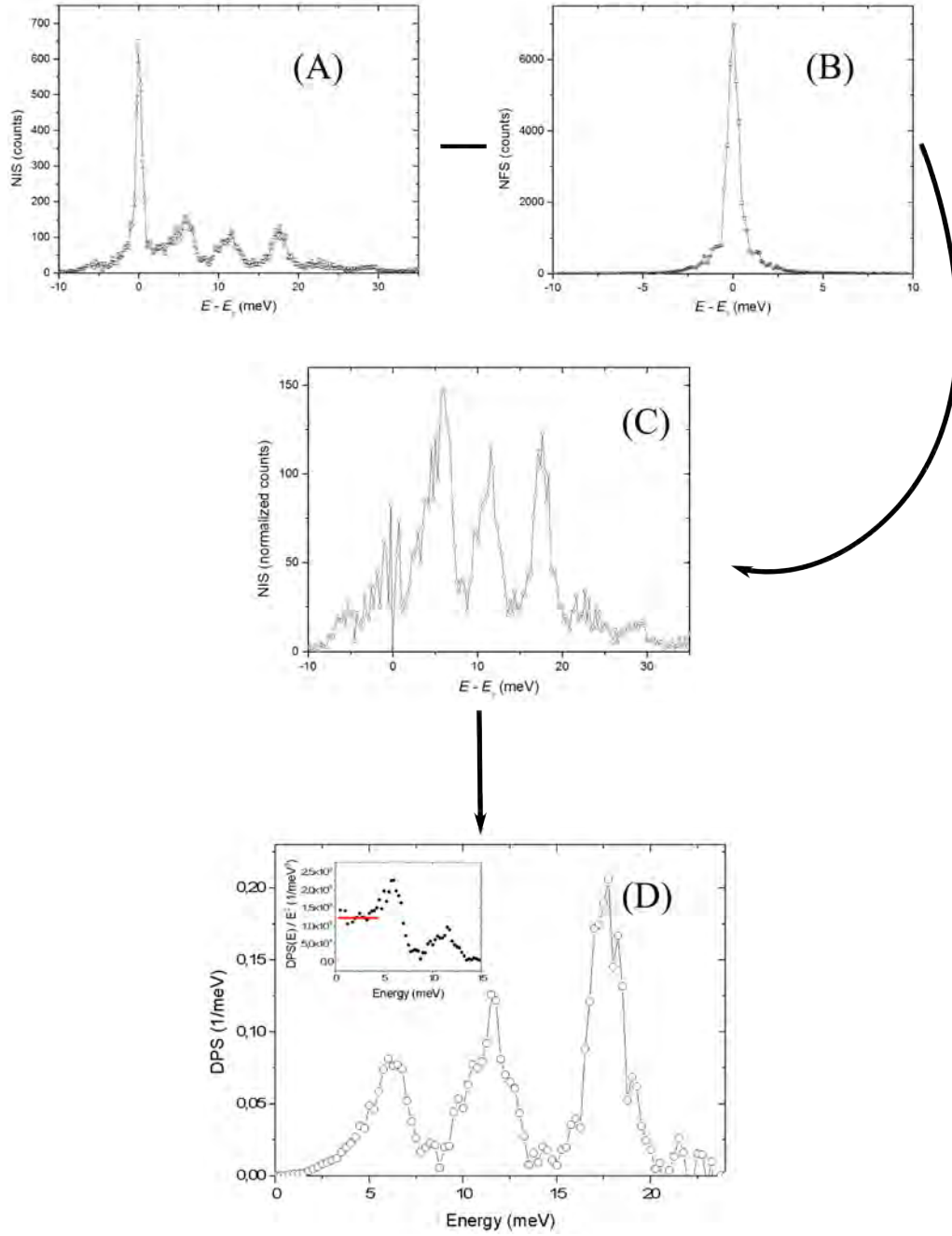


Figure 3.11: Procedure of treatment of NIS spectrum: (A) acquired NIS spectrum, (B) acquired energy dependence of NFS, (C) Normalized NIS spectrum after subtraction of elastic line, (D) derived density of phonon states. The inset in the panel (D) shows determination of Debye level $\lim_{E \rightarrow 0} \frac{g(E)}{E^2}$. E is the energy of the incident photons, E_γ is the resonance energy. The spectra were measured on Tellurium single crystal at 32(5) K with the incident beam along c -direction [88]. The asymmetry of the NIS spectrum in (A) is determined by the temperature dependence of the occupancy of the phonon states (see text).

- Normalization of the NIS spectrum (panel (A) in Fig. 3.11)

As mentioned before, the NIS spectrum is proportional to σ_{NIS} with a proportionality coefficient. The proportionality coefficient can be found by a normalization of the NIS spectrum using the so-called sum rules given by Lipkin [89]. The normalization procedure using sum rules relates moments of the NIS spectrum to nuclear or material parameters.

For instance, the 1st moment of NIS spectrum is equal to the recoil energy of a free nucleus:

$$\langle E^1 \rangle = \int_{-\infty}^{+\infty} S(E) E dE = E_R \quad (3.52)$$

The acquired spectrum is normalized to satisfy this condition.

- Subtraction of elastic scattering contribution $\delta(E)$ (panels (B) and (C) in Fig. 3.11)

The normalized NIS spectrum is now equal to the NIS absorption cross-section convoluted with the instrumental function of the monochromator. The instrumental function should be measured in the forward scattering channel (panel (B) in Fig. 3.11) and subtracted from NIS by numerical deconvolution (panel (C) in Fig. 3.11) [67].

After the subtraction of the elastic contribution the Lamb-Mössbauer factor can be calculated:

$$f_{LM} = 1 - \int_{-\infty}^{-0} S(E) dE - \int_{+0}^{+\infty} S(E) dE \quad (3.53)$$

At this step, the sample temperature can be determined precisely by the detailed balance rule [67]. This rule defines the asymmetry of the NIS spectrum and defines the ratio of created and annihilated phonons. Phonons obey Bose-Einstein statistics and the occupancy of phonon states is proportional to $e^{-E/k_B T}$ [21]. Therefore, $I(E)$ and $I(-E) e^{E/k_B T_S}$ will be equal at the sample temperature T_S [67]. The asymmetry of the NIS spectrum becomes more pronounced at low temperatures due to the low occupancy of phonon states.

- Subtraction of the multi-phonon contribution (panels (C) and (D) in Fig. 3.11)

Next, the contribution from the multiphonon term should be subtracted. In the harmonic approximation the n-phonon contribution depends recursively on the one-phonon function $S_1(E)$:

$$S_{n+1}(E) = \int S_n(E') S_1(E - E') dE' \quad (3.54)$$

As shown in Ref. [87] the one-phonon term $S_1(E)$ can be obtained by the so-called Fourier-Log method. It assumes that $S_1(E)$ is calculated by:

$$S_1(E) = f_{LM} F^{-1} \left[F(\delta(E)) \ln \left(1 + \varphi \frac{F(I) - F(\delta(E))}{f_{LM} F(\delta(E))} \right) \right] \quad (3.55)$$

with F and F^{-1} being operators of the Fourier and inverse Fourier transform, respectively. The function φ is introduced in order to avoid numerical truncation problems with the division by $F(\delta(E))$. It is given by:

$$\varphi = \min \left[1, \left| \frac{F(I) F(\delta(0))}{F(\delta(E)) F(I(0))} \right| \right]. \quad (3.56)$$

Finally, the phonon density of states $g(|E|)$ is obtained from $S_1(E)$:

$$g(|E|) = \frac{S_1(E) E (1 - e^{-E/k_B T})}{E_R} \quad (3.57)$$

Several important thermodynamic properties can be derived from $g(|E|)$ [67].

For instance, the vibrational part of the internal energy per atom can be found by:

$$U = \frac{3}{2} \int_0^\infty g(E) E \frac{e^{E/k_B T} + 1}{e^{E/k_B T} - 1} dE \quad (3.58)$$

The lattice specific heat per atom at constant volume is given by the temperature derivative of U :

$$C_v = 3k_B \int_0^\infty g(E) \frac{(E/k_B T)^2 e^{E/k_B T}}{(e^{E/k_B T} - 1)^2} dE \quad (3.59)$$

The vibrational entropy per atom can be calculated with:

$$S = 3k_B \int_0^\infty g(E) \left[\frac{e^{E/k_B T} + 1}{e^{E/k_B T} - 1} \frac{E/k_B T}{2} - \ln \left(e^{E/2k_B T} - e^{-E/2k_B T} \right) \right] dE \quad (3.60)$$

The speed of sound can be determined from the measurements of density of phonon states. It is related to the so-called Debye level (reduced DPS) $\lim_{E \rightarrow 0} \frac{g(E)}{E^2}$ and the mass of the oscillator m (here, mass of the resonant nucleus) by:

$$v_{Deb} = \frac{\sqrt[3]{\lim_{E \rightarrow 0} \frac{g(E)}{E^2} 2\pi^2 \rho}}{\hbar} \quad (3.61)$$

The procedure of obtaining $g(E)$ described above involves however several uncertainties. First, the multiphonon contribution is given by $(-\ln(f_{LM}))^n/n!$ [67] and can be significant especially when the Lamb-Mössbauer factor f_{LM} is low, typically lower than 0.3. In this case the recursive relation (eq. (3.54)) is only a very rough approximation. Second, the measured materials only roughly follow the harmonic oscillator model. The subtraction of the elastic peak and multiphonon contribution calculation may become not precise enough in the presence of large anharmonicity. In order to eliminate the uncertainties, information derived from the higher moments of the NIS spectrum can be used for the cross-check of the calculation of $g(E)$.

Higher moments of NIS spectrum contain information on the material properties as shown in the Refs.[67, 89, 72]. For instance, the 2^{nd} moment is proportional to the mean kinetic energy per phonon in the direction of the wave-vector of incident x-rays:

$$\langle E^2 \rangle = \int_{-\infty}^{+\infty} S(E) E^2 dE = 4E_R \langle T(k) \rangle \quad (3.62)$$

the 3^{rd} moment is proportional to the mean force constant $\langle F \rangle$ and $\langle \omega_k^2 \rangle$, the mean square phonon frequency of modes in the direction of \mathbf{k} vector:

$$\langle E^3 \rangle = \int_{-\infty}^{+\infty} S(E) E^3 dE = \frac{2\hbar^2 E_R}{M} \langle F \rangle = E_R \hbar^2 \langle \omega_k^2 \rangle \quad (3.63)$$

An additional cross-check of quality of DPS calculation can be made by comparing the Lamb-Mössbauer factor f_{LM} obtained from NIS spectrum by equation (3.53) and f_{LM} calculated directly from DPS by equation (3.27).

Finally, one should emphasize that NIS measures lattice vibrations of only one sort of nuclei and in the direction parallel to the wave-vector of incident x-rays, thus, the DPS obtained by this method is usually called partial, projected DPS. The special software [77, 90] is available for the treatment of NIS spectra.

4 Experimental Techniques

4.1 Set-up for Nuclear Resonance Scattering

In this section the experimental set-up for nuclear resonance scattering (NRS) is discussed. The focus is set on two branches of NRS, nuclear forward (NFS) and nuclear inelastic scattering (NIS). Although the two methods and information obtained by them are different, the two main challenges for experimentalists are the same. In this chapter several technical challenges of NRS experiments are discussed.

First, NRS has a very narrow energy bandwidth compared to that of the broadband undulator radiation. The unwanted signal from electronic scattering should be reduced by reduction of the bandwidth of the radiation. This is done by monochromators. For the purpose of hyperfine spectroscopy by NFS, a degree of monochromatization $\Delta E/E$ less than 10^{-5} is required. This degree of monochromatization cannot be achieved with conventional double-crystal monochromators (DCM) present at any beamline, and an additional monochromator with moderate resolution and optimized transmission is necessary. This is the case for the medium resolution monochromator described here with the focus on NFS on Ir compounds. A monochromator for NIS should in addition feature a very high energy resolution. Here, a degree of monochromatization $\Delta E/E < 10^{-8}$ is needed in order to resolve phonon spectra. This kind of monochromator is presented with the example of a sapphire backscattering monochromator. It has high transmission due to the large angular acceptance of backscattering geometry, high resolution due to the precise temperature control and sapphire crystal quality, and can be applied for NRS on many isotopes with nuclear transitions in the 20-50 keV range.

A second important feature of NRS is the time delay of the nuclear resonance signal. Indeed, the electronic scattering occurs in the fs-ps time range, while NRS has a characteristic decay time of ps- μ s. Since the separation between synchrotron pulses is on the order of hundred ns and there is almost no SR emitted between the pulses, the NRS signal can be acquired mostly without any background. Fast detectors with high dynamic range and fast electronics synchronized with the bunch clock of the synchrotron are used for the time discrimination of the NRS signal. Furthermore, an optimized detector can also help to solve the detector overload problem while working with a large energy bandwidth.

The next section gives several theoretical and practical aspects of high-resolution monochromators and detection systems used for NRS. The two following sections are dedi-

cated to the transmission-optimized medium resolution monochromator for NRS on Ir compounds and the backscattering high-resolution sapphire monochromator, both constructed and commissioned within the framework of this thesis.

4.2 High-Resolution Monochromators

Monochromatization is a vital feature for many studies. For instance, it provides access to energy resolving spectroscopic techniques for studies of properties of condensed matter. The main physical quantities of interest are dispersion relations of electronic, vibrational and magnetic excitations; detailed information on the crystallographic structure can be collected in x-ray diffraction experiments which in turn requires the application of monochromators [1]. In the special case described in this work, the monochromators are used in order to: a) reduce the flux entering the detector by reducing energy bandwidth relevant to a sharp Mössbauer transition and thus to avoid detector overload in NFS experiments; b) perform nuclear inelastic scattering (NIS) experiments with an energy resolution sufficient to resolve phonon spectra.

The monochromatization of the x-rays in the energy range of Mössbauer transition is achieved by Bragg diffraction from single crystals. Bragg's law can be written as:

$$E = \frac{hc}{2d \cdot \sin(\Theta_B)} \quad (4.1)$$

with E the energy of the reflected radiation, d the interplanar distance, Θ_B the Bragg angle, h the Planck constant, and c the speed of light in vacuum. The interplanar distance d is related to the lattice constant a and Miller indexes of a reflection, h,k,l , by $d = \frac{a}{\sqrt{h^2+k^2+l^2}}$ for crystals with cubic symmetry which are commonly used for monochromators. The incident radiation has usually a wide spectrum of wavelengths. One can see from eq. (4.1) that a crystal oriented to the incident beam at a particular angle Θ can filter radiation of a particular wavelength (energy). A crystal can thus be considered as a wavelength selector, a monochromator (greek: "mono" - single and "chroma" - colour), and the process of wavelength selection is called monochromatization.

Usually, monochromatization at present SR sources is done by gradual decrease of the energy bandwidth, as shown in the Fig. 4.1. At the first stage the radiation from the undulator is pre-monochromatized from a 50-100 eV to a 2-5 eV bandwidth. This is done usually by two silicon crystals utilizing the same Bragg reflection. The major purpose of this monochromator, also called double-crystal monochromator (DCM) or high heat load monochromator, is to reduce the heat load of the undulator radiation and to decrease the

bandwidth to a moderate degree of $\Delta E/E = 10^{-4} - 10^{-5}$. At the same time the spectral photon flux, defined as the flux of photons in a energy bandwidth [ph/s/eV] should not be deteriorated by the DCM. The crystals are usually cooled in order to provide an active heat sink for the thermal energy delivered to them. The high, several kW, heating power of the beam is indeed a very challenging problem since it can not only destroy the crystals but also provides a local deformation of the silicon. Thus the DCM crystals are maintained at a temperature close to 125 K where the thermal expansion coefficient of silicon is close to zero [91]. It was demonstrated that diamond is advantageous to silicon for high heat load applications due to the higher reflectivity and high transmission [92], however, large volume perfect diamond crystals are difficult to produce.

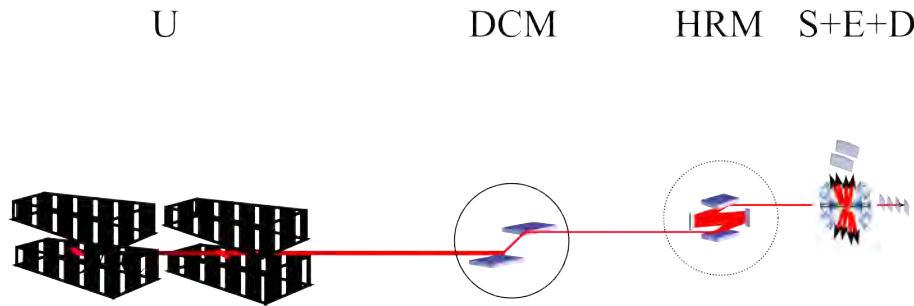


Figure 4.1: A layout of a beamline. U: undulator; DCM: double crystal monochromator; HRM: inline high-resolution monochromator; S+E+D: sample with sample environment and detectors.

The degree of monochromatization provided by the DCM is not sufficient for phonon spectroscopy, but already suitable for performing other experiments with SR, such as powder diffraction, small-angle scattering, photoemission spectroscopy, fluorescence and absorption spectroscopy, imaging [1]. In an experiment the DCM is adjusted to transmit the desired x-ray energy and the undulator gap is tuned to the maximum photon flux at this energy.

Monochromatization with a DCM is sufficient for most beamlines at a synchrotron radiation facility. However, techniques like nuclear resonance scattering (NRS) and inelastic x-ray scattering (IXS) demand high-resolution monochromators (HRMs). In this case, an HRM is placed downstream from the source after the DCM as seen in the Fig. 4.1, and provides monochromatization down to a meV bandwidth and in some special cases, down to a sub-meV bandwidth⁴.

An expression for the energy resolution of a monochromator can be obtained by taking total differential of E in eq.(4.1) and dividing it by the E given in eq.(4.1):

⁴However, the energy resolution of the DCM can be sufficient for NRS experiments with very high resonance energies, as shown for the 90 keV nuclear resonance in ⁹⁹Ru [93]

$$-\frac{\Delta E}{E} = \frac{\Delta d}{d} + \Delta\theta \cot\theta_B \quad (4.2)$$

For perfect crystals $\frac{\Delta d}{d} \rightarrow 0$ and the energy resolution depends on the angular deviation from the Bragg's law, $\Delta\theta$, and the Bragg angle θ_B only. Thus, the energy resolution can be increased by decreasing of the angular deviation $\Delta\theta$ and by using Bragg reflections with high Bragg angles (large Miller indices).

In near perfect crystals used for monochromators multiple scattering effects are not negligible, which means that multiple refraction and reflection on lattice planes becomes pronounced [94]. Due to multiple scattering effects the reflection occurs not at the exact angle θ_B but in a region around the Bragg angle, called Darwin width θ_D [94]. For a symmetrical Bragg reflection with Bragg angles $\theta_B < \pi/2$ by several milliradians, the angular acceptance corresponds to the Darwin width of the reflection. The dynamical scattering theory gives $\Delta\theta_D$ as follows:

$$\Delta\theta_D = \frac{r_e h^2 c^2}{\pi} \frac{2}{V E^2 \sin(2\theta_B)} |F_H| e^{-M} P \quad (4.3)$$

where r_e is the classical electron radius; V the volume of the unit cell; e^{-M} the temperature dependent Debye-Waller factor given by the temperature dependent rigidity of the lattice; P the polarization factor which is $P = 1$ for σ -polarized (case of SR) or $P = \cos(2\theta_B)$ for π -polarized radiation.

$F_H = \sum_n \left[(f_n^{(0)}(\mathbf{H}) + f'_n(E) + i f''_n(E)) e^{i\mathbf{H} \cdot \mathbf{r}_n} \right]$ is the structure factor for a given Bragg reflection with atomic form factor $f_n^{(0)}(\mathbf{H})$, anomalous scattering corrections $f'_n(E)$ and $f''_n(E)$, reciprocal lattice vector \mathbf{H} , and vector \mathbf{r}_n of an atom n . The coefficients $f_n^{(0)}$, $f'_n(E)$, and $f''_n(E)$ can be determined by Hartree-Fock-Slater calculations, usually tabulated values are used [95, 96]. Note that reflections with $\mathbf{H} \cdot \mathbf{r}_n = \frac{\pi}{2}n$ do not allow Bragg scattering as F_H for these reflections is zero. For crystals with cubic symmetry the set of reflections is most limited. For instance, for the cubic diamond structure, such as Si, only reflections with all odd Miller indexes h, k, l or with $h + k + l = 4j$ ($j = 1, 2, 3, \dots$) are allowed.

As shown in eq. (4.2) the energy resolution can be improved by using reflections with high Bragg angles, however, from the eq. (4.3) one can see that the angular acceptance of the reflection decreases with increasing Bragg angle and is typically lower than $1 \mu\text{rad}$ for reflections with Bragg energy in the 20-30 keV range. In contrast, the radiation after the DCM has a divergence of several μrad and thus will not be fully transmitted by reflections with low ΔE . The beam after DCM should therefore be collimated or the angular acceptance of the HRM should be improved. The collimation can be done by asymmetri-

cally cut crystals, i.e. crystals with reflecting planes not parallel to their physical surface [97]. In this case, the incident beam with a divergence of $\Delta\theta_{in} = \Delta\theta_D/\sqrt{b}$ is accepted by the crystal and the divergence of the reflected beam is $\Delta\theta_{out} = \Delta\theta_D\sqrt{b}$ with b - asymmetry parameter which is defined as:

$$b = \frac{\sin(\theta_B - \alpha)}{\sin(\theta_B + \alpha)} \quad (4.4)$$

where α is the asymmetry angle, the angle between reflecting planes and the physical surface of the crystal.

Thus, in the usual approach to design a high-resolution monochromator [97] one crystal with a large asymmetry angle accepts the photon flux after the DCM and provides a highly collimated beam to match the acceptance of the reflection in the following crystal which provides a narrow, sub-meV to meV, energy bandwidth (Fig. 4.2). In total, the monochromator consists of a set of 3 or 4 crystals. The last crystal brings the reflected beam back into the direction of the incoming beam which is desired in experiments [97].

The task of designing a high-resolution monochromator can be simplified by using a graphical approach called DuMond diagrams. A DuMond diagram depicts the relation between energy (wavelength) and Bragg angle of the beam (Fig.4.3). In the general case, the relation is given by a reciprocal sinus function (eq.(4.1)) but in a narrow energy or angle region, the dependence can be approximated by a line with the slope determined by $\cot\theta_B$ and the slope is also called DuMond tangent. Since multiple scattering effects are not negligible for perfect crystals, the lines on the DuMond diagram have finite thickness given by the Darwin width of the reflection and, in case of an asymmetrical reflection by the Darwin width and asymmetry parameter b of the reflection. In a monochromator setup with multiple crystals, the DuMond diagrams for the incident and reflected waves for each crystal is drawn in one graph. The area built by the intersection of these areas represents the bandpass of the monochromator in (E, θ) - space. The height of the crossover area is thus an estimation of the energy bandpass of the monochromator (see Fig. 4.3).

Besides the DuMond diagram approach, in some cases, the energy bandpass can be calculated using approximations. For dispersive setting of crystals, which is the case of the monochromator for NRS on Ir compounds, the energy bandpass can be approximated by a Gaussian function [72]:

$$\Delta E = E \frac{\sqrt{\Delta\theta_1^2 + \Delta\theta_2^2}}{\tan\theta_1 + \tan\theta_2} \quad (4.5)$$

where $\Delta\theta_1$ and $\Delta\theta_2$ are the acceptances of the first and the second crystal, and θ_1 and θ_2 are the Bragg angles for the first and second crystal, respectively.

The approximation by a Gaussian function and DuMond diagram approach usually overestimates the energy bandpass by a factor of 1.5-2 [72, 98]. Exact values of the energy bandpass can be obtained by numerical calculations using expressions given by the dynamical scattering theory.

One should note, as seen in the Fig.4.2, that schemes with multiple crystals are usually complicated in design and have several drawbacks at photon energies above 30 keV. First, the structure factor F_H of elemental semiconductors used in these monochromators significantly decrease with the energy. Second, the angular acceptance drops with energy proportionally to $1/E^2$ at any Bragg angle, except for angles $\Theta = \frac{\pi}{2} \pm \delta$ with $\delta \lesssim \text{mrad}$ [97]. The third difficulty emerges for studies at resonance energies since Bragg reflections take only discrete values in a crystal, and it is especially challenging to find a reflection with a suitable energy bandwidth. Indeed, in crystals with high symmetry, such as cubic Si and Ge, many lattice reflections are forbidden or degenerate due to the multiple-beam diffraction [99]. Fourth, the extremely asymmetrical crystal cuts result in a large beam size after collimation, on the order of several dozens of mm. Thus, a crystal with perfect crystallinity over a large volume is required. Finally, multiple-crystal constructions have many moving parts and it is desirable to maintain the precision of the movement of each part at least within the Darwin width of the reflection, which is technically difficult. For high order reflections the angular width can be as small as 100 nrad, thus, the mechanical setup should be able to rotate the crystals with that precision or better.

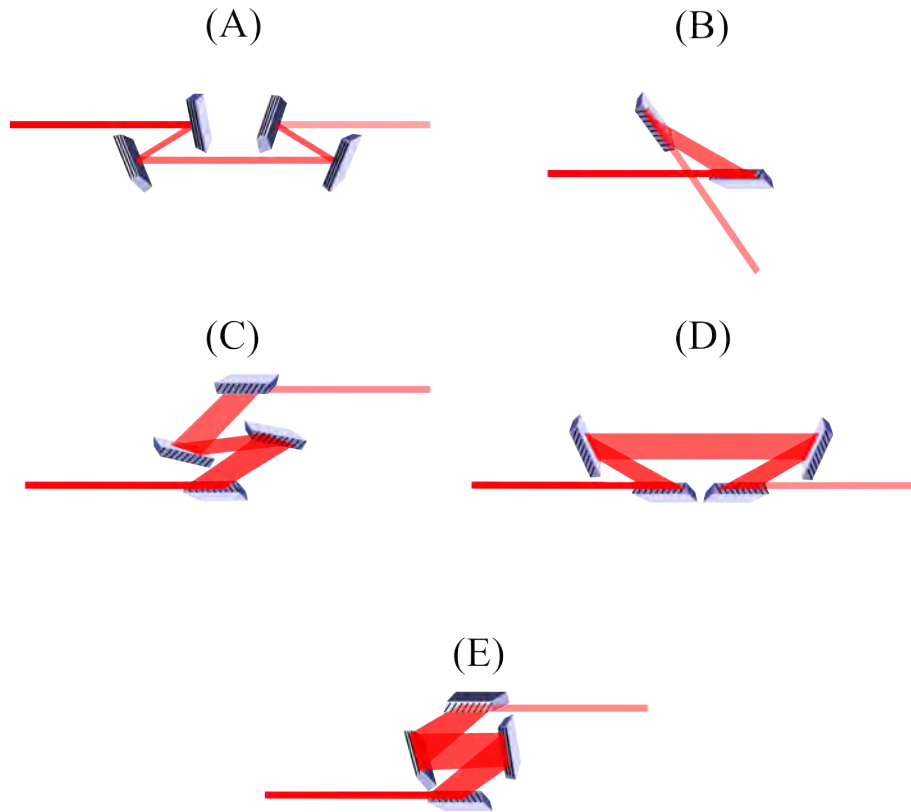


Figure 4.2: The most popular constructions of multiple-crystal high-resolution monochromators: (A) channel-cut crystals with symmetric reflections, low angular acceptance, meV resolution; (B) two asymmetrical cut crystals: first uses low-order reflection, second high-order reflection cut in opposite way, does not change beam size and divergence; (C) nested scheme, preserves beam direction and assures high energy resolution; (D) four-bounce scheme of (B), high energy resolution, beam path is preserved; (E) nested scheme: low order reflection asymmetrical cut, second high-order reflection close to backscattering, high energy resolution, the beam direction is preserved. Inspired by [2, 97].

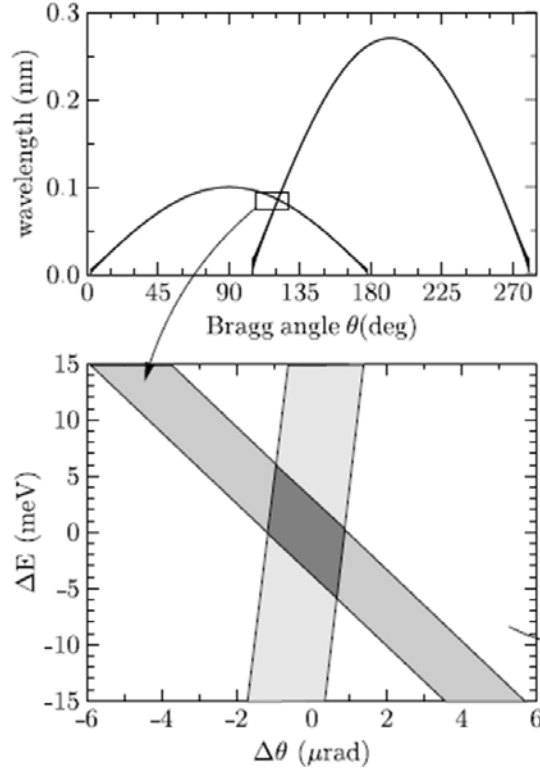


Figure 4.3: DuMond diagrams for two crystals. Lower panel: magnified region of intersection of the curves from the upper panel [2].

The constraints of the multiple-crystal monochromators described above led to the development of backscattering monochromators. Bragg's law given by eq.(4.1) in backscattering geometry $\Theta = \frac{\pi}{2} \pm \delta$ with $\delta \approx m\text{rad}$ reduces to a simple relation [99]:

$$E = \frac{hc}{2d_{hkl}} \quad (4.6)$$

Note that the interplanar distance d_{hkl} depends on the lattice parameter, which is an intrinsic property of the crystal, and strongly depends on the temperature of the crystal. Therefore, the energy of the monochromatized radiation may be tuned by varying the temperature of the crystal.

The backscattering geometry has several prominent advantages compared to multiple-crystal geometry. First, the angular acceptance is of the order of a few mrad at 20-50 keV and decreases with energy proportionally to $1/E$ [99]. As the angular divergence after the DCM is in the order of few dozens of μrad , a backscattering monochromator consisting of one single crystal can easily cover the incoming beam divergence. Also, the high angular acceptance permits a higher count rate in the experiments with a highly diverging beam. A prominent example of such experiments is momentum-resolving inelastic x-ray scattering, where the back-reflections are used for energy analysis. Here, the

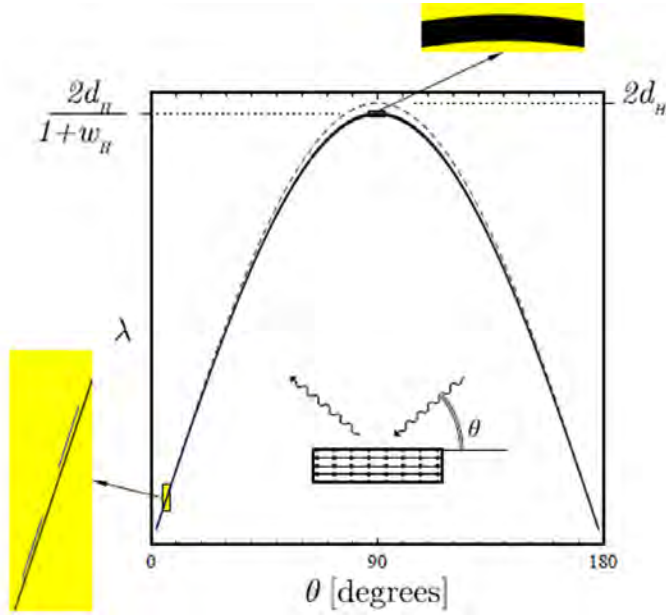


Figure 4.4: DuMond diagram. The solid line is given by the dynamical scattering theory, the dashed line is the prediction in the kinematical approximation. Note that for a given angular divergence the energy bandwidth is the smallest for the Bragg angles $\theta \approx 90^\circ$ [99].

studied radiation is scattered from the sample in the whole solid angle 4π and thus, the analyzer should be able to cover as large solid angle as possible [100]. Another feature of backscattering is the smallest energy bandwidth at a given angular divergence of the beam incident on the crystal, as seen in the Fig. 4.4 [99].

Furthermore, a backscattering monochromator consists of less moving parts and is comparatively easy in operation. The change of the reflected X-ray energy is achieved by changing the temperature of the crystal which is practically a tuning of the interplanar distances, while the Bragg angle is kept constant [99]. This way of operation requires an extremely precise temperature control over a wide temperature range [101, 102, 103]. Indeed, one can show that the energy E of photons in backscattering geometry depends on the temperature via temperature dependency of interplanar distances d_{hkl} derived from the temperature expansion [99]:

$$\frac{dE}{dT} = \frac{E}{d_{hkl}} \frac{d(d_{hkl})}{dT} \quad (4.7)$$

For instance, with the given temperature expansion of silicon, for x-ray energies $E = 37.13$ keV (the energy of the nuclear resonance in ^{121}Sb), and a crystal temperature of 1025 K we could obtain for the corresponding (2 6 32) Bragg reflection:

$$\frac{dE}{dT} = -0.159 \text{ [eV/K]} \quad (4.8)$$

when the Bragg angle is several mrad away from $\pi/2$ (backscattering geometry). Obviously, the temperature of the crystal should be changed with 1-10 mK precision for tuning of the energy with a sub-meV to meV precision.

Theoretical [104, 105] and experimental [106, 107] studies have shown the possibility of both lowest energy bandwidth and weak dependence of energy bandwidth on the energy. The energy range was 1-10 keV in the experiments and Si and Ge crystals with cubic symmetry were used [106, 107]. The production technology of Si and Ge crystals has significantly evolved and the monochromators constructed by using this type of crystals deliver energy bandwidths beyond 100 μeV at photon energies up to 22 keV [108, 109].

A special emphasis in the part of this work dedicated to the backscattering monochromator is set to NRS on isotopes which have transition energies ranging from 20 to 50 keV. For application of cubic Si and Ge crystals for these studies two major challenges emerge. First, the Debye-Waller factor and thus the structure factor and reflectivity are small at photon energies higher than 20 keV. This fact results in a low efficiency of the monochromator. Second, a back-reflection suitable for resonance energy is difficult to find due to the high symmetry of the crystals. Moreover the effect of multiple-beam diffraction does reduce the reflectivity of reflections. It was shown that the reflectivity of particular reflections in cubic crystals drops drastically by approaching the Bragg angle close to $\pi/2$ [110]. Notably, the effect becomes more pronounced at the narrow energy bandwidth of the incident x-rays [111]. The effect of damping of reflectivity is attributed to the transition from two-beam to multiple-beam diffraction regime [112]. In case of the multiple-beam regime the scattering channel is open not only for the back-reflection but also for another reflection and intensity of incident rays is distributed mostly into reflections away from backscattering [99].

To overcome the problems, it was suggested [99] and confirmed experimentally [113, 114, 103, 115] that crystals with non-cubic symmetry, like single crystal corundum Al_2O_3 , can be used as a backscattering monochromator for NRS studies on the isotopes with energies of transitions being in the range 20-40 keV. Indeed, the density of reflections in energy is very high in Al_2O_3 as compared to Si (see Fig.4.5) and the reflectivity is much higher, especially at energies higher than 30 keV and at low temperatures. High energies accessible with sapphire monochromator are also the best probe of the sapphire crystal quality by NRS: using the high-order reflections with a small energy bandwidth allows revealing small deviations in a crystal structure. Moreover, the access to highly monochromatized high-energy x-rays has stimulated the search for new resonances, allows probing sample properties more deeper in the bulk, provides higher signal in high-pressure studies (both

due to the larger penetration depth of high-energy x-rays), and establishes a tool for the studies of new interesting phenomena. It was shown that other crystals with non-cubic symmetry can be used as backscattering monochromator, for instance, polytypes of SiC could be an appropriate choice instead of Al_2O_3 [113]. However, the quality of corundum crystals is currently surpassing that of SiC [116].

A large part of this work is dedicated to the construction and first tests of the sapphire backscattering monochromator (BS HRM) at the P01 beamline of PETRA III. A layout of a typical experiment with a backscattering monochromator is shown in the Fig. 4.6. Note the distances shown on the lower part of the figure for P01 beamline and for ID18 beamline at ESRF. The larger distance between the BS HRM and sample at P01 beamline allows larger separation between direct and reflected beams without perturbing backscattering condition, and larger sample environment can be used.

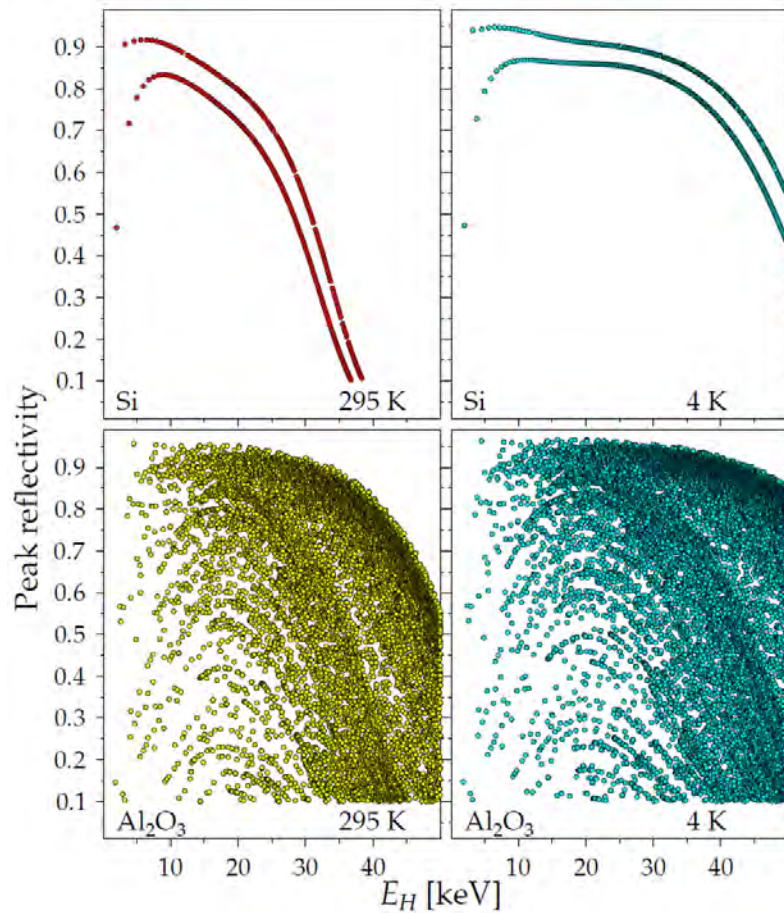


Figure 4.5: Peak reflectivity of all Bragg reflections in Si (upper panels) and Al_2O_3 (lower panels) at 295 K and 4 K. Reproduced from Ref. [99].

In the experiment at the beamline (Fig. 4.6), the sample, sample environment, and detectors are placed far away from the high-resolution monochromator. In some applications of the backscattering monochromator, such as experiments with diamond anvil cells, a

focusing of the beam down to some μm is desired. Thus, focusing mirrors [1], lenses [117], or Fresnel zone plates [1] can be introduced into the setup. These optical elements can be massive and thus more space is desired to place them. An especially crucial situation is when focusing in experiments with a backscattering monochromator is necessary. In that case a long distance between sample and HRM can help to gain sufficient space for focusing devices. From the figure 4.6 one can see the advantage of the almost 90 m long beamline P01. Here, the distance between direct and reflected beam can be as large as 20-40 mm without losing the advantages of the almost exact backscattering geometry which are the small energy bandwidth and its weak dependence on energy.

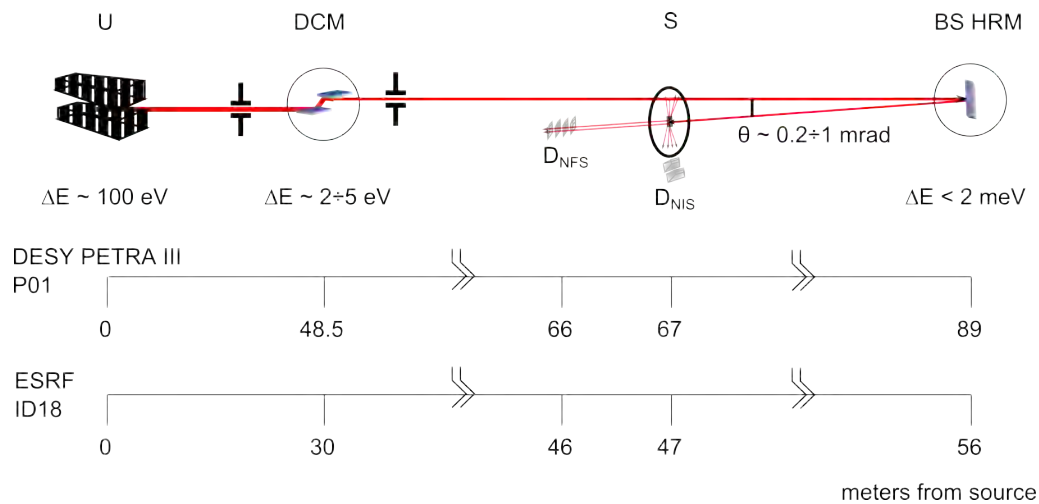


Figure 4.6: Layouts of the backscattering experiments at P01 beamline of PETRA III and ID18 beamline of ESRF. U: two undulators; DCM: double crystal monochromator; BS HRM: backscattering high-resolution monochromator; S: sample; D_{NFS} and D_{NIS} : detectors for NFS and NIS, respectively.

4.3 Detection of NRS signal

Several requirements should be fulfilled by detectors and electronics for an efficient detection of the NRS signal. First, the electronically scattered or transmitted synchrotron pulse, the so-called prompt pulse, has a typical flux of 10^7 - 10^{10} ph/s, whereas the NRS flux can be less than 1 ph/s. Thus, the detector should sustain the high prompt flux and be able to acquire single delayed photons between the SR pulses. Second, a fast recovery time is desired. The acquisition system must be able to recover as soon as possible after the prompt pulse and detect delayed NRS photons. Third, a time resolution of better than 1 ns is desired to be able to resolve the important features in time-spectra. Finally, the detection system should have very low noise level and high quantum efficiency in the 10-100 keV energy range, where most Mössbauer isotopes have their transitions. The detectors have usually two applications, NFS and NIS. Notably, detectors for NFS can have small area and thickness. They can be stacked in order to achieve the best time resolution and maximum efficiency at high photon energies. The detectors for NIS should have a large area in order to cover an as large as possible solid angle due to the fluorescent character of NIS radiation.

4.3.1 Avalanche photodiode detector

Silicon avalanche photodiodes (APDs) have been elaborated as fast and convenient detectors for NRS [74]. Like in almost all semiconductor detectors for x-ray energies less than 100 keV, the signal generation in APDs is based on photoelectric absorption of x-rays followed by creation of electron-hole pairs [118]. The current of the charge carriers is further amplified and measured by downstream electronics [118]. An APD device is, however, unique by its high gain values for current and low signal-to-noise ratio defined by its design.

The doping and electric field profiles of an APD determine the operation properties of the detector. Generally, when high reverse bias is applied, there is a region with high gradient of electric field called region of amplification [74]. X-rays impinging the charge depletion region create electron-hole pairs due to photoelectric absorption and Compton scattering. At room temperature each 3.6 eV of deposited energy creates one electron-hole pair on average. The created electrons drift to the amplification region with typical drift velocities of 100 $\mu\text{m}/\text{ns}$ at room temperature. Electrons entering this region, ionize the dopants, and an avalanche of electrons is built [118]. The avalanche propagating in the silicon results in a drop of its resistivity which is acquired and amplified by the detector pre-amplifier [118].

The two main parameters which describe a silicon APD are its active thickness and its capacitance [74]. Both parameters determine efficiency, time resolution and recovery time of APD [74]. Time resolution is usually given by the width of the leading edge of the APD signal and the recovery time by its trailing edge (Fig. 4.7b) [74]. Typically, APD with an active thickness less than $100\text{ }\mu\text{m}$ provide the desired time resolution of less than 1 ns. Larger active thicknesses result in larger drift times for electrons and impair time resolution. For APD with an active thickness less than $100\text{ }\mu\text{m}$ the quantum efficiency is low for the photon energies higher than 20 keV. Fig.4.7a shows the attenuation length of x-rays in silicon versus photon energy. For energies in the range 20-80 keV the desired thickness of silicon is in the 3-20 mm range. The capacitance of a diode has a large impact on recovery time as shown in fig. 4.7b. It is clear that APDs with smaller area and thus smaller capacitance have very short recovery time but cover a small solid angle of the beam resulting in less efficiency. The problem of low quantum efficiency can be solved by stacking many APDs along the beam and inclining them so that the beam-path along the diode is maximal (Fig.4.7c). Problems of low time resolution and slow recovery time can be solved by using thin, small area APDs with low capacitance [74]. Such an APD detector consisting of 16 APDs was built by the company ATIM and used at the P01 beamline (Fig.4.7d)

One preamplifier is connected to each APD and builds an RC chain with the APD. Once the resistivity in the RC chain drops, a voltage pulse is sent by the pre-amplifier to the downstream electronics. High-energy x-rays have a large penetration depth and thus a higher probability to be detected after being scattered by objects in the experimental hutch. Radiation re-scattered from these objects is delayed in time and will also be acquired by the detector leading to the background in NRS time spectra. Therefore proper shielding of detectors by heavily absorbing materials like lead or tantalum is desired for experiments with high-energy x-rays.

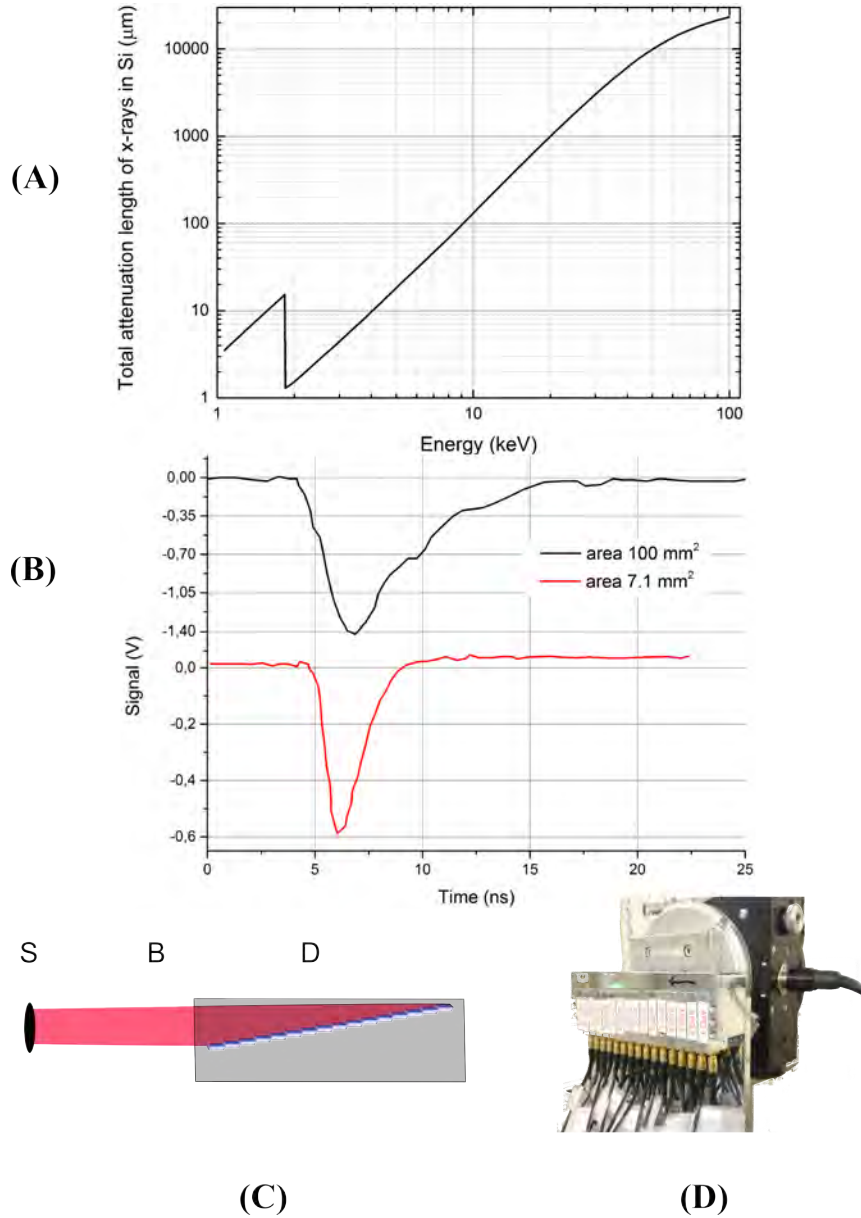


Figure 4.7: Properties and setup of silicon APD detectors: (A) energy dependence of the total (Rayleigh and Compton scattering) attenuation length of x-rays in silicon; (B) time response to Ag K-shell fluorescence radiation (22-24 keV) of APDs with area 7.1 mm² (capacitance of ~ 15 pF) and 100 mm² (capacitance of ~ 120 pF); (C) sketch of a multi-element detector: a stack of thin small area APDs in the housing (D) is inclined relative to the beam (B) scattered by the sample (S); (D) photo of the 16-element APD detector used at P01 beamline.

4.3.2 Detector electronics

A layout of the acquisition electronics for NRS experiments is shown by the block diagram in the fig. 4.8. The voltage pulse from the pre-amplifier (PA) is fed into a constant-fraction discriminator (CFD). This device provides a pulse of fixed length and amplitude once the voltage on the input is higher than the set threshold. One output signal from this CFD is sent to a counter which counts all events, including prompt and delayed, and thus is used for optimizing the flux during an experiment. A second CFD output is fed into a second CFD which is gated by a veto pulse triggered by the bunch clock signal. The veto signal is adjusted in arrival time and width in order to block the CFD operation for several ns before and after the SR pulse. Thus, the second CFD delivers output signals only for delayed photons. The output of the second CFD is also used as an input signal to the counter of the delayed quanta. Information from this counter can be used for instance for the optimization of the monochromator energy and for measuring the delayed fluorescence in NIS. Also, the output signal from the second CFD is used for acquisition of NFS time spectra. For this purpose the output of the second CFD starts the time-to-amplitude converter (TAC) while the TAC is stopped by the bunch clock signal. Thus, the time difference between arrival of the delayed photon and the prompt pulse is converted into a voltage pulse proportional to the time difference. This voltage is then digitized by the analog-to-digital converter (ADC) and analyzed by the multi-channel analyzer (MCA). Thus, the channel number in the MCA is proportional to the time difference between the arrival of the delayed photon and the prompt pulse.

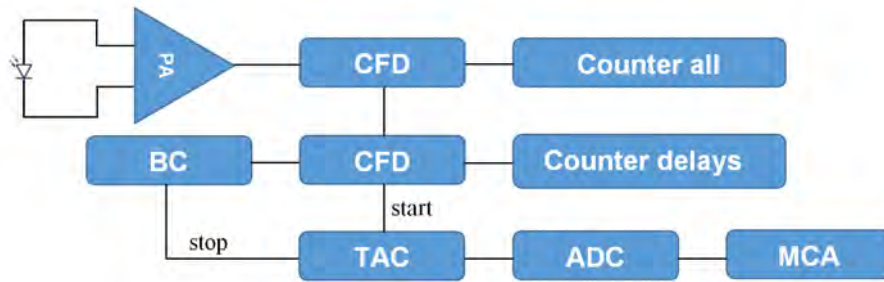


Figure 4.8: Layout of electronics for measuring NRS. See text for the details.

4.4 Beam purity

The NRS technique measures the delayed signal from a nuclear decay in-between the synchrotron bunches [20]. In an ideal case, far from the resonance energy, no other signals should be present in the time slot between the bunches. However, in reality a parasitic signal between the bunches is always present. It originates from electronic noise in the acquisition system, detected cosmic rays and SR from so-called side bunches.

Due to some features of the particle acceleration process, accelerators provide potential wells along the particle travel path. These potential wells are called buckets. The buckets can be filled by bunches of particles on purpose, and several buckets can be empty. The side buckets, between the main buckets filled on purpose, aimed to be empty, but these can be filled by mistake or particles in the main buckets can spread into the neighboring buckets due to the Coulomb repulsion inside a main bunch. Bunches of particles in the side buckets are called "side bunches".

Background measurements can be acquired and subtracted from the measured signal. This is done by tuning the energy of the incident x-rays away from the nuclear resonance energy followed by the acquisition of time spectra at the detuned energy. In some cases the background can be large and can perturb the measured data. In the following, the techniques that aim to reduce or exclude the parasitic signals are discussed. The first reason of these signals, electronic noise in the acquisition scheme, can be completely avoided by setting a higher threshold in the detection electronics. The impact of detected cosmic x-rays is complex to predict, though events involving cosmic rays are rare with count rates less than 0.01 Hz. Side bunches in the ring are a common reason of background in NRS experiments forcing to late start counting times. Experience shows that the presence and intensity of side bunches is specific for each accelerator ring and each operation mode. Indeed, this factor is most problematic for NRS studies and needs special attention during the measurements at the beamline. In the PETRA ring, the side bunches may appear in the time slot from -16 to $+16$ ns around the main bunch (Fig. 4.9, upper panel) due to the 8 ns separation between the bunches in the injector chain. It is not critical for NRS studies on long-living excited states, but becomes an issue for the short-living states like ^{121}Sb and ^{193}Ir studied in this work (see table 4.1).

During this work, an APD detector was installed at the P01 beamline for monitoring the beam purity. Several modes and electron beam cleaning techniques have been tested and evaluated in collaboration with the accelerator operation group. In each test, the relative intensity of side bunches compared to the intensity of the main bunch was acquired. We observed that some beam cleaning procedures can significantly remove side bunches but also reduce the intensity of the main bunch which is not acceptable. A cleaning procedure

not affecting the main bunch intensity was found.

Figure 4.9 shows the time structure of the beam before the studies and after the optimal cleaning procedure was established. One can see that the intensities of the side bunches later than 3 ns decreased by about 2 orders of magnitude or side bunches disappeared completely. This improvement allows one to acquire NRS signals starting from 4 ns after the main bunch. Thus, the NRS studies on short living isotopes are accessible, as shown in the table 4.1.

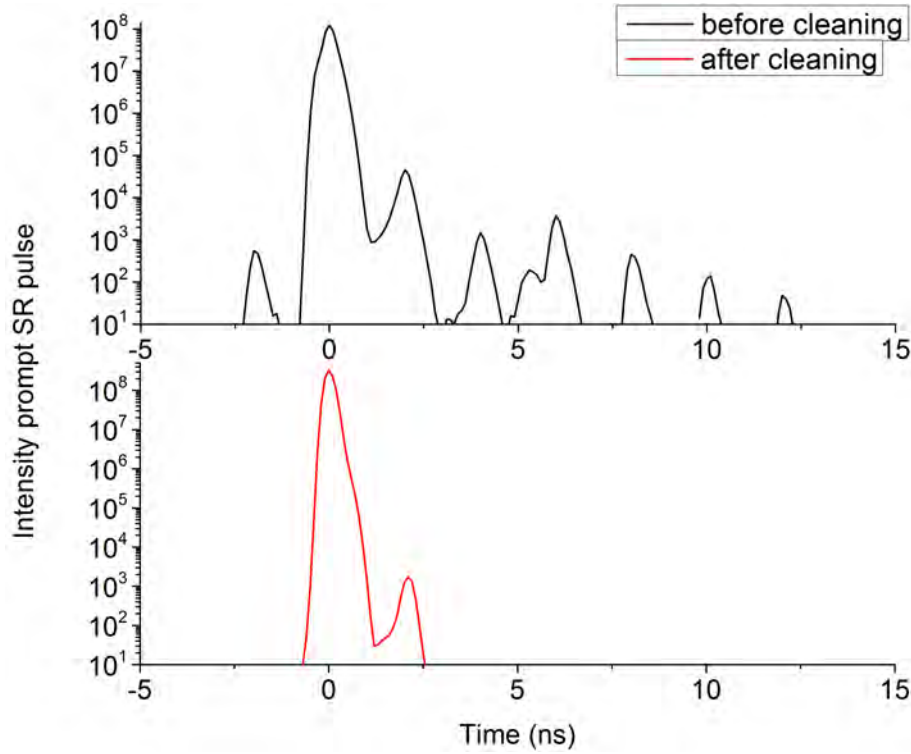


Figure 4.9: Beam time structure in the PETRA ring: before and after the optimal cleaning procedure was established. The time spectra are acquired in several seconds.

Isotope	E_{γ} , [keV]	Life time, [ns]
^{57}Fe	14.4	141
^{119}Sn	23.9	26
^{125}Te	35.5	2.1
^{121}Sb	37.1	5
^{193}Ir	73.0	8.8

Table 4.1: Energy and lifetimes of several excited states studied by NRS.

4.5 Monochromator for NFS on Ir compounds

4.5.1 Design

The design of the medium resolution monochromator (MRM) for the ^{193}Ir resonance is governed by the properties of the x-ray beam at 73 keV. Particularly at the P01 beamline the x-rays with energy 73 keV are provided by the 17th harmonic of two 32 mm period undulators, and monochromatized by the DCM with two Si (3 1 1) reflections. The beam downstream the DCM has an angular divergence of 5.2 μrad and a size of 2.5 x 0.75 mm² (horizontal x vertical) at the position of the monochromator. The energy bandwidth of the 73 keV photons incident on the monochromator is 8(2) eV (see Appendix A.4).

The purpose of the medium resolution monochromator is to allow high spectral flux for NFS experiments rather than achieving high resolution. As explained before the bandwidth of a monochromator for NFS must be sufficiently small in order to avoid detector overload. Multi-bounce high-resolution monochromators can be used for NFS as well. However, the construction of such a monochromator for energies as high as 73 keV would assume the use of very high order of Bragg reflections which have very small angular acceptance, as shown in Chapter 4.2. The efficiency of this type of monochromator would be very low. Backscattering monochromators based on sapphire provide a suitable angular acceptance, as shown in Chapter 4.2, but sapphire crystals do not have sufficient quality over large volume and cannot provide high reflectivity at photon energies as high as 73 keV. Instead, a two-reflection monochromator can be used as shown in Refs. [97, 72, 61]. This type of monochromator consists of two asymmetrically cut silicon crystals in dispersive geometry. Using this principle, a MRM for the ^{193}Ir resonance was developed (s. fig. 4.11). It is installed downstream of the DCM (fig. 4.12 and 4.15). The first crystal makes use of the Si (4 4 0) reflection in order to collimate the beam. The divergence of the beam reflected by the first crystal matches the angular acceptance of the subsequent energy-resolving Si (6 4 2) reflection in the second crystal. The main parameters of the crystals are shown in the table 4.2. The corresponding DuMond diagram and transfer function calculated by the dynamical scattering theory are shown in fig. 4.10.

High-energy x-rays pose a challenge for the preparation of the silicon crystals and for the mechanics to be used for moving the crystals. The important factors which influence the crystal quality are bulk purity, roughness of the surface, and thickness of the damaged surface layer. Bulk purity of the silicon and the process of the crystal preparation determine these factors, and therefore should be described in detail.

	First crystal	Second crystal
Reflection	(4 4 0)	(6 4 2)
Bragg angle, [degree]	5.072	6.716
Asymmetry parameter b	0.11	2.6
Incoming angle, [degree]	1.002	9.716
Outcoming angle, [degree]	9.142	3.716
Angular acceptance of the incident beam, [μrad]	2.35	0.25
Angular divergence of the diffracted beam, [μrad]	0.26	0.65
Beam spot size on the crystal, [mm]	57.2	53.9
Vertical size of reflected beam, [mm]	9.0	3.5
ΔT of reflection (see eq. (4.9)), [mK] [mm]	10.3	0.83
FWHM of instrumental function, [meV]	112	
Attenuation length of the 73 keV photons in Si, [mm]	22	

Table 4.2: Main design parameters of the MRM for 73 keV x-rays.

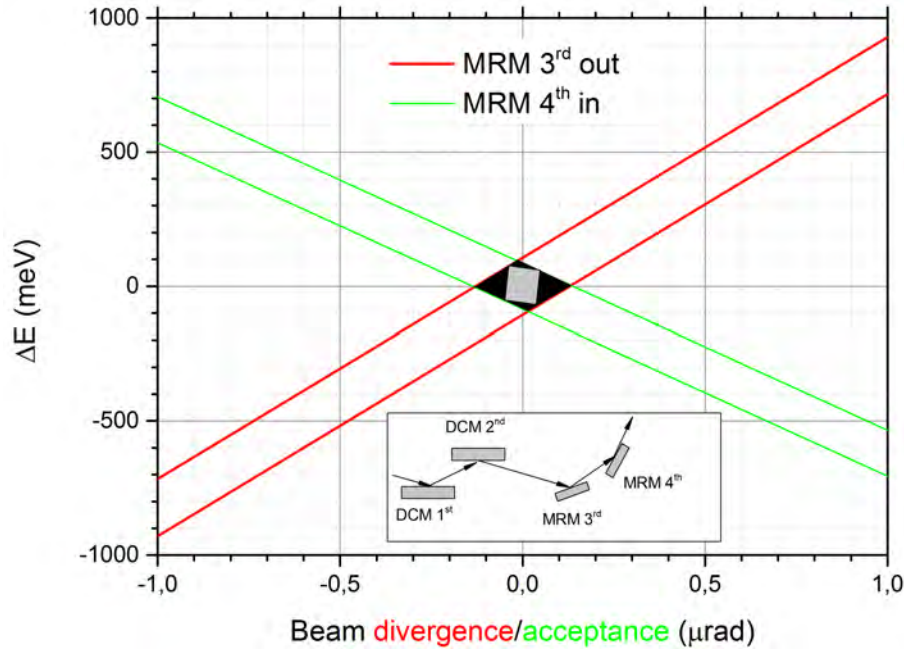


Figure 4.10: DuMond diagram for the setup of MRM for 73 keV x-rays. The bandpass is shown by the gray polygon as calculated by the dynamical scattering theory.

First, the rather large volume of the crystal penetrated by 73 keV x-rays (see table 4.2) demands an excellent quality of bulk silicon. In this work silicon ingots grown by the zone melting method have been used. The resistivity of the silicon ingots was $> 2.65 \text{ k}\Omega\cdot\text{cm}$. The bulk material is considered to be of sufficient quality, although it might have an influence on the spectral reflectivity as shown by utilizing very pure silicon with resistivity of $70 \text{ k}\Omega\cdot\text{cm}$ in the work [108]. Cutting of the crystals from the ingot results in a damaged layer on the crystal surface which contains distortion of the crystalline order and may also contain the cutting products such as wire material and diamond particles used in the cutting process. The thickness of the damaged layer is roughly $30 \mu\text{m}$ [119]. In order to remove the damaged layer the crystals have been etched in a solution of hydrofluoric acid, acetic acid and nitric acid with a ratio of 1:2:3 volume parts for several hours at room temperature. As a result $50 \mu\text{m}$ of material were removed from the surface. To achieve a planar mirror surface, the crystals have been lapped with a SiC slurry. The lapping again resulted in a damaged layer of about $20\text{--}30 \mu\text{m}$ thickness. In order to remove this layer, a polishing by cloth has been done afterwards. This polishing process has removed about $60 \mu\text{m}$ of material. Thus, the distorted surface layer resulting from the preparation of the crystals has been removed and has negligible impact on the performance of the crystals.

The most crucial issue in the design of the monochromator mechanics is the very small angular acceptance of the second crystal that is in the order of hundreds of nano-radians. Obviously, the mechanical setup should be able to move the crystal with the angular step

size of this order or better. The angular positioning of the crystals is provided by two motorized stages (fig.4.11, produced by Kohzu Precision Co., Ltd., Japan) which allow step size of 24 nrad or smaller [120]. The divergence of 250 nrad which can be accepted by the 2nd crystal (s. table 4.2) is significantly larger than the angular resolution of the mechanics and therefore the mechanics should be able to resolve the reflection on the 2nd crystal.

Additionally, the mounting of the crystal on the stages is crucial. A tight fixation does induce a curvature of the crystals, the effect is significant even for thick crystals, as it is denoted in the work on monochromatization of 67 keV x-rays for NRS on ⁶¹Ni isotope [61]. In this work the MRM crystals were placed onto the holders, without squeezing, thus, the mounting prevented curvature of the crystals.

Further, the temperature stability of the two crystals could become an issue due to the small acceptance of the 2nd crystal. Using Bragg's law one can show that a reflection is shifted by as much as its angular acceptance $\Delta\theta$ when the temperature is changed by ΔT [72]:

$$\Delta T = \frac{\Delta\theta}{\alpha \cdot \tan(\theta_B)} \quad (4.9)$$

Here, α is the coefficient of thermal expansion of silicon at room temperature, $2.57(3) \cdot 10^{-6} \text{ K}^{-1}$ [121, 122]. At large Bragg angles θ_B and small acceptance of the reflection $\Delta\theta$, the influence of the temperature change becomes more pronounced. For this setup the change of the temperature of the second crystal by just 0.83 K will already shift the reflection by 250 nrad and thus spoil transmission. Temperature measurements have been done at the P01 beamline in order to measure the temperature stability inside the hutch. A resistive temperature sensor and a special temperature acquisition system with sensitivity better than $200 \mu\text{K}^5$ were used in the measurements. The measurements show that the temperature stability inside the hutch is better than 200 mK during 4 days (s. Figure 4.13) which corresponds to a shift of the Bragg energy by 37.5 meV. The shift is much smaller than the energy bandpass of the monochromator.

Heating by the photon beam is nearly constant, since the electron current in the PETRA ring change by 2% at highest (so-called top-up mode), providing a temperature change of less than 20 mK by photon beam heating [91, 123]. The heat load by the photon beam is thus easy to manage for this monochromator. Therefore, the impact of temperature should not be significant for this monochromator in the conditions present at the beamline.

The energy change is done by rotating of the Bragg angles of the first and second crystals

⁵The temperature acquisition system is described in detail in the next section 4.6.

with non-equivalent step sizes given by the following coupling factor:

$$\frac{\delta\theta_2}{\delta\theta_1} = 3.3267 \quad (4.10)$$

where $\delta\theta_1$ and $\delta\theta_2$ are the angular steps of rotation of the first and second crystal. The energy step is related to the change of the angles by the equation:

$$\delta E = -\frac{\delta\theta_2}{\tan(\theta_2) + 2\tan(\theta_1)} E \quad (4.11)$$

here θ_1 and θ_2 are the Bragg angles of the first and second crystal and E is the energy of the incident x-rays.

For this particular monochromator, an energy step is related to an angular step as

$$\delta E \text{ [eV]} = 6480 (\delta\theta_2 [\text{degree}] - 1.11\delta\theta_1 [\text{degree}]) \quad (4.12)$$

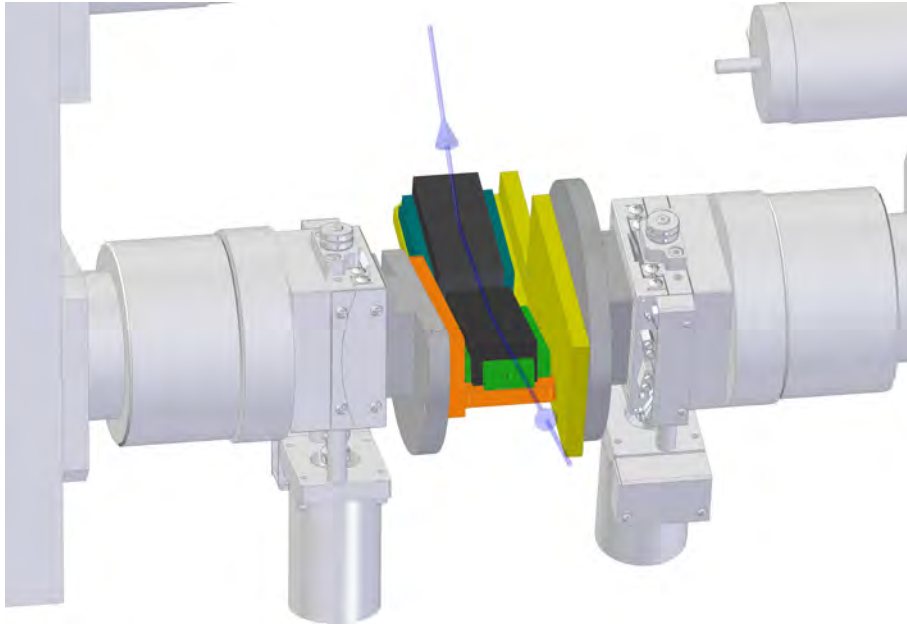


Figure 4.11: CAD-model of the MRM. The blue arrows indicate the beam path.

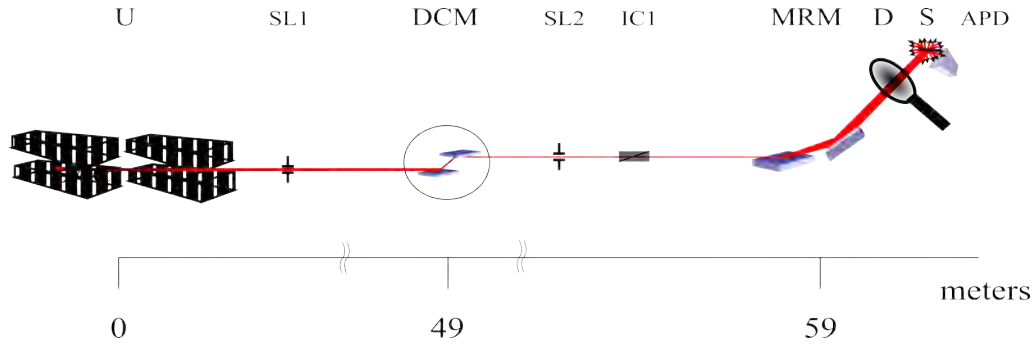


Figure 4.12: Sketch of the experimental setup for nuclear fluorescence measurements at the 73 keV resonance of ^{193}Ir . U - two undulators, SL1 and SL2 - slits, DCM - double crystal monochromator, IC1 - ionization chamber, MRM - medium-resolution monochromator, D - PIN diode detector, S - sample, APD - APD detector.

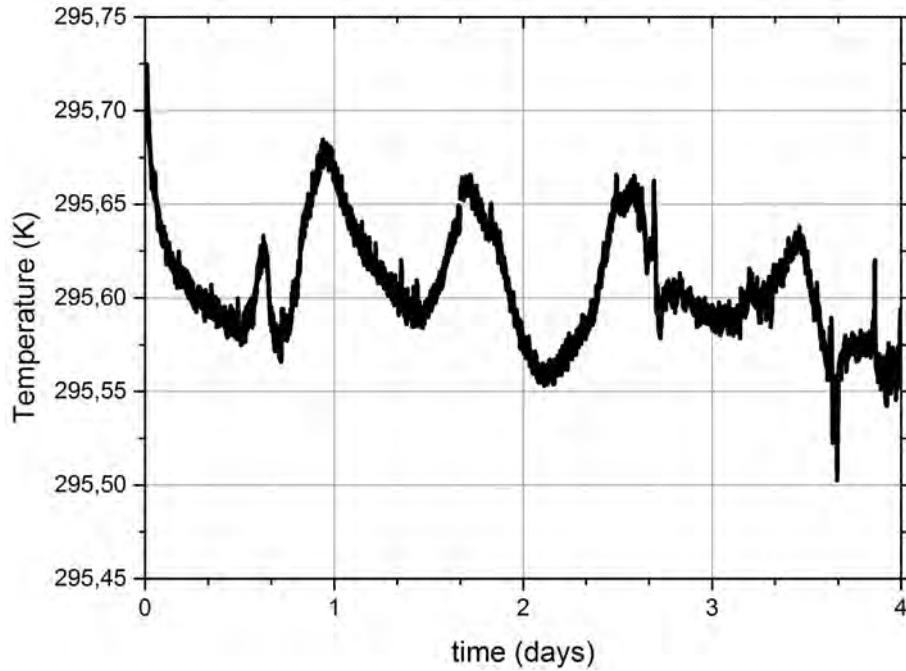


Figure 4.13: Temperature stability in the experimental hutch at the P01 beamline. The temperature deviations have an RMS of 27.5 mK and an amplitude of 130 mK, which is much less than ΔT of Bragg reflections utilized in the monochromator (see table 4.2).

4.5.2 Performance of the monochromator

The instrumental function of the monochromator can be measured with NFS. In this case the energy bandwidth of the forward scattered photons is a convolution of the energy bandpass of the monochromator and the linewidth of the nuclear resonance. The natural linewidth of the ^{193}Ir resonance is 75 neV while the energy bandpass of the MRM is on the order of hundreds of meV. The natural linewidth can therefore be well approximated

by a delta function. The energy bandwidth of forward scattered photons is then equal to the energy bandpass of the MRM.

However, the first NFS experiments on a resonance with not precisely known energy are challenging. A rough estimation of the resonance energy, alignment of the upstream optics and measurements of efficiency of the monochromator can be done by measuring nuclear fluorescence. Resonant fluorescence is easy to observe while making energy scans in a wide range with less time-consuming large energy steps. The technique is particularly useful when side bunches are present in the ring (see Chapter 4.4) and nuclear forward scattering signal cannot be detected starting at late times after excitation due to the speed-up effect (see Chapter 3.4). The incoherent inelastic scattering channel (nuclear fluorescence) is not affected by the speed-up of nuclear decay and significant signal is still present at late times after excitation which is particularly useful for short-living excited states. The radiation scattered in the inelastic channel follows the exponential decay with a time constant equal to the natural lifetime of the resonant state. It is therefore a precise probe for the natural lifetime of the resonance. The signal measured in the inelastic channel is, however, a convolution of the instrumental function with the inelastic scattering function which is generally unknown but can be as broad as the instrumental function of the MRM when Lamb-Mössbauer factor is low, which is the case for high-energy resonances. Thus, nuclear fluorescence cannot be used for detailed characterization of the monochromator. In this work, the preliminary characterization of MRM and search for the resonance was done using inelastic scattering channel and then, after development of the beam cleaning procedure and improving the APD detector, the resonant signal was found in the NFS channel and the instrumental function was measured.

The setup for the nuclear fluorescence experiment is shown in the fig. 4.12. The undulator radiation was pre-monochromatized by the DCM down to eV-bandwidth and later down to hundreds of meV by the MRM. The photon beam after the MRM impinges on the Ir metal powder sample (S) that is attached to the APD detector and maintained at room temperature. An APD detector with an active area of $10 \times 10 \text{ mm}^2$ and standard NRS electronics have been used to detect the resonant photons. By these means we monitor the delayed fluorescence radiation with photon energies of 11.2, 12.8, and 13.4 keV corresponding to the L- fluorescence lines of Iridium. The energy of the incident beam on the MRM has been pre-calibrated with absorption measurements at the K-edge of Iridium at 76.111 keV. This pre-calibration was done in order to: (i) reduce the energy range to be scanned and (ii) to find the nuclear resonance in ^{193}Ir with the DCM, since the DCM mechanics is not precisely calibrated for 73 keV photons. After that, energy of the DCM was scanned around 73 keV in order to find the ^{193}Ir resonance. The time-integrated signal was acquired starting from 9 ns after the synchrotron bunch. In this first experiment the presence of spurious bunches at 8 ns after the main bunch prevented an earlier start of signal acquisition with respect to the synchrotron bunch. A big effort of the PETRA ma-

chine group and the members of the Photon Science group allowed establishing a beam cleaning procedure (s. chapter 4.4). By means of this procedure, the spurious bunches were reduced and early, 4-5 ns start times for counting became accessible.

The nuclear ^{193}Ir resonance was found monitoring nuclear fluorescence and resonance energy was refined to 73.04(8) keV. The lifetime of the resonance transition has been determined to 8.4(2) ns (fig. 4.14) by fitting of exponential decay to the experimental time spectrum. The obtained value is in good agreement with the literature value of 8.79(22) ns [124]. The photon flux incident on the monochromator was measured by a nitrogen-filled ionization chamber (IC1, fig. 4.12) to $7.8 \cdot 10^{10}$ ph/s⁶ at the resonant energy and an electron current of 95 mA in the PETRA ring. The flux downstream of the MRM was measured to $6 \cdot 10^8$ ph/s by PIN diode (D, fig. 4.12) in the same conditions.

A NFS experiment sometimes requires a complex sample environment like cooling, application of strong magnetic fields or high pressures. The beam reflected by the MRM is deflected by 23° with respect to the incident beam (fig. 4.15). This does not pose any problem for the installation of sample environment in NFS experiments since sample can be placed before the MRM without any influence on the results of the NFS experiment. The MRM device is called analyzer in this case. Therefore, the Ir sample was placed upstream of the MRM. In order to maximize the count-rate in NFS, the sample was mounted in a helium closed cycle cryostat and cooled to 13 K (sample1, fig. 4.15). Another Ir foil sample (sample2, fig. 4.15) was installed on the NIS detector downstream the MRM and maintained at room temperature. Nuclear fluorescence was measured on this foil in order to follow the instabilities in the DCM and tune its energy to the resonant one. Once the resonance was found in the NIS channel, the energy of the DCM was fixed. In the following the MRM was moved into the beam and the energy of the MRM was scanned in order to find the resonant transition in the forward scattering channel.

⁶Measured at 57 m from the photon source, beam size on IC1 was determined by slits with opening 4x0.4 mm² (horizontal x vertical) placed close to the IC1

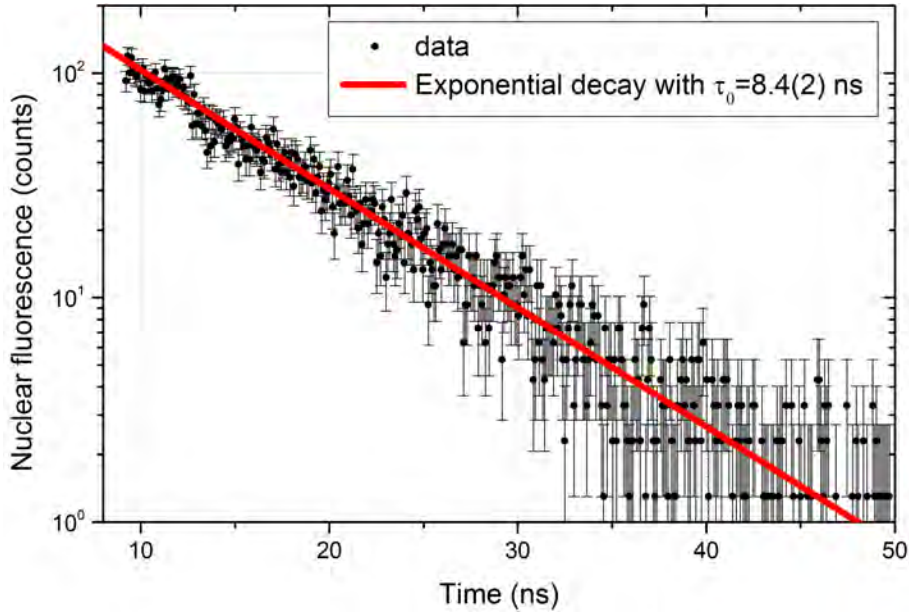


Figure 4.14: Time-spectrum of x-rays scattered in the inelastic channel showing an exponential decay with the natural lifetime $\tau_0 = 8.4(2)$ ns.

The resonance was found in forward scattering channel. The energy of the resonance was determined to 72.90(8) keV which is 3.207 keV lower than the K- absorption edge of Iridium. The error in the absolute value of the resonance energy was determined as 3σ from the point of the maximum of the derivative of the K-edge of Iridium. The obtained value of 72.90(8) keV is lower than the literature value of 73.045(5) keV received by measurements of internal conversion time dependence in Ref. [125]. In fact, the value of 73.045(5) keV is only one value reported in the literature with such a high accuracy. Analysis of literature values from 1960 to 2016 (reference databases [124, 126]) shows that the most frequently mentioned resonance energy value is 73.0 keV, with an error of ~ 0.1 keV.

Following the observation of the resonance, the optics setup was optimized. The optimization does involve scans of the vertical and horizontal position of the MRM crystals with the beam in order to find the best spot showing the highest reflectivity and the smallest energy bandwidth. The measurement of the instrumental function is carried out by scanning the energy of the MRM which is done by scanning the Bragg angles of both crystals synchronized with the coupling factor given by equation (4.12). The obtained instrumental function is shown in fig. 4.16. The FWHM of the experimental curve is 158(8) meV while dynamical scattering theory predicts 112 meV (FWHM) for this setup. The broadening can be explained by insufficient perfection of the volume of silicon crystals that is traced out by the x-ray beam. The beam spot sizes on the crystals and penetration depth are very high at the energy used here (see table 4.2), thus, it is more probable to meet a defect in the monochromator crystals with the beam. After

optimization, a typical count-rate of 6-7 Hz has been achieved in NFS by a 100 μm Ir thick foil. The achieved count-rates allowed the collection of NFS spectra in a reasonable time of a few hours, as shown in Chapter 5.2. The measured properties of the MRM are summarized in table 4.3.

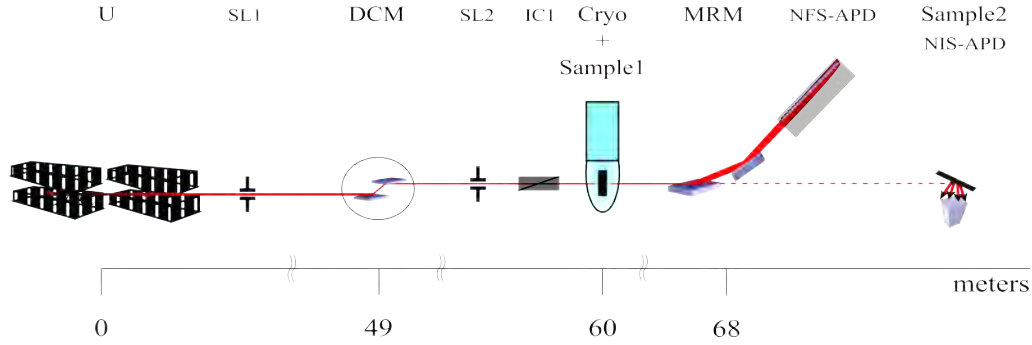


Figure 4.15: Sketch of the experimental setup for NFS measurements on the 73 keV resonance of ^{193}Ir . U - two undulators, SL1 and SL2 - slits, DCM - double crystal monochromator, IC1 - ionization chamber, MRM - medium-resolution monochromator, D - PIN diode detector, Cryo+sample1 - sample for NFS in the closed cycle He cryostat, NFS-APD - APD detector for NFS, sample2 - sample for check of photon energy, NIS-APD - APD detector for check of the photon energy.

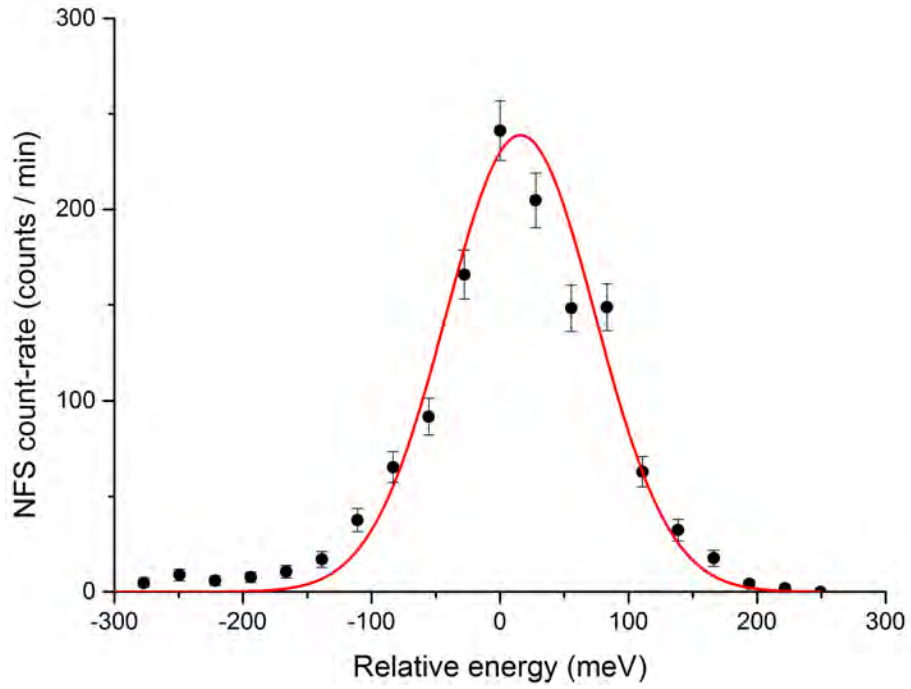


Figure 4.16: Instrumental function of the MRM at 72.90(8) keV. Red line: fit by a Gaussian distribution with FWHM 158(8) meV.

Parameter	Value
Energy bandpass, [meV]	158(8)
Photon flux after MRM, [ph/s]	$6 \cdot 10^8$
Photon flux per natural linewidth of ^{193}Ir resonance, [ph/s/ Γ]	280

Table 4.3: Summary of the measured properties of the MRM.

4.6 Al₂O₃ backscattering monochromator

In this section the design and performance of the backscattering monochromator is discussed. The precise temperature control and quality of the crystal are the most essential parts of a backscattering monochromator. As shown in the chapter 4.2 change of the Bragg energy in backscattering geometry is proportional to the thermal expansion of the crystal. Thermal expansion of sapphire is typically in the range of $(1..6) \cdot 10^{-6} \text{ K}^{-1}$. Using equation (4.7), it can be estimated that the Bragg energy is changed by typically 0.1-1 meV when the temperature of the sapphire crystal is changed by 1 mK. Consequently, the temperature of the crystal should be controlled with an accuracy of 0.1 to 1 mK in order to be able to resolve the back-reflection. Also, for the energy (temperature) scans the temperature step size must have the same precision or better in order to provide sufficient energy resolution in NIS scans. Here, two challenges emerge: first, the temperature change should be measured with the best precision, and second, the temperature should be controlled with high accuracy. The design of the monochromator cryostat and the temperature control system is adapted to fulfill these requirements.

It is worth to mention the parameters of the pre-monochromator (DCM) at the P01 beamline since it defines the properties of the beam incident on the backscattering monochromator. The DCM hosts two pairs of Si crystals, one using the (1 1 1) and another one utilizing the (3 1 1) reflection. For most experiments using the backscattering monochromator the (1 1 1) crystal pair is used due to the larger angular acceptance for the undulator radiation resulting in a higher transmission.

4.6.1 Design

The sapphire backscattering monochromator built for the P01 beamline is shown in fig. 4.17. The main element is a two-stage flow cryostat with copper heat exchangers.

Cold nitrogen gas is used as a coolant, however, any gas can be used which is not reactive to copper, nickel, stainless steel and NBR⁷ resin. The cryostat operates with overpressure, having atmospheric pressure on the outlet. The operation with overpressure provides gas flow which can be adjusted by flow meter valve at the cryostat exhaust assuring a better temperature control. The cold gas circulates in the spiral channels of the larger primary and smaller secondary copper heat exchanger and the gas temperature stabilizes down to sub-mK deviations around the set point. The cold nitrogen is produced by evaporation of liquid nitrogen from a Dewar and supplied to the cryostat via a gas transfer line. The gas temperature is stabilized by pre-heating in the gas transfer line. The accuracy of the temperature stabilization at the cryostat inlet is 200-500 mK. The heat exchanger chamber

⁷NBR (Nitrile-Butadiene Rubber) is the resin commonly used for vacuum sealing.

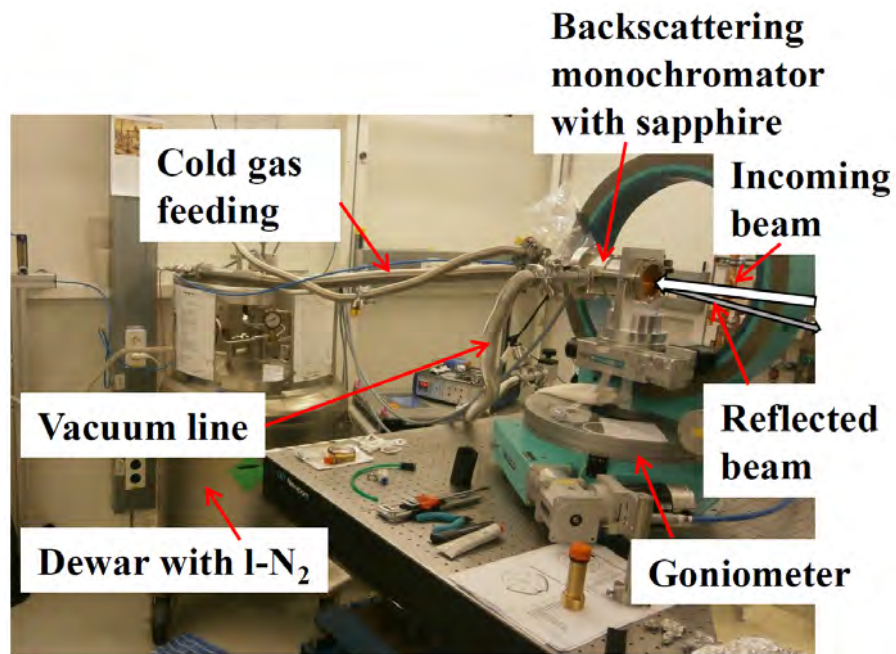
including the crystal holder is thermally insulated from the outer cryostat wall in order to avoid thermal transport and resulting loss of the cooling power. After passing the heat exchangers, the tempered cold gas flows inside the crystal enclosure and regulates the temperature of the crystal. The gas is then released at the outlet. The typical flow rate is 200-500 liters of nitrogen gas per hour during operation between 150 and 400 K with ~ 1 bar overpressure in l-N₂ dewar.

The measurement of the gas temperature is performed by a platinum PT1000 resistor. A Keithley 3706 digital multimeter⁸ is used for reading of the resistance values. This device reduces noise by a factor of 2 and requires 10 times smaller test currents for measuring 1 kOhm resistances compared to the frequently used 100 Ohm resistances. Thus, the PT1000 resistors with 1088 kOhm resistance at room temperature have been chosen for operation of this cryostat. A software-based PID temperature controller [101] reads the resistance provided by the Keithley device, compares it with the set resistance, calculates the voltage desired, and the voltage is applied to the cryostat's constantan heating wire by a power supply connected to the controller. The PID controller was optimized by the Ziegler-Nichols method [127]. During optimization it was noticed that the use of any differential coefficient reduces the stability of the temperature control, thus, only proportional and integral coefficients have been applied to control the temperature. The sensitivity of the temperature measurements depends on the integration time of the voltage reading by the Keithley multimeter. Additionally, the sensitivity depends on the number of channels that are read sequentially. The sensitivity dependence on the integration time is shown in fig. 4.18. As follows from this figure, the sensitivity of temperature measurements can be improved by a factor 10 with an optimal integration time and proper grounding of the measurement circuit, leading to an accuracy of 0.1-0.2 mK. For the purpose of grounding the current probes of the first and fourth channels of the digital multimeter are attached to the earth ground electrode in the device rack. The crystal temperature is measured by a second PT1000 resistor attached to the crystal. The resistor is attached to the crystal mechanically, with a thin layer of silver paste in between the crystal and the resistor. Another channel in the Keithley multimeter is used for reading of the resistance values of this thermosensor.

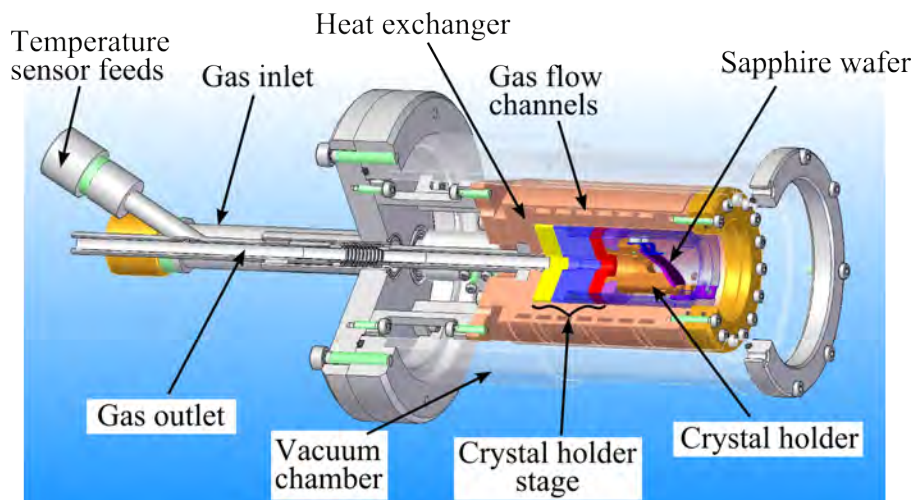
The backscattering cryostat hosting the sapphire crystal is installed 89 m downstream of the undulator source and reflects the beam towards the sample that is located 21 m further upstream. The monochromator has been tested for temperature stability without heat load from the impinging beam in order to evaluate the precision of the temperature measurements at a crystal temperature of 275 K. The temperature point 275 K was chosen because at this temperature the copper heat exchangers of the cryostat have a relatively high heat capacity which provides a challenge for the reactivity of the temperature control. Furthermore, this temperature point corresponds to the energy of 46.5 keV pho-

⁸the device has 7.5 digits resolution for the resistance range under scope.

tons reflected by the $(2\ 9\ \overline{11}\ 92)$ sapphire back-reflection with $\Delta E/\Delta T = -0.258\text{ meV/mK}$. Large $\Delta E/\Delta T$ demands on very small temperature steps ΔT in order to achieve a low energy resolution ΔE , thus, this reflection is a good probe for the quality of the temperature control. The results of the temperature control tests are shown in Fig. 4.19. An average of RMS deviations of 0.181 mK relative to the set point of 275 K was achieved during each temperature stabilization. 8 temperature stabilization runs of 1 hour each were performed in order to reveal the repeatability of the control. The achieved precision of 0.181 mK corresponds to an energy drift of the monochromator by $46.6\ \mu\text{eV}$ during 1 hour at the energy of 46.5 keV. The temperature scans around the temperature 275 K have been carried out with a temperature ramp of 230 mK/min during 30 min (fig. 4.20).



(a)



(b)

Figure 4.17: Setup (a) and cross-section (b) of the backscattering monochromator (outer heat exchanger is not shown).

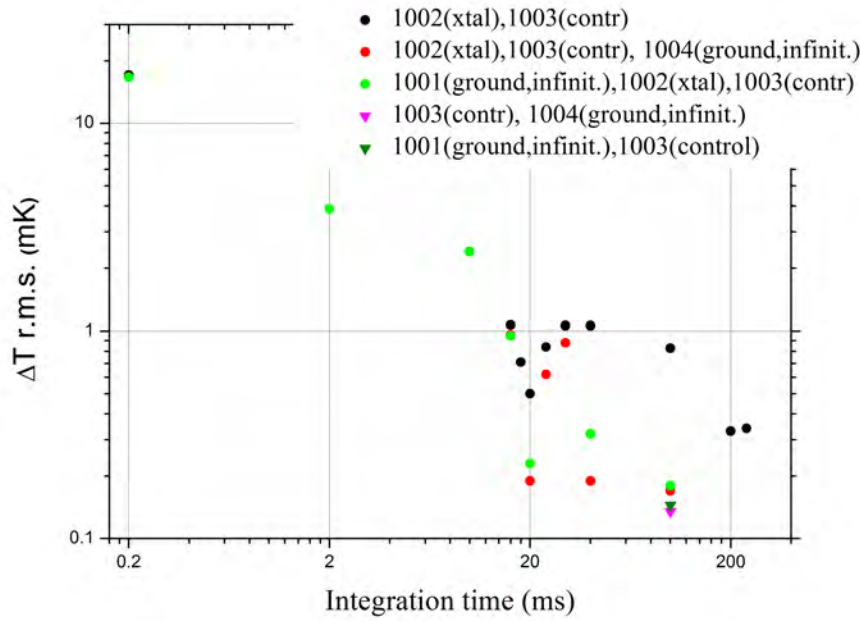


Figure 4.18: Sensitivity of temperature measurements at room temperature for different reading rates and number of channels. Current probe of the channels 1001 and 1004 are grounded, the circuit is opened. Channels 1002 and 1003 are used to measure resistances of platinum temperature probes (PT1000).

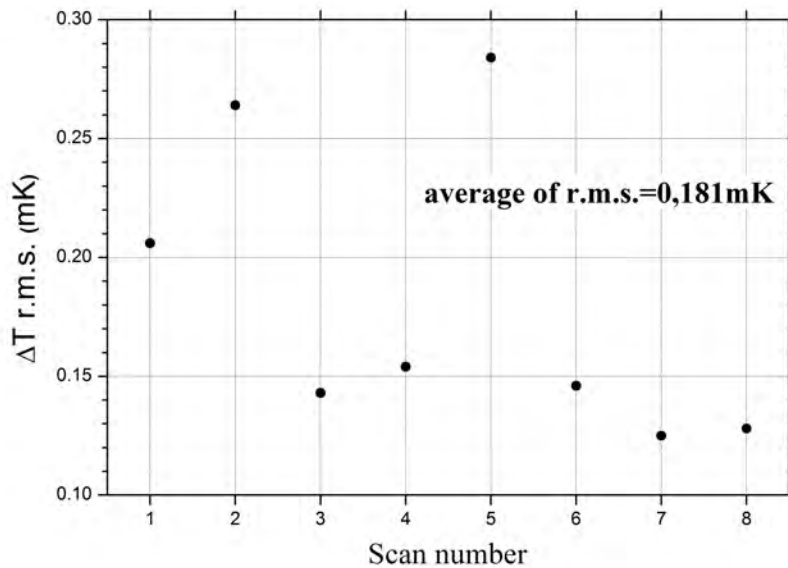


Figure 4.19: Temperature stability during temperature control at 275 K. The duration of each scan is 1 hour.

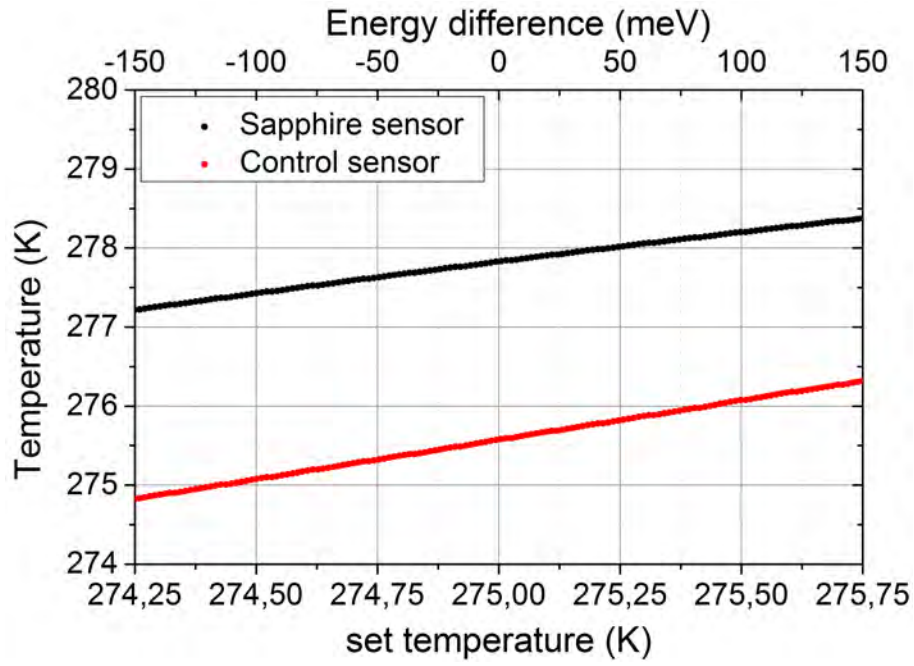


Figure 4.20: Temperature control at 275 K with a fast, 230 mK/min, temperature change. The deviation from linearity is 9.8 mK (RMS) in a temperature range of 1.5 K. The offset in absolute temperature is determined by spatial separation of "sapphire" and "control" sensors.

4.6.2 Performance at 23.88 keV at the ^{119}Sn nuclear resonance

The backscattering monochromator was installed and tested for the first time at the P01 beamline at the energy of the ^{119}Sn nuclear resonance at 23.88 keV. In this first experiment the temperature stability and precision of the temperature control were tested under heat load by the x-ray beam. Since the temperature of the crystal corresponding to the Bragg energy of the resonant quanta is a fixed well-defined value, the nuclear resonance provides the possibility to measure temperature gradients by mapping of the instrumental function of the particular reflection over the sapphire crystal surface. In this case the temperature shown by the thermosensor at the maximum of resonance will be different for different spots on the crystal. There is no need to place several thermosensors in different positions to measure temperature gradients. However, an error in the obtained data can emerge when the direct beam or the beam from a strong reflection hits the thermosensor. Thus, the thermosensor was attached to the edge of the crystal which should reduce the temperature effect of the beam.

During the experiment the PETRA ring was operated in 40 bunch mode, resulting in 192 ns separation between the bunches. The standard double-crystal monochromator (DCM) was operated using the pair of Si (1 1 1) reflections. It was tuned to the energy 23.879 keV. The DCM reduced the bandwidth of the undulator radiation down to 3 eV around the ^{119}Sn resonance. A powder of SnO_2 enriched in the ^{119}Sn isotope to 95 % has been placed into the direct beam. The direct beam attenuated by the sample and the quanta reemitted by ^{119}Sn nuclei have been reflected by the Al_2O_3 crystal. A sapphire crystal of disk shape with 18 mm diameter and 5 mm thickness was used. The crystal was grown by heat-exchange method [128], having HEMEX grade⁹. The crystal surface was mechanically polished. Additionally, the crystal quality of another sapphire, grown by the Kyropoulos technique [128] with low pulling rate (wafer #1 in Ref. [129]) was inspected. That crystal was 1 mm thick; the crystal surface was first chemically etched and later mechanically polished.

In the experiment, the Al_2O_3 crystal has to be oriented in a way, that it reflects photons with 23.879 keV, corresponding to the energy of the Mössbauer transition in ^{119}Sn at the 2θ angle close to 180° . The corresponding crystallographic planes $(4\ 4\ \bar{8}\ 45)$ should be oriented perpendicular to the beam. This has been done by an orientation matrix which connects Euler angles and Miller indices of the crystal. The Euler angles define three rotation degrees of freedom which allow one to bring the crystal from any arbitrary to a defined position. Thus, an orientation matrix can be used to determine the orientation of the crystal. For the purpose of finding the orientation matrix, a fluorescence screen was installed close to the monochromator. First, the crystal was maintained at room temper-

⁹HEMEX is trademark of GT Advanced Technologies Inc., 243 Daniel Webster Highway, Merrimack, NH 03054, USA.

ature and the energy of the DCM was changed. Reflections with Bragg angles close to 90° (back-reflections) have been observed on the fluorescence screen. Moving the fluorescence screen closer to the monochromator allows one to observe more back-reflections which can be used for orientation. This can be particularly useful for reflections with low reflectivity. When a back-reflection was found on the fluorescence screen, it was put into the backscattering regime, i.e. into the spot of the direct beam, using the goniometer and tuning energy of pre-monochromator. The procedure is repeated for several back-reflections in order to reduce the statistical error in determination of the orientation matrix. The azimuthal and polar angles have been used to calculate the orientation matrix of the crystal setup. Once the matrix was determined, the crystal was oriented to match the $(4\ 4\ \bar{8}\ 45)$ reflection and the temperature of the crystal was reduced to 192 K, which is the temperature of the Bragg energy coinciding with the resonant energy. In the following the energy of the pre-monochromator was refined to optimize the transmission of the setup. X-rays reflected from the Al₂O₃ crystal have been detected by a stack of APD detectors installed upstream of the backscattering monochromator.

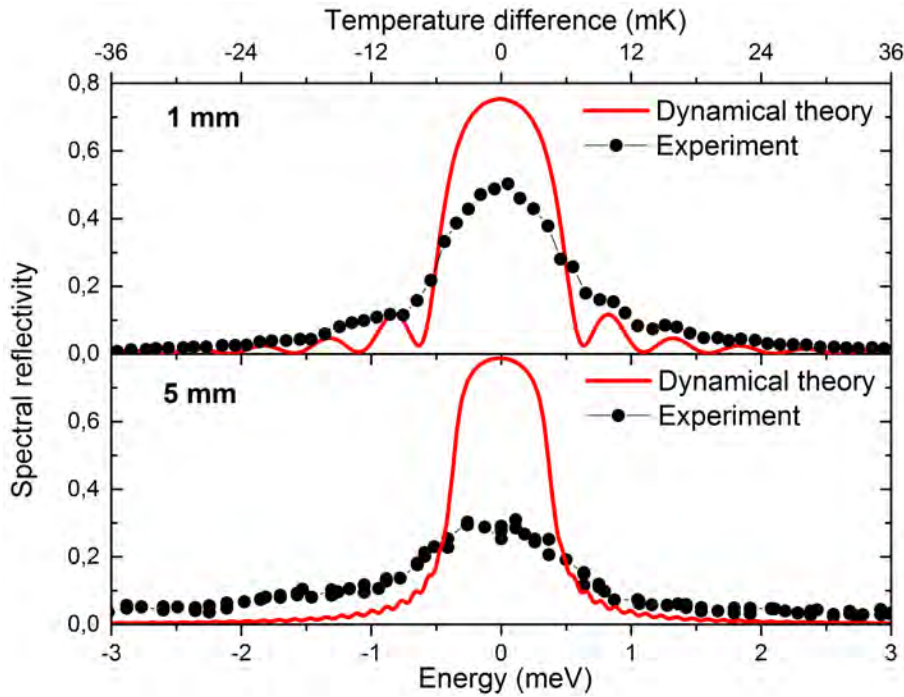


Figure 4.21: Spectral reflectivities of 1 mm thick and 5 mm thick sapphire crystals measured around ^{119}Sn resonance energy of 23.88 keV (Energy difference 0). Red lines: values calculated by the dynamical theory of x-ray diffraction.

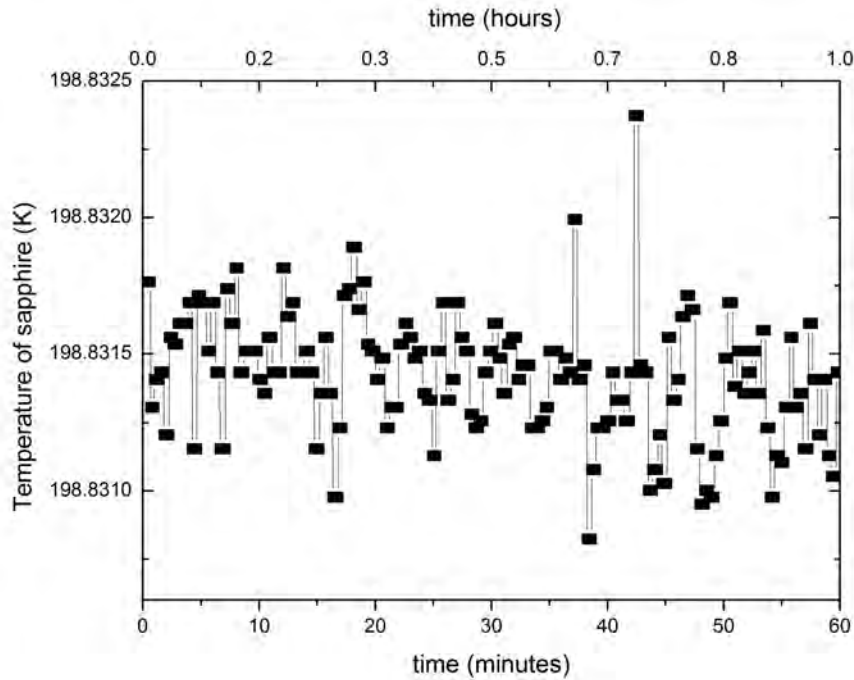


Figure 4.22: Measured temperature stability during temperature control with heat load by 23.88 keV x-ray beam. The RMS value is 0.7 mK during 1 hour.

The best position on the crystal was found. At this position an energy bandwidth of 1.3(1) meV (FWHM) and relatively symmetric shape of the instrumental function have been achieved, as shown in fig. 4.21. The obtained temperature stability at the sapphire crystal was 0.7 mK (r.m.s.) (fig. 4.22) which corresponds to an energy uncertainty of 0.06 meV. This value is much smaller than the FWHM of the instrumental function. Therefore, for this Mössbauer transition the quality of the temperature control is the least important factor that deteriorates the resolution of the monochromator.

There could be two reasons which deteriorate the energy bandwidth measured in experiment. Firstly, the crystal imperfections such as dislocations and stacking faults are the reasons for the broadening of the instrumental function as shown in Ref. [99]. Second, the temperature gradients along the sapphire crystal might influence the resolution. In Ref. [114] it was shown that a temperature gradient of 0.1 mK may explain broadening of up to 10 meV. By mapping the sapphire temperature at resonant energy with respect to the position of the incident beam on the crystal one can estimate temperature gradients present in the system. Though the position of the temperature sensor to the beam might influence the measurements, the impact of this effect is not too high because the crystal is thick and the thermosensor is placed on the edge of the crystal. The temperature map is shown in the fig. 4.23 for the 5 mm thick sapphire crystal. The temperature gradient is roughly 100 mK/mm in some regions on the crystal.

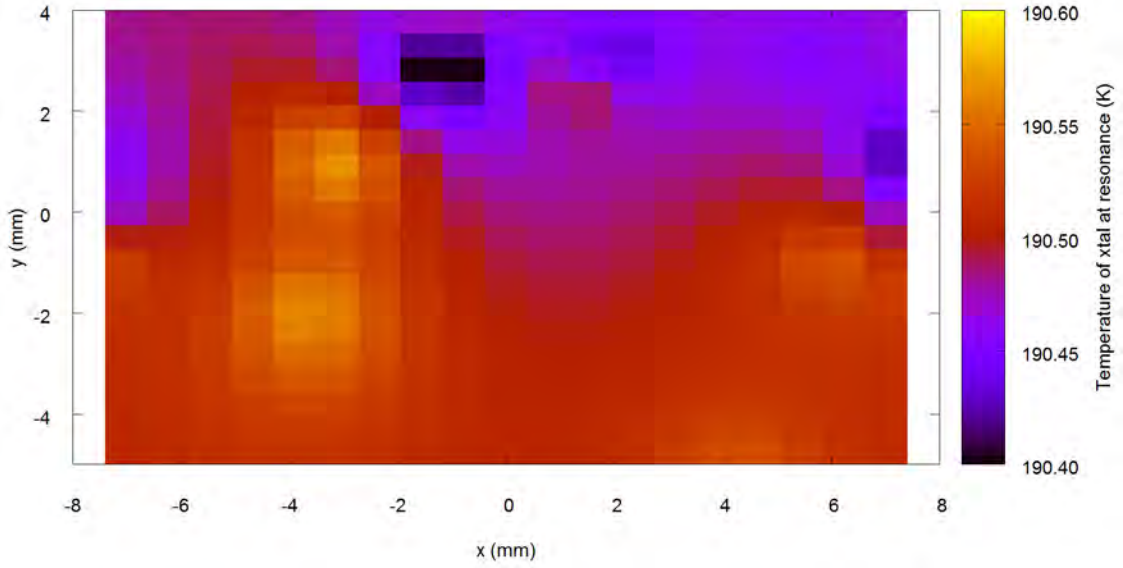


Figure 4.23: *Temperature map for the 5 mm thick sapphire crystal. The temperature is taken at the maximum of instrumental function (s. text).*

The high reflectivity of the crystal results in a higher flux from the monochromator, which is desired in NRS experiments. Thus, it is very important to measure this parameter. The photon flux upstream and downstream of the BS HRM was measured by a 300 μm thick silicon PIN diode and a 100 μm thick APD, respectively. The flux incident on the BS HRM was $8.1 \cdot 10^{12}$ ph/s (or $2.7 \cdot 10^{12}$ ph/s/eV) at 23.8793 keV. The measured photon flux after the BS HRM was $1.6 \cdot 10^9$ ph/s at this energy. This corresponds to a sapphire spectral reflectivity of 26.6 %, or $3.1 \cdot 10^4$ photons per natural linewidth Γ of the ^{119}Sn resonance.

4.6.3 Performance at 37.13 keV at the ^{121}Sb nuclear resonance

The backscattering experiment at the energy 37.13 keV had the same setup and alignment procedure as described before. However, here the energy of the pre-monochromator was set to 37.13 keV. In this experiment the resonance of interest was ^{121}Sb at 37.1292(5) keV [103]. The flux of the beam incident on the BS HRM was measured to be $1.7 \cdot 10^{12}$ ph/s. This value agrees well with the calculated flux value [130] of $1.2 \cdot 10^{12}$ ph/s. The (8 16 $\overline{24}$ 40) sapphire back-reflection was used for this energy. The thickness of the utilized sapphire crystal was 1 mm. For this reflection the energy slope $\Delta E/\Delta T = -0.16$ meV/mK and the temperature for the Bragg energy is 237 K. The lifetime of the ^{121}Sb resonance, 5 ns, is rather small. Therefore, the time window for counting should be opened very early after the excitation pulse. The side bunches in the PETRA ring did not allow one to start counting earlier than 9 ns. Thus, the NRS signal has been collected with 9 ns starting time after the excitation pulse. The resonance of ^{121}Sb has been excited and the instrumental function of the sapphire backscattering monochromator was measured using NFS. At the best spot of the crystal, the acquired instrumental function has a full width at half-maximum of 3.2(4) meV. The rocking curve and fitted Lorentzian function are shown in fig. 4.24. For this particular energy and reflection the energy bandwidth of the monochromator is about factor of 5 higher than the 0.61 meV energy bandwidth predicted by theory. This deviation is much larger than the deviation by a factor of 2 observed at 23.88 keV photon energy in this work. This deviation can be explained by the larger penetration depth of the 37.13 keV x-rays and slightly different orientation of the sapphire crystal. Indeed, the extinction length for 37.13 keV is 845 μm and for 23.88 keV x-rays it is 273 μm and therefore more defects in the crystal are probed by 37.13 keV photons than it is for 23.88 keV photons. Moreover, the atom density in the $\langle 8\ 16\ \overline{24}\ 40 \rangle$ direction in sapphire is higher than that in the $\langle 4\ 4\ \overline{8}\ 45 \rangle$ direction due to higher atomic density in the former direction. Thus, the probability of a defect to appear in the $\langle 8\ 16\ \overline{24}\ 40 \rangle$ direction is higher than that for the $\langle 4\ 4\ \overline{8}\ 45 \rangle$ direction. The flux after the monochromator was measured as $8.1 \cdot 10^7$ ph/s, which corresponds to the reflectivity of 18.6%, or $1.4 \cdot 10^3$ photons per natural linewidth of the ^{121}Sb resonance.

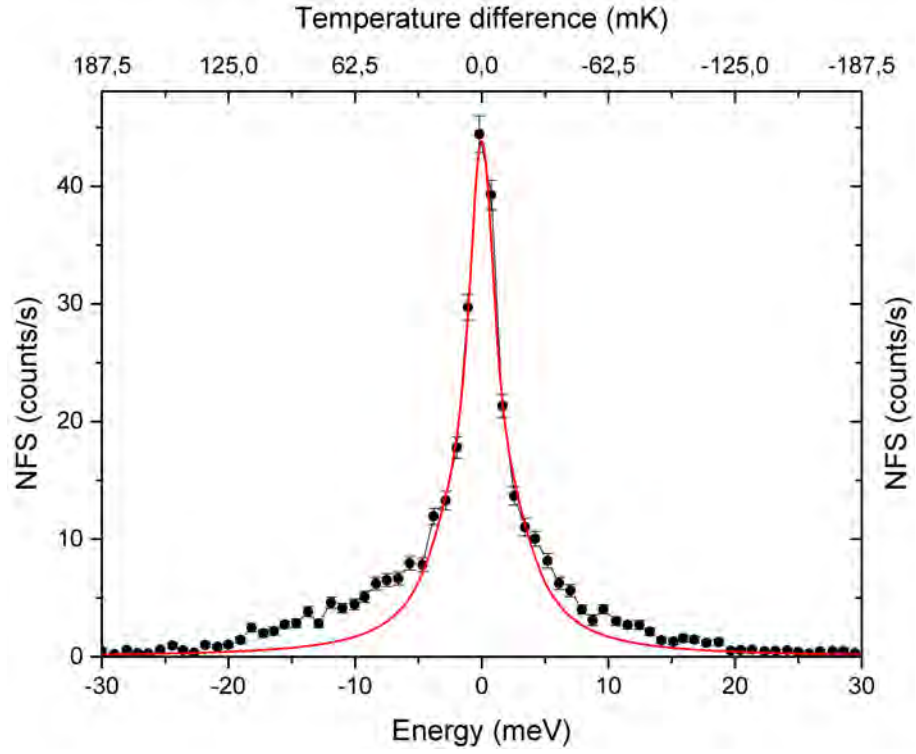


Figure 4.24: Instrumental function of a 5 mm thick sapphire crystal measured around the ^{121}Sb resonance energy of 37.1292(5) keV (resonance energy is set to 0). Red line: fit by the pseudo-Voigt function with FWHM 3.2(4) meV. The binning is 1 meV/point.

Feasibility study: NFS on Sb_2O_3

The first feasibility studies of the backscattering monochromator at the ^{121}Sb resonance have been done before the cleaning procedure for the PETRA ring has been established (see chapter 4.4). In these studies, late starting times for counting with respect to the synchrotron bunch resulted in a low countrate, however, the acquisition of NFS spectra on ^{121}Sb was possible (fig. 4.25). Since the cubic Sb_2O_3 is frequently used as a reference in NFS experiments on ^{121}Sb , most informations are known about the sample [114] and the NFS spectrum can be fitted to the experimental data.

The software package CONUSS [77] has been used to calculate and fit the NFS to the experimental data, see fig. 4.25. The obtained quadrupole splitting of $16.4(3)\Gamma$ (Γ is the natural linewidth of 37.13 keV resonance in ^{121}Sb) resembles the literature value of $16.7(4)\Gamma$ [114]. However, it is slightly smaller than the value of $17.9(4)\Gamma$ given by earlier MS studies in Ref. [131] and the value of 17.4Γ given in the review [132]; both references, [131] and [132], provide values for cubic modification of Sb_2O_3 . It was shown in Ref. [133] that the quadrupole splitting for Sb^{V} in cervantite is $15.6(4)\Gamma$, which is lower than the quadrupole splitting of $17.4(4)\Gamma$ for Sb^{III} in cubic Sb_2O_3 reported in the same Ref. [133]. In order to examine this effect on NFS data, a model with two non-equal sites should be applied. However, the low statistics of the data does not allow an appropriate fit.

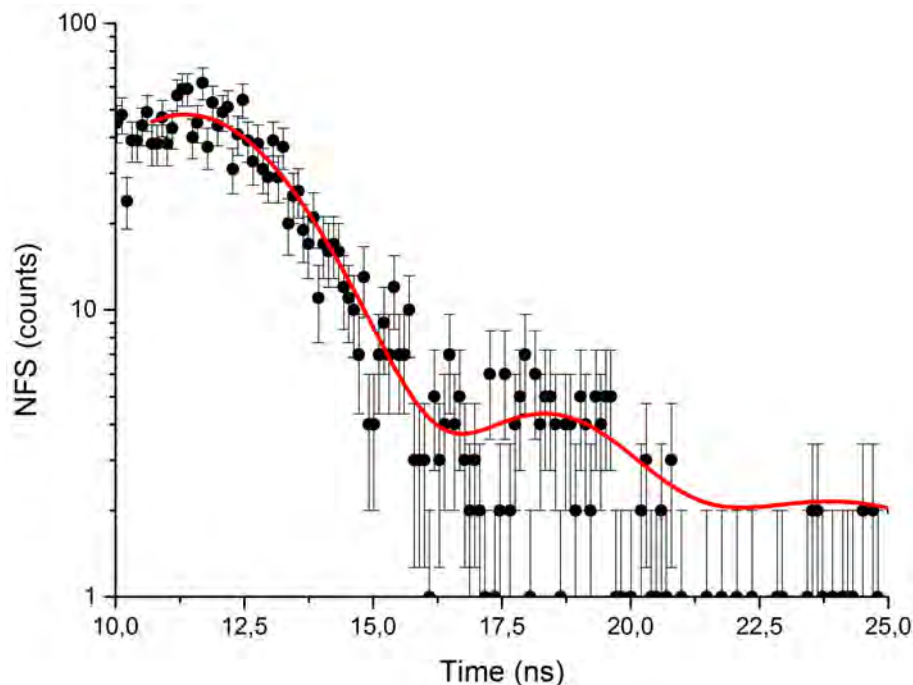


Figure 4.25: NFS spectrum measured on Sb_2O_3 powder with ^{121}Sb resonance. Red line: NFS spectrum calculated by the software CONUSS.

5 Nuclear Forward Scattering at the ^{193}Ir resonance

5.1 Iridium and the 73 keV Mössbauer resonance in ^{193}Ir

The element iridium is a $5d$ transition metal with seven $5d$ -, two $6s$ - valence electrons and a $[\text{Xe}] 4f^{14}$ configuration of the core electron shell. Under normal conditions Ir crystallizes in a face-centered cubic lattice with the space group $Fm\bar{3}m$ (number 225 [134]).

Iridium gained significant interest in recent years as a component of the transition metal oxide compounds (TMO). The puzzle of magnetic and electric interactions in these compounds became highly interesting due to the observation of high-temperature superconductivity in cuprate perovskite compounds. Many novel electronic states have been proposed for these compounds, especially antiferromagnetic and Mott-insulator states. Recent theoretical studies have shown that superconductivity could also be possible in other TMO compounds, e.g. in Ruddlesden-Popper (RP) phases of the $\text{Sr}_{n+1}\text{Ir}_n\text{O}_{3n+1}$ iridates (with n being the number of layers of SrIrO_3 separated by layers of SrO) [7, 11]. The structure of these compounds is the same as that of the cuprates and their low-energy excitations can also be modeled by Hubbard-type interactions [7]. However, in contrast to the cuprates, a two orders of magnitude larger spin-orbit interaction (SOC) is present in the iridate compounds which might impact the conditions for superconductivity. A novel $j_{eff} = 1/2$ state was proposed theoretically and observed experimentally [13, 37]. The large SOC and observed locking of the magnetic moment to the rotation of the IrO_6 octahedra [36] might lead to interesting phenomena like Dzyaloshinsky-Moriya interaction [36] and gaps in the spin-wave spectrum. There is therefore a high scientific interest in these compounds as they provide a possibility to study correlations of electrons in the presence of strong spin-orbit coupling and establish modeling techniques for these phenomena.

Elemental iridium itself is one of the least investigated metals in terms of lattice dynamics. The lack of data stands in contrast to the large number of first principle calculations. Inelastic Neutron Scattering (INS), the most common method of phonon dispersion studies, is technically difficult to carry out due to the high Ir absorption cross-section for neutrons. This cross-section is 425 barn [39] while elements typically studied with INS have cross-sections in the 0.01-10 barn range. Despite of the experimental challenges, iridium is an interesting model system for studies of thermal properties and lattice dynamics. It

can withstand temperatures as high as 2000°C , together with osmium and tungsten being one of the most temperature resistant metals. It is extremely resistive to acids, bases and oxygen, having one of the highest resistivity to these media. Iridium is one of the least abundant elements in the earth crust, though its concentrations are the highest in several geological structures like impact craters and igneous deposits formed by intrusions from the lower Earth mantle. Studies of structure and dynamics in these formations have high scientific impact. Technological applications of iridium are very important, for instance, doping construction alloys used in the high-demanding applications like aircraft and spacecraft with iridium does significantly increase hardness and temperature or chemical resistivity of the materials.

Conventional MS was already employed for studies of hyperfine interactions and lattice dynamics of Ir compounds. Therefore, the information on Mössbauer transitions in Ir is available [57, 58] and should be reviewed in detail. The naturally occurring Mössbauer isotopes of Iridium are ^{191}Ir and ^{193}Ir . The isotopes have Mössbauer transitions at 82 and 129 keV, and at 73 and 139 keV, respectively. Although the Mössbauer effect was discovered with the 129 keV resonance of ^{191}Ir [62, 63], 129 keV as well as 139 keV transitions are not of practical importance due to the high energy and low Lamb-Mössbauer factors. Sources for MS on Ir cannot be easily prepared. The excited states of ^{191}Ir can be produced by the β^- decay of ^{191}Os or by electron capture from ^{191}Pt , with a lifetime of 22 days and 4 days, respectively. ^{191}Os is produced by neutron activation of Os in the reaction $^{190}\text{Os}(n,\gamma)^{191}\text{Os}$. The production of the ^{191}Ir isotope via ^{191}Pt is carried out by irradiation of Ir with protons or deuterons, $^{191}\text{Ir}(p,n)^{191}\text{Pt}$ or $^{191}\text{Ir}(d,2n)^{191}\text{Pt}$. The β^- decay of ^{191}Os exhibits a less complicated emission spectrum, however, the 82 keV level in ^{191}Ir is weakly populated in this decay and thus challenging for studies with MS. Moreover, the preparation of sources for MS with ^{191}Ir is complicated due to the low abundances of ^{191}Ir and ^{191}Os . Therefore, in most Ir Mössbauer spectroscopy studies, the ^{193}Ir isotope has been used. The source can be produced by neutron activation of Os, $^{192}\text{Os}(n,\gamma)^{193}\text{Os}$, using $> 95\%$ enrichment in ^{192}Os . The source has a relative small lifetime of 45 hours but recoilless emission is relative intense due to the high Debye temperature of Os. The source is not a perfect single-line source because Os has a hexagonal crystal cell and the source produces an unresolved quadrupole doublet with a line separation of 0.48 mm/s corresponding to $\approx 1.6\text{ }\Gamma$. Several studies suggested the use of alloys with Os with Pt or Nb which have cubic lattice and emit almost a single line [57]. However, the preparation of sources is deteriorated by high-temperature melting of highly activated ^{193}Os . Obviously, the source preparation for conventional MS on Ir is complicated while NRS does not require any radioactive source.

As mentioned above, the 129 keV transition in ^{191}Ir was not used after the discovery of the Mössbauer effect due to the high energy and low recoilless probability for this transition. For NRS studies this isotope is not accessible so far because the brilliance of

photons with energies higher than 100 keV is still low even at modern photon sources. For the same reasons, the 139 keV transition in ^{193}Ir is currently not interesting for MS and NRS studies.

The transitions with energies of 73 keV and 82 keV are of particular interest for MS and NRS studies: their properties should be reviewed in detail. Table 5.1 shows the comparison of the main parameters of these two Mössbauer transitions.

Parameter	^{191}Ir	^{193}Ir
Natural abundance, [%]	37.3	62.7
Spin of the excited state	+1/2	+1/2
Spin of the ground state	+3/2	+3/2
E_γ , [keV]	82	73*
Lifetime, [ns]	4.1	8.4
Γ , [neV]	110	75
f_{LM} for Ir at 4 K	0.46	0.37*
Recoil energy E_R , [meV]	19.1	14.8
Internal conversion coefficient	10.9	6.8
Nuclear resonance cross section σ_0 , 10^{-20} [cm ²]	1.35	3.06
Electronic absorption length in Ir at resonance energy E_γ , [μm]	55	175

Table 5.1: Properties of the Mössbauer transitions in Iridium. The parameters are given for transitions with $E_\gamma < 100$ keV. The advantages of the 73 keV transition in ^{193}Ir are shown in bold. Compiled from Refs. [2, 57, 124].

* The values are corrected in this work

Comparing the properties of the two transitions, the most interesting and practical for NRS on iridium is the resonance in ^{193}Ir at 73 keV. The ^{193}Ir isotope has a high natural abundance of 62.7% and therefore no isotopic enrichment is necessary. The 73 keV transition has also slightly lower energy and longer lifetime. The longer lifetime of the corresponding excited state is beneficial for NFS. Furthermore, the 73 keV transition has a higher resonance cross section which again results in higher count-rates in NFS. The energy of the transition is high: while electronic scattering techniques usually involve low-energy photons which do not permit the use of complex sample environments such as high-field magnets and pressure cells, NRS does not have this limitation due to the

very large absorption lengths for 73 keV photons.

Finally, it is worth to mention that the K-edge of electronic absorption of Ir is at 76.111 keV [135] which is slightly higher than the nuclear transition at 73 keV. Thus, the conversion coefficient is lower than that for 82 keV, resulting in slightly higher intensity of NFS. The proximity of the nuclear resonance energy to the energy of the K-edge provides a remarkable feature of high electronic absorption length at the nuclear resonance energy (see table 5.1). This is of benefit for achieving high NFS countrates with thick samples. Moreover, the proximity of the K-edge to the nuclear resonance results in a technical advantage: the energy of the nuclear resonance can be determined with higher accuracy by calibration with electronic absorption in Ir. Indeed, for such a small difference in energies, the non-linearity in movement of the Bragg angle is negligible: the measured movement of the Bragg angle is equal to the set movement with a high accuracy. The error in the energy of the nuclear resonance will be given mainly by the error in the energy of the K- absorption edge.

5.2 Lattice dynamics in Ir studied with NFS

The first observation of nuclear resonance scattering by ^{193}Ir described in Chapter 4.5 encouraged a simple first application of NFS. It was decided to measure NFS on Ir due to the following reasons. First, elemental Ir is one of the least-studied materials in terms of lattice dynamics: only few reports about density of phonon states and diffraction data exist in the literature. The NFS spectra measured at different temperatures reveal the temperature dependence of the Lamb-Mössbauer factor, the atomic displacement, and the Debye temperature, and thus measuring NFS widens the knowledge about lattice dynamics [54, 52]. Second, the evaluation of NFS spectra on Ir is simplified because Ir exhibits no macroscopic magnetic order in the 10-300 K temperature range under scope. Moreover, Ir atoms in fcc-Ir show a coordination with cubic symmetry [136]. Therefore, the hyperfine interactions in fcc-Ir can be neglected [58, 57]. Comparing the optimal thickness values from table 3.1 in the theory part, the thicknesses of the sample foils were chosen as 100 μm and 200 μm .

The measured NFS time spectra are shown in the fig. 5.1a and 5.1b by black symbols. The background contribution is determined from the time spectrum acquired at a photon energy 6.5 eV below the resonance energy. The background countrate is 0.2 Hz. The background time spectrum is scaled by the acquisition time of the NFS spectrum and subtracted from it.

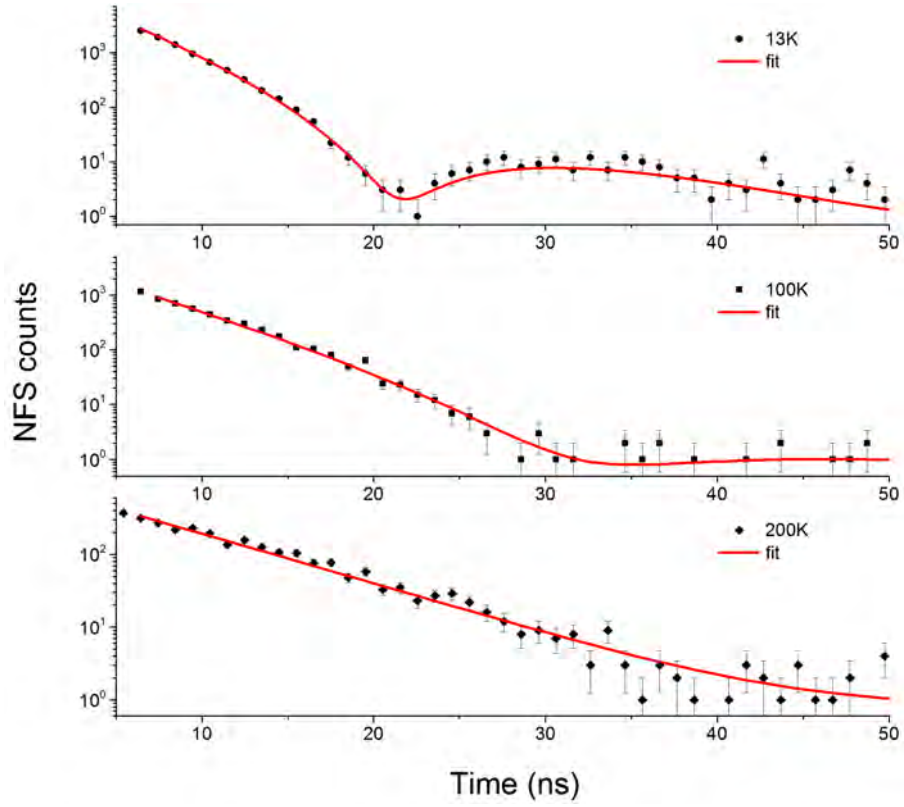
The NFS beating patterns can be described by the dynamical theory of NRS ([2] and chapter 3.4). The fits to the NFS spectra are shown in the fig. 5.1a, 5.1b by the red lines and the measured spectra are shown by the black dots. In the fig. 5.1b the green dashed line shows the time dependence of the natural decay of the excited state of ^{193}Ir . The speed-up of the intensity in the measured NFS spectra due to the finite thickness of the Ir foils is clearly visible even at room temperature.

The Lamb-Mössbauer factor derived from the effective thickness is shown in fig. 5.2 by the black symbols for four temperature points. The temperature dependence of the Lamb-Mössbauer factor can be approximated by equation (3.24) with the Debye temperature $\theta_{Deb} = 309(30)$ K (fig. 5.2, solid line).

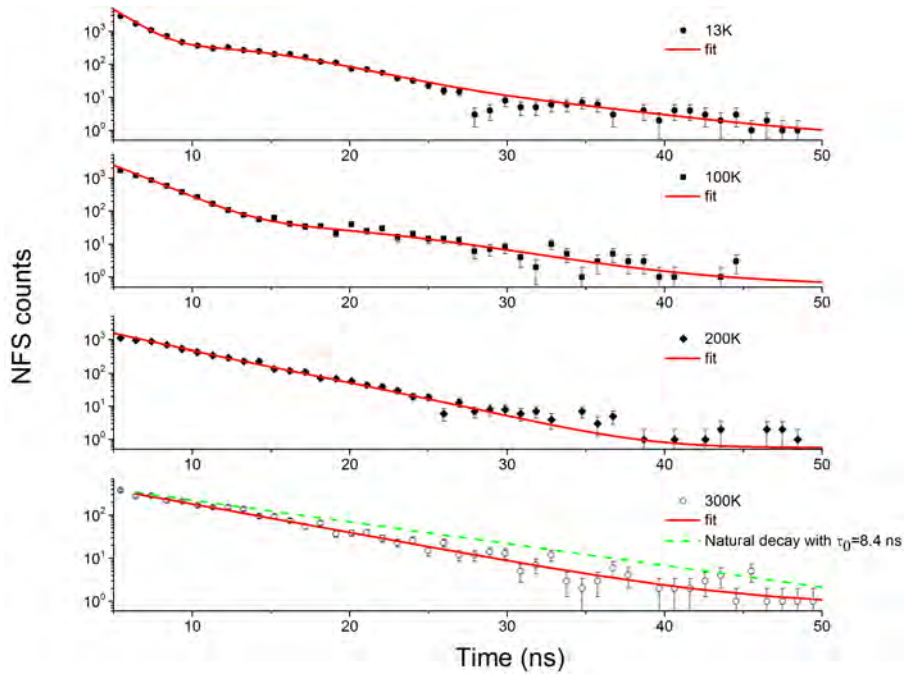
Besides Mössbauer spectroscopy, the main experimental method used to obtain Debye temperature θ_{Deb} is the measurement of the specific heat capacity. However, this method weights all lattice vibrations as well as heat capacity originating from electrons. In contrast, the Lamb-Mössbauer factor is determined mainly by phonons with low excitation energy. Therefore, the Debye temperature value obtained by heat capacity measurements is higher than that measured by microscopic NRS and MS techniques. Comparing the microscopic measurement techniques, the of values of θ_{Deb} obtained with neutron scattering

and Mössbauer effect should be in a good agreement, whereas the x-ray scattering will give lower values of θ_{Deb} [52].

There are different values of the Debye temperature for iridium reported in the literature (table 5.3). Calculations give values of θ_{Deb} as 266 K [137], 282 K [138], whereas measurements of specific heat capacity give different values from 260 to 350 K and to 430 K with an extrapolation to 0 K temperature [68]. Interestingly, Low-Energy-Electron Diffraction measurements on single crystals of Ir show the possibility to image the contributions of longitudinal and transversal vibration modes to θ_{Deb} [139]. In that study the values of θ_{Deb} have been reported as 245-285 K, depending on the orientation of the crystal. The Debye temperature value obtained in this work from the temperature dependence of the Lamb-Mössbauer factor (fig. 5.2) is in agreement with the literature values given above, and in a remarkable agreement with the value of 316 K received in measurements of electrical resistivity at low temperatures reported in Ref. [138].



(a)



(b)

Figure 5.1: Experimental NFS time spectra (points) and fits to them (lines, only effective thickness and its Gaussian distribution are fitted) for: (a) 100 μm Ir foil, (b) 200 μm Ir foil.

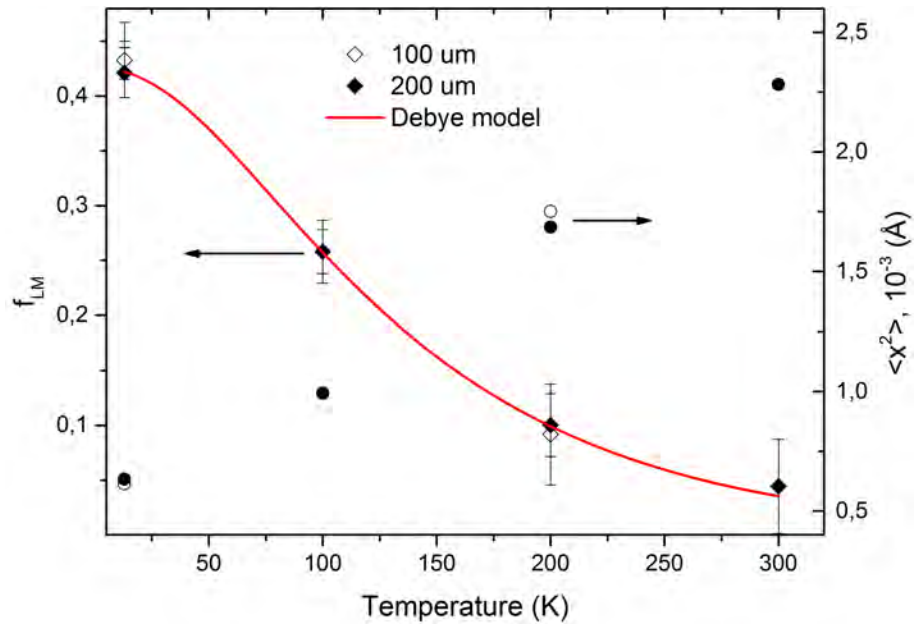


Figure 5.2: Temperature dependence of the Lamb-Mössbauer factor and the mean atomic displacement parameter in Ir. The red line shows the fit with the Debye model with a Debye temperature of 309(30) K. Empty symbols correspond to the data acquired on the 100 μm thick sample and filled symbols correspond to the data measured on the 200 μm thick sample.

Since NFS probes the displacement of the nucleus and its close surrounding, the result presents more the adiabatic part of lattice dynamics. At this point, the obtained values of f_{LM} and θ_{Deb} should be compared with literature values measured by different methods which probe different time scales of lattice vibrations. In this work inelastic neutron scattering and x-ray diffraction experiments are carried out in order to verify literature data and obtain the lacking information on the phonon density of states and atomic displacement parameter.

The measurements of lattice dynamics by neutron scattering on Ir is challenging due to the high absorption of neutrons by ^{193}Ir nuclei. However, several experimental and theoretical studies of the DPS do exist in literature [140, 141, 142, 143]. The results of previous studies can be divided into two categories:

- set of studies showing maximum phonon energies of 33-37 meV and a square root (Debye) behavior up to 15-20 meV [140, 141]
- another set of studies showing phonon maximum phonon energies at 24-27 meV and a square root (Debye) behavior up to 12-16 meV [142, 143]

The INS experiment was carried out with the wide angular-range chopper spectrometer (ARCS) at the Oak Ridge National Laboratory neutron spallation source [144]. The energy of incident neutrons was fixed to 45 meV and the energy resolution of the spectrometer was 1.4 meV (FWHM).

The DPS derived from the INS scattering function is shown in fig. 5.3. A quantitative comparison of the DPS measured in this work and the one reported in literature shows that the DPS measured in this work does resemble the theoretical calculations from the Ref. [143]. The maximum phonon frequency and energy are 6 THz and 25 meV, respectively. This value is in a very good agreement with the values 5.8-6.5 THz (24-27 meV) obtained by *ab initio* calculations in the works [142, 143]. The mode with energy 23 meV reported in Ref. [143] does resemble the mode at 23 meV measured in this work. The softer mode observed in this work at 17.5 meV is slightly shifted to higher energies and broadened compared to the calculated one. The shift to higher energies implies a higher force constant. It is worth to mention that the 17.5 and 23 meV modes in the DPS obtained in this work have lower intensity than those given by Ref. [143]. Softer modes in the 0-12 meV range observed in this work are more pronounced than those given by calculation.

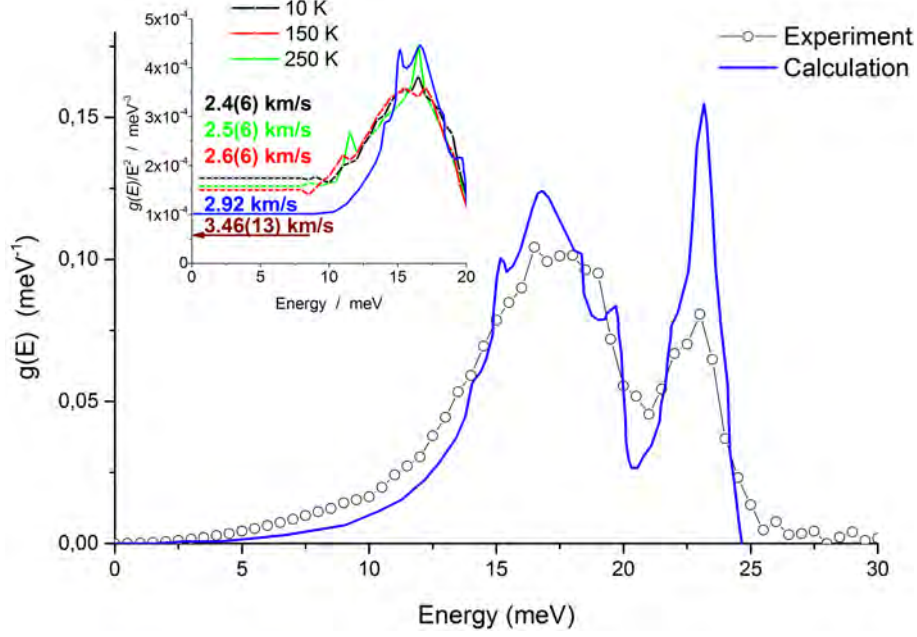


Figure 5.3: Density of phonon states in Ir: measured by inelastic neutron scattering (black dots) and calculated in Ref. [143] (blue line). The inset shows the reduced DPS indicating the Debye levels and corresponding Debye sound velocities as reported in Ref.[145] (brown arrow), derived from the DPS reported in Ref. [143], and derived from the DPS measured in this work for Ir at 10 K (black), 150 K (red), and at 250 K (green).

Several thermodynamic properties can be derived from the DPS measured by INS. Notably, the DPS measured at the temperatures 10, 150, and 250 K do not differ significantly. Thus, in the following the values are given for the measurements at 150 K and the value in brackets shows the deviation of the values measured at 10 and 250 K from that measured at 150 K. The internal energy per atom U determined by equation (3.58) is 26.2 meV. The specific heat per atom C_V is determined to 0.65 $\mu\text{eV/K}$. The entropy per atom is obtained as 0.22 $\mu\text{eV/K}$. The mean force constant is obtained as 236 N/m, slightly lower than force constant of 254.78 N/m reported by *ab initio* calculations for the direction along $[0\ 0\ 1]$ [143]. This can be seen in the fig. 5.3: the softer modes are more intense in the experimental spectrum. Data extracted from INS measurements are summarized in table 5.2.

Parameter	Value
Internal energy per atom, [meV/at]	26.2(1)
Specific heat per atom, [$\mu eV/K/at$]	0.65(9)
Entropy per atom, [$\mu eV/K/at$]	0.22(2)
Mean force constant, [N/m]	236(30)
Bulk modulus*, [GPa]	363(10)
Shear modulus*, [GPa]	224(10)
Speed of sound**:	
Transversal, [km/s]	3.15(13)
Longitudinal, [km/s]	5.35(18)
Debye, [km/s]	3.46(13)

Table 5.2: Lattice dynamics properties of Ir studied by INS.

* Determined from the puls-echo and high pressure XRD studies (s. text)

** Determined from the bulk and shear moduli (s. text)

The speed of sound obtained from the Debye level of the DPS measured in this work at 10 K is 2.4(6) km/s. This value is lower than the value of 4.8 km/s obtained by calculations in Ref. [146], and the discrepancy reasons should be discussed in detail. The speed of sound is the parameter which characterizes the propagation of elastic waves in a material. It is thus determined by the response of the material to elastic deformation. The response is generally described by bulk and shear moduli K and G which give the response to isotropic and shear stress, respectively. There is therefore the speed of sound for the wave with polarization perpendicular to the wave propagation, transversal speed of sound, and the speed of sound for the wave with polarization along to the wave propagation, longitudinal speed of sound. These parameters are determined by equations:

$$v_{trans} = \sqrt{\frac{G}{\rho}} \quad (5.1)$$

and

$$v_{long} = \sqrt{\frac{K + \frac{4}{3}G}{\rho}}, \quad (5.2)$$

respectively, with ρ - density of the material

There are several techniques which can be used for the determination of the elastic response. The most popular methods are the pulse-echo method, measurements of hydrostatic lattice compressibility by XRD, and density of phonon states measurements at low energy transfer by IXS, NIS and INS. The pulse-echo method probes the time delay of the elastic wave propagation and measures directly bulk and shear moduli. The speeds of sound are defined by equations (5.1) and (5.2).

The second technique, the measurements of hydrostatic lattice compressibility by XRD, provides information about bulk modulus which can be compared to the results obtained by pulse-echo. From the measurements of density of phonon states the speed of sound can be determined from the Debye level which was defined by eq. (3.61) in the Chapter 3.4.2. In order to compare the results obtained by the pulse-echo method and XRD compression experiment with that obtained by IXS, NIS and INS, the Debye speed of sound can be written in terms of the transversal and longitudinal speed of sound:

$$v_{Deb} = \left(1/3 \cdot \left(\frac{1}{v_{long}^3} + \frac{2}{v_{trans}^3} \right) \right)^{-1/3} \quad (5.3)$$

The results of a pulse-echo experiment on Ir are reported in Ref. [145]. From the data given in work [145] a bulk modulus of 363 GPa and a shear modulus of 224 GPa can be derived¹⁰. The bulk modulus obtained by the pulse-echo technique is in a good agreement with the value of 347(44) GPa obtained in the XRD study of the compressibility reported in the Ref. [147]. Using the value of bulk and shear moduli obtained by the pulse-echo technique the transversal and longitudinal speeds of sound are determined to 3.15(13) km/s and 5.35(18) km/s, respectively. The Debye speed of sound derived from these values by equation (5.3) is $v_{Deb}=3.46(13)$ km/s.

A Debye level of $\lim_{E \rightarrow 0} \frac{g(E)}{E^2} = 1.7(12) \cdot 10^{-4} \text{ meV}^{-3}$ is obtained by INS in this work. Using the equation (3.61) the Debye speed of sound is determined to 24_{-4}^{+6} km/s which is smaller in average than 3.5(1) km/s which corresponds to a Debye level of $0.59 \cdot 10^{-4} \text{ meV}^{-3}$. In fact, the speed of sound determined by INS is strongly affected by the large contribution of elastic scattering at small energy transfer. The problem is well known for evaluation of data obtained by inelastic scattering techniques and a detailed description is given in Ref. [148]. A possible solution of the problem is the reduction of the tails in instrumental function of the INS spectrometer which can be achieved by an improvement of the optics for the incident neutrons.

Interestingly, the density of phonon states in fcc-Ir is similar to that in fcc- γ -Fe (fig. 5.4).

¹⁰Unfortunately, the errors for the elastic constants are not reported in Ref. [145]

Indeed, a good agreement between the DPS of Ir and that of γ -Fe can be achieved by compression of the energy scale of the DPS for γ -Fe by 0.7. The factor 0.7 can be explained by three contributions: first the relation between lattice parameters of iron, $a(\gamma\text{-Fe})$, and iridium, $a(\text{Ir})$ should be considered. Second, the relation between the atomic masses of iron, $M(\text{Fe})$, and iridium, $M(\text{Ir})$, should be taken into account.

$$\frac{E(\text{Fe})}{E(\text{Ir})} = 0.7 = \frac{a(\gamma\text{-Fe})}{a(\text{Ir})} \cdot \left(\frac{M(\text{Fe})}{M(\text{Ir})} \right)^{\frac{1}{2}} \cdot 2.2 \quad (5.4)$$

Third, the coefficient 2.2 might be related to the Grüneisen parameters of iridium (2.35, as reported in Ref. [149]) and iron (2.3, as calculated in Ref. [150]).

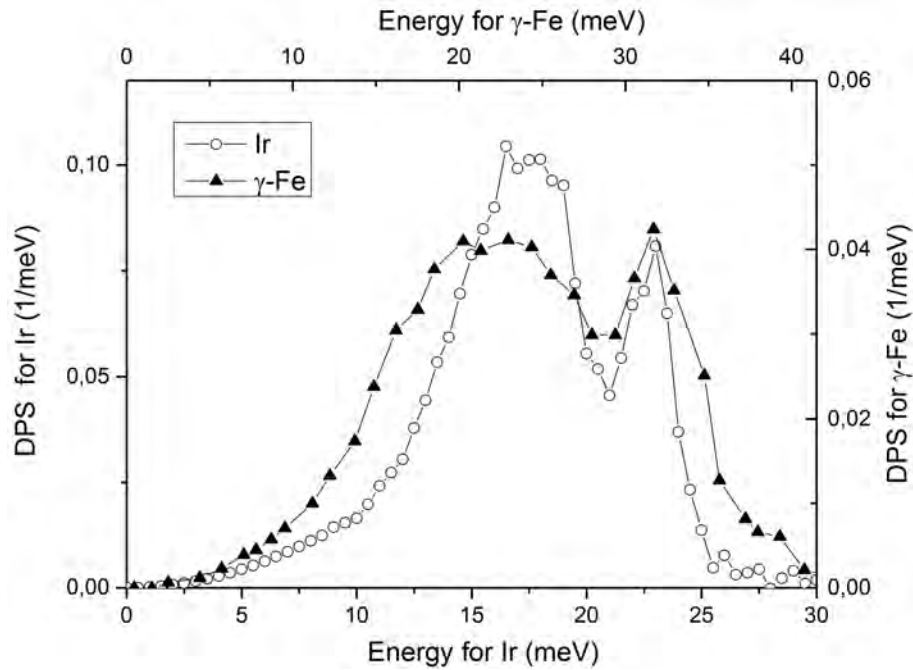


Figure 5.4: Comparison of DPS in two fcc metals: DPS measured on Ir in this work and DPS obtained for γ -Fe in the work [151].

Further insight into the lattice dynamics is given by the atomic displacement parameter measured by XRD. In this work the room-temperature XRD on Ir was carried out at the P02.1 diffraction beamline of PETRA III [152]. The purity of Ir powder sample was 99.95 %. The wavelength at the beamline was fixed to 0.20715(1) nm and the geometry of the experiment including distance between sample and detector, inclination of detector to the beam was determined with a LaB_6 powder diffraction standard¹¹. The obtained XRD pattern was integrated using the software Fit2D [153] and analyzed by the Rietveld method [154] using the software JANA2006 [155]. The lattice parameter of Ir of 3.8399(22) Å obtained in this work resembles the value of 3.8394 Å¹² given by early NIST report [136] and in a good agreement with the value of 3.8392(6) Å reported in the recent comprehensive review on the crystallographic properties of Ir, Ref. [156]. The isotropic atomic displacement parameter U_{iso} is derived from the measured data and shown in the table 5.3. It should be noted that the atomic displacement obtained from XRD is affected by site occupation or disorder, while NFS probes one-particle displacements.

A summary of XRD, neutron scattering, and NFS measurements is given in the table 5.3. The values obtained from the DPS reported in the Ref. [143] and Debye temperature θ_{Deb} obtained from heat capacity measurements are also presented. The fig. 5.3 and the comparison table 5.3 show very good agreement between the data obtained by NFS, INS and *ab initio* calculations.

¹¹ LaB_6 exhibits a high Debye-Waller factor and well-defined room-temperature XRD pattern. Therefore, it is widely used as standard reference for calibration of distances in XRD experiments.

¹²Unfortunately, Ref. [136] does not provide the error for this value.

Method	θ_{Deb} [K]	U_{iso} or $\langle x^2 \rangle$ $10^{-4} [\text{\AA}^2]$	f_{LM}
Heat capacity [68]	350-400(20) at 10-20 K	4.8-5.5 at 10-20 K**	0.47-0.52 at 10-20 K*
XRD	200(40)**	38(9)	
Neutron scattering	Debye behavior up to 10 meV	6.9(26)**	0.39(16)#
NFS	309(30)*** MS: 335(9) [69]	6.2(12) at 13 K**	0.43(8) at 13 K MS: 0.37 at 4 K [57]
<i>ab initio</i> calculations [143]	Debye behavior up to 10 meV	6.4**	0.42#

Table 5.3: Lattice dynamics properties of Ir studied by different methods.

* calculated from θ_{Deb} assuming Debye model (3.24) ** derived from f_{LM} assuming classical approximation (3.20) *** calculated from f_{LM} assuming Debye model (3.24) # derived from DPS using (3.27)

6 Hyperfine interactions in iridium compounds

6.1 Electric hyperfine interactions in IrO_2 and in SrIrO_3

The successful NFS experiments on elemental Ir provided the perspectives for studies of more complex systems like Ir oxide compounds. Looking for a simple test sample for NFS, iridium (IV) oxide can be considered. IrO_2 shows strong spin-orbit coupling and a small gap in the spin-wave dispersion, resulting in the easy conversion of charge current into a spin current and vice versa [9], the phenomena called direct and inverse spin Hall effect [157]. The charge or spin current can be induced by thermal activation: in this case it is called spin Seebeck effect [158]. It was demonstrated that both effects are significant in IrO_2 , and which is more important, the resistivity of IrO_2 is higher than that in Pd, V, Au, Pt metals, which also demonstrate high spin Hall and Seebeck effects and typically are used for detection of spin currents [158, 9]. Strong spin-orbit coupling and unusual transport effects inspire studies of microscopic electronic and magnetic properties of IrO_2 .

Bulk IrO_2 shows paramagnetic behavior and metallic type of electric conductivity in the 10-300 K range, according to recent studies of macroscopic magnetism and charge transport in this compound [159]. The oxide has a tetragonal crystal lattice of rutile type and 3-fold symmetry of the coordination polyhedron of Ir [160]. The coordination of Ir is not cubic, but shows a significant tetragonal distortion [160], see inset in fig. 6.1. Thus, an axially symmetric quadrupole interaction is expected in this compound [54]. To the best of our knowledge, no microscopic magnetism was reported by XRMS, RIXS, XMCD, or neutron scattering techniques. IrO_2 is a good reference sample for the first NFS measurements on Ir oxides, since the data might be interpreted by the simple model of electric hyperfine interactions.

The experimental setup was the same as shown in the fig. 4.15 in the Chapter 4.5. We cooled down the standard powdered IrO_2 ¹³ to 16 K using the standard Helium closed cycle cryostat. The sample was accurately attached to a massive sample holder and thermally stabilized by several insulation layers. The PETRA ring was operated in the 40-bunch mode (192 ns spacing between bunches) and the ring current was 100 mA. The NFS time spectra have been acquired with a 15-element APD detector (see Chapter 4.3).

¹³the sample was obtained from Sigma Aldrich Corporation, the purity is reported to be 99.9% wt.

An external magnetic field of 0.53(5) T was applied to the sample (zero-field cooling) in order to examine possible magnetism on the Ir nucleus.

The time spectra are shown in the fig. 6.1 by black markers. Sufficient number of counts was collected in 3 hours in both experiments, without (upper panel of the fig. 6.1) and with applied external field (lower panel in the fig. 6.1).

The obtained data were interpreted by a model with only two fit parameters: the quadrupole splitting $\Delta E_Q = \frac{eQV_{zz}}{2}$ and the effective thickness $T_{eff} = \sigma_N f_{LM} N_R d$ (σ_N is the cross-section of nuclear resonance scattering, f_{LM} is the Lamb-Mössbauer factor, N_R is the number of resonant nuclei and d is the sample thickness). The fitting of the model to experimental data was performed with CONUSS software [77] specially improved for the calculations of hyperfine interactions in the presence of M1+E2 radiation mixture in ^{193}Ir using formalism given in Ref. [76] (Chapter 3.4). The fits to the measured time spectra (red lines in fig. 6.1) show very good agreement with the experimental data. A quadrupole splitting of 2.76(2) mm/s (8.96(7) Γ or 672(5) neV) was obtained. This value is in a very good agreement with the value of 2.71(6) mm/s (8.8(2) Γ or 660(15) neV) measured by conventional MS and reported in the Ref. [161] and slightly lower compared to 3.0(2) mm/s (9.7(7) Γ or 730(50) neV) given in the earlier publication [162]. Calculating the NFS spectra for several possible quadrupole interaction energy values, it was found that the beating period can be related to quadrupole interaction energy by a simple relation:

$$\Delta E_Q [\mu\text{eV}] \cdot T [\text{ns}] \approx 4.14. \quad (6.1)$$

We determined the Lamb-Mössbauer factor to be 0.32(4) at 16 K. The Debye temperature was estimated to be 230(30) K. No detectable effect is observed upon the application of the external magnetic field (lower panel in the fig. 6.1), and the time spectrum was interpreted by the same model. In other words, a possible magnetic hyperfine interaction in IrO_2 could be not larger than that which can be resolved by the NFS technique. The resolution of NFS is determined by the time-resolution of the APD detector and should be discussed briefly. The time resolution of the APDs used in this work is $\sim 0.4(1)$ ns. Analyzing the time spectra for parallel oriented electric and magnetic hyperfine fields on the Ir nucleus, one can notice that a change of the magnetic hyperfine field by 0.53 T leads to a shift of the beatings in NFS time spectrum for a magnetically ordered material. Particularly, the time spectrum shift by 0.04 ns which is an order of magnitude beyond the resolution of the detector. An improved acquisition system should be implemented for detection of such a small time shifts of beating patterns. Particularly, fast backend-electronics which digitizes signals from APD directly, without using CFD and gating technique, can be used. Such system built on a field-programmable electronics (FPGA)

was recently demonstrated in Ref. [163], and could be applied for NRS studies on Ir.

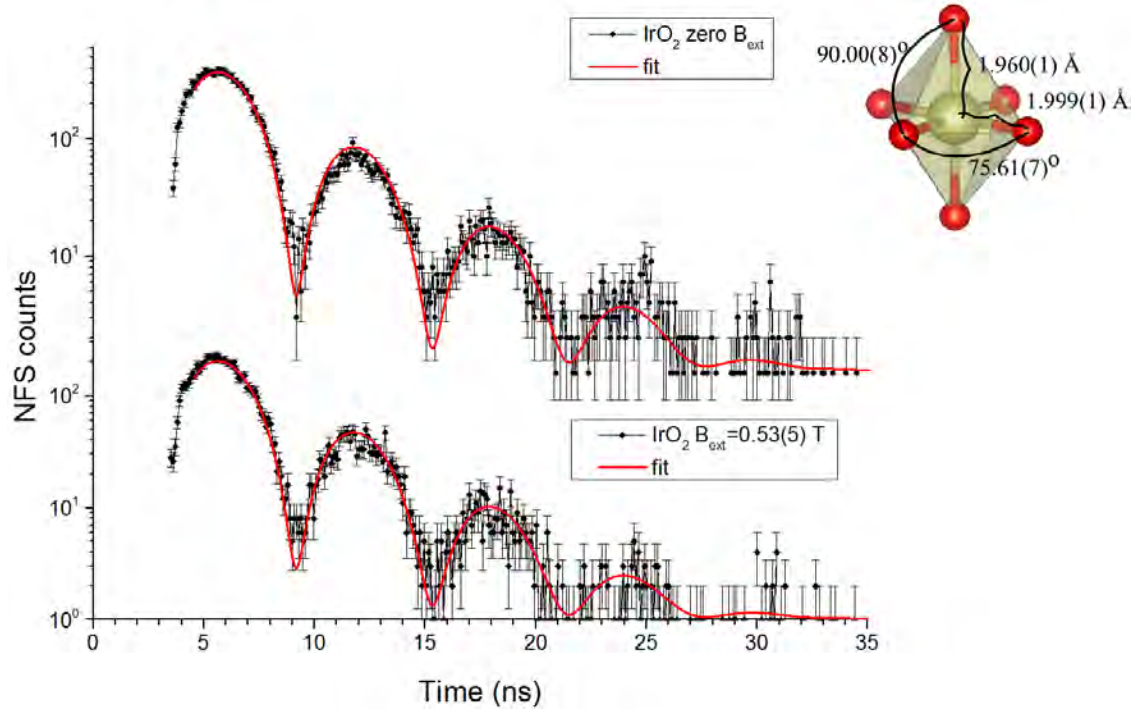


Figure 6.1: NFS time spectra acquired (black markers) on IrO_2 at 16 K without external magnetic (upper panel) and with 0.53(5) T field (lower panel, zero-field cooling). The fits to the time spectra are shown by red lines. The inset shows local coordination of Ir in IrO_2 as reported in Ref. [160].

The most intriguing object for NFS studies are the members of the Ruddlesden-Popper (RP) series of strontium iridates $\text{Sr}_{n+1}\text{Ir}_n\text{O}_{3n+1}$. The understanding of the physics in these compounds was recently improved by studies of RIXS [35, 32, 29], magnetic scattering of x-rays [11, 15] and neutrons [19, 17], as well as exploring the macroscopic properties like conductivity and magnetization of these materials [164, 10]. However, several puzzles like the origin of the magnetism and the impact of the d -orbitals configuration on the electronic structure remain unsolved [7, 10]. This work is the first attempt to determine microscopic magnetic and electric properties in iridates by means of NFS.

The parent compound of the RP series, SrIrO_3 is a good starting point for studies of NFS on strontium iridates. This compound shows paramagnetic behavior and significant trigonal distortion of the IrO_6 octahedra (see inset in fig. 6.2) [165]. Thus, one can expect a quadrupole splitting of the ^{193}Ir nuclear levels without hyperfine magnetic interaction.

We acquired NFS time spectra on powdered SrIrO_3 at 15 K and at 108 K. Using the CONUSS software [77], the NFS time spectra were fitted by a pure quadrupole interaction model. The result is shown in figure 6.2. The effective thickness of the sample was very small, $T_{eff} \approx 0.4$, and therefore the NFS beating pattern is solely determined by hyperfine interactions.

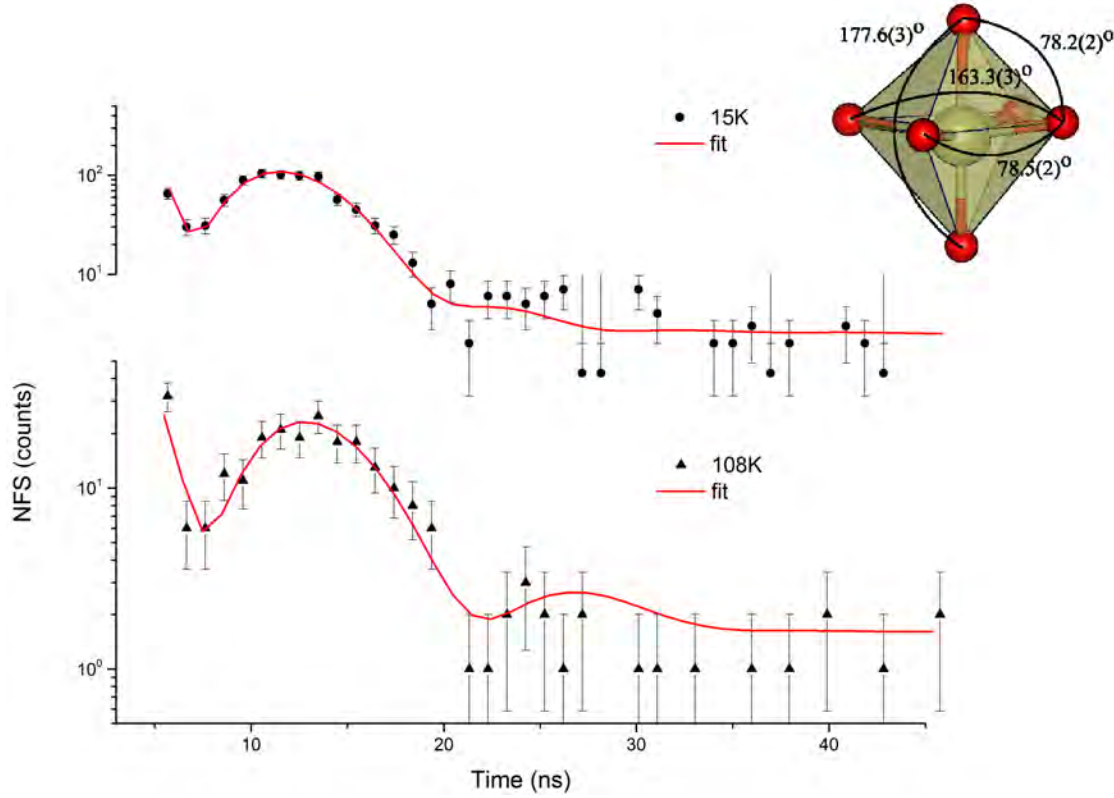


Figure 6.2: NFS time spectra acquired (black markers) on SrIrO_3 at 15 and 108 K. The fitted spectra are shown by red lines. The inset shows geometry of the IrO_6 polyhedron in this compound as reported in Ref. [166].

From the fit we obtained a quadrupole splitting of 1.24(5) mm/s ($4.0(2)\Gamma$ or 302(12) neV) at 15 K, in very good agreement with the value of 1.26 mm/s (4.1Γ or 307 neV) mentioned in the Ref. [167] (conventional MS). With an increase of temperature from 15 K to 108 K the oscillation frequency decreases (fig. 6.2) which is a fingerprint of a decreasing quadrupole splitting. The quadrupole splitting obtained from the fit is 1.08(5) mm/s ($3.5(2)\Gamma$ or 263(12) neV) for 108 K, smaller than at 15 K. To the best of our knowledge, no change of Ir coordination symmetry is reported for the temperature range under scope. Therefore, the change in quadrupole splitting is most likely related to a change in the population of the electronic levels at higher temperature. The effect is well known from MS on ^{57}Fe compounds ($3d$ electron systems) [54] and theoretically explained by Ingalls in Ref. [168].

6.2 Combined hyperfine interactions in Sr_2IrO_4

It is very interesting to explore magnetism in iridates since the correlation between magnetism, superconductivity and origin of magnetism in these compounds remains a puzzle [7]. A good model system can be the perovskite Sr_2IrO_4 which is well-studied with macroscopic techniques, like resistivity and magnetic susceptibility, and microscopic techniques utilizing x-ray scattering on electrons and neutron scattering [11, 16, 10]. This compound shows weak ferromagnetic behavior at temperatures below 240 K [16, 169, 170]; most intriguing is the pronounced anisotropy in magnetization along and perpendicular to the c-axis in this compound reported in Ref. [16, 169]. Recent studies of microscopic magnetism by RIXS [37, 171] revealed the canted antiferromagnetic order in IrO_6 layers and the net magnetic moments ordered antiparallel along the [001] direction below 240 K (see inset in fig. 6.3). The magnetic structure was confirmed by several XRMS and RIXS studies [11, 12], by μSR [172], combined EMR, IR and Raman [170] studies, and by measurements of microscopic magnetoresistance [173]. Studies of neutron diffraction [17, 19] confirm the magnetic structure proposed in Ref. [37] as well, though a neutron scattering study Ref. [18] revealed that magnetic moments in IrO_6 layers orient along [001] direction under doping with Mn and the positions of the diffraction peaks are the same as that reported in Ref. [37] for the case with applied external magnetic field. Interestingly, a magnetic transition occurs in this compound in the presence of an external magnetic field as it was found from magnetic susceptibility measurements in Refs. [16, 169, 37] (see panels (C) and (E) in fig. 1.3). The field which triggers this transition is relatively small: the net magnetic moments of the IrO_6 layers as seen along c-axis may order ferromagnetically already at 0.2 T (panels (C) and (E) in fig. 1.3) as reported by RIXS study in Ref. [37] and by magnetoresistance studies in Ref. [173].

In contrast to the x-ray scattering techniques applied for studies on Sr_2IrO_4 so far, the NFS technique probes the magnetic hyperfine field directly, without involving complex models for scattering function [20, 2]. Moreover, NFS probes magnetism and electronic structure locally, at Ir nucleus only [40, 2]. We measured NFS on Sr_2IrO_4 single crystalline samples. All crystals exhibit the form of platelets with (001) planes being parallel to the largest surface areas. The typical crystal thickness is small and $\sim 30\text{-}70\ \mu\text{m}$ with $1\times 3\ \text{mm}^2$ lateral size. Therefore, the 5 crystals have been stacked along the beam in order to increase the NFS count-rate. The orientation of the crystals was carried out using polarized Raman spectroscopy with a 532 nm laser. Particularly, the Raman signal intensity from the B_{2g} mode ($380\ \text{cm}^{-1}$) [174] was measured owing to that it is maximal if the polarization of the incident laser beam is parallel to [100] or [010] direction in Sr_2IrO_4 , as shown in the Ref. [174]. Careful parallel alignment of each crystal in the stack is necessary. Assembling the sample stack under the microscope, each crystal was carefully pushed by

tweezers and the focus depth change was measured. Knowing the length of each crystal and change of focus depth, the deviation angle from ideally parallel crystal stacking was estimated as $\sim 8\text{--}12$ degree. For the NFS experiment the crystals have been installed so that the (001) plane in Sr_2IrO_4 was perpendicular to the incident beam and the crystallographic direction $[100]$ or $[010]$ was parallel to the σ -polarization vector of the incident SR beam (see sketches in fig. 6.3 and fig. 6.4).

In order to explore the impact of the magnetic transition on the hyperfine interactions on the Ir nuclei in this compound, we acquired NFS spectra in the presence of an external magnetic field and compared it with the data obtained without field. The sample was cooled down to 15 K prior to applying a magnetic field (zero-field cooling). The magnetic field of 0.53(5) T was applied perpendicular to the wavevector of the incident beam and in the horizontal plane (see sketch in inset to fig. 6.4).

The time spectrum acquired without external field shows a pronounced beating pattern. Accepted magnetic structure for Sr_2IrO_4 (Refs. [37, 36, 171] and inset in fig. 6.3) is most probably correct in essence, and therefore any candidate structure used to fit the NRS data must respect its essential features. Assuming the same orientation of the nuclear hyperfine field as that of the magnetic moments reported in Refs. [37, 36, 171] (see inset in fig. 6.3), the magnetic lattice with eight magnetic sites and the field vectors residing in the a - b plane can be assumed for fitting the experimental time spectrum. The time spectrum has been treated by dynamical theory of nuclear resonance scattering using the software CONUSS [77], and the result is shown in fig. 6.3. Evidently, the model cannot explain the measured time spectrum.

However, the data can be explained by another model which assumes magnetic field vectors oriented slightly out of the a - b plane. Orientation of the magnetic fields assumed by this model is shown in the fig. 6.4, (B) and (C). The corresponding time spectrum was fitted to the experimental data. It is shown in the upper panel of fig. 6.4, (A) by the red line. We found that the magnetic field vectors do not reside in a - b plane, but these are slightly, by $\sim 9\text{--}30$ degree, deflected from the a - b plane. The deflection angles are higher than the misalignment angles measured during the sample preparation.

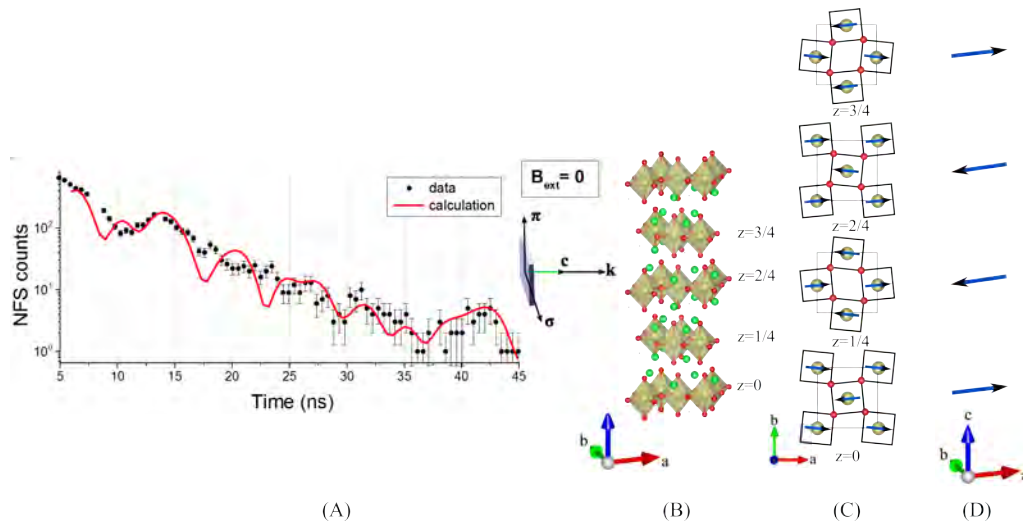


Figure 6.3: (A): NFS time spectrum of Sr_2IrO_4 at 15 K without external field (black markers) and the time spectrum calculated assuming the magnetic order given by measurements with XRS technique in Refs. [37, 36, 171] (red line). (B): crystal structure of Sr_2IrO_4 according to Ref. [16]. (C): Magnetic stacking pattern along the c -axis according to Refs. [37, 36] and (D): ordering of the net magnetic moments in IrO_6 layers according to Ref. [37].

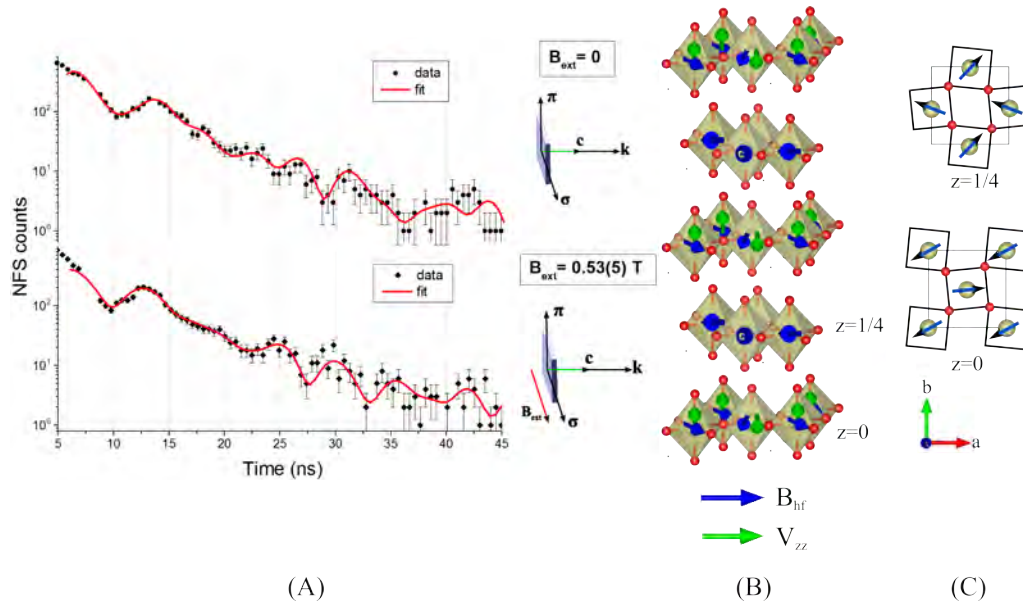


Figure 6.4: (A): NFS time spectra of Sr_2IrO_4 at 15 K without external field (upper panel) and in 0.53(5) T field (lower panel). The inset shows the direction of the external field with \mathbf{k} being the wavevector and σ is the polarization of incident photons. The fitted time spectra are shown by the red lines. (B): magnetic and electronic structure of Sr_2IrO_4 revealed by the analysis of the time spectra. Magnetic hyperfine field is shown by the blue arrows, and the green arrows show the orientation of EFG quantization axis. (C): magnetic stacking pattern along the c -axis shown by the projections of magnetic fields onto the a - b plane.

In the zero-field case (fig. 6.4 (A), upper panel) magnetic hyperfine fields exhibit the same magnitude of 24.2(2) T for each site; this value is in a very good agreement with the value of 24 T obtained by conventional MS study and reported in Ref. [57]. Analysing the obtained NFS time spectra, the quadrupole splittings of 1.40(2) mm/s (4.55(7)Γ or 341(5) neV) and of 2.01(3) mm/s (6.52(3)Γ or 489(2) neV) were revealed at the 2nd and at the 4th site, respectively. We derived the main component of EFGs along quantization axis $V_{zz1} = 9.1(1) \cdot 10^{21}$ V/m² for one site, and $V_{zz2} = 1.30(1) \cdot 10^{22}$ V/m² for another site. The addition of the EFG in the model is justified since the symmetry of the Ir site in Sr₂IrO₄ is low, $\bar{1}$ [16], and because the time spectrum cannot be interpreted by magnetic hyperfine interactions only. A study on isostructural Sr₂RuO₄ by conventional Mössbauer spectroscopy with 90 keV resonance in ⁹⁹Ru reported in Ref. [175] shows zero EFG in Sr₂RuO₄, while speculating on the zero EFG in Sr₂IrO₄. Indeed, the EFG in Sr₂IrO₄ is not reported in the earlier review of ¹⁹³Ir Mössbauer spectroscopy work Ref. [57], providing a speculation about its absence. Another study of Sr₂RuO₄ with NMR in ¹⁰¹Ru, Ref. [176], reports on a non-zero quadrupole splitting of 14 neV and the main component of EFG along quantization axis, $V_{zz} = 6.4 \cdot 10^{20}$ V/m². Such small EFG could not be observed by conventional Mössbauer spectroscopy with 90 keV resonance in ⁹⁹Ru.

In order to discuss the quadrupole splitting further, its description (Chapter 3.1) should be recalled. According to its definition, quadrupole splitting occurs due to a non-symmetric charge distribution around the nucleus. Two origins of such a distribution are possible: (i) non-symmetric charge distribution from surrounding ions, inclusively the scenario of lacking oxygen ions in IrO₆ octahedra in the particularly measured sample; (ii) charge distribution determined by valence orbitals of Ir. In order to check the hypothesis of oxygen deficiency, we measured XANES at the Ir L₃-edge (11.215 keV, ionization of 2p_{3/2} states) on the Sr₂IrO₄ sample, since this technique probes local environment of Ir. In case of oxygen deficiency, the XANES would demonstrate additional peaks near the white line. The measurements were carried out at the P65 beamline of PETRA III and standard ionization chambers have been used for measuring photon flux incident onto and transmitted through the sample. The incident photons have been pre-monochromatized by DCM with a pair of Si (1 1 1) crystals. In order to reduce line broadening, the sample was cooled down to liquid nitrogen temperature, and another pair of DCM crystals, Si (3 1 1), with lower energy bandpass was used. XANES on an IrO₂ sample was also measured and served as a reference, since Ir is present in the valence state Ir(IV) in Sr₂IrO₄ and in IrO₂. XANES studies on Sr₂IrO₄ are available in the literature Refs. [28]. The analysis of the XANES spectrum in Ref. [28] did not reveal oxygen deficiency. The XANES spectra obtained in this work are shown in fig. 6.5; the XANES spectrum for Sr₂IrO₄ given in Ref. [28] is also displayed in the figure for comparison.

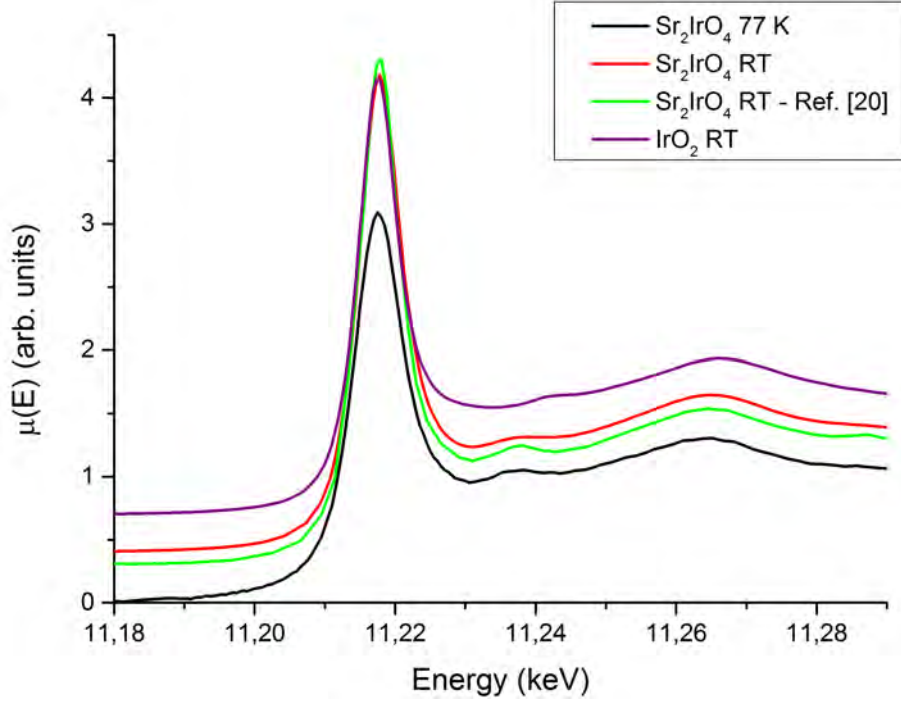


Figure 6.5: XANES spectra acquired on Sr_2IrO_4 sample studied in this work and in work Ref. [28]. XANES spectrum of IrO_2 is given referencing to the same valence of Ir(IV).

We found that the XANES spectrum acquired on our sample resembles the spectrum published in Ref. [28] and is similar to that acquired on IrO_2 . Therefore, the non-zero quadrupole splitting in Sr_2IrO_4 observed by NFS might be explained by an asymmetry in the distribution of Ir valence electrons. It is worth to note that the effect should be larger for iridates than for ruthenates due to the more elongated $5d$ -valence orbitals in Ir and one d -electron less in Ru.

The time spectrum acquired on Sr_2IrO_4 in an external magnetic field shows several features (lower panel in fig. 6.4, (A)). First, the intensity minima are shifted towards time zero (the excitation pulse) indicating a higher magnetic hyperfine field or a change in the direction of the hyperfine field. Second, the widths of the beats become smaller, suggesting the idea of a different magnetic structure. The applied field $B_{\text{ext}}=0.53(5)$ T contributes with the energy of about $\mu_B \cdot B_{\text{ext}} \sim 31 \mu\text{eV}$ and the sample temperature of 15 K corresponds to the $k_B \cdot T \sim 1.3 \text{ meV}$ energy contribution. These values are far beyond the energies of Heisenberg antiferromagnetic interaction of 60 meV and Dzyaloshinskii-Moriya interaction of 27 meV reported for Sr_2IrO_4 in Ref. [35] and in Ref. [36, 164]. Also, the high crystal field in the -60..35 meV range was measured for this compound [36]. Therefore, at the present experimental conditions magnetic order inside a IrO_6 layer could not be broken, though, canting angles between hyperfine fields may slightly change. Following to this argumentation, we assume the model with the four non-equal Ir sites, as it was applied for the treatment of the zero-field case.

Applying the external magnetic field, we found that magnetic moments and electric field gradients at Ir nucleus do not change their orientation within the statistical uncertainty of the fit, which is $\sim \pm 3..10$ degree. This error values are similar to the misalignment angles measured during sample preparation by stacking of the Sr_2IrO_4 crystals. The magnitude of EFG does not change with the applied external magnetic field. In contrary, the magnitude of magnetic hyperfine fields does change from 24.2(2) T to 25.5(2) T, which is equal to a 5(1) % effect. The effect might be related to the so-called hyperfine anomaly effect which states a non-uniform distribution of Fermi contact field due to the non-spherical shape of the nucleus (Bohr-Weisskopf effect). Theoretical work Ref. [177] predicted that the effect is significant for heavy nuclei with odd number of protons, thus it is especially pronounced in the ^{193}Ir nucleus, as shown in Refs. [57, 60]. The measurements with conventional MS showed that the effect induces a 6.3(5)% difference in nuclear g -factors for the measurements in external magnetic field and in zero-field on IrF_6 [178, 57], and a 7.2(4) % difference was reported in Ref. [60] for on Ir diluted in Fe, though in external fields of ~ 7 T. Contributions of spin and orbital fields, \mathbf{B}_{dip} and \mathbf{B}_{orb} , to effective hyperfine field can be obtained by measuring hyperfine field in external magnetic fields since \mathbf{B}_{dip} and \mathbf{B}_{orb} are uniformly distributed along the nucleus, and Fermi contact field is not.

Concluding the results of this section, it is important to accent that the NFS technique pave a simple way of probing magnetism and electric charge distribution in Ir compounds. Especially for high-pressure studies there is a clearly benefit of small absorption due the high photon energy and the possibility to distinguish orientation of magnetic moments due to the polarization dependence. Recent studies of iridate compounds point to the interesting phenomena occurring at high pressures: particularly, in the study [15] the metallization of ground state in $\text{Sr}_3\text{Ir}_2\text{O}_7$ was observed at the moderate pressure of 54 GPa. However, the impact of magnetic ordering on metal-insulator transition is not clear for this case study and could be the subject of the further investigations. NFS at 73 keV resonance in Ir will help to reveal magnetism and electronic structure at high pressures since such NFS experiments can be carried out on small samples and are not significantly affected by absorption.

7 Density of phonon states in Ag-Sb-O compounds

The sapphire backscattering monochromator designed and tested at the P01 beamline provided access to vibrational spectroscopy on Sb-containing compounds (see Chapter 4.6). A Nuclear Inelastic Scattering (NIS) experiment on two compounds from the $\text{Ag}_{2-x}\text{Sb}_{2+x}\text{O}_{6+y}$ series, AgSbO_3 and AgSb_3O_7 was performed as the first scientific application.

Recalling the information on $\text{Ag}_{2-x}\text{Sb}_{2+x}\text{O}_{6+y}$ given in the introductory chapter 2, one oxidation state of antimony, Sb(V), is present in AgSbO_3 , while both Sb(III) and Sb(V) states can be found in AgSb_3O_7 (fig. 2.2). Measuring the temperature dependence of nuclear resonant absorption, it is noticed that the area of the single line (absorption at the Sb(V) site) and the area of the doublet (absorption at the Sb(III) site) decrease corresponding to the decrease of the Lamb-Mössbauer factors. The Lamb-Mössbauer factor of the Sb(V) site is higher (0.84(2) at 10 K) and decreases slower with temperature than that of the Sb(III) site (fig. 7.1). At room temperature, the Lamb-Mössbauer factor for the Sb(III) site is very low, being equal to 0.14(4) at room temperature, while for the Sb(V) site it remains relatively large at high temperatures, being equal to 0.71(2) at room temperature (fig. 7.1). Therefore, vibrations of Sb(III) practically contribute mainly to multiphonon excitations in the NIS spectrum of AgSb_3O_7 at high temperatures. Since NIS probes vibrations in a site-specific way, measuring the temperature dependence of the density of phonon states in AgSb_3O_7 may allow to separate the contribution of Sb(III) and of Sb(V) vibrations to the total vibrational spectrum of Sb. The density of phonon states at the Sb(V) sites in these compounds can be extracted from the NIS spectra measured even at room temperatures due to the high Lamb-Mössbauer factor of Sb(V) and low multiphonon contribution to NIS spectrum.

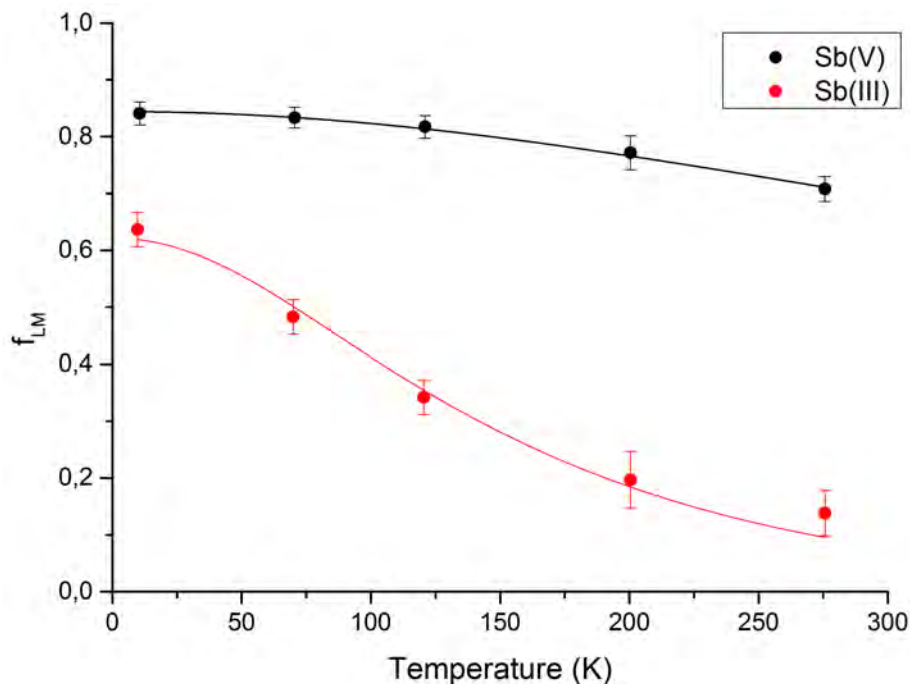


Figure 7.1: Lamb-Mössbauer factors for Sb(III) (red markers) and Sb(V) (black markers) sites in AgSb_3O_7 obtained by temperature dependent measurements with Mössbauer spectroscopy. The lines show the corresponding fits with the Debye model. Debye temperatures of 875(13) K and of 335(14) K have been obtained for Sb(V) and Sb(III), respectively.

NIS on ^{121}Sb at 37.13 keV was carried out at the P01 beamline with the sapphire backscattering monochromator. The NIS spectra and instrumental function of the monochromator are shown in the fig. 7.2. All samples have natural abundance of the ^{121}Sb isotope and the measurements were performed by repetitive scanning up and down the sapphire crystal temperature for about 1.5 h; the NIS counts were binned and summed up in order to reduce statistical errors. The resolution in NIS spectra was 3.2(4) meV determined by the full width at half maximum of the instrumental function (inset to fig. 7.2). The temperature of the AgSbO_3 sample was 180(2) K, while the AgSb_3O_7 sample was measured at 170(2) K and at room temperature of 296(1) K. The sample temperatures have been determined by comparing phonon creation and annihilation parts of the NIS spectra, owing to the fact that the occupancy of phonon states is proportional to $e^{-E/k_B T}$ (see discussion of NIS formalism in chapter 3.4.2).

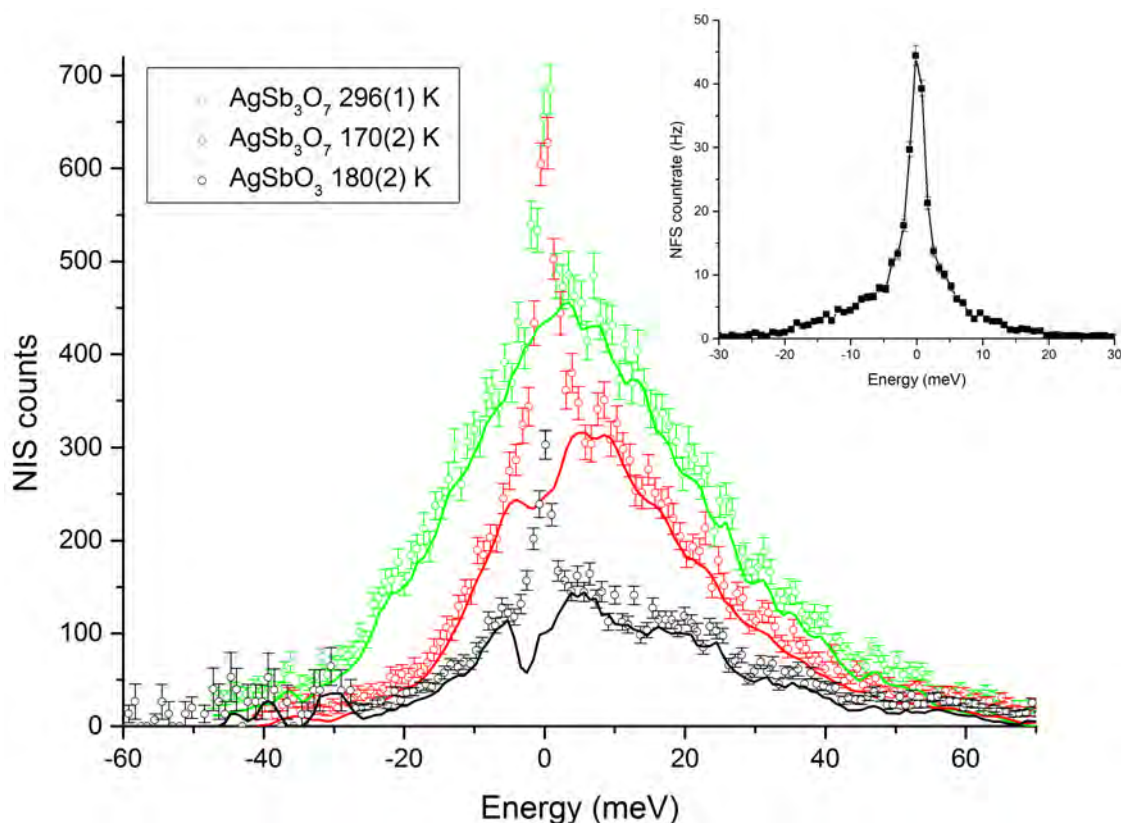


Figure 7.2: NIS spectra measured on AgSbO_3 at 180(2) K and on AgSb_3O_7 at 170(2) K and at 296(1) K. The lines show the corresponding spectra with subtracted elastic lines and corrected for the background. The inset shows the instrumental function of the sapphire BS HRM with FWHM of 3.2(4) meV measured around 37.1292(5) keV resonance energy (denoted as 0 keV).

The density of phonon states and the lattice dynamics parameters have been derived from NIS using Fourier-Log method described in Chapter 3.4.2. The DPS is shown in the fig. 7.3 and the relevant parameters are given in the table 7.1.

The density of phonon states (DPS) in AgSbO_3 (fig. 7.3, panel (A)) exhibits significant contributions of vibrations with energies above 20 meV. Particularly interesting are the two features at 37 and 57 meV, which are much less pronounced in the phonon spectra of AgSb_3O_7 . Since Sb in AgSbO_3 is present only in the Sb(V) state, the modes with energies 37 and 57 meV can be related to the vibrations of Sb(V) ions. The higher mean force constant in AgSbO_3 (table 7.1) provides an additional fingerprint of stronger bonding in the O-Sb(V)-O chain compared to the O-Sb(III)-O chain.

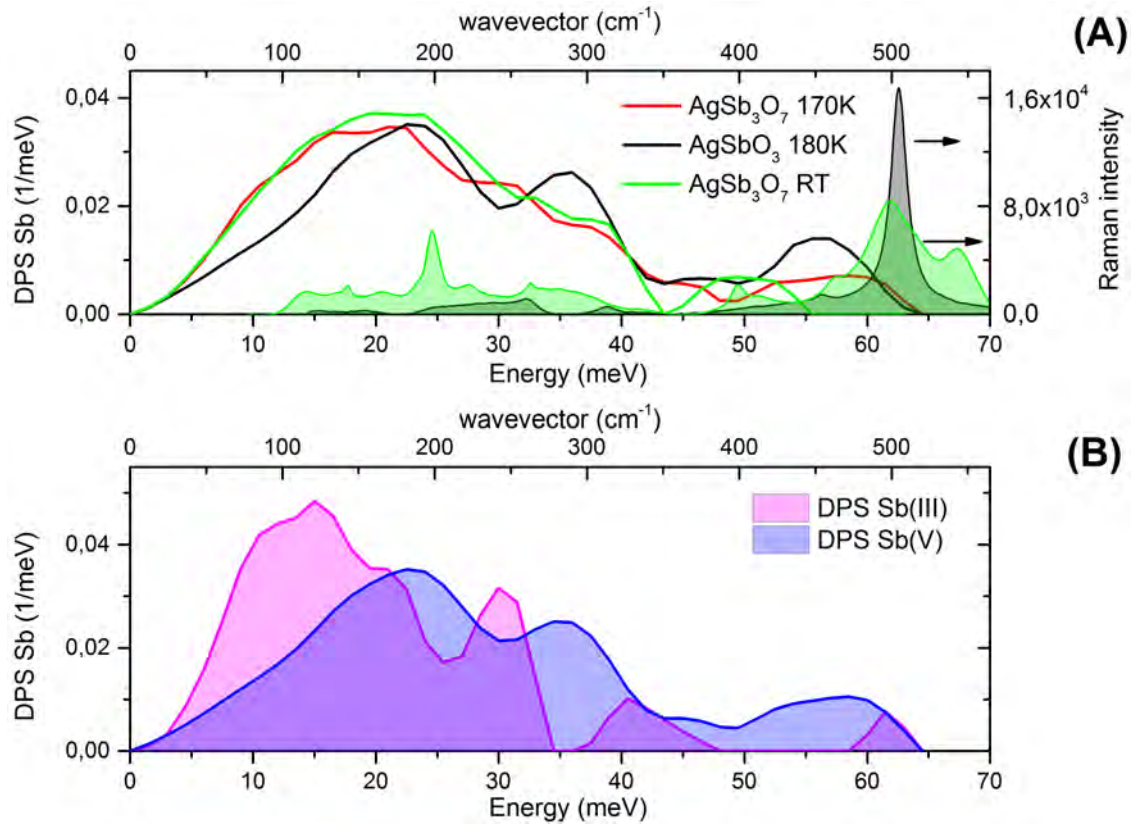


Figure 7.3: (A): Phonon density of states for Sb ions in AgSbO₃ (vibrations of Sb(V)) at 180(2) K, in AgSb₃O₇ at 170(2) K (contributions from vibrations at both Sb(III) and Sb(V) sites), and in AgSb₃O₇ at 296(1) K (vibrations of Sb(V) only). The grey and the green regions show Raman spectra from AgSbO₃ at 296(1) K and from AgSb₃O₇ at 296(1) K, respectively. (B): Density of phonon states of Sb(III) (magenta regions) and of Sb(V) (blue regions) in AgSb₃O₇ derived from DPS for AgSb₃O₇ and AgSbO₃ shown in the panel (A) (see text for calculation details).

Compound	$\langle F \rangle$ [N/m]	v_{Deb}^* [km/s]
AgSb ₃ O ₇ at 170(2) K	242(121)	2.7(5)
AgSb ₃ O ₇ at room temperature	400(12)	2.5(8)
AgSbO ₃ at 180(2) K	520(61)	2.8(5)

Table 7.1: Lattice dynamics properties for AgSbO₃ and AgSb₃O₇.

* density is assumed to be 6.8(3) g/cm³ as reported in work Ref. [48].

The DPS of Sb in AgSb₃O₇ measured at 170 K and at room temperature do not show significant differences (fig. 7.3, panel (A)). The force constants are also equal within the experimental error. At a first glance this observation might give a wrong impression that the contributions from different sites to the whole vibration spectrum are not distinguishable from each other comparing the DPS measured at 170 K and at room temperature. However, the contributions can be distinguished by comparing the vibrational spectra of AgSbO₃ and AgSb₃O₇ at different temperatures (s. panel (A) in fig. 7.3). For the sake of convenient analysis the chemical formula of AgSbO₃ should be re-written to Ag₂Sb₂^VO₆. According to the neutron scattering and the Mössbauer spectroscopy measurements reported in Ref. [45], AgSb₃O₇ can be re-written to AgSb^{III}Sb₂^VO₇. Therefore, two Sb(V) ions are present in Ag₂Sb₂O₆ (2/2 of Sb(V) vibrations) and there is one Sb(III) ion and two Sb(V) ions in AgSb₃O₇ (vibrations of 1/3 Sb(III) plus 2/3 vibrations of Sb(V)). Following this consideration the DPS for Sb(III) can be obtained by:

$$g(\text{Sb (III) in AgSb}_3\text{O}_7) = 3 \cdot g(\text{Sb in AgSb}_3\text{O}_7) - 2 \cdot g(\text{Sb in AgSbO}_3) \quad (7.1)$$

where g denotes DPS. The normalization of the DPS to 1 should be done, $\int_0^{E_{max}} g(\text{Sb (III) in AgSb}_3\text{O}_7) dE \equiv 1$, where E_{max} is the maximal phonon energy. Analogous to this procedure, the DPS of Sb(V) can be obtained by:

$$g(\text{Sb (V) in AgSb}_3\text{O}_7) = \frac{3 \cdot g(\text{Sb in AgSb}_3\text{O}_7) - g(\text{Sb (III) in AgSb}_3\text{O}_7)}{2} \quad (7.2)$$

with $\int_0^{E_{max}} g(\text{Sb (V) in AgSb}_3\text{O}_7) dE \equiv 1$.

The received site-specific DPS are shown in the panel (B) in fig. 7.3. Note that the DPS for Sb(V) is the same as DPS in AgSbO_3 (vibrations of Sb(V) only) which is the cross-check of the technique applied for separating DPS here. Thermodynamic parameters of Sb(III) and Sb(V) sites, including the Lamb-Mössbauer factors, have been derived from the DPS and shown in table 7.2. The Lamb-Mössbauer factor for Sb(III) at 175(7) K is 0.25 and 0.11 at 296(5) K. These values resemble the Lamb-Mössbauer factors of 0.23 and 0.14 measured for Sb(III) site with conventional Mössbauer spectroscopy at the corresponding temperatures and reported in Ref. [45]. The Lamb-Mössbauer factor for Sb(V) at 180(2) K is 0.37, which is roughly twice lower than Lamb-Mössbauer factor of 0.78 reported in Ref. [45]. The difference might be related to the problem of precise measurements of line area in conventional MS for a high effective thickness. Alternatively, the discrepancy might be related to the insufficient statistics of NIS data for phonon energies above 65 meV.

From the figure 7.3 panel (B) it is evident that the contribution from vibrations of Sb(III) in AgSb_3O_7 is significant at the low energies, while at high energies the contribution from Sb(V) vibrations is dominating. Higher energies of lattice vibrations and higher force constant lead to the general conclusion that the Sb(V)-O bonds in AgSb_3O_7 and in AgSbO_3 are shorter than Sb(III)-O bonds in AgSbO_3 (see sketch in figure 7.4).

Site	T [K]	θ_{Deb} [K]	f_{LM}	$\langle x^2 \rangle$ $10^{-3} [\text{\AA}^2]$	$\langle F \rangle$ [N/m]	v_{Deb} [km/s]	C_v [Jmol ⁻¹ K ⁻¹]
Sb(III)	175(7)	238(10)	0.25 Ref. [45]: 0.23	3.9	254	2.2(3)	21
Sb(III)	296(5)	238(10)	0.11 Ref. [45]: 0.14	6.2	242	2.4(6)	23
Sb(V)	180(2)	287(10)	0.37 Ref. [45]: 0.78	2.8	472	2.3(6)	18

Table 7.2: Site-specific parameters derived from DPS in AgSbO_3 and in AgSb_3O_7 : Debye temperatures θ_{Deb} , Lamb-Mössbauer factors f_{LM} , mean square atomic displacement parameters $\langle x^2 \rangle$, mean force constants $\langle F \rangle$, v_{Deb} Debye speeds of sound, and heat capacities C_v .

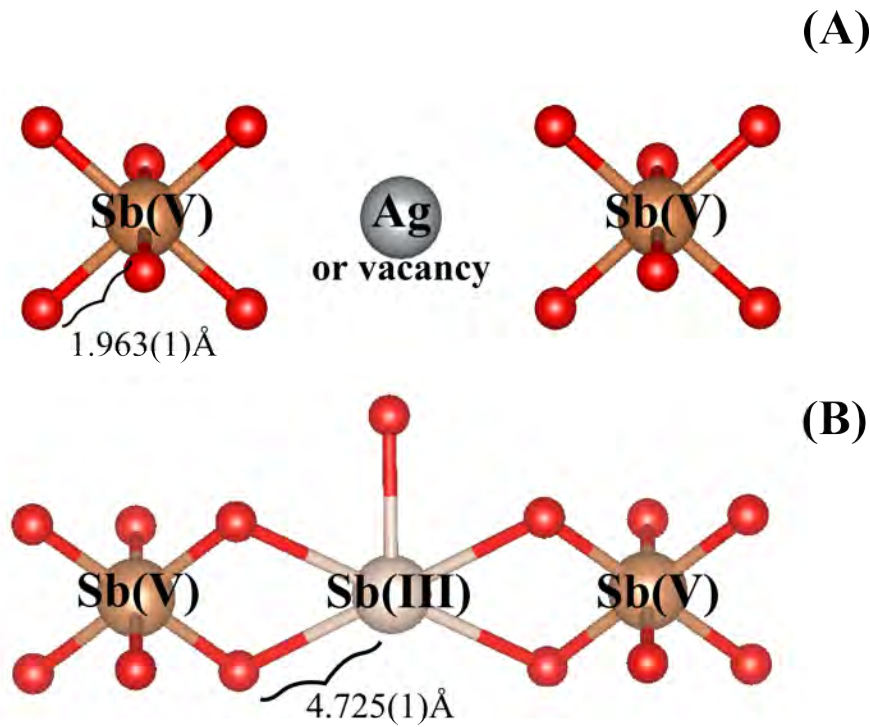


Figure 7.4: Local crystallographic environment of Sb in AgSbO_3 (panel A), only Sb(V) is present, and in AgSb_3O_7 (panel B)), which shows both Sb(III) and Sb(V). Note that the bonds in Sb(V)-O are shorter than Sb(III)-O. Bond lengths are given according to those in Ref. [47].

The room temperature Raman spectroscopy on AgSbO_3 and on AgSb_3O_7 was carried out in order to explore the vibrational spectrum further. A Bruker Senterra II Raman microscope with 532 nm-laser of 2 mW power and 50 μm aperture was used, resulting in a wavevector resolution of about 2 cm^{-1} . The obtained spectra are shown in the fig. 7.3 panel (A) by filled regions. A strong mode at 63 meV is visible in the Raman spec-

trum of AgSbO_3 (region filled by grey colour). This mode is not observable in the NIS spectrum. The modes at 24 meV, at 36 meV, and at 56 meV revealed by NIS are not very pronounced in the Raman spectrum. Comparing the DPS obtained by room-temperature NIS and room-temperature Raman spectroscopy for AgSb_3O_7 (green colours), one can notice pronounced similarities. Particularly, the mode at 24 meV in the Raman spectrum resembles the feature in the 20-24 meV range in the DPS. This mode is not seen in the Raman spectrum for the crystallographically more-ordered AgSbO_3 . The mode at 49 meV in AgSb_3O_7 can be measured by both Raman and NIS spectroscopy. This mode could be the same mode as that at 56 meV in AgSbO_3 but red-shifted due to the slightly different symmetry in AgSb_3O_7 .

The Debye sound velocity has been derived from the density of phonon states using equation (3.61). It is considered to be in the 2.4-2.8 km/s range for AgSbO_3 and AgSb_3O_7 at the two given temperatures. Using the values of sound velocity v_{Deb} obtained here and the unit cell parameter a from Ref. [48], an upper energy limit for acoustic modes can be found by equation $E_{up} = \frac{h v_s}{2a}$ [179], where h is the Planck's constant. For the AgSbO_3 and AgSb_3O_7 compounds we obtained $E_{up} \sim 25$ meV and ~ 11 meV, respectively. The Sb DPS in AgSb_3O_7 is given mostly by Sb(III) vibrations in the energy range up to 15 meV (s. panel (B) in fig. 7.3). Therefore, vibrations of Sb(III) may exhibit mostly acoustic mode character and play a dominant role in elastic properties of AgSb_3O_7 .

Discussing the errors in values measured by NIS, it should be noted that the values of the sound velocity are almost the same within the experimental error. The NIS data measured in the proximity to the elastic line are strongly affected by the width of the instrumental function, as seen from the large errors of speed of sound values (tables 7.1 and 7.2). A further improvement of energy resolution down to the theoretical limit of 0.3 meV is necessary for studies of small effects in speed of sound. Particularly, the quality of sapphire monochromator crystals should be improved by reducing the number of defects in sapphire, as shown in Ref. [99]. A way to improve sapphire quality for NRS applications was shown Ref. [129] by reducing dislocation density linked to the choice of a proper growth technique and to the lower crystallization rates.

8 Conclusions and Outlook

In this thesis I show the first synchrotron-based Mössbauer spectroscopy studies on iridium compounds, and the development of vibrational spectroscopy on antimony compounds. Both topics have been elaborated at the Nuclear Resonance Scattering (NRS) station at the P01 high-resolution dynamics beamline of PETRA III for the first time, extending its capability for non-iron Mössbauer resonances with transition energies beyond 20 keV. Two novel devices have been developed: a monochromator for 73 keV photons with medium, 158(8) meV resolution for the purpose of hyperfine spectroscopy on iridium compounds, and a highly-, meV-resolving backscattering monochromator based on a sapphire crystal for the purpose of vibrational spectroscopy on the Mössbauer resonances with the transition energies in the 20-50 keV range. Inspired by the high transition energies and low lifetimes of the resonances employed in this work, the detection of NRS signal was significantly improved at the beamline.

In the Chapter 3 I showed the impact of the hyperfine interactions on the nuclear levels in ^{193}Ir . The effects of the symmetry and magnetic fields in the proximity to the Ir nucleus are discussed and several specific cases are depicted. I review the formalism of NRS in the Chapter 3.4, with the focus on the iridium compounds. Particularly, the thickness optimization and countrate estimation procedures are described in detail and typical values are derived for elemental Ir. The impact of hyperfine interactions on nuclear resonant absorption and scattering, including its polarization dependence is discussed with the focus on Ir compounds. Furthermore, the nuclear response to polarized radiation is discussed for several typical experimental arrangements. Concluding the theoretical aspects, I briefly describe the treatment of the nuclear inelastic scattering data.

A significant part of this work is dedicated to the technological aspects of the experiments at the beamline. In this context, the main features of the design and operation of monochromators and detectors are discussed in the Chapter 4. The focus is set onto the high-resolution monochromators and backscattering geometry of monochromatization. According to the given treatment, the design of two monochromators is described. The performance of the first one, a silicon-based monochromator for 73 keV x-rays, was characterized via NRS on ^{193}Ir in elemental Ir. To the best of our knowledge, this monochromator provides the best energy resolution of 158(8) meV and the highest spectral flux of 280 [ph/s/Å] at this energy. Another monochromator was developed and elaborated for the beamline. It is dedicated to vibrational spectroscopy by nuclear inelastic scattering on any Mössbauer resonance with transition energy in the 20-50 keV range. The monochro-

mator is based on backscattering from a sapphire crystal. The two main elements of this monochromator, precise temperature control and quality of sapphire crystal, are studied by nuclear forward scattering on SnO_2 and Sb_2O_3 . The acquired instrumental functions have widths of 1.3(1) meV and 3.2(4) meV (FWHM) at 23.88 keV and 37.15 keV, respectively. This result shows the reliability of vibrational spectroscopy on Sn and Sb compounds at the P01 beamline.

Shortly after the successful tests of the related beamline components, the first NRS studies on iridium-containing compounds have been carried out starting from studies of lattice dynamics in elemental Ir. Especially it was found that NRS on iridium is possible even at room temperature. The main parameters of the lattice dynamics such as Lamb-Mössbauer factor, atomic displacement parameter, mean force constant, vibrational entropy and speed of sound are measured on elemental Ir by combining NFS, INS, and XRD techniques. An excellent agreement between experimental data and *ab initio* calculations given in the literature is shown, and several challenges in measuring elastic properties by scattering techniques are discussed.

The findings of the first Nuclear Forward Scattering experiments on iridium compounds are presented in Chapter 6. Analysis of the data shows pure quadrupole interactions in metallic IrO_2 , supporting the conclusion that macroscopic magnetism is absent in this compound. The obtained magnitude of the quadrupole splitting is in a very good agreement with the value given by conventional Mössbauer spectroscopy. A reasonable statistics can be collected in 3 hours for this compound under the current experimental conditions. Continuing the exploration of non-magnetic iridate compounds, NFS experiment on metallic SrIrO_3 was carried out. Using the dynamical theory of NRS and a dedicated software, CONUSS, specially upgraded for the calculation of NRS on 73 keV resonance in ^{193}Ir , the temperature dependence of the quadrupole splitting was determined for this compound. Broadening the applications of NFS on Ir, first NRS studies of magnetism in insulating Sr_2IrO_4 were carried out. The magnetic fields at the Ir nucleus does not significantly change their orientation with applying an external magnetic field of 0.53(5) T, though, the magnitude of hyperfine field does change. All data obtained from Sr_2IrO_4 can be modeled by a canted antiferromagnetic lattice. Though, in contrast to the results of the previous studies reporting on magnetic moments canted in the a-b plane, we show that the moments are oriented slightly out of the a-b plane. This observation might explain why the superconductivity was not observed so far in Sr_2IrO_4 , since the energy desired for electron transport in a-b plane is higher than it is for the magnetic moments located inside a-b plane. The achieved results demonstrate that NRS is a powerful research tool for studies on iridium compounds due to the high energy of resonant photons and the high natural abundance of the ^{193}Ir isotope.

The second scientific part of this work is dedicated to vibrational spectroscopy with Nuclear Inelastic Scattering (NIS). By means of highly resolved, 3.2(4) meV - NIS at 37.1292(5) keV, details in the vibrational spectra of antimony sites have been revealed

in the water splitting Ag-Sb-O compounds with pyrochlore structure. The results show site- and valence-specific vibrational modes of antimony in these compounds. Studying NIS spectra of these compounds, it was possible to separate the contribution of Sb(III) and Sb(V) vibrations to the whole spectrum of Sb vibrations owing to the different Lamb-Mössbauer factors for Sb(III) and Sb(V) species.

While a relatively large amount of fundamental research was explored in this thesis, it should be emphasized that the applied techniques are new and it is still necessary to improve them. In the area of NFS on iridates a vast amount of fundamental problems can be explored. Interestingly, that IrO_2 attracts much attention in solid state research due to the pronounced spin Hall, spin Seebeck effects, and energy gaps in spin-wave spectrum [157, 158, 9, 180]. Particularly interesting could be the study of the multilayer systems of IrO_2 which may potentially deliver high sensitivity to the spin waves, placing also the interesting technical challenge of measuring nuclear Bragg reflection from thin film multilayers containing Ir.

An enormous magnetic hyperfine field of about 140(2) T was reported for the Ir-Fe bulk alloys [57]. Owing to this and knowing about magnetic proximity effects in thin films [26], one could imagine an interesting fundamental study of correlations of interlayer magnetic moments in Ir-Fe multilayers. The origin of magnetic proximity effects in such multilayers could be completely different from that revealed in multilayers based on Fe [181, 182] due to the large admixture of orbital moment to the total angular momentum resulting in insulating states in Ir. Furthermore, the collective quantum states in multilayer structures with Ir and interesting effects like electromagnetically induced transparency [183] and collective Lamb shift [184, 185] might be completely different from those demonstrated in Fe multilayers [183, 185, 186, 187] due to the large hyperfine fields at Ir nuclei [57] and pronounced contribution of angular momentum of electrons to the effective hyperfine field on Ir [57, 60]. Moreover, measuring very high hyperfine fields in iridates provides access to precise determination of nuclear parameters like nuclear g -factors and testing quantum electrodynamics by measuring hyperfine anomaly (Bohr-Weisskopf effect [177]) [60, 188, 189] in Ir nucleus.

The both nuclear reflectometry experiments, on IrO_2 and on Ir-Fe multilayers, require that the photon beam after the monochromator is directed horizontally. A new in-line monochromator for 73 keV x-rays should be built providing access to nuclear reflectometry studies on iridium compounds, nowadays complicated due to the beam orientation. Following the idea of reflectivity measurements, the direction of magnetic moments in iridate perovskites and pyrochlores can be directly determined using the polarization dependence of NFS [2]. The single crystals of these compounds are available in a reasonable size. It is worth to mention that cation and anion sublattices in pyrochlore iridates can be studied separately, since most of the cations like Sm and Eu are Mössbauer-active and NFS and NIS are already established for them [20, 103]. Particularly, the sapphire backscattering monochromator, which is already in operation, can be used for combined

studies on several isotopes [103].

A study of the isomer shift in iridium compounds can be interesting. While the change in the isomer shift along the Ruddlesden-Popper (RP) series of strontium iridates $\text{Sr}_{n+1}\text{Ir}_n\text{O}_{3n+1}$ is not significant, as shown in Ref. [57], for other topological systems such as Na_xIrO_y ($2 \leq x \leq 3$, $3 \leq y \leq 5$) the oxidation state of iridium varies in a broad range from (IV) to (VI), corresponding to the isomer shift difference as high as 2 mm/s ($\approx 6.5\Gamma$ or 490 neV) [57, 58].

Measuring the temperature dependence of the quadrupole splitting can reveal the level splitting of the ground state in iridates [54]. The theoretical model for the treatment of temperature dependence of quadrupole splitting exists [168], widely used for studies of crystal fields in ^{57}Fe compounds (3d electron systems) [54, 190] and can be applied to iridates.

Pressure is an effective tool for tuning electronic and magnetic properties. A bright spectrum of interesting problems can be unraveled with the development of the high-pressure technique for NRS on ^{193}Ir at 73 keV. For instance, Donnerer et al. have reported recently the pressure-induced metallization of insulating $\text{Sr}_3\text{Ir}_2\text{O}_7$ at 54 GPa believed to be concomitant with the quenching of the orbital moment [15]. As it was shown by Perlow *et.al.* in Ref. [60], orbital and spin contribution to the total hyperfine field on Ir nucleus can be distinguished using hyperfine anomaly effect. A device for focussing 73 keV x-rays is necessary owing to the small sample size used in high-pressure studies. Once such a device is developed, measurements of magnetism with high pressure NRS will provide many new interesting insights into the interplay between magnetism and metal-insulator transitions.

The energy resolution achieved in NIS with the sapphire backscattering monochromator is high, but not sufficiently high for several applications like precise determination of elastic properties and resolving fine features in vibrational spectra of glasses and compounds which demonstrate very localized modes. There is a demand for direct measurements of lattice vibrations because such measurements can clarify the origin of the low thermal and high electric conductivity in antimony pyrochlore compounds [148]. Pursuing this challenge, the quality of the accessible sapphire crystals should be improved.

A Appendix

A.1 Modern x-ray sources: parameters and operation modes

X-ray tubes and their modifications such as tubes with rotating anode and liquid-metal anode used nowadays have numerous advantages: they are compact, not expensive and provide high photon flux. The energy spectrum of light delivered by an x-ray tube consists of a continuous part defined by the acceleration voltage, and of an intense narrow part defined by the electronic fluorescence of the anode material. The light produced by a x-ray tube is spatially distributed in the whole solid angle 4π , therefore x-ray tubes cannot deliver beam with high spectral density. The quality parameter "brilliance" of any photon source is defined as flux of photons in the beam $[ph/s]$ normalized by angular divergence $[mrad^2]$, energy bandwidth $[0.1\%bandwidth]$ of the beam and size of the beam source $[mm^2]$ [1]:

$$Brilliance = \frac{\frac{photons}{second}}{mrad^2 \cdot mm^2 \cdot 0.1\%bandwidth} \quad (A.1)$$

Many schemes exist to overcome brilliance limitations of x-ray tubes but the parameter remains low compared to synchrotron radiation (SR) sources. Also, by using x-ray tubes it is difficult to maintain a time-structured beam desired in experiments. SR sources have three unique properties which allow to perform the experiments described in this work. First, the radiation is of high brilliance: it is intense and well collimated. Second, the radiation has a time structure which allows for measuring of the time-delayed NRS signal. Finally, SR is linearly polarized in the plane of the synchrotron ring.

Synchrotron radiation has first been observed as a parasitic effect in particle accelerators where it is produced by deflecting of a charged particle travelling with relativistic speed. Since particles with low mass emit more radiation than heavier particles when deflected, electrons are mostly used to produce synchrotron radiation. In order to provide basic idea of synchrotron radiation an electron accelerator chain with storage ring is described briefly. A layout of the accelerator chain is shown in the fig. A.1. Electrons are produced by thermoemission or by field emission in vacuum. Further, the particles are accelerated in a linear accelerator by a periodic RF field which shapes the electron beam into bunches of electrons. After acceleration in the linear accelerator the electron bunches are usually post-accelerated in a booster ring in order to reach the desired electron energy at which

the electron bunches are injected into a storage ring. The latter accelerates the travelling bunches of electrons in sections of the ring using microwave fields. The microwave field is applied to the particles *synchronously* with the arrival of a bunch of particles into the accelerating section, thus the name synchrotron. In a storage ring the energy of the electron beam is maintained at a certain level compensating the energy loss during revolution of the bunches in the ring, while in synchrotrons the energy of the bunches is increased in each revolution. The relativistic electrons in the storage ring emit the x-rays in a cone at the bending sections of the ring. The opening angle of the cones is given by:

$$\sigma = \frac{1}{\gamma} \quad (\text{A.2})$$

with $\gamma = \frac{E}{m_0 \cdot c^2}$, where m_0 - rest mass and E is the energy of the particle. Thus, the synchrotron radiation shows a sharp collimation in the order of dozens of μrad .

Since the advent of the first sources a lot of R&D has been made resulting in very reliable SR sources of the 3rd generation. At these facilities periodic magnetic structures are installed in straight sections of the storage ring (fig. A.1 A.2). Passing by these sections, particles perform high-frequent oscillations, emitting x-rays at each oscillation bend. The insertion device is called undulator if the emitted x-rays superimpose coherently. The opening angle of undulator radiation is smaller by a factor of \sqrt{N} compared to that of the SR at a bending magnet A.2:

$$\sigma_u = \sigma \cdot \sqrt{\frac{1 + k^2/2}{2 \cdot i \cdot N}} \quad (\text{A.3})$$

where N is the number of periods of the undulator (typically $N \leq 50$), $k = 0.0934 \cdot l [mm] \cdot B [T]$ with l is the undulator period length, B is the magnetic field, and i is the number of harmonic (Fig.A.2). Thus, undulator devices are aiming to increase the brilliance of SR providing more photon flux and collimation down to several μrad . Sufficient flux for NRS experiments is provided by large storage rings operating at electron energy $> 3\text{GeV}$ equipped with undulators [20]. The most important properties of two synchrotron radiation facilities of 3rd generation are given in the table A.1. Some of the properties can slightly change with the operation mode of the ring.

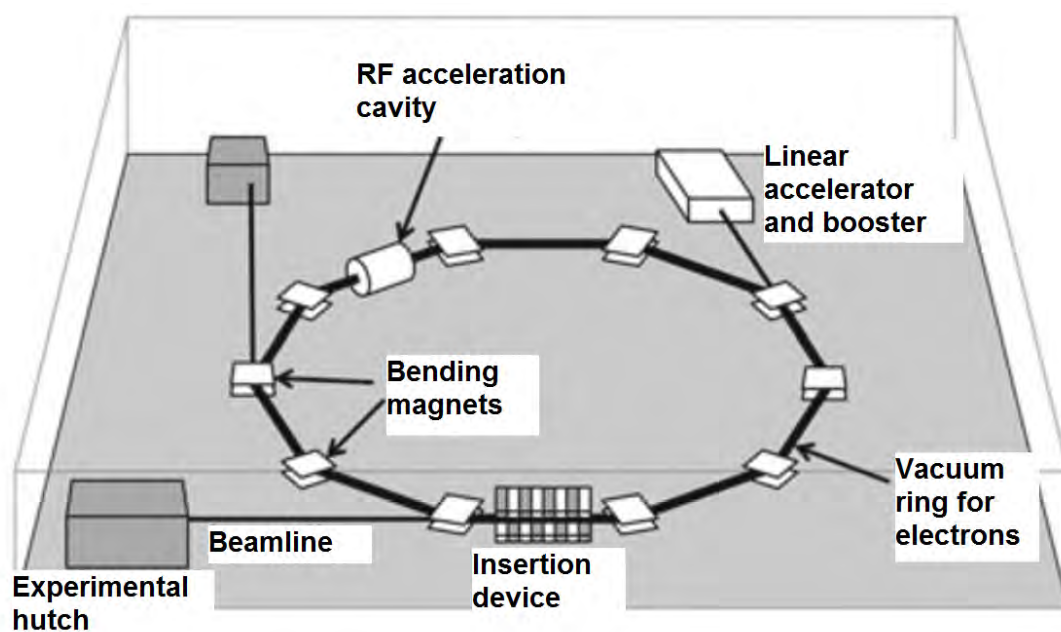


Figure A.1: A layout of an accelerator chain [191]

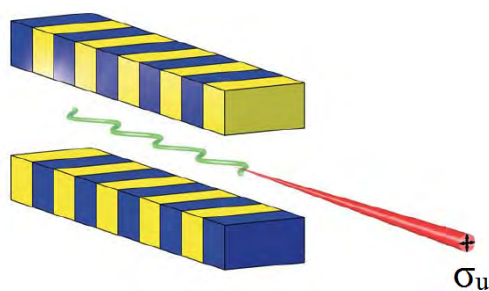


Figure A.2: Undulator [1]

Property	PETRA III	ESRF
Circumference, [m]	2304	844
Particle energy, [GeV]	6	6
Emittance (horizontal×vertical), [nm · rad × nm · rad]	1×0.01	48×0.048
Brilliance, $\left[\frac{\text{photons}}{\text{second}} \frac{1}{\text{mrad}^2 \cdot \text{mm}^2 \cdot 0.1\% \text{ bandwidth}} \right]$	10^{21}	10^{20}
Properties of undulators		
Property	PETRA P01 beamline*	ESRF ID18 beamline**
Period of magnetic structure, mm	32	27
Number of periods N	312 (2×156)	159 (3×53)
Energy of fundamental harmonic, keV	6.1 (gap of 13 mm)	7.2 (gap of 11.0 mm)
Beam divergence as calculated with eq.(A.3), μrad	2.1	2.3

Table A.1: Properties of PETRA III and ESRF photon sources used for NRS studies as on 2016 [192, 193]

* at the 73 keV photon energy (nuclear resonance in ^{193}Ir)

** at the 67 keV photon energy (nuclear resonance in ^{61}Ni)

The time structure of SR, the so called filling pattern of the ring with bunches of electrons, is characteristic for each SR source. It is defined by the radio frequency of accelerating sections, also called "RF frequency". This frequency determines minimal time separation between the bunches. The main parameters which characterize the filling pattern are the ring current in [A] (or [Co/s]), number of bunches, and time separation between bunches. For the PETRA ring the injection rate is very high, the beam injected typically every several seconds as soon as the ring current drops for one percent, the so-called top-up operation mode. This ensures constant heat load on the x-ray optics and thus more stable photon beam for experiments at the beamlines. The RF frequency of the PETRA storage ring is 500 MHz, therefore the minimal separation between the bunches in the PETRA ring is 2 ns ($1/5 \cdot 10^8 = 2$). However, only each 4th bucket is filled at the mode with maximal number of bunches (960 bunches). The parameters of several filling patterns for

PETRA ring are given in the table [A.2](#).

Number of bunches	Time separation between SR pulses, [ns]
40	192
60	128
120	64
240	32
480	16
960	8

Table A.2: *Parameters of filling patterns for the PETRA ring*

A.2 Operation code for MCA device at P01 beamline

The operation code for MCA device at P01 beamline makes use of TANGO's MCA8715 class. The listing is given below.

```

1  #!/usr/bin/env python
2  # usage: mca_acq [hutch: e.g. eh1, eh2, or eh3] [number of data bank of
    ↪ mca] [total_acquisition_time (sec)] [readout_interval_time (sec
    ↪ )]
3
4  from PyTango import *
5
6  import sys
7  import time
8  import os
9  import signal
10
11 infinite_loop = 0
12
13 def signal_handler(signal, frame):
14     if signal == 2:
15         signl="Ctrl+C"
16         print "\nYou pressed", signl, "! Acquisition is aborted!"
17         mca_device.Stop()
18         sys.exit(0)
19
20 def mca_full_name():
21     mca = sys.argv[2]
22     if sys.argv[1] == "eh1":
23         mca_device_name = "haspp01eh1:10000/p01/mca/eh1.0" +
    ↪ mca
24     if sys.argv[1] == "eh2":
25         mca_device_name = "haspp01eh2:10000/p01/mca/eh2.0" +
    ↪ mca
26     if sys.argv[1] == "eh3":
27         mca_device_name = "haspp01eh3:10000/p01/mca/eh3.0" +
    ↪ mca
28     return mca_device_name
29
30 if len(sys.argv) < 2:
31     print "\nUsage:"
32     print "mca_acq [eh1, eh2, or eh3] [number of mca bank] [
    ↪ total_acquisition_time (sec)] [readout_interval_time (
    ↪ sec)]\n"
33     print "total_acquisition_time and readout_interval_time are

```

```
    ↪ optional.\n"
34     print "If not given, the total_acquistion will be infinite and
    ↪ the readout_interval_time 1 sec"
35     os._exit(1)
36 elif len(sys.argv) == 3:
37     infinite_loop = 1
38     acq_time = -1
```

A.3 Script for a grid simulation in CONUSS

This script provides access to the multiple parameter simulation using CONUSS [77] software, version 2.1.1. In the example script the magnitudes of EFG and magnetic hyperfine field are simulated. However, any parameters incl. angles and EFG asymmetry can be simulated.

```

1  #!/usr/bin/env python
2  # no % signs
3  # Bhf integer, QS float with %.1f
4  # before running make directories fit and backup
5
6  import sys
7  import fileinput
8  import subprocess
9  import datetime
10 import os
11 import time
12 from shutil import copyfile
13
14 #make backup of mif file
15 FilePath = '214_9K.mif'
16 FilePathcng='backup/214_9K'
17 modifiedTime = os.path.getmtime(FilePath)
18 timeStamp = datetime.datetime.fromtimestamp(modifiedTime).strftime("_%
    ↪ b%d%y_%H%M%S")
19 FilePathcng1=FilePathcng+"_bck"+timeStamp+".mif"
20 copyfile(FilePath, FilePathcng1)
21
22 # define fit file
23 FilePathfit = '214_9K.fit'
24 FilePathfitcng='fit/214_9K'
25
26 bashCommand = "kctl"
27
28 #borders Bhf
29 bhfmin=int(raw_input("Input Bhf min  "))
30 bhfmax=int(raw_input("Input Bhf max  ")) +1
31 bhfgrid=5
32 bhf=bhfmin
33
34 #borders QS
35 qsmin=float(raw_input("Input QS min  "))
36 qsmax=float(raw_input("Input QS max  "))
37 qsgrid=0.2

```

```

38 qs=qsmin*10
39 j=0
40
41 #print borders Bhf
42 print range(bhfmin,bhfmax)
43
44 #print borders QS
45 print range(int(10*qsmin),int(10*qsmax))
46
47 # replacing and running fit
48 while bhf < bhfmax:
49     qs=qs-qsgrid*j*10
50     j=0
51     for i, line in enumerate(fileinput.input(FilePath, inplace=1)):
52         sys.stdout.write(line.replace(' (7.1.4) magnetic hyperfine
53             ↪ field / T                :: ', ' (7.1.4) magnetic hyperfine
54             ↪ field / T                :: '+str(bhf)+' *')) # replacing Bhf
55             ↪ value
56         sys.stdout.write(line.replace(' (7.1.7) quadrupole
57             ↪ splitting', ' (7.1.7) quadrupole splitting /
58             ↪ mm/s :: '+str(qs/10)+' *')) # replace 'qs' and
59             ↪ write
60     while qs < int(10*qsmax) :
61         for i, line in enumerate(fileinput.input(FilePath, inplace=1)):
62             sys.stdout.write(line.replace(' (7.1.7) quadrupole
63                 ↪ splitting / mm/s                :: ', ' (7.1.7)
64                 ↪ quadrupole splitting / mm/s        :: '+str(qs
65                 ↪ /10.)+' *')) # replacing QS value
66         print "Making Bhf ",bhf," Tesla and QS ",qs/10.," mm/s"
67         process = subprocess.Popen(bashCommand.split(), stdout=
68             ↪ subprocess.PIPE)
69         output = process.communicate()[0]
70         FilePathfitcng1=FilePathfitcng+"_"+str(bhf)+"_"+str(qs/10.)+"."
71             ↪ fit"
72         copyfile(FilePathfit, FilePathfitcng1)
73         qs=qs+qsgrid*10
74         j=j+1
75         time.sleep(3)
76     bhf=bhf+bhfgrid

```

A.4 Some properties of the 73 keV photon beam at the P01 beamline

beamline

The properties of the 73 keV beam have been measured at P01 beamline using its standard DCM and MRM. The Si (3 1 1) reflections were used in the DCM. The PETRA ring was operated in 40-bunch mode (192 ns time distance between the bunches) and the ring current was 95 mA. The measurement setup was the same as in fig. 4.12. The beam size between the DCM and MRM was defined by a slit. The divergence of the beam incident on the DCM was measured by scanning the angle of the 2nd crystal in DCM. The acquired curve is shown on the fig. A.3. Its shape can be approximated by a Gaussian with the FWHM 8.46(1) μ rad.

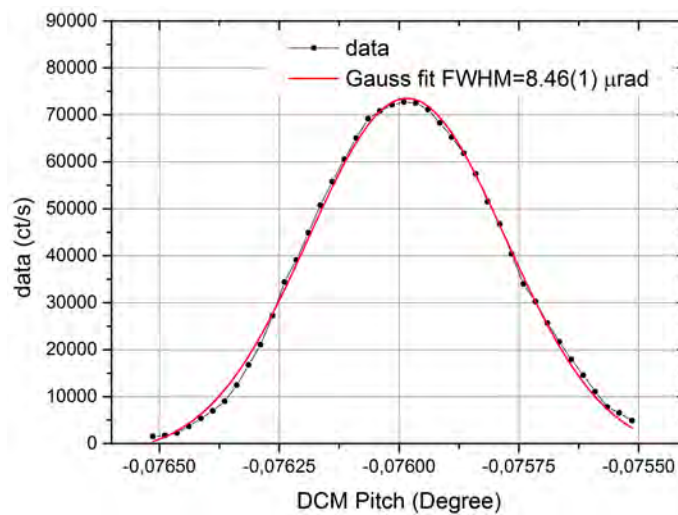


Figure A.3: Rocking curve of P01 beamline DCM at 73 keV.

The energy bandwidth of the DCM has been measured by scanning its Bragg angle and acquiring nuclear incoherent scattering events from Ir (fig. A.4). The measured data can be approximated by Gaussian function with the FWHM of 8.1(11) eV. The angular width of Si (3 1 1) reflection is shown in the fig. A.4 by top x-axis. The shape of this curve can be approximated by Gaussian function with the FWHM 6.5(8) μ rad.

Next, we measured angular divergence of the beam incident on the MRM. For that the both crystals of the MRM have been moved synchronously, and the beam intensity after the MRM has been measured by an APD detector. The measured curve "angular movement vs. intensity" is shown on the fig. A.5. The FWHM of this curve is 5.17(7) μ rad which is smaller than the 8.46(1) μ rad width of the DCM rocking curve in fig. A.3.

Horizontal and vertical profiles of the beam incident onto and reflected by the MRM were measured by closing the slit between DCM and MRM to 0.1x0.1 mm² and scanning

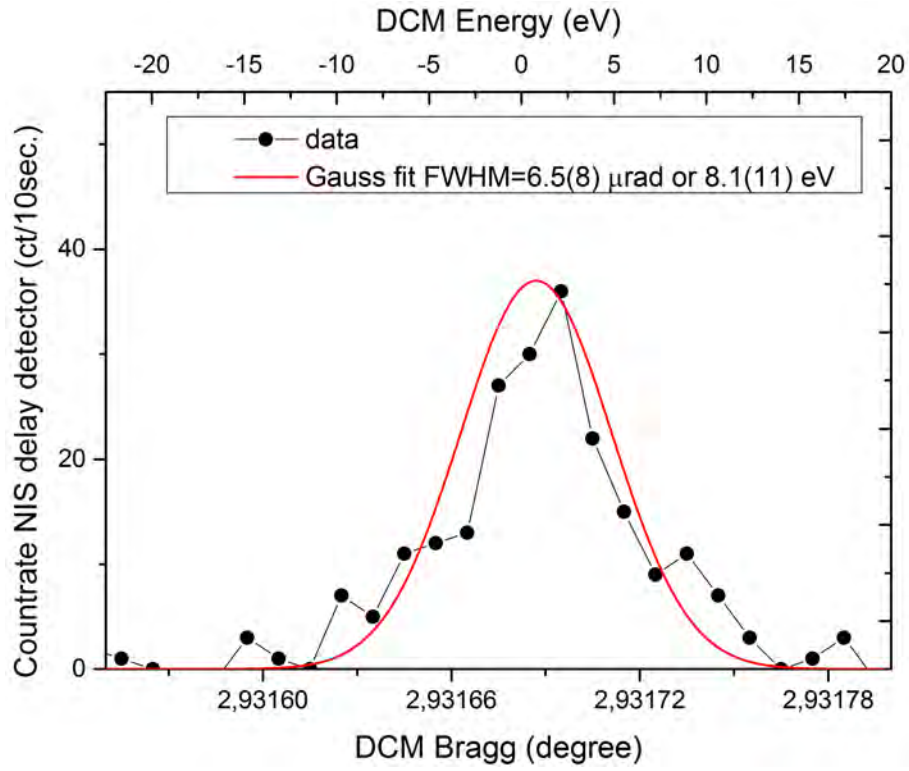


Figure A.4: Divergence of the beam reflected by DCM and its energy width.

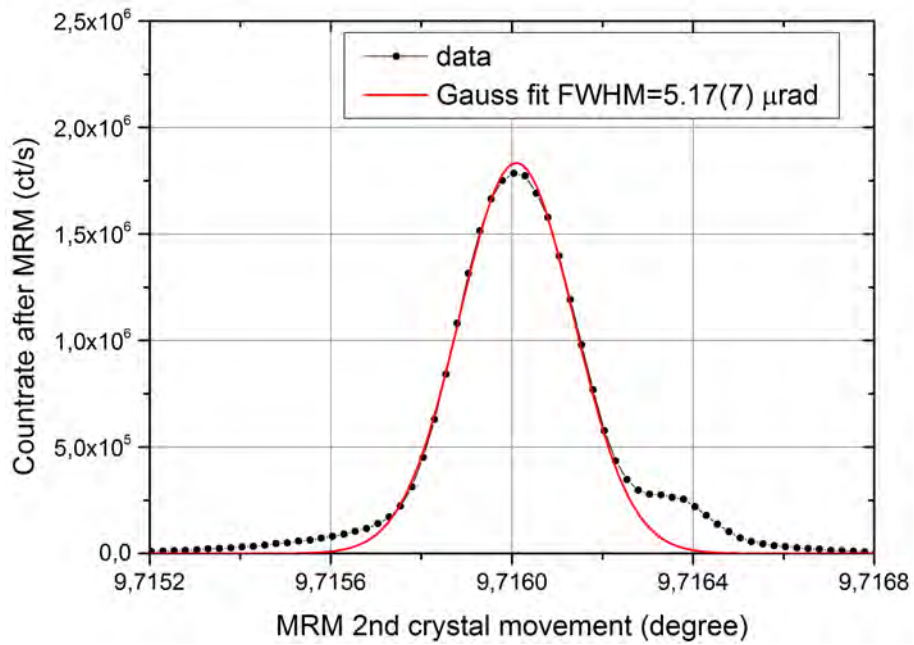


Figure A.5: Divergence of the beam incident on MRM.

them horizontally and vertically. The results are shown in the fig. A.6, a and b, respectively. The beam profiles exhibit asymmetric shapes, notably, a satellite beam is present in vertical direction between DCM and MRM.

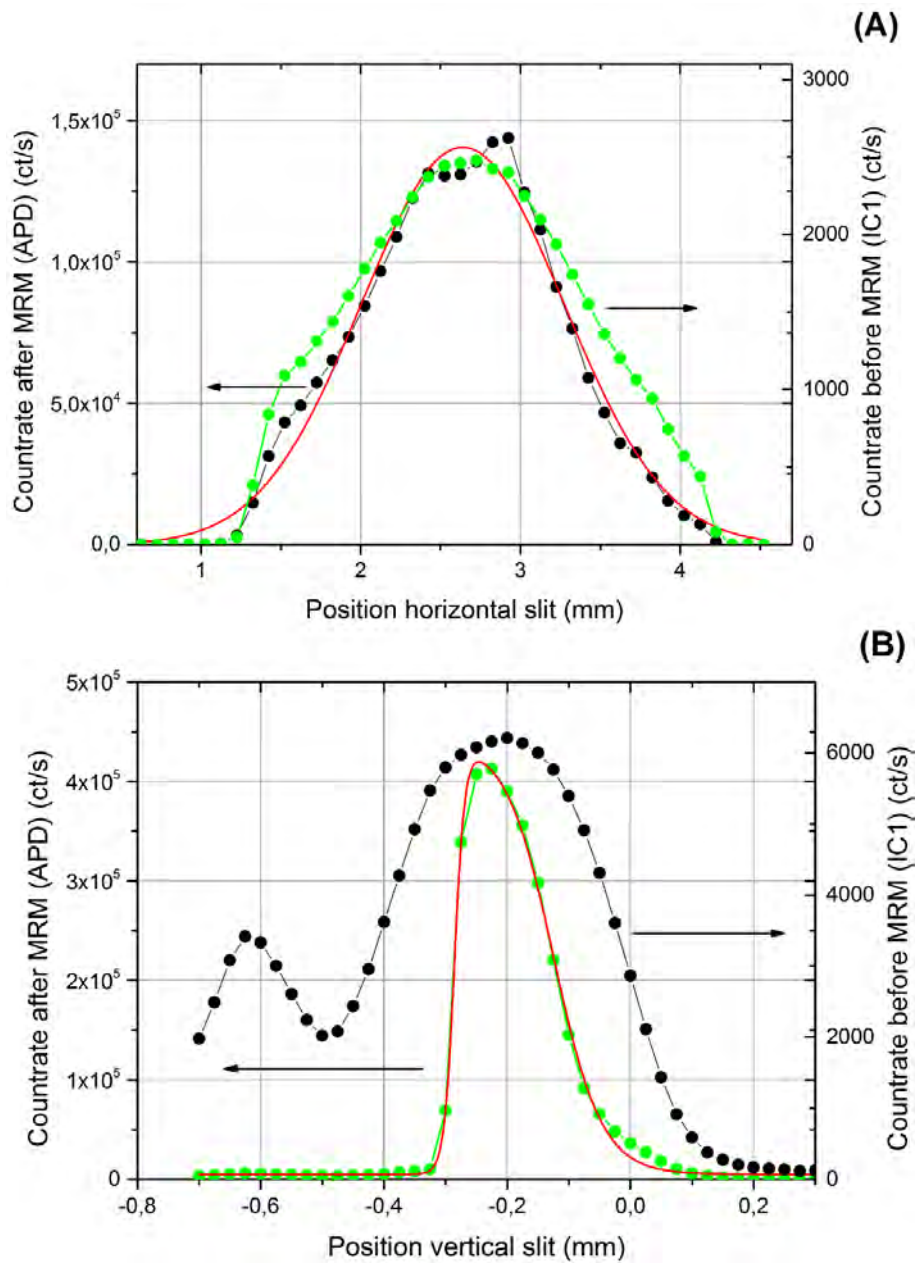


Figure A.6: Horizontal (A) and vertical (B) beam sizes before and after the MRM.

Bibliography

- [1] J. Als-Nielsen and D. F. McMorrow. *Elements of Modern X-ray Physics*. Wiley, 2011. ISBN 9781119970156. URL <https://books.google.fr/books?id=r1qlboWlTRMC>.
 - [2] R. Röhlberger. *Nuclear condensed matter physics with synchrotron radiation: basic principles, methodology and applications*, volume 208 of *Springer tracts in modern physics*. Springer, Heidelberg, 2004. doi: 10.1007/b86125. URL <http://www.springer.com/de/book/9783540232445>.
 - [3] A. Furrer, T. Strässle, and J. Mesot. *Neutron Scattering in Condensed Matter Physics*. Series on neutron techniques and applications. World Scientific, 2009. ISBN 9789810248314. URL <https://books.google.de/books?id=3epAAQAAIAAJ>.
 - [4] P.A. Lee. From high temperature superconductivity to quantum spin liquid: progress in strong correlation physics. *Reports on Progress in Physics*, 71(1):012501, 2008. URL <http://stacks.iop.org/0034-4885/71/i=1/a=012501>.
 - [5] G. Kotliar and D. Vollhardt. Strongly correlated materials: Insights from dynamical mean-field theory. *Physics Today*, 57:53, 2004. URL <http://dx.doi.org/10.1063/1.1712502>.
 - [6] E. Dagotto. Correlated electrons in high-temperature superconductors. *Rev. Mod. Phys.*, 66:763–840, Jul 1994. doi: 10.1103/RevModPhys.66.763. URL <http://link.aps.org/doi/10.1103/RevModPhys.66.763>.
 - [7] W. Witczak-Krempa, G. Chen, Y.B. Kim, and L. Balents. Correlated quantum phenomena in the strong spin-orbit regime. *Ann. Rev. of Cond. Matt. Phys.*, 5(1):57–82, 2014. doi: 10.1146/annurev-conmatphys-020911-125138. URL <http://www.annualreviews.org/doi/abs/10.1146/annurev-conmatphys-020911-125138>.
 - [8] Y. K. Kim, O. Krupin, J. D. Denlinger, A. Bostwick, E. Rotenberg, Q. Zhao, J. F. Mitchell, J. W. Allen, and B. J. Kim. Fermi arcs in a doped pseudospin-1/2 heisenberg antiferromagnet. *Science*, 345(6193):187–190, 2014. ISSN 0036-8075. doi:
-

- 10.1126/science.1251151. URL <http://science.sciencemag.org/content/345/6193/187>.
- [9] K. Fujiwara, Y. Fukuma, J. Matsuno, H. Idzuchi, Y. Niimi, Y. Otani, and H. Takagi. 5d iridium oxide as a material for spin-current detection. *Nat. Comm.*, 4:2893, Dec 2013. URL <http://dx.doi.org/10.1038/ncomms3893>.
- [10] G. Cao and L. De Long. *Frontiers of 4d- and 5d- Transition Metal Oxides*. World Scientific Publishing Company, 2013. ISBN 9789814374859. URL <https://books.google.de/books?id=DRzNnQEACAAJ>.
- [11] St. Boseggia. Magnetic order and excitations in perovskite iridates studied with resonant x-ray scattering techniques. Phd thesis University College London, 2015. URL <http://discovery.ucl.ac.uk/1459969/>.
- [12] H. Gretarsson. X-ray spectroscopy studies of iridates and iron based superconductors. Phd thesis University of Toronto, 2013. URL <https://tspace.library.utoronto.ca/handle/1807/43567>.
- [13] B. J. Kim, Hosub Jin, S. J. Moon, J.-Y. Kim, B.-G. Park, C. S. Leem, Jaejun Yu, T. W. Noh, C. Kim, S.-J. Oh, J.-H. Park, V. Durairaj, G. Cao, and E. Rotenberg. Novel $J_{\text{eff}} = 1/2$ mott state induced by relativistic spin-orbit coupling in Sr_2IrO_4 . *Phys. Rev. Lett.*, 101:076402, Aug 2008. doi: 10.1103/PhysRevLett.101.076402. URL <http://link.aps.org/doi/10.1103/PhysRevLett.101.076402>.
- [14] G. Jackeli and G. Khaliullin. Mott insulators in the strong spin-orbit coupling limit: From Heisenberg to a quantum compass and Kitaev models. *Phys. Rev. Lett.*, 102:017205, Jan 2009. doi: 10.1103/PhysRevLett.102.017205. URL <http://link.aps.org/doi/10.1103/PhysRevLett.102.017205>.
- [15] C. Donnerer, Z. Feng, J. G. Vale, S. N. Andreev, I. V. Solovyev, E. C. Hunter, M. Hanfland, R. S. Perry, H. M. Rønnow, M. I. McMahon, V. V. Mazurenko, and D. F. McMorrow. Pressure dependence of the structure and electronic properties of $\text{Sr}_3\text{Ir}_2\text{O}_7$. *Phys. Rev. B*, 93:174118, May 2016. doi: 10.1103/PhysRevB.93.174118. URL <http://link.aps.org/doi/10.1103/PhysRevB.93.174118>.
- [16] M. K. Crawford, M. A. Subramanian, R. L. Harlow, J. A. Fernandez-Baca, Z. R. Wang, and D. C. Johnston. Structural and magnetic studies of Sr_2IrO_4 . *Phys. Rev. B*, 49:9198–9201, Apr 1994. doi: 10.1103/PhysRevB.49.9198. URL <http://link.aps.org/doi/10.1103/PhysRevB.49.9198>.
- [17] Chetan Dhital, Tom Hogan, Z. Yamani, Clarina de la Cruz, Xiang Chen, Sovit
-

-
- Khadka, Zhensong Ren, and Stephen D. Wilson. Neutron scattering study of correlated phase behavior in Sr_2IrO_4 . *Phys. Rev. B*, 87:144405, Apr 2013. doi: 10.1103/PhysRevB.87.144405. URL <http://link.aps.org/doi/10.1103/PhysRevB.87.144405>.
- [18] S. Calder, G.-X. Cao, M. D. Lumsden, J. W. Kim, Z. Gai, B. C. Sales, D. Mandrus, and A. D. Christianson. Magnetic structural change of Sr_2IrO_4 upon Mn doping. *Phys. Rev. B*, 86:220403, Dec 2012. doi: 10.1103/PhysRevB.86.220403. URL <http://link.aps.org/doi/10.1103/PhysRevB.86.220403>.
- [19] Feng Ye, Songxue Chi, Bryan C. Chakoumakos, Jaime A. Fernandez-Baca, Tongfei Qi, and G. Cao. Magnetic and crystal structures of Sr_2IrO_4 : A neutron diffraction study. *Phys. Rev. B*, 87:140406, Apr 2013. doi: 10.1103/PhysRevB.87.140406. URL <http://link.aps.org/doi/10.1103/PhysRevB.87.140406>.
- [20] E. Gerdau and H. DeWaard. Nuclear resonant scattering of synchrotron radiation. *Hyperf. Inter.*, 123–124(1-4), 1999. ISSN 0304-3843. doi: 10.1023/A:1017073002352. URL <http://dx.doi.org/10.1023/A:1017073002352>.
- [21] N.W. Ashcroft and N.D. Mermin. *Solid State Physics*. Saunders College, Philadelphia, 1976.
- [22] Y. Maeno, H. Hashimoto, K. Yoshida, S. Nishizaki, T. Fujita, J. G. Bednorz, and F. Lichtenberg. Superconductivity in a layered perovskite without copper. *Nature*, 372(6506):532–534, Dec 1994. doi: 10.1038/372532a0. URL <http://dx.doi.org/10.1038/372532a0>.
- [23] S. Sugano, Y. Tanabe, and H. Kamimura. *Multiplets of Transition-metal Ions in Crystals*. Academic Press Inc, 1970.
- [24] E. Francisco and L. Pueyo. Theoretical spin-orbit coupling constants for 3d ions in crystals. *Phys. Rev. B*, 37:5278–5288, Apr 1988. doi: 10.1103/PhysRevB.37.5278. URL <http://link.aps.org/doi/10.1103/PhysRevB.37.5278>.
- [25] L. F. Mattheiss. Electronic structure of RuO_2 , OsO_2 , and IrO_2 . *Phys. Rev. B*, 13: 2433–2450, Mar 1976. doi: 10.1103/PhysRevB.13.2433. URL <http://link.aps.org/doi/10.1103/PhysRevB.13.2433>.
- [26] S. Blundell. *Magnetism in Condensed Matter*. Oxford Master Series in Condensed Matter Physics. OUP Oxford, 2001. ISBN 9780198505914. URL <https://books.google.de/books?id=OGhGmgEACAAJ>.
-

- [27] A. Abragam and B. Bleaney. *Electron paramagnetic resonance of transition ions*. International series of monographs on physics. Clarendon P., 1970. URL <https://books.google.de/books?id=hSVRAAAAMAAJ>.
- [28] J. P. Clancy, N. Chen, C. Y. Kim, W. F. Chen, K. W. Plumb, B. C. Jeon, T. W. Noh, and Young-June Kim. Spin-orbit coupling in iridium-based 5d compounds probed by x-ray absorption spectroscopy. *Phys. Rev. B*, 86:195131, Nov 2012. doi: 10.1103/PhysRevB.86.195131. URL <http://link.aps.org/doi/10.1103/PhysRevB.86.195131>.
- [29] M. Moretti Sala, K. Ohgushi, A. Al-Zein, Y. Hirata, G. Monaco, and M. Krisch. CaIrO_3 : A spin-orbit mott insulator beyond the $j_{\text{eff}} = 1/2$ ground state. *Phys. Rev. Lett.*, 112:176402, Apr 2014. doi: 10.1103/PhysRevLett.112.176402. URL <http://link.aps.org/doi/10.1103/PhysRevLett.112.176402>.
- [30] A. P. Mackenzie, S. R. Julian, A. J. Diver, G. J. McMullan, M. P. Ray, G. G. Lonzarich, Y. Maeno, S. Nishizaki, and T. Fujita. Quantum oscillations in the layered perovskite superconductor Sr_2RuO_4 . *Phys. Rev. Lett.*, 76:3786–3789, May 1996. doi: 10.1103/PhysRevLett.76.3786. URL <http://link.aps.org/doi/10.1103/PhysRevLett.76.3786>.
- [31] A. Damascelli, D. H. Lu, K. M. Shen, N. P. Armitage, F. Ronning, D. L. Feng, C. Kim, Z.-X. Shen, T. Kimura, Y. Tokura, Z. Q. Mao, and Y. Maeno. Fermi surface, surface states, and surface reconstruction in Sr_2RuO_4 . *Phys. Rev. Lett.*, 85:5194–5197, Dec 2000. doi: 10.1103/PhysRevLett.85.5194. URL <http://link.aps.org/doi/10.1103/PhysRevLett.85.5194>.
- [32] M. Moretti Sala, S. Boseggia, D. F. McMorrow, and G. Monaco. Resonant x-ray scattering and the $j_{\text{eff}}=1/2$ electronic ground state in iridate perovskites. *Phys. Rev. Lett.*, 112:026403, Jan 2014. doi: 10.1103/PhysRevLett.112.026403. URL <http://link.aps.org/doi/10.1103/PhysRevLett.112.026403>.
- [33] M. Moretti Sala, M. Rossi, S. Boseggia, J. Akimitsu, N. B. Brookes, M. Isobe, M. Minola, H. Okabe, H. M. Rønnow, L. Simonelli, D. F. McMorrow, and G. Monaco. Orbital occupancies and the putative $j_{\text{eff}} = 1/2$ ground state in Ba_2IrO_4 : A combined oxygen K-edge XAS and RIXS study. *Phys. Rev. B*, 89:121101, Mar 2014. doi: 10.1103/PhysRevB.89.121101. URL <http://link.aps.org/doi/10.1103/PhysRevB.89.121101>.
- [34] R. Coldea, S. M. Hayden, G. Aeppli, T. G. Perring, C. D. Frost, T. E. Mason, S.-W. Cheong, and Z. Fisk. Spin waves and electronic interactions in La_2CuO_4 . *Phys.*
-

- Rev. Lett.*, 86:5377–5380, Jun 2001. doi: 10.1103/PhysRevLett.86.5377. URL <http://link.aps.org/doi/10.1103/PhysRevLett.86.5377>.
- [35] J. Kim, D. Casa, M. H. Upton, T. Gog, Y.-J. Kim, J. F. Mitchell, M. van Veenendaal, M. Daghofer, J. van den Brink, G. Khaliullin, and B. J. Kim. Magnetic excitation spectra of Sr_2IrO_4 probed by resonant inelastic x-ray scattering: Establishing links to cuprate superconductors. *Phys. Rev. Lett.*, 108:177003, Apr 2012. doi: 10.1103/PhysRevLett.108.177003. URL <http://link.aps.org/doi/10.1103/PhysRevLett.108.177003>.
- [36] S. Boseggia, H.C. Walker, J. Vale, R. Springell, Z. Feng, R.S. Perry, M.M. Sala, H.M. Rønnow, S.P. Collins, and D.F. McMorrow. Locking of iridium magnetic moments to the correlated rotation of oxygen octahedra in Sr_2IrO_4 revealed by x-ray resonant scattering. *J. of Phys.: Cond. Matt.*, 25(42):422202, 2013. URL <http://stacks.iop.org/0953-8984/25/i=42/a=422202>.
- [37] B. J. Kim, H. Ohsumi, T. Komesu, S. Sakai, T. Morita, H. Takagi, and T. Arima. Phase-sensitive observation of a spin-orbital mott state in Sr_2IrO_4 . *Science*, 323(5919):1329–1332, 2009. ISSN 0036-8075. doi: 10.1126/science.1167106. URL <http://science.sciencemag.org/content/323/5919/1329>.
- [38] C. Donnerer, M. C. Rahn, M. Moretti Sala, J. G. Vale, D. Pincini, J. Stremper, M. Krisch, D. Prabhakaran, A. T. Boothroyd, and D. F. McMorrow. All-in-all-out magnetic order and propagating spin waves in $\text{Sm}_2\text{Ir}_2\text{O}_7$. *Phys. Rev. Lett.*, 117:037201, Jul 2016. doi: 10.1103/PhysRevLett.117.037201. URL <http://link.aps.org/doi/10.1103/PhysRevLett.117.037201>.
- [39] Institut Laue-Langevin. Neutron data booklet, 1993. URL <https://www.ill.eu/quick-links/publications/>.
- [40] R. Röhlberger, E. Witthoff, E. Gerdau, and E. Lüken. Observation of nuclear diffraction from multilayers with a $\text{Fe}/^{57}\text{Fe}$ superstructure. *J. of Appl. Phys.*, 74(3):1933–1937, 1993. doi: 10.1063/1.354776. URL <http://dx.doi.org/10.1063/1.354776>.
- [41] S. Y. Reece, J. A. Hamel, K. Sung, Th. D. Jarvi, A. J. Esswein, J. J. H. Pijpers, and D. G. Nocera. Wireless solar water splitting using silicon-based semiconductors and earth-abundant catalysts. *Science*, 334(6056):645–648, 2011. ISSN 0036-8075. doi: 10.1126/science.1209816. URL <http://science.sciencemag.org/content/334/6056/645>.
- [42] A. Fujishima and K. Honda. Electrochemical photolysis of water at a semicon-

- ductor electrode. *Nature*, 238(5358):37–38, Jul 1972. doi: 10.1038/238037a0. URL <http://dx.doi.org/10.1038/238037a0>.
- [43] J. Garcia-Martinez and Z.L. Wang. *Nanotechnology for the Energy Challenge*. Wiley, 2013. ISBN 9783527665129. URL <https://books.google.de/books?id=T3yXXTTXnzYC>.
- [44] E. M. Sobalvarro. Structural studies of pyrochlore and scheelite semiconductors for solar fuel production. Master thesis Stony Brook University, 2016.
- [45] B. Cao, D. Weinstein, B. Klobes, R.P. Hermann, K. Maeda, K. Domen, and P.G. Khalifah. Hidden vacancies in Ag-Sb-O pyrochlores: visible light absorbing semiconductors with activity for O₂ and H₂ evolution. in press, 2016.
- [46] T. Kako, N. Kikugawa, and J. Ye. Photocatalytic activities of AgSbO₃ under visible light irradiation. *Catalysis Today*, 131(1):197–202, 2008. ISSN 0920-5861. doi: <http://dx.doi.org/10.1016/j.cattod.2007.10.094>. URL <http://www.sciencedirect.com/science/article/pii/S0920586107006220>.
- [47] H. Mizoguchi, H. W. Eng, and P. M. Woodward. Probing the electronic structures of ternary perovskite and pyrochlore oxides containing Sn⁴⁺ or Sb⁵⁺. *Inorg. Chem.*, 43(5):1667–1680, 2004. doi: 10.1021/ic034551c. URL <http://dx.doi.org/10.1021/ic034551c>.
- [48] G. Laurita, K. Page, A. W. Sleight, and M. A. Subramanian. Structural investigation of the substituted pyrochlore AgSbO₃ through total scattering techniques. *Inorg. Chem.*, 52(19):11530–11537, 2013. doi: 10.1021/ic401860j. URL <http://dx.doi.org/10.1021/ic401860j>.
- [49] K.N. Liou. *An Introduction to Atmospheric Radiation*. International Geophysics. Elsevier Science, 2002. ISBN 9780080491677. URL <https://books.google.de/books?id=mQ1DiDpX34UC>.
- [50] W. Liu, X. Liu, Y. Fu, Q. You, R. Huang, P. Liu, and Zh. Li. Nanocrystalline pyrochlore AgSbO₃: Hydrothermal synthesis, photocatalytic activity and self-stable mechanism study. *Applied Catalysis B: Environmental*, 123–124:78 – 83, 2012. ISSN 0926-3373. doi: <http://dx.doi.org/10.1016/j.apcatb.2012.04.033>. URL <http://www.sciencedirect.com/science/article/pii/S0926337312001737>.
- [51] S.M. Sze and K.K. Ng. *Physics of Semiconductor Devices*. Wiley, 2006. ISBN 9780470068304. URL <http://onlinelibrary.wiley.com/book/10.1002/0470068329>.
-

-
- [52] Y.L. Chen and D.P. Yang. *Mössbauer Effect in Lattice Dynamics: Experimental Techniques and Applications*. Wiley, 2007. ISBN 9783527611430. URL <http://eu.wiley.com/WileyCDA/WileyTitle/productCd-352740712X.html>.
- [53] G. Laurita, J. Vielma, F. Winter, R. Berthelot, A. Largeau, R. Pöttgen, G. Schneider, and M.A. Subramanian. From $\text{Ag}_2\text{Sb}_2\text{O}_6$ to $\text{Cd}_2\text{Sb}_2\text{O}_7$: Investigations on an anion-deficient to ideal pyrochlore solid solution. *J. of Sol. Stat. Chem.*, 210(1):65–73, 2014. ISSN 0022-4596. doi: <http://dx.doi.org/10.1016/j.jssc.2013.11.007>. URL <http://www.sciencedirect.com/science/article/pii/S0022459613005446>.
- [54] Ph. Gütlich, E. Bill, and A. X. Trautwein. *Mössbauer Spectroscopy and Transition Metal Chemistry Fundamentals and Applications*. Springer, Heidelberg, 2011. doi: 10.1007/978-3-540-88428-6.
- [55] A. I. Chumakov and R. Rüffer. Nuclear inelastic scattering. *Hyperf. Inter.*, 113(1):59–79, 1998. ISSN 1572-9540. doi: 10.1023/A:1012659229533. URL <http://dx.doi.org/10.1023/A:1012659229533>.
- [56] G. Schatz and A. Weidinger. *Nukleare Festkörperphysik: kernphysikalische Messmethoden und ihre Anwendungen*. Teubner-Studienbuecher : Physik. Teubner, 1997. ISBN 9783519230793. URL <https://books.google.de/books?id=OGzuxs0wt1IC>.
- [57] F. E. Wagner. Mössbauer spectroscopy with $^{191,193}\text{Ir}$. *Hyperf. Inter.*, 13(1):149–173, 1983. ISSN 1572-9540. doi: 10.1007/BF01027249. URL <http://dx.doi.org/10.1007/BF01027249>.
- [58] R.L. Mössbauer, M. Lengsfeld, W. von Lieres, W. Potzel, P. Teschner, F.E. Wagner, and G. Kaindl. Nuclear gamma resonance study of the Ir–Fe and Ir–Ni alloy systems. *Z. Naturforsch. A*, 26, 1971. ISSN 0932-0784. URL <https://www.degruyter.com/view/j/zna.1971.26.issue-3/zna-1971-0303/zna-1971-0303.xml>.
- [59] O. Leupold, K. Rupprecht, and G. Wortmann. Electronic and magnetic transitions in europium compounds studied by nuclear forward scattering of synchrotron radiation. *Struct. Chem.*, 14(1):97–107, 2003. ISSN 1572-9001. doi: 10.1023/A:1021625211669. URL <http://dx.doi.org/10.1023/A:1021625211669>.
- [60] G. J. Perlow, W. Henning, D. Olson, and G. L. Goodman. Hyperfine anomaly in ^{193}Ir by Mössbauer effect, and its application to determination of the orbital part of hyperfine fields. *Phys. Rev. Lett.*, 23:680–682, Sep 1969. doi: 10.1103/PhysRevLett.23.680. URL <http://link.aps.org/doi/10.1103/PhysRevLett.23.680>.
-

- [61] I. Sergueev, A. I. Chumakov, T. H. Deschaux Beaume-Dang, R. Rüffer, C. Strohm, and U. van Bürck. Nuclear forward scattering for high energy Mössbauer transitions. *Phys. Rev. Lett.*, 99:097601, Aug 2007. doi: 10.1103/PhysRevLett.99.097601. URL <http://link.aps.org/doi/10.1103/PhysRevLett.99.097601>.
- [62] R. L. Mössbauer. Kernresonanzfluoreszenz von Gammastrahlung in ^{191}Ir . *Zeitschrift für Physik*, 151(2):124–143, 1958. ISSN 0044-3328. doi: 10.1007/BF01344210. URL <http://dx.doi.org/10.1007/BF01344210>.
- [63] R. L. Mössbauer. Kernresonanzabsorption von Gammastrahlung in ^{191}Ir . *Naturwissenschaften*, 45(22):538–539, 1958. ISSN 1432-1904. doi: 10.1007/BF00632050. URL <http://dx.doi.org/10.1007/BF00632050>.
- [64] W. Sturhahn. Nuclear resonant spectroscopy. *Journal of Physics: Condensed Matter*, 16(5):S497, 2004. URL <http://stacks.iop.org/0953-8984/16/i=5/a=009>.
- [65] G. J. Long, R. P. Hermann, F. Grandjean, E. E. Alp, W. Sturhahn, Ch. E. Johnson, D. E. Brown, O. Leupold, and R. Rüffer. Strongly decoupled europium and iron vibrational modes in filled skutterudites. *Phys. Rev. B*, 71:140302, Apr 2005. doi: 10.1103/PhysRevB.71.140302. URL <http://link.aps.org/doi/10.1103/PhysRevB.71.140302>.
- [66] R. P. Hermann, R. Jin, W. Schweika, F. Grandjean, D. Mandrus, B. C. Sales, and G. J. Long. Einstein oscillators in thallium filled antimony skutterudites. *Phys. Rev. Lett.*, 90:135505, Apr 2003. doi: 10.1103/PhysRevLett.90.135505. URL <http://link.aps.org/doi/10.1103/PhysRevLett.90.135505>.
- [67] A.I. Chumakov and W. Sturhahn. Experimental aspects of inelastic nuclear resonance scattering. *Hyperf. Inter.*, 123(1):781–808, 1999. ISSN 1572-9540. doi: 10.1023/A:1017052730094. URL <http://dx.doi.org/10.1023/A:1017052730094>.
- [68] G. T. Furukawa, M. L. Reilly, and J. S. Gallagher. Critical analysis of heat–capacity data and evaluation of thermodynamic properties of Ruthenium, Rhodium, Palladium, Iridium, and Platinum from 0 to 300 K. A Survey of the Literature Data on Osmium. *J. of Phys. and Chem. Ref. Data*, 3(1):163–209, 1974. doi: 10.1063/1.3253137. URL <http://scitation.aip.org/content/aip/journal/jpcrd/3/1/10.1063/1.3253137>.
- [69] B. R. Bullard, J. G. Mullen, and G. Schupp. Mössbauer line-shape parameters for ^{183}W and ^{191}Ir in metallic tungsten and iridium. *Phys. Rev. B*, 43:7405–7415, Apr
-

-
1991. doi: 10.1103/PhysRevB.43.7405. URL <http://link.aps.org/doi/10.1103/PhysRevB.43.7405>.
- [70] G.V. Smirnov. General properties of nuclear resonant scattering. *Hyperf. Inter.*, 123(1):31–77, 1999. ISSN 1572-9540. doi: 10.1023/A:1017007520099. URL <http://dx.doi.org/10.1023/A:1017007520099>.
- [71] H. Grünsteudel. Nuclear resonant scattering of synchrotron radiation on iron containing biomimetic compounds. PhD thesis Universität Lübeck, 1998.
- [72] A. Barla. Development of ^{119}Sn nuclear resonance scattering of synchrotron radiation and first applications. Phd thesis Universität zu Köln, 2000. URL <http://www.ph2.uni-koeln.de/204.html>.
- [73] B. Ravel and M. Newville. ATHENA, ARTEMIS, HEPHAESTUS: data analysis for X-ray absorption spectroscopy using IFEFFIT. *J. of Synchr. Rad.*, 12(4):537–541, Jul 2005. doi: 10.1107/S0909049505012719. URL <https://doi.org/10.1107/S0909049505012719>.
- [74] A. Q. R. Baron, S. Kishimoto, J. Morse, and J.-M. Rigal. Silicon avalanche photodiodes for direct detection of X-rays. *J. of Synchr. Rad.*, 13(2):131–142, Mar 2006. doi: 10.1107/S090904950503431X. URL <http://dx.doi.org/10.1107/S090904950503431X>.
- [75] J.P. Hannon and G.T. Trammell. Coherent γ -ray optics. *Hyperf. Inter.*, 123(1):127–274, 1999. ISSN 1572-9540. doi: 10.1023/A:1017011621007. URL <http://dx.doi.org/10.1023/A:1017011621007>.
- [76] W. Sturhahn and E. Gerdau. Evaluation of time-differential measurements of nuclear-resonance scattering of x rays. *Phys. Rev. B*, 49:9285–9294, Apr 1994. doi: 10.1103/PhysRevB.49.9285. URL <http://link.aps.org/doi/10.1103/PhysRevB.49.9285>.
- [77] W. Sturhahn. CONUSS and PHOENIX: Evaluation of nuclear resonant scattering data. *Hyperf. Inter.*, 125(1):149–172, 2000. ISSN 1572-9540. doi: 10.1023/A:1012681503686. URL <http://dx.doi.org/10.1023/A:1012681503686>.
- [78] Y. V. Shvyd'ko. MOTIF: Evaluation of time spectra for nuclear forward scattering. *Hyperf. Inter.*, 125(1):173–188, 2000. ISSN 1572-9540. doi: 10.1023/A:1012633620524. URL <http://dx.doi.org/10.1023/A:1012633620524>.
- [79] W.M. Visscher. Study of lattice vibrations by resonance absorption of nu-
-

- clear gamma rays. *Annals of Physics*, 9(2):194–210, 1960. URL <http://www.sciencedirect.com/science/article/pii/0003491660900282>.
- [80] K. S. Singwi and A. Sjölander. Resonance absorption of nuclear gamma rays and the dynamics of atomic motions. *Phys. Rev.*, 120:1093–1102, Nov 1960. doi: 10.1103/PhysRev.120.1093. URL <http://link.aps.org/doi/10.1103/PhysRev.120.1093>.
- [81] H. Weiß and H. Langhoff. Observation of localized modes in TbO_x using the Mößbauer effect. *Zeitschrift für Physik B Condensed Matter*, 33(4):365–368, 1979. ISSN 1431-584X. doi: 10.1007/BF01319926. URL <http://dx.doi.org/10.1007/BF01319926>.
- [82] H. Weiss and H. Langhoff. Observation of one phonon transitions in terbium by nuclear resonance fluorescence. *Phys. Lett. A*, 69(6):448 – 450, 1979. ISSN 0375-9601. doi: [http://dx.doi.org/10.1016/0375-9601\(79\)90404-3](http://dx.doi.org/10.1016/0375-9601(79)90404-3). URL <http://www.sciencedirect.com/science/article/pii/0375960179904043>.
- [83] M. Seto, Y. Yoda, S. Kikuta, X. W. Zhang, and M. Ando. Observation of nuclear resonant scattering accompanied by phonon excitation using synchrotron radiation. *Phys. Rev. Lett.*, 74:3828–3831, May 1995. doi: 10.1103/PhysRevLett.74.3828. URL <http://link.aps.org/doi/10.1103/PhysRevLett.74.3828>.
- [84] W. Sturhahn, T. S. Toellner, E. E. Alp, X. Zhang, M. Ando, Y. Yoda, S. Kikuta, M. Seto, C. W. Kimball, and B. Dabrowski. Phonon density of states measured by inelastic nuclear resonant scattering. *Phys. Rev. Lett.*, 74:3832–3835, May 1995. doi: 10.1103/PhysRevLett.74.3832. URL <http://link.aps.org/doi/10.1103/PhysRevLett.74.3832>.
- [85] A.I. Chumakov, R. Rüffer, H. Grünsteudel, H. F. Grünsteudel, G. Grübel, J. Metge, O. Leupold, and H. A. Goodwin. Energy dependence of nuclear recoil measured with incoherent nuclear scattering of synchrotron radiation. *Europhys. Lett.*, 30(7): 427, 1995. URL <http://stacks.iop.org/0295-5075/30/i=7/a=009>.
- [86] R. Rüffer and A.I. Chumakov. Nuclear inelastic scattering. *Hyperf. Inter.*, 128(1): 255–272, 2000. ISSN 1572-9540. doi: 10.1023/A:1012643918108. URL <http://dx.doi.org/10.1023/A:1012643918108>.
- [87] W. Sturhahn and V.G. Kohn. Theoretical aspects of incoherent nuclear resonant scattering. *Hyperf. Inter.*, 123(1):367–399, 1999. ISSN 1572-9540. doi: 10.1023/A:1017071806895. URL <http://dx.doi.org/10.1023/A:1017071806895>.
-

-
- [88] R.P. Hermann and I. Sergueev. Measurements of phonon density of states in Te single crystal. Unpublished, 2011.
- [89] Harry J. Lipkin. Mössbauer sum rules for use with synchrotron sources. *Hyperf. Inter.*, 123(1):349–366, 1999. ISSN 1572-9540. doi: 10.1023/A:1017019822825. URL <http://dx.doi.org/10.1023/A:1017019822825>.
- [90] V.G. Kohn and A.I. Chumakov. DOS: Evaluation of phonon density of states from nuclear resonant inelastic absorption. *Hyperf. Inter.*, 125(1):205–221, 2000. ISSN 1572-9540. doi: 10.1023/A:1012689705503. URL <http://dx.doi.org/10.1023/A:1012689705503>.
- [91] A. I. Chumakov, I. Sergeev, J.-Ph. Celse, R. Rüffer, M. Lesourd, L. Zhang, and M. Sánchez del Río. Performance of a silicon monochromator under high heat load. *J. of Synchr. Rad.*, 21(2):315–324, Mar 2014. doi: 10.1107/S1600577513033158. URL <http://onlinelibrary.wiley.com/doi/10.1107/S1600577513033158/abstract>.
- [92] Yu. Shvyd'ko, St. Stoupin, V. Blank, and S. Terentyev. Near-100 % Bragg reflectivity of x-rays. *Nat. Photon.*, 5(9):539–542, Sep 2011. ISSN 1749-4885. doi: 10.1038/nphoton.2011.197. URL [10.1038/nphoton.2011.197](http://dx.doi.org/10.1038/nphoton.2011.197).
- [93] D. Bessas, D. G. Merkel, A. I. Chumakov, R. Rüffer, R. P. Hermann, I. Sergueev, A. Mahmoud, B. Klobes, M. A. McGuire, M. T. Sougrati, and L. Stievano. Nuclear forward scattering of synchrotron radiation by ^{99}Ru . *Phys. Rev. Lett.*, 113:147601, Oct 2014. doi: 10.1103/PhysRevLett.113.147601. URL <http://link.aps.org/doi/10.1103/PhysRevLett.113.147601>.
- [94] A. Authier. *Dynamical Theory of X-ray Diffraction*. IUCr Crystallographic Symposia Series. Oxford University Press, 2001. ISBN 9780198559603. URL https://books.google.de/books?id=uW9B_ZwoM-QC.
- [95] D. T. Cromer and J. B. Mann. X-ray scattering factors computed from numerical Hartree–Fock wave functions. *Acta Cryst. A*, 24(2):321–324, Mar 1968. doi: 10.1107/S0567739468000550. URL <https://doi.org/10.1107/S0567739468000550>.
- [96] L. Kissel and R. H. Pratt. Corrections to tabulated anomalous-scattering factors. *Acta Cryst. A*, 46(3):170–175, Mar 1990. doi: 10.1107/S0108767389010718. URL <https://doi.org/10.1107/S0108767389010718>.
- [97] T.S. Toellner. Monochromatization of synchrotron radiation for nuclear resonant scattering experiments. *Hyperf. Interact.*, 125(1):3–28, 2000. ISSN 1572-9540. doi:
-

- 10.1023/A:1012621317798. URL <http://link.springer.com/article/10.1023%2FA%3A1012621317798>.
- [98] U. Pelzer. Development of ^{121}Sb nuclear forward scattering and high pressure applications. PhD thesis Universität zu Köln, 2013. URL <http://kups.ub.uni-koeln.de/5391/>.
- [99] Yu. Shvydko. *X-ray optics: high-energy-resolution applications*. Springer-Verlag Berlin Heidelberg, 2004. ISBN 9783540408901 3540408908 9783642059926 3642059929. URL <http://dx.doi.org/10.1007/978-3-540-40890-1>.
- [100] A.Q.R. Baron. Introduction to high-resolution inelastic x-ray scattering. arxiv preprint 1504.01098. 2015. URL <https://arxiv.org/abs/1504.01098>.
- [101] M. Lucht. Eine hochstabile Temperaturregelung: Anwendungen in der Monochromatisierung und der exakten Bragg-Rückstreuung von Synchrotronstrahlung. Diploma thesis Universität Hamburg, 1998.
- [102] P. van der Linden, H.-C. Wille, and Yu. V. Shvyd'ko. High resolution sapphire Bragg backscattering monochromator. *AIP Conf. Proc.*, 879(1):915–917, 2007. doi: 10.1063/1.2436210. URL <http://aip.scitation.org/doi/abs/10.1063/1.2436210>.
- [103] I. Sergueev, H.-C. Wille, R. P. Hermann, D. Bessas, Yu. V. Shvyd'ko, M. Zajaac, and R. Rüffer. Milli-electronvolt monochromatization of hard x-rays with a sapphire backscattering monochromator. *J. of Synchr. Rad.*, 18(5):802–810. ISSN 0909-0495, 1600-5775. doi: 10.1107/S090904951102485X. URL <http://scripts.iucr.org/cgi-bin/paper?S090904951102485X>.
- [104] A. Caticha and S. Caticha-Ellis. Dynamical theory of x-ray diffraction at Bragg angles near $\pi/2$. *Phys. Rev. B*, 25:971–983, Jan 1982. doi: 10.1103/PhysRevB.25.971. URL <http://link.aps.org/doi/10.1103/PhysRevB.25.971>.
- [105] A. Caticha and S. Caticha-Ellis. Dynamical diffraction of x-rays by thin crystals at Bragg angles near $\pi/2$. *Phys. Stat. Sol. (a)*, 119(1):47–54, 1990. ISSN 1521-396X. doi: 10.1002/pssa.2211190106. URL <http://dx.doi.org/10.1002/pssa.2211190106>.
- [106] W. Graeff and G. Materlik. Millielectron volt energy resolution in Bragg backscattering. *Nucl. Instr. and Meth. in Phys. Res*, 195(1):97 – 103, 1982. ISSN 0167-5087. doi: 10.1016/0029-554X(82)90764-9. URL <http://www.sciencedirect.com/science/article/pii/0029554X82907649>.
-

-
- [107] V. I. Kushnir and E. V. Suvorov. X-ray backscattering on perfect crystals $2\theta \approx \pi$. *Phys. Stat. Sol. (a)*, 122(1):391–404, 1990. ISSN 1521-396X. doi: 10.1002/pssa.2211220138. URL <http://dx.doi.org/10.1002/pssa.2211220138>.
- [108] T. S. Toellner, J. Collins, K. Goetze, M. Y. Hu, C. Preissner, E. Trakhtenberg, and L. Yan. Ultra-stable sub-mev monochromator for hard x-rays. *J. Synchr. Rad.*, 22 (Pt 5):1155–1162, Sep 2015. ISSN 0909-0495. doi: 10.1107/S1600577515012230. URL <http://www.ncbi.nlm.nih.gov/pmc/articles/PMC4542453/>.
- [109] Yu. Shvyd'ko, S. Stoupin, K. Mundboth, and J. Kim. Hard-x-ray spectrographs with resolution beyond 100 μeV . *Phys. Rev. A*, 87:043835, Apr 2013. doi: 10.1103/PhysRevA.87.043835. URL <http://link.aps.org/doi/10.1103/PhysRevA.87.043835>.
- [110] S. Kikuta, Y. Imai, T. Iizuka, Y. Yoda, X.-W. Zhang, and K. Hirano. X-ray diffraction with a Bragg angle near $\pi/2$ and its applications. *J. of Synchr. Rad.*, 5(3):670–672, May 1998. doi: 10.1107/S0909049597018621. URL <https://doi.org/10.1107/S0909049597018621>.
- [111] J. P. Sutter, E. E. Alp, M. Y. Hu, P. L. Lee, H. Sinn, W. Sturhahn, T. S. Toellner, G. Bortel, and R. Colella. Multiple-beam x-ray diffraction near exact backscattering in silicon. *Phys. Rev. B*, 63:094111, Jan 2001. doi: 10.1103/PhysRevB.63.094111. URL <http://link.aps.org/doi/10.1103/PhysRevB.63.094111>.
- [112] T. Jach, Y. Zhang, R. Colella, M. de Boissieu, M. Boudard, A. I. Goldman, T. A. Lograsso, D. W. Delaney, and S. Kycia. Dynamical diffraction and x-ray standing waves from atomic planes normal to a twofold symmetry axis of the quasicrystal AlPdMn. *Phys. Rev. Lett.*, 82:2904–2907, Apr 1999. doi: 10.1103/PhysRevLett.82.2904. URL <http://link.aps.org/doi/10.1103/PhysRevLett.82.2904>.
- [113] Yu.V. Shvyd'ko and E. Gerdau. Backscattering mirrors for x-rays and Mössbauer radiation. *Hyperf. Inter.*, 123(1):741–776, 1999. ISSN 1572-9540. doi: 10.1023/A:1017048629185. URL <http://dx.doi.org/10.1023/A:1017048629185>.
- [114] H.-C Wille, Yu. V. Shvyd'ko, E. E. Alp, H. D. Rüter, O. Leupold, I. Sergueev, R. Rüf-fer, A. Barla, and J. P. Sanchez. Nuclear resonant forward scattering of synchrotron radiation from ^{121}Sb at 37.13 keV. *Europhys. Lett.*, 74(1):170–176. ISSN 0295-5075, 1286-4854. doi: 10.1209/epl/i2005-10494-2. URL <http://iopscience.iop.org/article/10.1209/epl/i2005-10494-2>.
- [115] B. Klobes, A. Desmedt, I. Sergueev, K. Schmalzl, and R.P. Hermann. ^{129}Xe nuclear
-

- resonance scattering on solid Xe and ^{129}Xe clathrate hydrate. *Europhys. Lett.*, 103(3): 36001, 2013. URL <http://stacks.iop.org/0295-5075/103/i=3/a=36001>.
- [116] Yu. Shvyd'ko. Private communication, 2014.
- [117] A. Snigirev, V. Kohn, I. Snigireva, A. Souvorov, and B. Lengeler. Focusing high-energy x rays by compound refractive lenses. *Appl. Opt.*, 37(4):653–662, Feb 1998. doi: 10.1364/AO.37.000653. URL <http://ao.osa.org/abstract.cfm?URI=ao-37-4-653>.
- [118] G.F. Knoll. *Radiation Detection and Measurement*. John Wiley & Sons, 2010. ISBN 9780470131480. URL <https://books.google.de/books?id=4vTJ7UDel5IC>.
- [119] M. Spiwek. Private communications with DESY crystal preparation laboratory, 2016.
- [120] F.-U. Dill. Measurements at P01 beamline, 2015.
- [121] Y. Okada and Y. Tokumaru. Precise determination of lattice parameter and thermal expansion coefficient of silicon between 300 and 1500 K. *J. of Appl. Phys.*, 56(2): 314–320, 1984. doi: 10.1063/1.333965. URL <http://dx.doi.org/10.1063/1.333965>.
- [122] R. Hull. *Properties of Crystalline Silicon*. EMIS datareviews series. INSPEC, 1999. ISBN 9780852969335. URL https://books.google.de/books?id=C_TWB_0rRLgC.
- [123] A.I. Chumakov. Private communications, 2017.
- [124] Brookhaven National Laboratory. ENDSF database, . URL <http://www.nndc.bnl.gov/ensdf/>. Accessed: 2016-10-18.
- [125] S. Kishimoto, Y. Yoda, Y. Kobayashi, S. Kitao, R. Haruki, and M. Seto. Evidence for nuclear excitation by electron transition on ^{193}Ir and its probability. *Nuclear Physics A*, 748(1/2):3 – 11, 2005. ISSN 0375-9474. doi: <http://dx.doi.org/10.1016/j.nuclphysa.2004.10.016>. URL <http://www.sciencedirect.com/science/article/pii/S0375947404011066>.
- [126] E. Achterberg, O.A. Capurro, G.V. Marti, V.R. Vanin, and R.M. Castro. Nuclear data sheets for $A=193$. *Nuclear Data Sheets*, 107(1):1 – 224, 2006. ISSN
-

-
- 0090-3752. doi: <http://dx.doi.org/10.1016/j.nds.2005.12.001>. URL <http://www.sciencedirect.com/science/article/pii/S0090375205001055>.
- [127] J.G Ziegler and N. B. Nichols. Optimum settings for automatic controllers. *Trans. of the ASME*, 64:759 – 768, 1942.
- [128] E.R. Dobrovinskaya, L.A. Lytvynov, and V. Pishchik. *Sapphire: Material, Manufacturing, Applications*. Micro- and Opto-Electronic Materials, Structures, and Systems. Springer US, 2009. ISBN 9780387856957. URL <https://books.google.de/books?id=IchDpFiLrGQC>.
- [129] V. E. Asadchikov, A. V. Butashin, A. V. Buzmakov, A. N. Deryabin, V. M. Kanevsky, I. A. Prokhorov, B. S. Roshchin, Yu. O. Volkov, D. A. Zolotov, A. Jafari, P. Alexeev, A. Cecilia, T. Baumbach, D. Bessas, A. N. Danilewsky, I. Sergueev, H.-C. Wille, and R. P. Hermann. Single-crystal sapphire microstructure for high-resolution synchrotron X-ray monochromators. *Cryst. Res. and Techn.*, 51(4):243–243, 2016. ISSN 1521-4079. doi: 10.1002/crat.201670008. URL <http://dx.doi.org/10.1002/crat.201670008>.
- [130] M. Tischer. Calculated photon flux at P01 beamline. Private communication, 2016.
- [131] S. L. Ruby, G. M. Kalvius, G. B. Beard, and R. E. Snyder. Interpretation of Mössbauer Measurements in Tin and Antimony. *Phys. Rev.*, 159:239–245, Jul 1967. doi: 10.1103/PhysRev.159.239. URL <http://link.aps.org/doi/10.1103/PhysRev.159.239>.
- [132] A. Svane. Calculations of hyperfine parameters in antimony compounds. *Phys. Rev. B*, 68:064422, Aug 2003. doi: 10.1103/PhysRevB.68.064422. URL <http://link.aps.org/doi/10.1103/PhysRevB.68.064422>.
- [133] G.G. Long, J.G. Stevens, and L.H. Bowen. ^{121}Sb Mössbauer spectra of antimony oxides. *Inorg. and Nucl. Chem. Lett.*, 5(10):799 – 804, 1969. ISSN 0020-1650. doi: 10.1016/0020-1650(69)80061-9. URL <http://www.sciencedirect.com/science/article/pii/0020165069800619>.
- [134] M.I. Aroyo. Forthcoming new edition of international tables for crystallography Volume A: Space-group symmetry. 2016. doi: 10.1107/97809553602060000114.
- [135] Lawrence Berkeley National Laboratory. X-ray data booklet, . URL <http://xdb.lbl.gov/>. Accessed: 2016-10-18.
- [136] H. E. Swanson. *Standard X-ray diffraction powder patterns*. U.S. Dept. of Commerce,
-

- National Bureau of Standards., Washington, 1955.
- [137] A. C. Egerton. Numerical values of chemical constants and frequencies of the elements. *Proc. of the Phys. Soc. of London*, 37(1):75, 1924. URL <http://stacks.iop.org/1478-7814/37/i=1/a=307>.
- [138] H.J. Kandiner. *Iridium*. Gmelin Handbook of Inorganic and Organometallic Chemistry - 8th edition. Springer Berlin Heidelberg, 2013. ISBN 9783662121283. URL <https://books.google.de/books?id=mImABwAAQBAJ>.
- [139] C.-M. Chan, E.D. Williams, and W.H. Weinberg. Debye temperatures of the (110) and (111) surfaces of Iridium by LEED. *Surf. Sci.*, 82(2):L577 – L581, 1979. ISSN 0039-6028. doi: 10.1016/0039-6028(79)90212-7. URL <http://www.sciencedirect.com/science/article/pii/0039602879902127>.
- [140] V. N. Antonov, V. Yu. Milman, V. V. Nemoshkalenko, and A. V. Zhalko-Titarenko. Lattice dynamics of fcc transition metals: A pseudopotential approach. *Z. für Phys. B Cond. Matt.*, 79(2):223–232, 1990. ISSN 1431-584X. doi: 10.1007/BF01406588. URL <http://dx.doi.org/10.1007/BF01406588>.
- [141] M.G. Kresch. Temperature dependence of phonons in elemental cubic metals studied by inelastic scattering of neutrons and x-rays. Phd thesis California Institute of Technology, 2009. URL <http://thesis.library.caltech.edu/4884/>.
- [142] J.K. Baria. Static and vibrational properties of transition metals. *Cz. J. of Phys.*, 52(8): 969–989, 2002. ISSN 1572-9486. doi: 10.1023/A:1019869606156. URL [10.1023/A:1019869606156](http://dx.doi.org/10.1023/A:1019869606156).
- [143] R. Heid, K.-P. Bohnen, K. Felix, K.M. Ho, and W. Reichardt. Ab initio phonon dynamics of Iridium. *J. of Phys.: Cond. Matt.*, 10(36):7967, 1998. URL <http://stacks.iop.org/0953-8984/10/i=36/a=007>.
- [144] D. L. Abernathy, M. B. Stone, M. J. Loguillo, M. S. Lucas, O. Delaire, X. Tang, J. Y. Y. Lin, and B. Fultz. Design and operation of the wide angular-range chopper spectrometer ARCS at the Spallation Neutron Source. *Rev. of Sci. Instr.*, 83(1): 015114, 2012. doi: 10.1063/1.3680104. URL <http://dx.doi.org/10.1063/1.3680104>.
- [145] R.E. MacFarlane, J.A. Rayne, and C.K. Jones. Temperature dependence of elastic moduli of Iridium. *Phys. Lett.*, 20(3):234 – 235, 1966. ISSN 0031-9163. doi: 10.1016/0031-9163(66)90340-4. URL <http://www.sciencedirect.com/science/article/pii/0031916366903404>.
-

-
- [146] G.V. Samsonov. *Handbook of the Physicochemical Properties of the Elements*. Springer US, 2012. ISBN 9781468460667. URL <https://books.google.de/books?id=ZzzjBwAAQBAJ>.
- [147] Y. Cerenius and L. Dubrovinsky. Compressibility measurements on Iridium. *J. of All. and Comp.*, 306(1–2):26 – 29, 2000. ISSN 0925-8388. doi: 10.1016/S0925-8388(00)00767-2. URL <http://www.sciencedirect.com/science/article/pii/S0925838800007672>.
- [148] A. Bosak, M. Krisch, A. Chumakov, I.A. Abrikosov, and L. Dubrovinsky. Possible artifacts in inferring seismic properties from x-ray data. *Phys. of the Earth and Plan. Inter.*, 260:14 – 19, 2016. ISSN 0031-9201. doi: 10.1016/j.pepi.2016.08.007. URL <http://www.sciencedirect.com/science/article/pii/S0031920116301765>.
- [149] H. P. Singh. Determination of thermal expansion of Germanium, Rhodium and Iridium by X-rays. *Acta Cryst. A*, 24(4):469–471, Jul 1968. doi: 10.1107/S056773946800094X. URL <https://doi.org/10.1107/S056773946800094X>.
- [150] E. Wasserman, L. Stixrude, and R. E. Cohen. Thermal properties of Iron at high pressures and temperatures. *Phys. Rev. B*, 53:8296–8309, Apr 1996. doi: 10.1103/PhysRevB.53.8296. URL <http://link.aps.org/doi/10.1103/PhysRevB.53.8296>.
- [151] G. Shen, W. Sturhahn, E. E. Alp, J. Zhao, T.S. Toellner, B. V. Prakapenka, Y. Meng, and H.-R. Mao. Phonon density of states in iron at high pressures and high temperatures. *Phys. and Chem. of Miner.*, 31(6):353–359, 2004. ISSN 1432-2021. doi: 10.1007/s00269-004-0403-1. URL <http://dx.doi.org/10.1007/s00269-004-0403-1>.
- [152] H.-P. Liermann, Z. Konôpková, W. Morgenroth, K. Glazyrin, J. Bednarčík, E. E. McBride, S. Petitgirard, J. T. Delitz, M. Wendt, Y. Bican, A. Ehnes, I. Schwark, A. Rothkirch, M. Tischer, J. Heuer, H. Schulte-Schrepping, T. Kracht, and H. Franz. The Extreme Conditions Beamline P02.2 and the Extreme Conditions Science Infrastructure at PETRAIII. *J. of Synchr. Rad.*, 22(4):908–924, Jul 2015. doi: 10.1107/S1600577515005937. URL <https://doi.org/10.1107/S1600577515005937>.
- [153] A. P. Hammersley, S. O. Svensson, M. Hanfland, A. N. Fitch, and D. Hausermann. Two-dimensional detector software: From real detector to idealised image or two-theta scan. *High Press. Res.*, 14(4-6):235–248, 1996. doi: 10.1080/08957959608201408. URL <http://dx.doi.org/10.1080/08957959608201408>.
-

- [154] H. M. Rietveld. A profile refinement method for nuclear and magnetic structures. *J. of Appl. Cryst.*, 2(2):65–71, Jun 1969. doi: 10.1107/S0021889869006558. URL [10.1107/S0021889869006558](https://doi.org/10.1107/S0021889869006558).
- [155] V. Petříček, M. Dušek, and L. Palatinus. Crystallographic computing system JANA2006: General features. *Z. f. Krist. - Cryst. Mat.*, 2229(5):345–352, May 2014. doi: 10.1515/zkri-2014-1737. URL <https://www.degruyter.com/view/j/zkri.2014.229.issue-5/zkri-2014-1737/zkri-2014-1737.xml>.
- [156] J. W. Arblaster. Crystallographic Properties of Iridium. *Plat. Met. Rev.*, 54(2):93–102, 2010. doi: 10.1595/147106710X493124. URL <http://www.ingentaconnect.com/content/matthey/pmr/2010/00000054/00000002/art00005>.
- [157] J. E. Hirsch. Spin hall effect. *Phys. Rev. Lett.*, 83:1834–1837, Aug 1999. doi: 10.1103/PhysRevLett.83.1834. URL <http://link.aps.org/doi/10.1103/PhysRevLett.83.1834>.
- [158] Zh. Qiu, D. Hou, T. Kikkawa, K. Uchida, and E. Saitoh. All-oxide spin Seebeck effects. *Appl. Phys. Expr.*, 8(8):083001, 2015. URL <http://stacks.iop.org/1882-0786/8/i=8/a=083001>.
- [159] Y. Hirata, K. Ohgushi, J.-i. Yamaura, H. Ohsumi, S. Takeshita, M. Takata, and T.-h. Arima. Complex orbital state stabilized by strong spin-orbit coupling in a metallic iridium oxide IrO₂. *Phys. Rev. B*, 87:161111, Apr 2013. doi: 10.1103/PhysRevB.87.161111. URL <http://link.aps.org/doi/10.1103/PhysRevB.87.161111>.
- [160] A. A. Bolzan, C. Fong, B. J. Kennedy, and C. J. Howard. Structural Studies of Rutile-Type Metal Dioxides. *A. Cryst. S. B*, 53(3):373–380, Jun 1997. doi: 10.1107/S0108768197001468. URL <https://doi.org/10.1107/S0108768197001468>.
- [161] U. Atzmony, E. R. Bauminger, D. Lebenbaum, A. Mustachi, S. Ofer, and J. H. Wernick. Mössbauer effect in Ir¹⁹³ in intermetallic compounds and salts of iridium. *Phys. Rev.*, 163:314–323, Nov 1967. doi: 10.1103/PhysRev.163.314. URL <http://link.aps.org/doi/10.1103/PhysRev.163.314>.
- [162] J.O. Thomson, A.H. Werkheiser, and M.W. Lindauer. Mössbauer measurements on the 73-kev state in Ir¹⁹³. *Rev. Mod. Phys.*, 36:357–361, Jan 1964. doi: 10.1103/RevModPhys.36.357. URL <http://link.aps.org/doi/10.1103/RevModPhys.36.357>.
- [163] C. Strohm, P. Würtz, I. Sergueev, O. Leupold, H.-C. Wille, R. Röhlberger, V. Schünemann, L. Dubrovinsky, A.I. Chumakov, and R. Rüffer. Fast digitizers
-

- for fully time resolved nuclear resonant scattering applications. International Conference on the Applications of the Mössbauer Effect ICAME 2015, Hamburg, 13 - 18 September 2015.
- [164] B. H. Kim, G. Khaliullin, and B. I. Min. Magnetic couplings, optical spectra, and spin-orbit exciton in 5d electron mott insulator Sr_2IrO_4 . *Phys. Rev. Lett.*, 109:167205, Oct 2012. doi: 10.1103/PhysRevLett.109.167205. URL <http://link.aps.org/doi/10.1103/PhysRevLett.109.167205>.
- [165] J. G. Zhao, L. X. Yang, Y. Yu, F. Y. Li, R. C. Yu, Z. Fang, L. C. Chen, and C. Q. Jin. High-pressure synthesis of orthorhombic SrIrO_3 perovskite and its positive magnetoresistance. *J. of Appl. Phys.*, 103(10):103706, 2008. doi: 10.1063/1.2908879. URL <http://scitation.aip.org/content/aip/journal/jap/103/10/10.1063/1.2908879>.
- [166] I. Qasim, B. J. Kennedy, and M. Avdeev. Synthesis, structures and properties of transition metal doped SrIrO_3 . *J. Mater. Chem. A*, 1:3127–3132, 2013. doi: 10.1039/C3TA00540B. URL <http://dx.doi.org/10.1039/C3TA00540B>.
- [167] G. K. Shenoy. *Mössbauer-Effect Isomer Shifts*. Springer US, Boston, MA, 1984. ISBN 978-1-4899-0462-1. doi: 10.1007/978-1-4899-0462-1_5. URL http://dx.doi.org/10.1007/978-1-4899-0462-1_5.
- [168] R. Ingalls. Electric-Field Gradient Tensor in Ferrous Compounds. *Phys. Rev.*, 133: A787–A795, Feb 1964. doi: 10.1103/PhysRev.133.A787. URL <http://link.aps.org/doi/10.1103/PhysRev.133.A787>.
- [169] G. Cao, J. Bolivar, S. McCall, J. E. Crow, and R. P. Guertin. Weak ferromagnetism, metal-to-nonmetal transition, and negative differential resistivity in single-crystal Sr_2IrO_4 . *Phys. Rev. B*, 57:R11039–R11042, May 1998. doi: 10.1103/PhysRevB.57.R11039. URL <http://link.aps.org/doi/10.1103/PhysRevB.57.R11039>.
- [170] M. Ge, Sh. Tan, Y. Huang, L. Zhang, W. Tong, L. Pi, and Y. Zhang. Magnetism of insulator Sr_2IrO_4 with strong spin \tilde{U} -orbit coupling. *J. of Magn. and Magn. Mat.*, 345:13 – 17, 2013. ISSN 0304-8853. doi: <http://dx.doi.org/10.1016/j.jmmm.2013.05.022>. URL <http://www.sciencedirect.com/science/article/pii/S030488531300351X>.
- [171] J. Kim, D. Casa, M. H. Upton, T. Gog, Young-June Kim, J. F. Mitchell, M. van Veenendaal, M. Daghofer, J. van den Brink, G. Khaliullin, and B. J. Kim. Magnetic excitation spectra of Sr_2IrO_4 probed by resonant inelastic x-ray scattering: Establishing links to cuprate superconductors. *Phys. Rev. Lett.*, 108:177003, Apr 2012.

- doi: 10.1103/PhysRevLett.108.177003. URL <http://link.aps.org/doi/10.1103/PhysRevLett.108.177003>.
- [172] M. Miyazaki, R. Kadono, M. Hiraishi, A. Koda, K. M. Kojima, K. Ohashi, T. Takayama, and H. Takagi. Evidence for ordered magnetic moments at oxygen sites in antiferromagnetic Sr_2IrO_4 and $\text{Sr}_3\text{Ir}_2\text{O}_7$. *Phys. Rev. B*, 91:155113, Apr 2015. doi: 10.1103/PhysRevB.91.155113. URL <http://link.aps.org/doi/10.1103/PhysRevB.91.155113>.
- [173] Ch. Lu, Sh. Dong, A. Quindeau, D. Preziosi, N. Hu, and M. Alexe. Dual gate control of bulk transport and magnetism in the spin-orbit insulator Sr_2IrO_4 . *Phys. Rev. B*, 91:104401, Mar 2015. doi: 10.1103/PhysRevB.91.104401. URL <http://link.aps.org/doi/10.1103/PhysRevB.91.104401>.
- [174] H. Gretarsson, N. H. Sung, M. Höppner, B. J. Kim, B. Keimer, and M. Le Tacon. Two-magnon raman scattering and pseudospin-lattice interactions in Sr_2IrO_4 and $\text{Sr}_3\text{Ir}_2\text{O}_7$. *Phys. Rev. Lett.*, 116:136401, Mar 2016. doi: 10.1103/PhysRevLett.116.136401. URL <http://link.aps.org/doi/10.1103/PhysRevLett.116.136401>.
- [175] M. DeMarco, G. Cao, J. E. Crow, D. Coffey, S. Toorongian, M. Haka, and J. Fridmann. Temperature dependence of the hyperfine magnetic field in SrRuO_3 measured by the ^{99}Ru Mössbauer effect. *Phys. Rev. B*, 62:14297–14300, Dec 2000. doi: 10.1103/PhysRevB.62.14297. URL <http://link.aps.org/doi/10.1103/PhysRevB.62.14297>.
- [176] K. Ishida, Y. Kitaoka, K. Asayama, S. Ikeda, S. Nishizaki, Y. Maeno, K. Yoshida, and T. Fujita. Anisotropic pairing in superconducting Sr_2RuO_4 : Ru NMR and NQR studies. *Phys. Rev. B*, 56:R505–R508, Jul 1997. doi: 10.1103/PhysRevB.56.R505. URL <http://link.aps.org/doi/10.1103/PhysRevB.56.R505>.
- [177] A. Bohr and V. F. Weisskopf. The influence of nuclear structure on the hyperfine structure of heavy elements. *Phys. Rev.*, 77:94–98, Jan 1950. doi: 10.1103/PhysRev.77.94. URL <http://link.aps.org/doi/10.1103/PhysRev.77.94>.
- [178] F. Wagner and U. Zahn. Mössbauer isomer shifts, hyperfine interactions, and magnetic hyperfine anomalies in compounds of iridium. *Z. f. Phys.*, 233(1):1–20, 1970. ISSN 0044-3328. doi: 10.1007/BF01396512. URL <http://dx.doi.org/10.1007/BF01396512>.
- [179] A. I. Chumakov, R. Rüffer, O. Leupold, and I. Sergueev. Insight to dynamics of molecules with nuclear inelastic scattering. *Struct. Chem.*, 14(1):109–119, 2003.
-

-
- ISSN 1572-9001. doi: 10.1023/A:1021677228507. URL <http://dx.doi.org/10.1023/A:1021677228507>.
- [180] K. Fujiwara, Y. Fukuma, H. Matsuno, J. Idzuchi, Y. Niimi, Y. Otani, and H. Tagaki. 5d iridium oxide as a material for spin-current detection. *Nat. Comm.*, 4:2893, Dec 2013. URL <http://dx.doi.org/10.1038/ncomms3893>.
- [181] K. Schlage, L. Bocklage, D. Erb, J. Comfort, H.-C. Wille, and R. Röhlsberger. Spin-structured multilayers: A new class of materials for precision spintronics. *Adv. Func. Mat.*, 26(41):7423–7430, 2016. ISSN 1616-3028. doi: 10.1002/adfm.201603191. URL <http://dx.doi.org/10.1002/adfm.201603191>.
- [182] K. Schlage, R. Röhlsberger, T. Klein, E. Burkel, C. Strohm, and R. Rüffer. Spatially resolved magnetic reversal in a multilayered exchange bias system. *N. J. of Phys.*, 11(1):013043, 2009. URL <http://stacks.iop.org/1367-2630/11/i=1/a=013043>.
- [183] R. Röhlsberger, H.-C. Wille, K. Schlage, and B. Sahoo. Electromagnetically induced transparency with resonant nuclei in a cavity. *Nature*, 482(7384):199–203, Feb 2012. ISSN 0028-0836. doi: 10.1038/nature10741. URL <http://dx.doi.org/10.1038/nature10741>.
- [184] R. Röhlsberger. The collective Lamb shift in nuclear γ -ray superradiance. *Hyperf. Inter.*, 204(1):89–96, 2012. ISSN 1572-9540. doi: 10.1007/s10751-011-0535-x. URL <http://dx.doi.org/10.1007/s10751-011-0535-x>.
- [185] R. Röhlsberger, K. Schlage, B. Sahoo, S. Couet, and R. Rüffer. Collective Lamb shift in single-photon superradiance. *Science*, 328(5983):1248–1251, 2010. ISSN 0036-8075. doi: 10.1126/science.1187770. URL <http://science.sciencemag.org/content/328/5983/1248>.
- [186] K. P. Heeg, H.-C. Wille, K. Schlage, T. Guryeva, D. Schumacher, I. Uschmann, K. S. Schulze, B. Marx, T. Kämpfer, G. G. Paulus, R. Röhlsberger, and J. Evers. Vacuum-assisted generation and control of atomic coherences at x-ray energies. *Phys. Rev. Lett.*, 111:073601, Aug 2013. doi: 10.1103/PhysRevLett.111.073601. URL <http://link.aps.org/doi/10.1103/PhysRevLett.111.073601>.
- [187] J. Haber, K. S. Schulze, K. Schlage, R. Loetzsch, L. Bocklage, T. Guryeva, H. Bernhardt, H.-C. Wille, R. Rüffer, I. Uschmann, G. G. Paulus, and R. Röhlsberger. Collective strong coupling of x-rays and nuclei in a nuclear optical lattice. *Nat. Phot.*, 10(7):445–449, Jul 2016. ISSN 1749-4885. URL <http://dx.doi.org/10.1038/nphoton.2016.77>.
-

- [188] P. Beiersdorfer, A. L. Osterheld, J. H. Scofield, J. R. Crespo López-Urrutia, and K. Widmann. Measurement of QED and hyperfine splitting in the $2s_{1/2}$ - $2p_{3/2}$ x-ray transition in Li-like $^{209}\text{Bi}^{80+}$. *Phys. Rev. Lett.*, 80:3022–3025, Apr 1998. doi: 10.1103/PhysRevLett.80.3022. URL <http://link.aps.org/doi/10.1103/PhysRevLett.80.3022>.
- [189] J. S. Grossman, L. A. Orozco, M. R. Pearson, J. E. Simsarian, G. D. Sprouse, and W. Z. Zhao. Hyperfine anomaly measurements in Francium isotopes and the radial distribution of neutrons. *Phys. Rev. Lett.*, 83:935–938, Aug 1999. doi: 10.1103/PhysRevLett.83.935. URL <http://link.aps.org/doi/10.1103/PhysRevLett.83.935>.
- [190] M. Herlitschke, A. L. Tchougreeff, A. V. Soudackov, B. Klobes, L. Stork, R. Dronskowski, and R. P. Hermann. Magnetism and lattice dynamics of FeNCN compared to FeO. *New J. Chem.*, 38:4670–4677, 2014. doi: 10.1039/C4NJ00097H. URL <http://dx.doi.org/10.1039/C4NJ00097H>.
- [191] A. Balerna and S. Mobilio. *Synchrotron Radiation: Basics, Methods and Applications*. Springer Berlin Heidelberg, 2015. ISBN 978-3-642-55315-8. doi: 10.1007/978-3-642-55315-8_1. URL http://dx.doi.org/10.1007/978-3-642-55315-8_1.
- [192] Machine design parameters for PETRA III. http://photon-science.desy.de/facilities/petra_iii/machine/parameters/index_eng.html. Accessed: 2016-10-18.
- [193] Machine design parameters for ESRF. <http://www.esrf.eu/home/UsersAndScience/Accelerators/parameters.html>. Accessed: 2016-10-18.
-

List of research achievements and publications

Publications

- Alexeev, P. and Asadchikov, V. and Bessas, D. and Butashin, A. and Deryabin, A. and Dill, F.-U. and Ehnes, A. and Herlitschke, M. and Hermann, R.P. and Jafari, A. and Prokhorov, I. and Roshchin, B. and Röhlberger, R. and Schlage, K. and Sergueev, I. and Siemens, A. and Wille, H.-C., *The sapphire backscattering monochromator at the Dynamics beamline P01 of PETRA III*, *Hyperfine Interactions* **237**, 59 (2016); doi: 10.1007/s10751-016-1291-8
- Asadchikov, V. E. and Butashin, A. V. and Buzmakov, A. V. and Deryabin, A. N. and Kanevsky, V. M. and Prokhorov, I. A. and Roshchin, B. S. and Volkov, Y. O. and Zolotov, D. A. and Jafari, A. and Hermann R.P., *Single-crystal sapphire microstructure for high-resolution synchrotron X-ray monochromators*, *Crystal Research and Technology* **51**, 290 (2016); doi: 10.1002/crat.201500343 - Journal Cover Page
- Jafari, A. and Sergueev, I. and Bessas, D. and Klobes, B. and Roschin, B.S. and Asadchikov, V. and Alexeev, P. and Härtwig, J.W. and Chumakov, A.I. and Wille, H.-C. and Hermann, R.P., *Rocking Curve Imaging of High Quality Sapphire Crystals in Backscattering Geometry*, *Journal of Applied Physics* **121**, 044901 (2017); doi: 10.1063/1.4974106

Posters

- Alexeev, P. and Asadchikov, V. and Bessas, D. *et al.*, *Towards meV resolution above 40 keV with sapphire X-ray ultraoptics*, ESRF User Meeting (Grenoble, 2014), DESY-2014-02505, <http://pubdb.xfel.eu/record/168361>
- Alexeev, P. and Wille, H.-C. and Sergueev, I. *et al.*, *High resolution monochromators for spectroscopy at high-energy Mössbauer transitions at the Dynamics Beamline P01*, ICAME 2015 (Hamburg, 2015), PUBDB-2015-04748
- Alexeev, P. and Wille, H.-C. and Leupold, O. *et al.*, *Electronic, Magnetic, and Vibrational Properties of Iridates studied by Nuclear Resonance Scattering*, Workshop "From Matter to Materials and Life" (MML), DESY (Hamburg, 2016), FZJ-2016-07549, <http://juser.fz-juelich.de/record/825069>
- Alexeev, P. and Glazyrin, K. and Sergueev, I. and Bednarcik, J. and Hermann, R.P., *High-pressure studies on filled and unfilled skutterudites*, 612. Wilhelm-Else-Heraeus-Seminar (Bad Honnef, 2016), PUBDB-2016-01617

Talks

- *The sapphire backscattering monochromator at the Dynamics beamline P01 of PETRA III*, DESY Photon Science Meeting (Hamburg, 2015)
- *The backscattering monochromator at P01 - commissioning and performance*, NRS Workshop at ICAME 2015 (Hamburg, 2015)
- *Annual reports on status of the PhD projects at the Research Center Jülich*, Jülich (2013-2015)
- *NRS at ^{193}Ir : First results from PETRA III*, NRS Workshop, (Hohwacht, 2016)
- *Magnetic and electronic structure of iridates revealed by Nuclear Resonance Scattering*, DESY Photon Science Meeting (Hamburg, 2017)

Acknowledgements

Concluding the carried out work, I would like to express my gratitude to my advisors, colleagues, and collaborators during a more than three years of work at DESY and Research Center Jülich.

First and foremost I offer my sincerest gratitude to my supervisor, Prof. Dr. Ralf Röhlsberger, who provided me the possibility to master my work in his group, catalyzed my attention on NRS studies and iridate physics, and supported me during all these years. Without his passion, fresh ideas, and efforts for connections with experts this work could not be possible. Thank you also for many perfectly organized group outings.

My thesis committee guided me through these years. My gratitude is to my Jülich supervisor Prof. Dr. Raphaël P. Hermann. Thank you for organizing my double-sided work at PETRA and Jülich, including many shuttle trips and connections with interesting people, organization of sapphire meetings. I very profited from all your activities. Thank you also for non-standard thinking and for neutron measurements on Ir metal. I would like to thank the director of JCNS-2 institute at Research Center Jülich Prof. Dr. Thomas Brückel for involving me into the institute's life.

I'm thankful to Prof. Dr. Kornelius Nielsch for careful reading and useful remarks, for his interest in NRS on non-iron resonances, possibility to participate in seminar in his group, and for participating in my thesis committee.

I would like to express my warm wishes to Dr. Hans-Christian Wille, the beamline responsible who supervised and advised me in my research activities during these years. Thank you very much for many beamtimes spent for commissioning of new devices and ideas, for your patience and careful reading of my manuscripts, proposals, and reports. Special thanks for the patient reading of the thesis draft during the rush hours at the beamline.

My rigorous wishes are pointed to Dr. Olaf Leupold, the physics genie and the teacher par excellence. I have a great honor to work with him in various projects at the beamline, enjoying his inspiration, cooperative mind, and solid background in quantum theory, NRS, monochromators, and beamline experiments. Without his persistence, patient and detailed explanations, and rigorous help with experiments many milestones of this work could not have been reached. I also very thankful to him for careful reading of the thesis draft, separating baloney ideas, correcting broken logic and my russian-german

english.

I'm grateful to the collaborators from University College London, who inspired me for studying iridate physics and who carefully pursued the development of Nuclear Resonance Scattering technique for iridates. I specially want to thank Prof. Desmond F. McMorrow for his goal-oriented views, huge professionalism and cooperativeness in experiment. Thank you for providing the large-sized single crystals of Sr_2IrO_4 which were the key object of NFS studies reported in this work. I'm thankful to Christian Donnerer for the careful explanations of iridate physics and referencing me to useful literature sources. Dr. Roman Chernikov is gratefully acknowledged for XAS measurements on iridates.

I want to thank Dr. Ilya Sergueev for many interesting discussions, help with experiments, explanation of many complex x-ray optics questions and useful hints to beamline operation and know-how. I'm proud to have a possibility of working with him and gaining many experimental and theoretical experience learning from him. I also thank him for help and assistance in many experiments at the beamline. I want to thank Dr. Konstantin Glazyrin for teaching me the interpretation of XRD patterns and useful software hints. I'm thankful to Dr. Rudolf Ruffer for the possibility to learn NRS and careful beamline operation during several experiments at ID18 (ESRF, France). His management techniques and enthusiasm are always a large work inspiration.

I acknowledge the Helmholtz Joint Research Group for financial support of the sapphire backscattering project (grant HRJRG-402). ORNL's neutron spallation source, Dr. Doug Abernathy and ARCS beamline staff is acknowledged for the INS measurements on Ir metal.

My sincere thanks goes to Dr. Marcus Herlitschke. Thank you for many beamtimes spent for Ir project during your rush hours, and for detailed explanation of NRS background.

A large part of this work is dedicated to the technical development at the beamline. I would like to thank beamline engineer Frank-Uwe Dill for many technical assistances at the beamline, and especially for the crystal holders for the 73 keV monochromator. I really profited from his accuracy and experience in mechanical setups. Engineers Andrey Siemens and Simon Mayer are gratefully acknowledged for engineering of several parts for the backscattering monochromator. Photon Science Sample environment group, especially to Anita Ehnes and Iris Schwark receive an outstanding acknowledgement for the preparation of the part for the backscattering monochromator and many technical assistances. Their flash-like and sophisticated technical ideas made many challenges acceptable.

Many experimental data measured in this work had to be interpreted by dynamical the-

ory of nuclear scattering. Dr. Wolfgang Sturhahn is greatly acknowledged for sharing the new CONUSS version for NRS on iridium with me, and several deep and very useful discussions concerning to radiation mixing and operation of CONUSS software.

I want to thank Dr. habil. Yuri V. Shvyd'ko for pointing me to several important theoretical papers on high-resolution monochromators, for his self-explaining work with sapphire backscattering monochromator, and software spectr/backspec/reflex which I intensively used in my work.

Many DESYaners, incl. Dr. André Rothkirch, Dr. Teresa Nunez and Photon Science IT department are highly acknowledged for implementing many software ideas. Especially I would like to thank Manfred Spiwek for preparing the silicon crystals for the medium resolution monochromator. Dr. Hanns-Peter Liermann and Dr. Martin Etter (P02 beamline) are acknowledged for the XRD measurements on elemental Ir.

I am thankful to my beamline mates Manuel Harder, Dr. Georg Spiekerman (don't forget Saure-Gurken-Zeit and Soul Kebab), Dr. Hlynur Gretarsson, Dr. Hasan Yavaş for a pleasant working atmosphere and our outings. Especially I thank Georg for teaching me the operation of the Raman setup and Hlynur for the discussions on iridate physics and interesting tricks in Raman spectroscopy which helped me to orient iridate crystal for NFS measurements. I thank my colleagues from the DESY's Magnetism and Coherent Phenomena Group, namely Kai Schlage and Cornelius Strohm for participating in several experiments and useful discussions of the results; Lars Bocklage, Christian Frederic Adolff, Carolin Behncke, Hanno Haber, Denise Erb, Tatyana Guryeva, Svenja Willing, Jade Comfort, Andrey Siemens and Jakob Gollwitzer are acknowledged for their individuality, commitment and humor forming a pleasant working atmosphere. I'm also thankful to Dr. Dimitris Bessas and Atefeh Jafari for their assistance in several beam-times, remarks on the manuscript for the backscattering monochromator, and sharing their experience from ESRF. I'm grateful to Dr. Benedikt Klobes for careful explanations of the Mössbauer effect and our endeavors into the theory of NIS. I thank my mates from the music band (a.k.a. "DESY MSK band") for our musical training evenings. Dr. Anna Pakhomova is acknowledged for our tango classes and the social atmosphere which made writing more relaxing. Dr.-Ing. Salman Steinholz (Düsseldorf) is acknowledged for the interesting engineering discussions and for his motivating point of view.

I thank the secretaries Barbara Daegener (Jülich), and Christina Newiger (DESY) for many answers on organizational questions and for making many paper work easy.

Family Plotnikow is greatly appreciated for hosting me during my spontaneous trips to Brandenburg a.d. Havel.

Last but not least, I want to thank my family, especially my mother, for her love, believe, and outstanding support during whole years.

Pavel Alexeev

Curriculum Vitae

Kroonhorst 57
22549 Hamburg
Germany

+49 176 648 537 88

alex.pavel@hotmail.de

11.08.1988



Education

- 2013–2017 **Ph.D. in physics**, *University Hamburg*, Hamburg, Germany.
Thesis: "Nuclear Resonance Scattering Study of Iridates, Iridium and Antimony Based Pyrochlores" (magna cum laude).
- 2009–2011 **Diploma in engineering**, *Technische Universität Bergakademie Freiberg*, Freiberg, Germany.
Thesis: "Investigation of oxygen distribution in Czochralski silicon crystals of diameter 210 mm grown in different conditions" (very good).
- 2005–2011 **Diploma in material science**, *National Research and Technological University "Moscow Institute for Steel and Alloys"*, Moscow, Russia.
Engineer in material science (very good).

Work experience

- July 2016 – **Scientist**, *Deutsches Elektronen-Synchrotron DESY*.
Development of hyperfine spectroscopy on iridates with synchrotron radiation; x-ray optics at P01 Dynamics Beamline.
- March 2013 – **Ph.D. student**, *Deutsches Elektronen-Synchrotron DESY and Forschungszentrum Jülich GmbH*.
June 2016
Development of the optics for hard x-rays at P01 Dynamics beamline of PETRA III x-ray source (sapphire and silicon monochromators for 10-80 keV x-rays); experiments on superconductors and thermoelectrics at the P01 beamline and at ID18 beamline of ESRF (Grenoble, France).
- August 2011 – **Process engineer**, *Bosch Solar Energy AG*, Arnstadt, Germany.
- February 2013 Technological support of 32 silicon crystal growth devices; technical support of quality control. Topics: optimization of silicon crystal growth process, design of hot zones; FTIR, luminescence measurements on silicon
- January– September Working student at
Institute of Electronic and Sensor Materials of
2010 Technische Universität Bergakademie Freiberg. Topics: capacitance spectroscopy, vapor deposition
- November Working student at
2005– Department for Silicon Crystal Growth of
September "Podolski Chimiko-Metallurgicheskiy Zavod" AG. Topics: resistivity and lifetime
2009 measurements on silicon, help with crystal growth process.

Skills

Physics	X-ray optics. Nuclear Resonance Scattering. Spin-orbit coupling effects in Iridium. Designing of high-resolution monochromators, synchrotron radiation beamline for highly resolving optics.
Material science	Silicon crystal growth via Czochralski and Heat-Exchange methods. Oxygen and carbon control in silicon. IR absorption spectroscopy, resistivity, carrier lifetime measurements on Si, Ge, GaAs, ZnO. Test of sapphire x-ray reflectivity. Probes of electronic structure in iridates.
Cryogenics	Designing of flow cryostats for 5-400 K temperatures. sub-mK precise temperature measurement and control.
Production	SAP, Bosch production norms.
Programming	C/C++, Python (incl. PyQT), Shell, TeX.
General purpose software	MS Windows, Linux, MS Office.
Specialized software	Origin, Autodesk Inventor, Solid Edge, MS Office.
Driver's license	Russian, German (both of B categories).

Languages

Russian	native language
German	DSH certificate, C2 level
English	Excellent, C2 level

Hobbies

Cross-country ski, swimming, guitar.